



Minimal models for finite particles in fluctuating hydrodynamics

Florencio Balboa Usabiaga

Departamento de Física Teórica de la Materia Condensada
Universidad Autónoma de Madrid

Director: Rafael Delgado Buscalioni

Memoria presentada para optar al grado de
Doctor en Ciencias Físicas

Madrid, Enero 2014

© Florencio Balboa Usabiaga, 2014
All rights reserved

Contents

Agradecimientos	9
Abstract / Prefacio	11
1 Introduction	13
1.1 Hydrodynamic time scales and the coarse-grain process	14
1.2 Flow regimes in single phase flows	16
1.3 Flow regimes in particulate flows	17
1.4 Computational methods for single phase and particulate flows	17
1.5 Thesis outline	19
2 Fluid equations of motion	21
2.1 Continuum formulation	22
2.1.1 Fluctuating Navier-Stokes equations	22
2.1.2 Conservative formulation	23
2.1.3 Linearized equations	23
2.1.4 Fluctuation dissipation balance	25
2.1.5 Incompressible limit	32
2.2 Spatial discretization	34
2.2.1 Discrete differential operators	35
2.2.2 Transport coefficients in the discrete formulation	37
2.2.3 Stochastic fluxes	39
2.2.4 Rigid boundaries	40
2.3 Temporal discretization	42
2.3.1 Explicit compressible scheme	43
2.3.2 Semi-implicit incompressible scheme	44
2.3.3 Semi-implicit compressible scheme	46
2.4 Validation	48
2.4.1 Explicit compressible scheme	49
2.4.2 Semi-implicit incompressible scheme	49
2.4.3 Semi-implicit compressible solver	51
2.4.4 Dynamic structure factor	52
3 Inertial coupling method	59
3.1 Equations of motion	62
3.2 The blob model	63
3.2.1 Derivation of the Inertial Coupling Method	64

3.3	Equations of the ICM	67
3.3.1	Equivalent forms of the equations of motion	68
3.3.2	Energy conservation	69
3.3.3	Fluctuation dissipation balance	70
3.3.4	Incompressible limit	72
3.4	Spatial discretization	74
3.4.1	Notes for the incompressible case	76
3.5	Temporal discretization	76
3.5.1	First order compressible scheme	76
3.5.2	Compressible scheme	79
3.5.3	Incompressible scheme	80
3.6	Validation	85
3.6.1	Steady flows and hydrodynamic radius R_H	86
3.6.2	Deterministic convergence	89
3.6.3	Hydrodynamic forces	92
3.6.4	Equilibrium distribution	94
3.6.5	Velocity autocorrelation function	96
3.6.6	Diffusion Coefficient	99
4	Blob thermomechanical properties	103
4.1	Blob compressibility	104
4.2	Numerical implementation	106
4.3	Energy conservation and equilibrium fluctuations	106
4.3.1	Energy conservation	106
4.3.2	Equilibrium fluctuations	107
4.4	Concluding remarks	109
5	Brownian dynamics	113
5.1	Introduction to the equations of Brownian dynamics	114
5.1.1	Free draining limit	116
5.2	Some Lagrangian methods for Brownian dynamics	116
5.2.1	Cholesky decomposition	117
5.2.2	Fixman's method	117
5.3	Eulerian-Lagrangian Brownian hydrodynamics	119
5.4	Benchmark: dynamics of a colloidal cluster	120
6	Application of fluctuating hydrodynamics: Giant fluctuations	123
6.1	Simplified theory	124
6.2	System modeling	126
6.3	Results	128
7	Applications of ICM: acoustic forces	133
7.1	Acoustic forces: theory	135
7.1.1	Monopolar acoustic forces	137
7.1.2	Dipolar acoustic forces	137
7.1.3	Standing planar waves	138
7.1.4	Acoustic forces in the blob model	138

7.2	Acoustic forces: simulations	139
7.2.1	Monopolar acoustic forces	139
7.2.2	Dipolar acoustic forces	140
7.2.3	Finite size effects: secondary radiation forces	140
7.2.4	Boltzmann distribution and standing waves	142
7.3	Concluding remarks	144
8	Application of Brownian dynamics: Polymers in shear flow	147
8.1	Polymer structure and dynamics: overview	148
8.1.1	Polymer structure	148
8.1.2	Polymer dynamics: the Rouse chain	149
8.1.3	Hydrodynamic effects: the Zimm chain	151
8.1.4	Flow time scales	152
8.2	Polymers in shear flow	152
8.3	Polymer models	154
8.4	Results	155
9	Conclusions / Conclusiones	163
9.1	English	163
9.2	Español	167
A	Fluctuation dissipation theorem	173
B	Finite differential operators in Fourier space	175
C	List of Publications	177
	Bibliography	179

Agradecimientos

Esta tesis es el resultado de la colaboración entre muchas personas con los que he tenido la suerte de trabajar y a los que me gustaría agradecer su ayuda. En primer lugar tengo que dar las gracias a mi director y colega Rafa que siempre ha encontrado tiempo para discutir sobre los problemas que hemos ido encontrando y con el que ha sido un verdadero placer trabajar. Espero haber aprendido de su capacidad para conectar problemas aparentemente lejanos y de su afán por encontrar nuevos temas de investigación. Su paciencia para preparar este manuscrito merecería unos agradecimientos aparte. También quiero agradecer la ayuda de Aleks Donev que prácticamente podría haber sido codirector de esta tesis y del que he intentado copiar parte de su rigor científico, aunque alcanzar su nivel parece difícil. Al resto de coautores también les tengo que dar las gracias porque parte de esta tesis es suya. Aunque no pudimos trabajar juntos durante esta tesis quiero mencionar a Dani Duque, la persona con la trabajé por primera vez un proyecto científico, ojalá podamos volver a colaborar en el futuro.

Fuera del ámbito científico se merecen una mención todas las personas con las que me he reído en estos años; otra vez a Rafa, porque lo que son risas no nos han faltado. A mis compañeros de despacho, Enrique, que me presentó al departamento cuando llegué, a Guilherme, Bernd y la última incorporación Fernando. A los compañeros de comidas, con los que ya no coincido (Pau, Shirley, Laura, Milica, Ferdinand ...) y a los que sigo viendo (Nacho, Stefan, Linda) y en general a todos los compañeros que pasaron por el C-V (Teresa, Diego, Dani ...). Y por último pero no menos importante a mi familia y a la gente del Navarra, ya son muchos años saliendo juntos aunque cada vez nos veamos menos.

Abstract / Prefacio

English

This thesis is devoted to the development of efficient numerical solvers for fluctuating hydrodynamics, in particular, for flows with immersed particles. In the first part of the thesis we develop numerical solvers able to work in a broad number of flow regimes with a high computational performance. To derive thermodynamically consistent set of equations in the continuum and discrete settings we have made use of the augmented Langevin formalism. This formalism predicts the form of the stochastic and thermal drift terms which should be included to satisfy the fluctuation dissipation balance. In this work the dynamic of the fluid is described by the fluctuating Navier-Stokes equations which we discretize with a finite volume method in a staggered grid. We found the staggered grid far superior to collocated grids in ensuring numerical stability for the solvers. Several numerical solvers have been developed to simulate both compressible and incompressible flows, in some cases allowing to use very large time steps thanks to the use of semi-implicit discretizations. The fluid solvers have been extended to solve the dynamics of solute particles. We have developed minimal resolution particle models based on the immersed boundary method. The fluid-particle coupling is based on a no-slip constraint which allows to capture the hydrodynamic forces from the Brownian limit to turbulence and even fast oscillating acoustic flows. All the solvers have been implemented in CUDA to run efficiently on graphical processing units (GPUs) and made available under a free software licence.

In the second part of the thesis we have applied our solvers to some interesting non-trivial problems. A common characteristic of all the problems considered is the high disparity of time scales involved; only by using efficient solvers and minimal models like the ones we derived in the first part of the thesis it is possible to tackle these problems. We have studied giant concentration fluctuations whose characteristic times spans over more than 6 orders of magnitude, proving that approximate Galerkin theories though very useful present discrepancies with experimental results of up to a 50%. Acoustic forces have also been studied, showing a good agreement between numerical results and the Gor'kov predictions. More interesting, we have found that the spatial distribution for a particle immersed in an acoustic potential is given by the Gibbs-Boltzmann distributions, a result that can be explained by the time scale separation between the sound modes and the particle diffusion. As a last application we studied the polymer tumbling under shear flow. This problem is better approached by specialized solvers for the infinite Schmidt number limit, which have also been derived. We found that the dynamic of the polymer in shear flow can be described by three characteristic times related with the flow strength and the polymer interactions.

Español

Esta tesis está dedicada al desarrollo de eficientes métodos numéricos para hidrodinámica fluctuante, en particular, para flujos con partículas inmersas. En la primera parte de la tesis hemos derivado métodos numéricos capaces de trabajar en un amplio rango de regímenes con una gran rendimiento computacional. Para derivar sistemas de ecuaciones termodinámicamente consistentes tanto en la formulación continua como discreta hemos usado el formalismo de Langevin generalizado. Este formalismo predice los términos estocásticos y de *drift* térmico necesarios para satisfacer el balance de fluctuación disipación. En esta tesis el fluido se describe por medio de las ecuaciones de Navier-Stokes fluctuantes, las cuales son discretizadas por un método de volúmenes finitos con mallas desplazadas. Hemos encontrado que el uso de mallados desplazados es muy superior comparado con mallados colocados para garantizar la estabilidad numérica de nuestros algoritmos. Varios métodos numéricos han sido desarrollados para simular tanto flujos compresibles como incompresibles, en algunos casos permitiendo el uso de pasos de tiempo muy largos gracias al uso de técnicas de discretización semi-implícitas. Los algoritmos para las ecuaciones de Navier-Stokes han sido ampliados para poder resolver la dinámica de partículas de sólido y hemos desarrollados modelos de resolución mínima basados en el método de fronteras inmersas (*immersed boundary method*). El acople partícula fluido se basa en la condición de no deslizamiento, la cual permite capturar las fuerzas hidrodinámicas desde el límite Browniano hasta turbulencia e incluso en campos acústicos. Todos nuestros algoritmos han sido implementados en CUDA para poder ser ejecutados eficientemente en tarjetas gráficas (GPU) y han sido liberados bajo una licencia de software libre.

En la segunda parte de la tesis hemos aplicado nuestros algoritmos para estudiar algunos problemas interesantes no triviales. Una característica común de todos los problemas estudiados es la gran disparidad las escalas de tiempo involucradas; sólo por medio del uso de modelos minimalistas y métodos numéricos eficientes como los que derivamos en la primera parte de la tesis es posible abordar estos problemas. Hemos estudiado fluctuaciones gigantes de concentración, cuyos tiempos característicos recorren más de 6 ordenes de magnitud, demostrando que las teorías aproximadas de tipo Galerkin aunque increíblemente útiles pueden mostrar discrepancias con los resultados experimentales de hasta un 50%. También han sido estudiadas las fuerzas acústicas, obteniéndose un buen acuerdo entre los resultados numéricos y los predichos por la teoría de Gor'kov. Más interesante, hemos observado que la distribución espacial de una partícula en un campo acústico viene dada por la distribución de Gibbs-Boltzmann, lo cual se puede explicar por la gran diferencia entre los tiempos característicos de los modos acústicos y del movimiento difusivo de la partícula. Como última aplicación hemos estudiado el movimiento rotatorio de un polímero bajo un flujo de cizalla. Este problema se puede abordar mejor con algoritmos especializados para trabajar en el límite de número de Schmidt infinito, los cuales también hemos derivado. Se ha encontrado que es posible describir la dinámica de un polímero en un flujo de cizalla por medio de tres tiempos característicos relacionados con la intensidad del flujo y las interacciones constitutivas del polímero.

Chapter 1

Introduction

Contents

1.1	Hydrodynamic time scales and the coarse-grain process	14
1.2	Flow regimes in single phase flows	16
1.3	Flow regimes in particulate flows	17
1.4	Computational methods for single phase and particulate flows	17
1.5	Thesis outline	19

Fluid mechanics is the natural science of liquid and gas flow. Its scope is probably one of the largest in physics, covering from few nanometers to parsecs and governing the dynamics of tiny colloids up to the motion of nebulae in the interstellar space. Such broad applicability come from solid foundations deeply rooted in few fundamental physics laws. Specifically, the basic set of hydrodynamic equations derive from the conservation of mass and momentum (Newton's Second Law) added to the First and Second Laws of thermodynamics which provide energy conservation and positive entropy production [de Groot 1984, Landau 1987].

The second fundamental leg of hydrodynamics is the continuum assumption which permits working with density fields (of mass, momentum, energy, etc.), instead of dealing with the much larger set of mechanical properties of the underlying fluid molecules. The continuum assumption requires some form of local equilibrium at each fluid infinitesimal point. This is needed for two reasons: First, from the thermodynamic side, local hydrodynamic variables (density, pressure, energy density, etc.) should be possibly defined and should satisfy the macroscopic relations (equation of state, etc.). Second, from a rheological standpoint, each fluid point should respond to the local strain in the same way as a macroscopic sample under the same (local) thermodynamic constraints. This means that all transport coefficients, viscosity, heat and mass diffusion should be at most functions of the set of hydrodynamic variables: such closure being coded in the constitutive relation of the material. These assumptions generally set the limit of applicability of deterministic hydrodynamics above micron scales. However, the hydrodynamic framework can be generalized in several ways like fluctuating hydrodynamics [Landau 1987, de Zárate 2006] or generalized hydrodynamics [Boon 1991]. Recently, some efforts are being directed to derive the hydrodynamic equations from first principles using projector operators techniques [Español 2004]. We believe this route will benefit the present work by providing connections with the microscopic dynamics of the system.

The goal of this thesis is to derive state of the art solvers for fluctuating hydrodynamics suitable for a broad class of flows and physical scales and allowing for further layers of complexity like boundaries, forcing terms and notably immersed particles. In deriving the equations of motion for different

systems we have followed two main guidelines: First, we adhere to the augmented Langevin formalism [Ramshaw 1986] to ensure that our continuum equations of motion respect the thermodynamics. We have found that this approach, closely related to the GENERIC formalism [Grmela 1997, Öttinger 2005], is quite useful to extend deterministic equations to the fluctuating regime in isothermal environments. This formalism reveals the necessity of including additional terms not present in the deterministic regime which in general are not easily predicted, such as the drift terms. Our second guideline has been to work with discretized operators which satisfy the essential relations of their continuum counterparts (notably, adjoint properties); therefore, ensuring conservation laws, fluctuation dissipation balance and other fundamental features. To solve the hydrodynamic equations of motion we have chosen to work with finite volume methods since they can naturally deal with stochastic terms and moreover they can use very large time steps compared with Lagrangian solvers such as smoothed particle hydrodynamics (SPH). Also, finite volume methods take advantage of all the knowledge acquired by the computational fluid dynamics (CFD) community over the years [Patankar 1980]. We have coupled these fluid solvers with another layer of algorithms to describe the dynamics of immersed particles (solute) [Dünweg 2009]. To that end, we have adapted the immersed boundary method (IBM) [Peskin 2002] and developed minimal resolved particle models able to solve, with considerable accuracy, the dynamics of solute particles in a wide number of flow regimes, with completely different Mach, Reynolds, Schmidt or Péclet numbers. Moreover, our minimal models can be extended to include non-trivial thermodynamic properties, such as particle compressibility, neglected in other approaches. Finally, to be really useful, a solver has to be efficiently implemented. We coded our solvers to run on graphical processing units (GPUs), with a single GPU providing the same computational power that a small cluster of CPUs for a much smaller price. Although fair performance comparisons between software is difficult, we can say that our code running on 1 GPU is at least as fast as a parallel code running on 100 CPU cores. Our codes have been made available under a free software license [Usabiaga] to contribute to the soft matter and computational fluid dynamics communities.

We expect that the numerical solvers derived in this thesis will become useful to study complex fluids and the wide number of technological applications around them. In fact, most of the methods derived in Chaps. 3 and 4 could be implemented, for example, in Lattice Boltzmann methods, which will expand the number of possible users. As a demonstration of the versatility of our solvers we will present results for nonequilibrium systems under quite different conditions. We will study giant fluctuations on binary mixtures [Vailati 2011], acoustic radiation forces [Settnes 2012] and polymer tumbling under shear flow [Smith 1999]. However, the same schemes or close variations of them can study other problems relevant to the soft matter community such as microfluidics and lab-on-a-chip technologies [Lenshof 2010], active matter [Marchetti 2013] or polymer melts [Doi 1994], just to name a few.

1.1 Hydrodynamic time scales and the coarse-grain process

Two of the main challenges to study complex fluids are the large number of degrees of freedom and the many length and time scales involved in a single system. Although the scope of hydrodynamics is much broader, to discuss the relevant length and time scales of fluctuating hydrodynamics it is very helpful to consider the motion of a colloid of typical radius $R = 1\mu\text{m}$ immersed in water [Padding 2006].

The fastest process relevant to the colloidal motion is the atomic collisions that originate the Brownian diffusion. These collisions take place at the scale of femtoseconds ($\tau_{\text{col}} = 10^{-15}\text{s}$). The next fastest process is the velocity decorrelation of the solvent molecules, typically, this process takes place one or two orders of magnitude later $\tau_f = 10^{-14} - 10^{-13}\text{s}$. These two processes are essential at submicron scales, however, as we will see in Chap. 2 it is possible to model thermal fluctuations without solving the

fluid at molecular scales. Usually, this is done by including Markovian stochastic forcing terms, which is well justified for times $t \gg \tau_f$, when the solvent molecules are really decorrelated.

The next times relevant to the colloidal dynamics are the transport of momentum by hydrodynamic modes. One can define the sonic time as the time it takes a sound wave to travel one colloidal radius, in water $\tau_c = R/c \approx 10^{-9}$ s. The other mechanism for the transport of momentum is vorticity diffusion which is controlled by the kinematic viscosity of the fluid ν . The time it takes the vorticity to diffuse over one colloidal radius is $\tau_\nu = R^2/\nu \approx 10^{-6}$ s, around 1000 times slower than the sonic time. This inherent separation of time scales makes evident the challenge of simulating hydrodynamic flows even for a Newtonian fluid.

The consideration of solute particles leads to some other time scales: The Brownian time τ_B measures the colloid velocity decorrelation time and it can be written as function of the viscous time and the particle fluid density ratio $\tau_B = (2/9)(\rho_p/\rho_f)\tau_\nu$. For most colloids τ_B and τ_ν are of the same order of magnitude (although there are special cases, like bubbles). τ_B gives the scale at which particle inertial effects are important even at low Reynolds numbers. Also, this time indicates how fast the particle velocity adapts to the surrounding flow velocity field due to the viscous drag. Neutrally buoyant particles are simply transported by the flow as passive tracers (at least in the limit of very small particles) while heavy particles deviate from the flow Lagrangian trajectories.

The slowest and in many problems most relevant time is the colloidal diffusion time. It can be defined as the time it takes a colloid to diffuse its own radius, typically $\tau_\chi = R^2/\chi = 1$ s. With this discussion we wanted to show that the relevant colloidal times are spanned over too many orders of magnitude to accurately resolve all of them. Moreover, the dependence of these times with the length scale is different for each of them. For example, the collision time τ_{col} arises from the molecular details of the solvent and therefore it is independent of the colloidal size. On the other hand, the sonic time τ_c grows linearly with the distance traveled by the acoustic waves and the diffusive times τ_ν and τ_χ grows with the square of the diffusive distance. One can see that these different scalings only broaden the separation of time scales.

Evidently, no numerical solver can simulate the dynamics of a system over 15 orders of magnitude, therefore, a coarse-graining procedure have to be employed. The idea behind the coarse-grain is to reduce the time scales (also the number of degrees of freedom) involving in the system while maintaining the correct physics at the level of resolution desired [Español 2004]. To address this problem we follow two routes simultaneously: First, we completely eliminate the fastest characteristic times of the system while maintaining their associated physical effects if necessary. For example, in our coarse-grained description we do not resolve the molecular scales, and in this way, the fastest process in the system is increased by 6 orders of magnitude (from $\tau_{\text{col}} = 10^{-15}$ s to $\tau_c = 10^{-9}$ s). However, the crucial effect of the molecular motion, generating the hydrodynamic fluctuations, is maintained by including Markovian stochastic terms in the hydrodynamic equations [Landau 1987]. Another example is the speed of sound c . If in a given problem the Mach number is small and the density fluctuations effects are not considered important it is possible to take the incompressible limit, i.e. $c \rightarrow \infty$, which consistently removes the sonic transport from the description. Our second coarse-grain strategy is to reduce the separation of time scales while preserving the correct hierarchy. This second route is problem dependent and it will be discussed in more detail whenever we use it. Just as an example consider the ratio between the viscous and colloidal diffusive times, the so-called Schmidt number $\text{Sc} \sim \tau_\chi/\tau_\nu$; in typical colloidal systems the Schmidt number takes values close to 10^6 , however, to recover the correct physics in most cases it is completely safe to reduce the separation of time scales to just two orders of magnitude [Padding 2006, Usabiaga 2013c].

1.2 Flow regimes in single phase flows

The scope of this work is length scales at which thermal fluctuations become important. The relevance of the fluctuations can be determined by the dimensionless Boltzmann number Bo , that measures the relative amplitude of the thermal fluctuations of some magnitude, for example, the fluid velocity $v(\mathbf{r}, t)$, respect to the steady state [Dünweg 2009]

$$\text{Bo} = \frac{(\langle v^2 \rangle - \langle v \rangle^2)^{1/2}}{\langle v \rangle} = \frac{1}{\langle v \rangle} \sqrt{\frac{k_B T}{\rho l^3}}, \quad (1.1)$$

where in the second equality we have used the mean square velocity of a volume of fluid l^3 at thermal equilibrium. The strong dependence with the system size, $\sim l^{-3/2}$, implies that at macroscopic lengths any nonvanishing flow tends to overcome the effect of the fluctuations. However, as the length scale is reduced the fluctuations becomes increasingly important. Also, Eq. (1.1) is important because it shows that fluctuations are the dominant process at any length scale if there are not macroscopic flows, i.e. $\langle v \rangle = 0$. The giant concentration fluctuations under microgravity studied in Chapter 6 illustrates an example of this fact.

Besides the above discussion about the importance of fluctuations in a wide number of length scales, in this thesis we will restrict our attention to some flow regimes. The limit of validity of our approach can be discussed upon the different dimensionless numbers that characterize the flow regimes. First, we will only consider systems where the continuum approximation for Newtonian flows is well justified. This condition holds if the characteristic observation length l is much larger than the molecular mean free path λ and it is obeyed for practically every length scale above the atomic scale if the Knudsen number Kn (the ratio between the molecular mean free path and the molecular size) is much smaller than one. This is indeed the case for liquids, which are the subject of study of this thesis. Therefore, we will always assume that $\text{Kn} \ll 1$. We want to stress, however, that even for rarefied gases the continuum approach is valid if the observation length is large enough.

Another important dimensionless number to take into account is the Mach number, which measures the ratio between the typical flow velocities v and the speed of sound c , i.e., $\text{Ma} = v/c$. In this thesis we will work with flows in the range $0 \leq \text{Ma} < 1$. A simple balance relation between convective and pressure forces indicates that $\rho v^2 \sim c^2 \delta \rho$, so $\text{Ma}^2 \sim \delta \rho / \rho$ and $\text{Ma} \rightarrow 0$ means that the density variations are negligible and the flow behaves as an incompressible fluid where the density is constant through all the sample. This limit is useful to eliminate fast degrees of freedom related to the sonic transport of momentum whenever they do not play an important role in the physics of the system. The low Mach limit corresponds to cases where density fluctuations are small but not negligible. For example, in ultrasonic forces induced by acoustic tweezers [Haake 2005a], where the flow velocity is still very small compared with the fluid speed of sound (equivalently when the density fluctuations are very small compared with the average density, $\delta \rho / \rho \ll 1$). Finally, some of the schemes developed in this thesis are appropriate (or can be modified) to work in fully compressible flows where the Mach number is large $\text{Ma} \sim 1$ but still do not present shock waves.

The Reynolds number $\text{Re} = vl/\nu$ measures the relative importance of the inertial forces $\sim \rho v^2/l$ over the viscous forces $\sim \eta v/l^2$ along a typical length size l , where η is the dynamic viscosity and $\nu = \eta/\rho$ the kinematic viscosity. We are interested in solvers able to work up to the turbulent regime $\text{Re} > 10^3$. The zero Reynolds regime is important in multitude of microflows, which usually are driven by viscous forces. However, there are a large number of applications where the Reynolds number is large and in fact, an active line of research is to study the effect of finite size solute particles in turbulent flows [Balachandar 2010].

The last dimensionless number that we use to characterize the flows is the Strouhal number, $St = \lambda/(v\tau)$. It is a measure of the ratio between the convective time λ/v and the characteristic time of the system τ . When $St \ll 1$ the flow varies very slowly and it can be approximated by a succession of steady states. We have developed schemes to work at arbitrary Strouhal numbers as well as specialized solvers for $St = 0$. This last limit allows us to neglect the unsteady inertia term, $\rho\partial_t v$, in the fluid equations of motion and to employ larger time steps.

1.3 Flow regimes in particulate flows

In the presence of particles some additional times and dimensionless numbers have to be considered. In the first place, at equilibrium particles follow a diffusive motion. The ratio between the particle diffusion coefficient and the kinematic viscosity gives the Schmidt number $Sc = \nu/\chi$. As we said, typical colloidal solutions have a very large Schmidt number ($Sc \sim 10^6$), we have developed schemes to work with arbitrary Sc and also a specialized solver for $Sc = \infty$, corresponding to the so called Brownian limit of hydrodynamics. This Brownian solver eliminates the stiffness associated with the viscous modes and therefore can use larger time steps.

If the fluid is not at thermal equilibrium other dimensionless numbers become relevant. Mainly the Péclet number $Pe = Rv/\chi = Re_p Sc$, which is just the the ratio between the advective and diffusive transport of particles over the colloid size and where $Re_p = vR/\nu$ is the particle Reynolds number, defined in terms of the particle radius R . The Péclet number indicates how important is the convective flow relative to the thermal diffusion, in the limit $Pe \gg 1$ thermal fluctuations can be neglected while for the rest of flow regimes they have to be taken into account. The particle Reynolds number determines the relevance of convection at the particle scale. Most of the previous studies in particle turbulence assume the point-particle limit [Balachandar 2010], where $Re_p = (R/l)Re \ll 1$ and the particles do not affect the fluid motion. However, that small (but finite) particles inside a turbulent flow ($Re \gg 1$ at macroscopic scales l), can provide a significant value of $Re_p \sim \mathcal{O}(1)$. This is an important regime for the turbulent community that it is trying to unveil the role of small (but finite size) particles in modifying the turbulent energy dissipation [Balachandar 2010].

In the next section we review the methods typically used for fluctuating hydrodynamics and discuss in what regimes they can work. Then, we explain our approach and how our numerical solvers are adequate for a large number of flow regimes.

1.4 Computational methods for single phase and particulate flows

We are interested in numerical solvers that can work in all the regimes considered above with a reasonable efficiency. Many solvers have been derived along the years but usually they are confined to a particular flow regime or present other kind of problems. There are several classifications that can help us to decide the best approach for fluctuating hydrodynamics. In this thesis we assume that the hydrodynamic fields are correctly described by the fluctuating Navier-Stokes equations, therefore, a first classification can be made between methods that solve those equations (with the necessary numerical approximations) and methods that reproduce the hydrodynamic motion by solving the dynamics of some idealized fluid model.

Between the second class of solvers there are popular methods such as dissipative particle dynamics (DPD) [Hoogerbrugge 1992, Español 1995], stochastic rotation dynamics (SRD) [Malevanets 1999, Padding 2006] or even the Lattice Boltzmann method [Ladd 1994, Dünweg 2009]. As we explained in the introduction, the hydrodynamic behavior naturally emerges from the conservation of mass and

momentum at large scales, therefore, it is not surprising that methods that obeys such conservation laws do recover the hydrodynamic behavior at the appropriate length scales. Even molecular dynamics can be used to model the Navier-Stokes equations although at a prohibitively high computational cost. The problem of all these methods is that they provide poor control of the fluid properties, such as its transport coefficients or equation of state. Moreover, to approximate the separation of time scales between different physical process, these methods usually require to use either many particles or too small time steps, which reduce their computational efficiency. Despite their problems it is fair to mention that these methods are also easy to implement and very versatile, in fact, they can easily include complex boundary conditions (specially DPD or SRD methods) and solute particles. These are some of the reasons why they have become so popular in the soft matter community.

The second class of solvers, that we favor, directly solve the fluctuating Navier-Stokes equations. These methods have the important advantage of providing an accurate control of the fluid properties. They can be further divided in Lagrangian and Eulerian solvers. The Lagrangian methods employ moving parcels of fluid that follow the Lagrangian trajectories to solve the fluid equations of motion. Eulerian methods solve the flow through fixed cells (or at fixed points) in the space, therefore, they require to discretize the space with either regular or unstructured meshes [Trottenberg 2001] that can remain fixed during the simulation or self adapt to the flow [Hu 2001, Griffith 2007]. Between the Lagrangian methods stand out the smoothed dissipative particle dynamics (SDPD) [Español 2003], a variant of the smoothed particle hydrodynamics (SPH) [Monaghan 1992] that includes thermal fluctuations. This method combines the advantages of the DPD methods with a good control of the fluid properties. However, it also share some of its disadvantages such as the necessity of use small time steps or very large number of particles to correctly describe hydrodynamic flows. Traditionally, the computational fluid dynamics community has preferred to use Eulerian solvers. They directly solve the Navier-Stokes equations, therefore, providing a perfect control of the equation of state and the fluid transport coefficients and moreover, they allow to use efficient solvers adapted to each flow regime and thus allowing for larger time steps. As the Lagrangian methods do, they can include thermal fluctuations in the form of stochastic forcing terms, as proposed by Landau, and can include boundary conditions (although to implement them is not so easy as with the Lagrangian descriptions). In this thesis we decided to use Eulerian solvers with regular grids because they are the most efficient solvers that can be found.

As we said, over the fluid solvers we include another layer of algorithms to solve the dynamics of solute particles such as colloids, polymers, membranes or other kind of structures. Some Eulerian solvers adapts the fluid mesh to follow the moving particles, such methods can provide very accurate results but only at a high computational cost [Hu 2001]. Other methods employ a fixed Eulerian mesh to solve the Navier-Stokes equations while the immersed particles move freely through the space, these are the so-called Eulerian-Lagrangian methods. This subgroup can employ very efficient solvers for the Navier-Stokes equations while they are still flexible enough to include all kind of immersed structures [Atzberger 2011]. The immersed boundary method (IBM) [Peskin 2002] is a prominent algorithm in the Eulerian-Lagrangian family. We will discuss in more detail the different kinds of solvers in the Chapter 3. Here we announce that we will use Eulerian-Lagrangian solvers together with a minimal resolved particle model inspired in the IBM and adapted to our Navier-Stokes solvers. Minimal models for particles immersed in liquids intend to capture the essence of complex fluid flows with low computational requirements. They are frequently used in the soft matter community to represent large solute molecules [Dünweg 2009] and also in turbulence, to represent particle laden flows [Balachandar 2010]. The main difference between our approach and other minimal models is the modeling of the fluid-particle coupling. Most methods assume that the fluid-particle force is correctly modelled by the Stokes drag $\mathbf{F} = \zeta(\mathbf{v} - \mathbf{u})$ where ζ is a friction coefficient and $(\mathbf{v} - \mathbf{u})$ the difference between the fluid and particle velocities at the particle site. However, such force is only appropriate for zero Reynolds number

and moreover, to capture very fast forcing such as acoustic forces it would require incredibly large friction coefficients which causes numerical problems. Following the IBM we treat the fluid-particle force as a Lagrangian multiplier to enforce what we shall loosely call “no-slip constraint”, which just reflects that the particle and the fluid at the particle site share the same velocity. An important outcome of this approach is that our coupling can correctly capture the drag force at high Reynolds numbers. We will show how this choice is adequate to study particulate flows in all the flow regimes considered in this introduction.

1.5 Thesis outline

As we said the research topic of this thesis is the development of efficient solvers for fluctuating hydrodynamics. We devote the first part of the thesis to present the numerical solvers while in the second part we prove their potential by studying some nontrivial problems. The thesis is divided into the following chapters:

- **Chapter 2** In this chapter we introduce the equations of fluctuating hydrodynamics for a Newtonian fluid described by its mass density, momentum and a passive scalar (in particular, a concentration field). Then, we present the augmented Langevin formalism that will be used during the thesis to derive systems of equations that obey the fluctuation dissipation balance (FDB). The important incompressibility limit ($\text{Ma} \rightarrow 0$) is discussed and then, we explain how to discretize the fluctuating hydrodynamic equations in space and time in a manner that respects the FDB. We finish this chapter with some validation tests for the developed schemes.
- **Chapter 3** Here we derive a minimal resolution model to simulate solid particles of solute immersed in a fluctuating fluid. We make use of the augmented Langevin formalism to ensure that our model is consistent with the FDB. After the equations in the continuum setting are derived and discussed we explain how to discretize them both in the compressible and incompressible settings. We finish the chapter by presenting a large number of tests to assert the ability of our method to study particulate flows in a wide number of flow regimes.
- **Chapter 4** We extend the minimal model presented in the previous chapter to simulate particles with a different compressibility than the one of the carrier fluid. We briefly discuss the possibility of extending this idea to include other thermodynamic properties in minimal models and how the equations of motion can be derived by using the augmented Langevin formalism introduced in Chap. 2.
- **Chapter 5** In this chapter we take the limits of $\text{Re} \rightarrow 0$ and $\text{Sc} \rightarrow \infty$ for the minimal model derived in Chap. 3. Then, we explain how to solve the equations by mean of purely Lagrangian and Eulerian-Lagrangian methods.
- **Chapter 6** Here we use the solvers of Chap. 2 to study the problem of giant fluctuations of concentration in a binary mixture under a temperature gradient. First, it is shown that a temperature gradient can create a concentration gradient due to the Soret effect. Next, it is shown that velocity fluctuations can advect concentration to create concentration fluctuations whose amplitudes diverge with the size of the fluctuations which can become macroscopic. The numerical results agree well with the experimental results of Vailati et al. [Vailati 2011] and show that an approximate Galerkin theory presents deviations up to a 50%.

- **Chapter 7** In this chapter an application of the schemes of Chaps. 3 and 4 is presented. We show that our schemes permit to reproduce the radiation forces exerted by acoustic forces on small particles with an arbitrary contrast factor. We create a standing planar pressure wave by introducing a periodic forcing in a plane of the simulation box. Under that pressure we show that the acoustic forces agree well with the Gor'kov potential forces [Gor'kov 1962]. This is a challenging test that most actual solvers are not able to track without a very high computational cost.
- **Chapter 8** In this chapter we study the dynamic of a single polymer chain under shear flow. This chapter serves us to present a possible application for the schemes derived in Chap. 5. We found that under shear, flexible polymer chains follow a periodic rotational motion controlled by the flow shear strength and whose dynamics can be described by three characteristic times. The tumbling time τ_{tumb} which controls the polymer rotational frequency in the shear flow, a diffusive time τ_{diff} , which measures the internal reorganization of the polymer chain and finally the lag time τ_{lag} , which measure the polymer's response time along the flow direction after a perturbation in the gradient direction. With just these three parameters the main features of a the polymer dynamics under shear can be explained.
- **Chapter 9** The main results of the thesis are summarized and we discuss some possible lines of research for the future.

Chapter 2

Fluid equations of motion

Contents

2.1	Continuum formulation	22
2.1.1	Fluctuating Navier-Stokes equations	22
2.1.2	Conservative formulation	23
2.1.3	Linearized equations	23
2.1.4	Fluctuation dissipation balance	25
2.1.5	Incompressible limit	32
2.2	Spatial discretization	34
2.2.1	Discrete differential operators	35
2.2.2	Transport coefficients in the discrete formulation	37
2.2.3	Stochastic fluxes	39
2.2.4	Rigid boundaries	40
2.3	Temporal discretization	42
2.3.1	Explicit compressible scheme	43
2.3.2	Semi-implicit incompressible scheme	44
2.3.3	Semi-implicit compressible scheme	46
2.4	Validation	48
2.4.1	Explicit compressible scheme	49
2.4.2	Semi-implicit incompressible scheme	49
2.4.3	Semi-implicit compressible solver	51
2.4.4	Dynamic structure factor	52

In this chapter we address the problem of how to simulate the dynamics of fluids at small scales, where the thermal fluctuation are important but the characteristic lengths are much larger than the molecular size. In a seminal work, Landau and Lifshitz [Landau 1987] proposed to include stochastic fluxes in the Navier-Stokes equations to recover the thermal fluctuation of the equilibrium state. Even if initially the approach by Landau was derived for the linearized version of the Navier-Stokes equations at equilibrium, it has become an standard approach to describe nonlinear systems or systems outside equilibrium [Español 1998, de Zárate 2006].

We present here a method that consistently includes thermal fluctuation in a finite volume scheme for the Navier-Stokes equations in both compressible and incompressible formulations. In section 2.1

we introduce the fluctuating hydrodynamic equations and discuss some of their relevant properties. In section 2.2 we present the spatial discretization of the fluid equations while in Section 2.3 several temporal integrators for compressible and incompressible flows are described. We finish the Chapter with Section 2.4 where we present some numerical results to validate our schemes.

2.1 Continuum formulation

2.1.1 Fluctuating Navier-Stokes equations

The most general setup considered in this work is a binary mixture of perfectly miscible fluids, where in addition to the velocity \mathbf{v} and mass density ρ , the system is described also by the mass density of one of the species ρ_1 , or by the mass concentration $c = \rho_1/\rho$. Although the perfect miscibility approximation may look quite artificial it is a good approximation for many systems, in particular in the limit of very low concentration of one of the species $c \ll 1$. Furthermore, we consider systems where the two species are ideal gases of identical molecular masses $M_1 = M_0$. In this case the mass diffusion coefficient χ times the density is constant $\rho\chi = \rho_0\chi_0$ [Bell 2010] and this will allow us to simplify the dissipative terms in the concentration equation.

The fluctuating Navier-Stokes equations for a compressible binary mixture of two perfect miscible fluids representing the conservation of mass, momentum and the mass of each species are

$$\partial_t \rho + \mathbf{v} \cdot \nabla \rho = -\rho \nabla \cdot \mathbf{v}, \quad (2.1)$$

$$\rho(\partial_t \mathbf{v} + \mathbf{v} \cdot \nabla \mathbf{v}) = -\nabla \pi + \eta \nabla^2 \mathbf{v} + \left(\zeta + \frac{\eta}{3}\right) \nabla(\nabla \cdot \mathbf{v}) + \nabla \cdot \Sigma, \quad (2.2)$$

$$\rho(\partial_t c + \mathbf{v} \cdot \nabla c) = \nabla \cdot (\rho\chi(\nabla c + c(1-c)S_T \nabla T) + \Psi), \quad (2.3)$$

where we have assumed that the shear η and bulk ζ viscosities are constant and that the pressure is a function of the density $\pi = \pi(\rho)$, usually $\pi(\rho) = c_T^2 \rho$ with c_T the isothermal speed of sound. Note that in general the equation of state may have a dependence on the concentration c , but we do not consider this case here. This is equivalent to a zero solutal expansion coefficient $(\partial\rho/\partial c) = 0$. The terms Σ and Ψ represent the stochastic fluxes introduced by Landau and Lifshitz to ensure the thermodynamic consistency in the evolution of the fluctuating fields [Landau 1987]. We will discuss those terms in Section 2.1.4.

The concentration equation illustrates how to include passive scalars into the model. The transport of other fields advected by the fluid velocity, like energy or temperature can be described by an equation similar to (2.3) [de Groot 1984]. In the left-hand side of the concentration equation we have the advective derivative

$$\frac{d}{dt} = \partial_t + \mathbf{v} \cdot \nabla, \quad (2.4)$$

which represents the transport of concentration by the velocity field. In the right-hand side we have a diffusive term times the mass diffusion coefficient χ , a gradient term times the Soret coefficient S_T and the divergence of the stochastic term Ψ . The equation does not include a chemical potential term because we are considering perfect miscible fluids. As we said, in our approximation $\rho\chi = \text{const.}$ which allows us to write the diffusive term in the Laplacian form $\rho\chi \nabla^2 c$. The Soret coefficient produces a mass diffusion for the species when there is a temperature gradient. We will consider problems with a stationary temperature profile $T = T(\mathbf{r})$ where the maximum temperature differences is a few percent. This allows us to make a further approximation, namely to treat the system as isothermal $T(\mathbf{r}) = T_0$ while however we retain the term $S_T \nabla T$ which acts as a forcing term in the concentration equation.

Note that for perfect miscible fluids the concentration field is coupled to the velocity and density fields but these fields are not coupled to the concentration.

To simplify our model we have not included the energy equation in the hydrodynamic description. In doing so we assume that the temperature profile is stationary and that the momentum and energy fields are uncoupled. This is a good approximation if the adiabatic coefficient is close to $\gamma = 1$, which uncouples the energy from the momentum equation in a first order approximation around the equilibrium state [Muller 2012]. We note that for water γ is indeed very close to 1, and therefore neglecting the energy equation seems a reasonable approximation for many problems.

2.1.2 Conservative formulation

In some situations it is preferable to work with the conserved variables density of mass ρ , momentum $\mathbf{g} = \rho\mathbf{v}$ and mass of one of the species $\rho_1 = \rho c$. For example, when implementing the equations it is better to use conserved variables to ensure that the conservation laws are obeyed up to the machine precision. Using the conservation of mass, the Navier-Stokes equations can be written in the conservative form

$$\partial_t \rho + \nabla \cdot \mathbf{g} = 0, \quad (2.5)$$

$$\partial_t \mathbf{g} + \nabla \cdot (\mathbf{g}\mathbf{v}) = -\nabla \cdot [\pi \mathbf{I} - \eta \bar{\nabla} \mathbf{v} - \zeta (\nabla \cdot \mathbf{v}) \mathbf{I}] + \nabla \cdot \boldsymbol{\Sigma}, \quad (2.6)$$

$$\partial_t \rho_1 + \nabla \cdot (\rho_1 \mathbf{v}) = \nabla \cdot [\rho \chi (\nabla c + c(1-c)S_T \nabla T)] + \nabla \cdot \boldsymbol{\Psi}, \quad (2.7)$$

where $\bar{\nabla} \mathbf{v} = (\nabla \mathbf{v} + (\nabla \mathbf{v})^T) - 2(\nabla \cdot \mathbf{v})\mathbf{I}/3$ is the symmetrized strain rate. In these equations the variation of any of the magnitudes $(\rho, \mathbf{g}, \rho_1)$ takes the form of the divergence of a tensor, which guarantees that $(\rho, \mathbf{g}, \rho_1)$ are locally conserved. The conservation of mass, Equation (2.1), can be substituted by the equation for $\rho_2 = (1-c)\rho$, the density mass of the second species. However, we have found that numerically it is better to work with the total density mass ρ . During the rest of the thesis we will use the Navier-Stokes equations in the form of Eqs. (2.1)-(2.3) or in the conservative form Eqs. (2.5)-(2.7), depending on the analysis performed.

2.1.3 Linearized equations

Before taking into account the stochastic terms it is convenient to derive the normal modes of the linearized equations [Boon 1991, Fabritiis 2007]. In this section we calculate the expressions for the normal modes using a general notation valid for the continuum and discrete settings. This notation will allow us later to derive the discrete version of the fluid transport coefficients. We focus on the mass density ρ , velocity \mathbf{v} and concentration c . The equilibrium state of the system is described by the mean values of these variables and the small fluctuations around them. Writing $\rho = \rho_0 + \delta\rho$, $\mathbf{v} = \mathbf{v}_0 + \delta\mathbf{v}$, $c = c_0 + \delta c$ and $\pi = \pi_0 + c_T^2 \delta\rho$ the dynamic equations of motion are, up to first order in the fluctuations,

$$\partial_t \delta\rho = -\mathbf{v}_0 \cdot \nabla \delta\rho - \rho_0 \nabla \cdot \delta\mathbf{v}, \quad (2.8)$$

$$\partial_t \delta\mathbf{v} = -\rho_0^{-1} c_T^2 \nabla \delta\rho - \mathbf{v}_0 \cdot \nabla \delta\mathbf{v} + \nu \nabla^2 \delta\mathbf{v} + \nu_B \nabla (\nabla \cdot \delta\mathbf{v}) + \rho_0^{-1} \nabla \cdot \boldsymbol{\Sigma}, \quad (2.9)$$

$$\partial_t \delta c = -\mathbf{v}_0 \cdot \nabla \delta c + \chi_0 \nabla^2 \delta c + \rho_0^{-1} \nabla \cdot \boldsymbol{\Psi}, \quad (2.10)$$

with the effective bulk viscosity $\nu_B = (\eta/3 + \zeta)/\rho_0$. Note that in thermal equilibrium $\nabla T = 0$. These linear equations can be written as

$$\partial_t \mathbf{U} = \mathbf{H} \cdot \mathbf{U} + \boldsymbol{\mathcal{K}}, \quad (2.11)$$

where we have arranged the hydrodynamic variables in the array $\mathbf{U} = (\delta\rho, \delta\mathbf{v}, \delta c)^T$, introduced the noise term \mathcal{K} (which will be discussed in the following subsection) and the hydrodynamic matrix \mathbf{H} , whose structure is

$$\mathbf{H} = \begin{pmatrix} \mathbf{H}_{\rho\rho}^{1\times 1} & \mathbf{H}_{\rho v}^{1\times 3} \mathbf{H}_{vc}^{1\times 1} \\ \mathbf{H}_{v\rho}^{3\times 1} & \mathbf{H}_{vv}^{3\times 3} \mathbf{H}_{vc}^{3\times 1} \\ \mathbf{H}_{cv}^{1\times 1} & \mathbf{H}_{cv}^{1\times 3} \mathbf{H}_{cc}^{1\times 1} \end{pmatrix}. \quad (2.12)$$

To calculate the normal modes we seek a solution of the equation (2.11) in Fourier space. First, let us define the inverse Fourier transform of a field ϕ by

$$\phi(\mathbf{r}) = \int \hat{\phi}(\mathbf{k}) e^{i\mathbf{k}\cdot\mathbf{r}} d^3k. \quad (2.13)$$

Using the above definition to transform the equation (2.11) one gets an expression for the hydrodynamic matrix \mathbf{H} in Fourier space. Since the Fourier modes of a linear set of equations are uncoupled, without loss of generality we consider the wave vector $\mathbf{k} = (k, 0, 0)$ for which the transformed hydrodynamic matrix takes the form

$$\widehat{\mathbf{H}}_{\mathbf{k}} = \begin{pmatrix} -\mathbf{v}_0 \cdot \widehat{\mathbf{G}}_{\mathbf{k}} & -\rho_0 \widehat{\mathbf{D}}_{\mathbf{k}} & 0 & 0 & 0 \\ -\rho_0^{-1} c_T^2 \widehat{\mathbf{G}}_{\mathbf{k}} & \nu_L \widehat{\mathbf{L}}_{\mathbf{k}} & 0 & 0 & 0 \\ 0 & 0 & \nu \widehat{\mathbf{L}}_{\mathbf{k}} & 0 & 0 \\ 0 & 0 & 0 & \nu \widehat{\mathbf{L}}_{\mathbf{k}} & 0 \\ 0 & 0 & 0 & 0 & -\mathbf{v}_0 \cdot \widehat{\mathbf{G}}_{\mathbf{k}} + \chi_0 \widehat{\mathbf{L}}_{\mathbf{k}} \end{pmatrix}. \quad (2.14)$$

Here we are denoting the Fourier transform of the gradient, divergence and Laplacian operators by $\widehat{\mathbf{G}}_{\mathbf{k}}$, $\widehat{\mathbf{D}}_{\mathbf{k}}$ and $\widehat{\mathbf{L}}_{\mathbf{k}}$ and we have introduced the longitudinal viscosity $\nu_L = (4\eta/3 + \zeta)/\rho_0$ ¹. In the continuum space the expression for these differential operator are just

$$\widehat{\mathbf{G}}_{\mathbf{k}} = i\mathbf{k}, \quad (2.15)$$

$$\widehat{\mathbf{D}}_{\mathbf{k}} = i\mathbf{k}, \quad (2.16)$$

$$\widehat{\mathbf{L}}_{\mathbf{k}} = -k^2, \quad (2.17)$$

however, it is convenient to conserve the general notation ($\widehat{\mathbf{G}}_{\mathbf{k}}$...) to extend the following results to the discrete case, as we do in Section 2.2.1. In the rest frame $\mathbf{v}_0 = 0$, the eigenvalues of $\widehat{\mathbf{H}}_{\mathbf{k}}$ obtained upon diagonalization of the hydrodynamic matrix and related to the shear, sound and concentration modes are

$$\omega_{1,2} = -\nu_{\text{ef}} k^2, \quad (2.18)$$

$$\omega_{3,4} = -\Gamma_{\text{ef}} k^2 \pm i s_{\text{ef}} k, \quad (2.19)$$

$$\omega_5 = -\chi_{\text{ef}} k^2. \quad (2.20)$$

The effective transport coefficients viscosity ν_{ef} , sound absorption Γ_{ef} , speed of sound s_{ef} and mass diffusion coefficient χ_{ef} are given by

$$\nu_{\text{ef}} = -\frac{\nu}{k^2} \widehat{\mathbf{L}}_{\mathbf{k}}, \quad (2.21)$$

$$\Gamma_{\text{ef}} = -\frac{\nu_L}{2k^2} \widehat{\mathbf{L}}_{\mathbf{k}}, \quad (2.22)$$

$$s_{\text{ef}} = -\frac{i}{2k} \sqrt{-4c_T^2 \widehat{\mathbf{D}}_{\mathbf{k}} \widehat{\mathbf{G}}_{\mathbf{k}} - \nu_L^2 \widehat{\mathbf{L}}_{\mathbf{k}}^2}, \quad (2.23)$$

$$\chi_{\text{ef}} = -\frac{\chi_0}{k^2} \widehat{\mathbf{L}}_{\mathbf{k}}. \quad (2.24)$$

¹Note that the longitudinal viscosity term is actually $(\nu \nabla^2 + \nu_B \nabla(\nabla \cdot))$, but for the wave vectors $\mathbf{k} = (k, 0, 0)$ it can be written as $\nu_L \nabla^2$

In the continuum setting these operators simplify to

$$\nu_{\text{ef}} = \nu, \quad (2.25)$$

$$\Gamma_{\text{ef}} = \frac{\nu_L}{2}, \quad (2.26)$$

$$s_{\text{ef}} = c_T \sqrt{1 - \Gamma_{\text{ef}}^2 k^2 / c_T^2}, \quad (2.27)$$

$$\chi_{\text{ef}} = \chi_0. \quad (2.28)$$

Therefore, in the continuum setting, the viscosity, the mass diffusion coefficient and the sound absorption are independent of the wavenumber. Also, for most wavenumbers $\Gamma_{\text{ef}} k \ll c_T$ and the speed of sound can be approximated by $s_{\text{ef}} \approx c_T$. For example, in water with $c_T = 1500 \text{ m/s}$ and $\Gamma = 1.9 \cdot 10^{-6} \text{ m}^2/\text{s}$ the square root of Eq. (2.27) vanishes for a wave length $\lambda \approx 8 \text{ nm}$, where the continuum approximation is questionable, and for $\lambda \gtrsim 30 \text{ nm}$ the speed of sound s_{ef} is almost constant. The hydrodynamic description of the fluid can be extended close to the molecular level by considering the wavenumber dependence of the transport coefficients [Boon 1991, Delgado-Buscalioni 2008a], but we will not consider this possibility here.

With the last approximation ($s_{\text{ef}} = c_T$) the normal modes in Fourier space are given by

$$\hat{\rho}_{\mathbf{k}}(t) = \left(\hat{\rho}_{\mathbf{k}}(0) \cos(c_T k t) - \frac{i \rho_0}{c_T k} \sin(c_T k t) \mathbf{k} \cdot \hat{\mathbf{v}}_{\mathbf{k}}(0) \right) e^{-\Gamma_T k^2 t} \quad (2.29)$$

$$\begin{aligned} \hat{\mathbf{v}}_{\mathbf{k}}(t) &= [\cos(c_T k t) k^{-1} \mathbf{k} \cdot \hat{\mathbf{v}}_{\mathbf{k}}(0) - i \sin(c_T k t) \hat{\rho}_0^{-1} c_T \hat{\rho}_{\mathbf{k}}(0)] \frac{\mathbf{k}}{k} e^{-\Gamma_T k^2 t} + \\ &\quad (\mathbf{I} - \mathbf{k} \mathbf{k} / k^2) \cdot \hat{\mathbf{v}}_{\mathbf{k}}(0) e^{-\nu k^2 t} \end{aligned} \quad (2.30)$$

$$\hat{c}_{\mathbf{k}}(t) = \hat{c}_{\mathbf{k}}(0) e^{-\chi_0 k^2 t}, \quad (2.31)$$

Where the velocity has two transverse modes associated with the viscous transport of vorticity [second term in Eq. (2.30)] and one longitudinal mode coupled with the density and associated with the sonic transport of momentum. Additionally, the concentration relax to equilibrium by an uncoupled dissipative mode.

We expect that the discrete version of the Navier-Stokes equations will recover the continuum normal modes for small enough wavevectors, in practice $kh < 1$ with h the meshwidth (see Section 2.2).

2.1.4 Fluctuation dissipation balance

In this section we present a general discussion of thermal fluctuations and the fluctuation-dissipation balance. The results derived here will be used to prove that the fluctuating Navier-Stokes equations obey the fluctuation dissipation balance in Section 2.1.4.2.

At scales below few micrometers the thermal agitation arising from the molecular motion starts to be revealed in the dynamics of fluid parcels controlling their diffusion and the Brownian motion of solute particles as well. The interplay between these thermal forces and cohesive and friction forces is reflected in the dynamic structure factor of the fluid [Segrè 1993, de Zárate 2006]. Thermal fluctuations can be modeled by including additional stochastic forcing terms in the Navier-Stokes equations (2.1)- (2.3). The stochastic nature of these terms is somewhat paradoxical because the motion of the solvent molecules is, at least in a classical picture, deterministic. It is the lack of information about the microscopic state which makes necessary to include a stochastic component in the description of the system [Donev 2013b].

To recover a dynamic consistent with the thermodynamics and statistical mechanics, not any stochastic forcing can be used. The prescription for the stochastic fluxes should generate fluctuations of the hydrodynamic fields that maximize the entropy at the equilibrium state. Equivalently, the dissipative and

stochastic terms should satisfy the fluctuation dissipation balance (FDB) [Landau 1987, de Zárate 2006]. For systems with conserved energy, the GENERIC formalism has proved very successful in deriving thermodynamic consistent equations [Grmela 1997, Öttinger 2005]. For isothermal systems, where the energy can fluctuate, it is better to use the formalism of augmented Langevin equations [Ramshaw 1986], although both approaches are closely related. Due to the importance of the thermal fluctuations in the work performed during this thesis we first present a general introduction to the augmented Langevin formalism, and then focus on the fluctuating Navier-Stokes equations.

We consider an isothermal system described by a set of coarse-grained variables \mathbf{U} with much larger characteristic times and length scales than the underlying microscopic variables. A typical example is a simple fluid, where the microscopic variables are the positions and momenta of the solvent molecules while the coarse-grained variables are the fluid mass and momentum density fields (ρ and \mathbf{g}). However, to select a right set of coarse-grained variables in a particular system is not always straightforward. A generally valid tip it is to select conserved quantities whenever it is possible, since they tend to be slow compared with the microscopic degrees of freedom. The dynamics of an isothermal system with coarse-grained variables \mathbf{U} and Hamiltonian \mathcal{H} can be described by the Augmented Langevin equation (here interpreted in the Ito sense) [Ramshaw 1986]

$$\partial_t \mathbf{U} = -\mathcal{N}(\mathbf{U}) \cdot \nabla_{\mathbf{U}} \mathcal{H} + \mathcal{K}(\mathbf{U}, \mathbf{W}) + (k_B T) \nabla_{\mathbf{U}} \cdot \mathcal{N}^*(\mathbf{U}), \quad (2.32)$$

where the star * denotes adjoint and the operator $\nabla_{\mathbf{U}}$ is understood to act as $\partial/\partial \mathbf{U}$. If the variables collected in \mathbf{U} are functions, e.g. fields, then $\partial/\partial \mathbf{U}$ should be treated as a functional derivative. We want to ensure thermodynamic consistency in the above Eq. (2.32). Notably, the equilibrium probability density function of the coarse-grained variables should be given by the Gibbs-Boltzmann distribution

$$P_{eq}(\mathbf{U}) = Z^{-1} \exp\left(-\frac{\mathcal{H}(\mathbf{U})}{k_B T}\right) \delta(\mathbf{U} - \mathbf{U}_0), \quad (2.33)$$

where Z is a normalization constant and $\delta(\mathbf{U} - \mathbf{U}_0)$ represent the possible conservation laws for the coarse-grained variables \mathbf{U} . Also, we would like that in the absence of thermal fluctuations the system relaxes by dissipating energy. To find out the required conditions it is convenient to decompose the mobility operator \mathcal{N} , where in the following we omit the possible dependence on the coarse-grained variables \mathbf{U} , into a skew-adjoint \mathcal{L} and a self-adjoint \mathcal{M} parts, i.e.,

$$\mathcal{L} = -\mathcal{L}^* = \frac{1}{2} (\mathcal{N}^* - \mathcal{N}), \quad (2.34)$$

$$\mathcal{M} = \mathcal{M}^* = \frac{1}{2} (\mathcal{N}^* + \mathcal{N}). \quad (2.35)$$

The skew-adjoint character of \mathcal{L} guarantees that

$$(\nabla_{\mathbf{U}} \mathcal{H})^T \cdot \mathcal{L} \cdot (\nabla_{\mathbf{U}} \mathcal{H}) = 0. \quad (2.36)$$

That is, \mathcal{L} conserves the energy. Also often, but not always, the operator \mathcal{L} is incompressible in the phase space of the coarse grained variables $\nabla_{\mathbf{U}} \cdot \mathcal{L} = 0$ which implies that the evolution of the coarse-grained variables due to \mathcal{L} is incompressible in the phase space

$$\nabla_{\mathbf{U}} \cdot (\mathcal{L} \cdot \nabla_{\mathbf{U}} \mathcal{H}) = 0. \quad (2.37)$$

On the other hand, the self-adjoint operator \mathcal{M} should be positive definite to guarantee that in absence of thermal fluctuations ($k_B T = 0$) the dynamic is purely dissipative, that is

$$\frac{d\mathcal{H}}{dt} = (\nabla_{\mathbf{U}} \mathcal{H})^T \cdot (\mathcal{L} - \mathcal{M}) \cdot (\nabla_{\mathbf{U}} \mathcal{H}) = -(\nabla_{\mathbf{U}} \mathcal{H})^T \cdot \mathcal{M} \cdot (\nabla_{\mathbf{U}} \mathcal{H}) \leq 0 \quad (2.38)$$

The last term in the Langevin equation (2.32), referred as thermal drift, ensures that the Gibbs-Boltzmann distribution (2.33) is the stationary solution of the Langevin equation. This is equivalent to say that the dynamic of the system in the phase space of the coarse-grained variables is incompressible with respect the Gibbs-Boltzmann distribution, as it is usually pointed out in the literature [Atzberger 2011, Usabiaga 2012]. In many cases of interest the dissipative matrix \mathcal{M} does not have an explicit dependence on the coarse-grained variables \mathbf{U} and the skew-adjoint operator \mathbf{L} is incompressible, then in those special cases the last term vanishes.

The only term that remains to be introduced is the stochastic forcing $\mathcal{K}(\mathbf{U}, \mathcal{W})$, which stochastic nature is modelled by a random Gaussian tensor $\mathcal{W}(\mathbf{r}, t)$. It is usually assumed that this tensor is delta correlated both in time and space

$$\langle \mathcal{W}(\mathbf{r}, t) \mathcal{W}(\mathbf{r}', t') \rangle = \delta(\mathbf{r} - \mathbf{r}') \delta(t - t'). \quad (2.39)$$

The delta correlation in time, or Markovian assumption, is a valid approximation when the coarse-grained variables evolve much more slowly than the microscopic degrees of freedom that generates the noise. Similarly, the delta correlation in space is a good approximation when the correlation length of the microscopic degrees of freedom is much smaller than the typical lengths described by the coarse-grained variables. To recover the Gibbs-Boltzmann equilibrium distribution the noise filter \mathcal{K} should obey the *fluctuation dissipation balance* in the form [Ramshaw 1986]

$$\begin{aligned} \langle \mathcal{K} \mathcal{K}^* \rangle &= k_B T (\mathcal{N} + \mathcal{N}^*) \delta(\mathbf{r} - \mathbf{r}') \delta(t - t') \\ &= 2k_B T \mathcal{M} \delta(\mathbf{r} - \mathbf{r}') \delta(t - t'). \end{aligned} \quad (2.40)$$

Note that by construction \mathcal{M} is a self-adjoint matrix. To finish the introduction of the augmented Langevin equations we remind that the Langevin equation (2.32) has an equivalent Fokker-Planck equation that determines the evolution of the probability distribution function of the coarse-grained variables [Ramshaw 1986, Risken 1989]

$$\partial_t P = \nabla_{\mathbf{U}} \cdot [\mathcal{N} \cdot (\nabla_{\mathbf{U}} \mathcal{H}) P + (k_B T) \nabla_{\mathbf{U}} \cdot (\mathcal{M} P) - (k_B T) (\nabla_{\mathbf{U}} \cdot \mathcal{N}^*) P]. \quad (2.41)$$

One can use this last equation to prove that the Gibbs-Boltzmann distribution [Eq. (2.33)] is indeed the equilibrium distribution function of the system.

2.1.4.1 Linearization

The systems we will study in this thesis are usually close to thermal equilibrium, therefore, analysis based on linear approximation are quite useful tools. We introduce some general properties of the augmented Langevin equation close to equilibrium and use these results to predict the covariance of the hydrodynamic fluctuating fields in the next section.

Close to equilibrium, the Hamiltonian can be approximated by a Taylor series around the steady state \mathbf{U}_0 ,

$$\mathcal{H}(\mathbf{U}) = \mathcal{H}(\mathbf{U}_0) + \frac{\partial \mathcal{H}(\mathbf{U}_0)}{\partial \mathbf{U}} \cdot \delta \mathbf{U} + \frac{1}{2} \delta \mathbf{U}^* \cdot \frac{\partial^2 \mathcal{H}(\mathbf{U}_0)}{\partial \mathbf{U}^2} \cdot \delta \mathbf{U}, \quad (2.42)$$

where $\delta \mathbf{U} = \mathbf{U} - \mathbf{U}_0$. Equilibrium states correspond to minima of the Hamiltonian, where the linear term in the expansion of the Hamiltonian vanishes. This implies that around equilibrium the Hamiltonian is quadratic in the fluctuations. The general properties of Gaussian distributions allow us to compute the

covariance of the fluctuating variables [Riskin 1989]

$$\begin{aligned} \mathbf{C}_{UU} &= \langle \delta \mathbf{U} \delta \mathbf{U}^* \rangle = Z^{-1} \int (\delta \mathbf{U} \delta \mathbf{U}^*) e^{-\frac{1}{2k_B T} \delta \mathbf{U}^* \cdot \frac{\partial^2 \mathcal{H}(\mathbf{U}_0)}{\partial \mathbf{U}^2} \cdot \delta \mathbf{U}} d(\delta \mathbf{U}) \\ &= k_B T \left[\frac{\partial^2 \mathcal{H}(\mathbf{U}_0)}{\partial \mathbf{U}^2} \right]^{-1}. \end{aligned} \quad (2.43)$$

In the linear regime approximation the augmented Langevin equation (2.32) reduces to

$$\partial_t \delta \mathbf{U} = \mathbf{H} \cdot \delta \mathbf{U} + \mathcal{K}, \quad (2.44)$$

with $\mathbf{H} = -(k_B T) \mathbf{N}(\mathbf{U}_0) \cdot \mathbf{C}_{UU}^{-1}$. It is interesting to note that the linearized Navier-Stokes (2.11) has this structure with \mathbf{H} being the hydrodynamic matrix (2.14). In the linear approximation, the FDB given by the Eq. (2.40) becomes

$$\langle \mathcal{K} \mathcal{K}^* \rangle = -(\mathbf{H} \cdot \mathbf{C}_{UU} + \mathbf{C}_{UU}^* \cdot \mathbf{H}^*) \delta(\mathbf{r} - \mathbf{r}') \delta(t - t'). \quad (2.45)$$

This is the form of the FDB presented in many works [Donev 2010b, Atzberger 2010]. The equation (2.45) is very useful to model and to study fluctuating systems. If \mathbf{C}_{UU} , the covariance of the coarse-grained variables at equilibrium it is known, the equation (2.45) can be used to determine the stochastic terms \mathcal{K} . On the other hand, if the expression for the stochastic term \mathcal{K} it is known at equilibrium, the equation (2.45) can be used to determine the covariance \mathbf{C}_{UU} of non-equilibrium states, assuming that the system is locally at equilibrium and therefore the equilibrium expression for \mathcal{K} is still valid.

2.1.4.2 FDB for the Navier-Stokes equations

In this section we want to do two things. First, we want to show that the Navier-Stokes equation can be cast into the augmented Langevin formalism, and therefore, to show that the fluctuating Navier-Stokes equations obey the fluctuation dissipation balance. Our second goal is to determine the expression for the stochastic terms Σ and Ψ in the equations (2.2) and (2.3) which so far remain undetermined. We will see also that the expression for the stochastic terms agree with the ones found by Landau and Lifshitz for the linearized Navier-Stokes equations [Landau 1987].

Along this section we will use as the primary variables, the density ρ , velocity \mathbf{v} and concentration c , although a similar analysis can be done using conserved variables. For the chosen variables the coarse-grained Hamiltonian of a compressible binary fluid is

$$\mathcal{H} = \int \left(\frac{1}{2} \rho \mathbf{v}^2 + \rho \varepsilon(\rho, c) \right) d^3 r, \quad (2.46)$$

where $\varepsilon(\rho, c)$ is the internal energy per unit of mass. Different expressions for the internal energy give different physics. Here, as in the section 2.1.1, we consider a mixture of perfectly miscible fluids. For this system, the derivatives of the internal energy of the fluid are related to the pressure π and the chemical potential μ by [Callen 1985, Morrison 1998, Bannon 2003]

$$\frac{\partial \rho \varepsilon}{\partial \rho} = \varepsilon(\rho, c) + \rho^{-1} \pi, \quad (2.47)$$

$$\frac{\partial \rho \varepsilon}{\partial c} = \rho \mu(c). \quad (2.48)$$

To derive the equations of motion of (ρ, \mathbf{v}, c) one needs the derivatives of the Hamiltonian respect to the coarse-grained variables,

$$\frac{\partial \mathcal{H}}{\partial \rho} = \frac{1}{2} \mathbf{v}^2 + \varepsilon(\rho, c) + \rho^{-1} \pi, \quad (2.49)$$

$$\frac{\partial \mathcal{H}}{\partial \mathbf{v}} = \rho \mathbf{v}, \quad (2.50)$$

$$\frac{\partial \mathcal{H}}{\partial c} = \rho \mu(c). \quad (2.51)$$

The augmented Langevin formalism also requires the definition of the mobility operator \mathcal{N} . To simplify the exposition we consider first the skew-adjoint part and then the self-adjoint part [recall Eqs. (2.34)-(2.35)]. The reversible part of the mobility that recovers the advective terms of the Navier-Stokes equations is

$$\mathcal{L} = \begin{pmatrix} 0 & -\nabla \cdot & 0 \\ -\nabla & \omega \rho^{-1} & (\nabla c) \rho^{-1} \\ 0 & -(\nabla c)^T \rho^{-1} & 0 \end{pmatrix}, \quad (2.52)$$

where the vorticity tensor is defined by

$$\omega_{ij} = \frac{\partial v_j}{\partial r_i} - \frac{\partial v_i}{\partial r_j}. \quad (2.53)$$

By simply applying \mathcal{L} to $\partial \mathcal{H} / \partial \mathbf{U}$ one recovers the non-dissipative terms of the Navier-Stokes equations (2.1)- (2.3), that is,

$$\partial_t \rho = -\nabla \cdot (\rho \mathbf{v}), \quad (2.54)$$

$$\partial_t \mathbf{v} = -\mathbf{v} \cdot \nabla \mathbf{v} - \rho^{-1} \nabla \pi, \quad (2.55)$$

$$\partial_t c = -\mathbf{v} \cdot \nabla c. \quad (2.56)$$

To derive these results it is necessary to make use of the thermodynamic relations (2.47)-(2.48) and the vector identity [Aris 1962]

$$\mathbf{v} \cdot \nabla \mathbf{v} = \nabla \left(\frac{\mathbf{v}^2}{2} \right) + (\nabla \times \mathbf{v}) \times \mathbf{v}. \quad (2.57)$$

From the Hamiltonian's derivatives (2.49)-(2.51) and the skew-adjoint operator \mathcal{L} a concentration dependent term could have been expected in the velocity equation. However, with our choice of the chemical potential, $\mu = \mu(c)$, all the concentration dependent terms in the velocity equation cancel. This result is specific for perfectly miscible fluids, in general, it is expected that the velocity equation contains a forcing term of the form $\mu \nabla c$ [Lowengrub 1998, Shang 2011].

As required by the augmented Langevin formalism, the operator \mathcal{L} is skew-adjoint ($\mathcal{L} = -\mathcal{L}^*$) because the vorticity tensor defined in Eq. (2.53) is antisymmetric and the divergence and gradient operators are negative adjoint of each other ($\nabla \cdot = -\nabla^*$), something easy to observe in Fourier space [see Eqs. (2.15)-(2.16)].

We consider now the stochastic forcing terms and the dissipative part of the mobility matrix. As we already know, both terms are related by the fluctuation dissipation balance $\langle \mathcal{K} \mathcal{K}^* \rangle = 2k_B T \mathcal{M} \delta(\mathbf{r} - \mathbf{r}') \delta(t - t')$. We postulate that the noise term has the form

$$\mathcal{K} = \begin{pmatrix} 0 \\ \mathcal{K}_v \\ \mathcal{K}_c \end{pmatrix} = \begin{pmatrix} 0 \\ \rho^{-1} \nabla \cdot \Sigma \\ \rho^{-1} \nabla \cdot \Psi \end{pmatrix}, \quad (2.58)$$

where Σ and Ψ are the stochastic terms derived by Landau Lifshitz [Landau 1987]

$$\Sigma = \sqrt{2\eta k_B T} \tilde{\mathcal{W}}_v + \left(\sqrt{\frac{\zeta k_B T}{3}} - \frac{\sqrt{2\eta k_B T}}{3} \right) \text{Tr}(\tilde{\mathcal{W}}_v) \mathbf{I}, \quad (2.59)$$

$$\Psi = \sqrt{\frac{2\chi\rho k_B T}{(\partial\mu/\partial c)}} \mathcal{W}_c = \sqrt{2\chi\rho Mc(1-c)} \mathcal{W}_c. \quad (2.60)$$

where M is the molecular mass of the solvent molecules, Tr represents the trace, $\tilde{\mathcal{W}}_v = (\mathcal{W}_v + \mathcal{W}_v^T)/\sqrt{2}$ and \mathcal{W}_v and \mathcal{W}_c are uncorrelated random Gaussian fields with covariances

$$\langle \mathcal{W}_v^{ij}(\mathbf{r}, t) \mathcal{W}_v^{kl}(\mathbf{r}', t') \rangle = \delta_{ik}\delta_{jl}\delta(t-t')\delta(\mathbf{r}-\mathbf{r}'), \quad (2.61)$$

$$\langle \mathcal{W}_c^i(\mathbf{r}, t) \mathcal{W}_c^j(\mathbf{r}', t') \rangle = \delta_{ij}\delta(t-t')\delta(\mathbf{r}-\mathbf{r}'), \quad (2.62)$$

and in the equation (2.60) we have used the chemical potential of a mixture of ideal gases of identical molecular mass M [Bell 2010].

Looking at the equation (2.58) one can see that in the momentum equation ($\rho\partial_t \mathbf{v} = \dots$) the stochastic fluxes are introduced like the divergence of a tensor, which guarantees that the conservation of linear momentum holds. However, it is not evident that the angular momentum, defined as $\mathbf{r} \times \rho\mathbf{v}$, is conserved. In fact, this depends on the specific expression of the stochastic tensor $\Sigma(\mathbf{r}, t)$. Hansen et al. [Hansen 2011] (see also [Ailawadi 1971]) showed that the use of a symmetric tensor $\Sigma(\mathbf{r}, t)$ (like in the Eq. (2.116)) ensures the conservation of angular momentum while a non-symmetric tensor does not conserve it. Although in principle non-conservation of the *macroscopic* angular momentum looks wrong from a physical point of view, we should remember that the fluid is composed of discrete components (molecules) that can contribute to the total angular momentum of the system which, of course, should be conserved. To be consistent, if one uses a non-symmetric tensor, an equation for the total angular momentum or for the microscopic spin should be included [Hansen 2011]. We assume that the microscopic angular momentum relaxes infinitely fast, so it does not contributes to the stress tensor [de Groot 1984] and it is not necessary to include their degrees of freedom in the description.

From the stochastic terms (2.58) one can compute the dissipative matrix \mathcal{M} using the fluctuation dissipation balance (2.40). Since the stochastic fields \mathcal{W}_v and \mathcal{W}_c are uncorrelated, \mathcal{M} is a block-diagonal matrix where the only nonzero components are \mathcal{M}_{vv} and \mathcal{M}_{cc} . First, we show how to compute the dissipative term in the concentration equation. The FDB, Eq. (2.40), and the stochastic term \mathcal{K}_c predict

$$2k_B T \mathcal{M}_{cc} \delta(\mathbf{r} - \mathbf{r}') \delta(t - t') = \langle \mathcal{K}_c \mathcal{K}_c \rangle = \rho^{-1} \nabla \cdot \langle \Psi \Psi^* \rangle (\nabla \cdot)^* \rho^{-1}. \quad (2.63)$$

Then, using the covariance of the random fields \mathcal{W}_c and the fact that the gradient and the divergence are negative adjoint ($(\nabla \cdot)^* = -\nabla$), it is possible to find

$$\mathcal{M}_{cc} = -\rho^{-1} \nabla \cdot \left(\chi \rho \left(\frac{\partial \mu}{\partial c} \right)^{-1} \right) \nabla \rho^{-1}. \quad (2.64)$$

To find the dissipative term in the concentration equation one should apply the dissipative matrix \mathcal{M}_{cc} to $\partial \mathcal{H}/\partial c$. Noticing that the chemical potential only depends on the concentration and therefore $\nabla \mu(c) = (\partial \mu / \partial c) \nabla c$, one gets

$$-\mathcal{M}_{cc} \cdot \left(\frac{\partial \mathcal{H}}{\partial c} \right) = \rho^{-1} \nabla \cdot (\rho \chi \nabla c). \quad (2.65)$$

This is exactly the dissipative term that appeared in the equation (2.3). In our model $\chi\rho = \text{const.}$ and as we said the dissipative term can be written as $\chi\nabla^2 c$.

It is possible to follow a similar procedure to find the dissipative matrix \mathcal{M}_{vv} from the stochastic terms \mathcal{K}_v . However, because the velocity is a vector field the derivation becomes more cumbersome. In the Appendix A we use indicial notation to derive the expression for the matrix \mathcal{M}_{vv} while here we just write the final result. In vector notation the dissipative matrix is

$$\mathcal{M}_{vv} = -\rho^{-1} \left[\eta \nabla^2 + \left(\zeta + \frac{1}{3}\eta \right) \nabla(\nabla \cdot) \right] \rho^{-1}. \quad (2.66)$$

The key elements to obtain this result are the fact that the divergence and the gradient are negative adjoint and that the Laplacian can be defined as the divergence of the gradient, $\nabla^2 = \nabla \cdot (\nabla)$. Applying this matrix to $\partial\mathcal{H}/\partial v$ one recovers the dissipative terms of the Navier-Stokes equation (2.2)

$$-\mathcal{M}_{vv} \cdot \left(\frac{\partial\mathcal{H}}{\partial v} \right) = \rho^{-1} \eta \nabla^2 v + \rho^{-1} \left(\zeta + \frac{1}{3}\eta \right) \nabla(\nabla \cdot v). \quad (2.67)$$

The only term that remains to be discussed it is the thermal drift $k_B T \nabla_U \cdot \mathcal{N}^* = k_B T \nabla_U \cdot (\mathcal{L} + \mathcal{M})$. As before, we focus first in the contribution that comes from the conservative operator \mathcal{L} and then in the contribution that comes from the dissipative matrix \mathcal{M} . Looking at the definition of \mathcal{L} one can see that the only possible contribution to the drift term are $(\partial\mathcal{L}_{vv}/\partial v)$ and $(\partial\mathcal{L}_{cv}/\partial c)$. However, because the dependencies of \mathcal{L} are linear in the spatial derivatives of v and c those contributions are zero, therefore

$$\nabla_U \cdot \mathcal{L} = 0. \quad (2.68)$$

On the other hand, the divergence of the dissipative matrix can contribute with two terms $(\partial\mathcal{M}_{vv}/\partial v)$ and $(\partial\mathcal{M}_{cc}/\partial c)$. The drift term in the momentum equation vanishes because for Newtonian fluids the viscosities are independent of the velocity. At the same time, one could expect a nonzero drift term in the concentration equation because \mathcal{M}_{cc} is not independent of the concentration c . However, for dissipative matrices of the form $\mathcal{M}_{cc} \propto \nabla \cdot (c(1-c)) \nabla \rho^{-1}$ all terms appearing in $(\partial\mathcal{M}_{cc}/\partial c)$ cancel as it can be seen by performing the functional derivative [Arfken 1985]. Note that this result is not general and in non-ideal mixtures non-trivial drift terms may appear.

We finish this section by introducing the static structure factor $\mathbf{S}(\mathbf{k})$. To characterize the steady state of a fluid and also to test the accuracy of any numerical scheme it is useful to study the covariance of the fluctuating fields. The covariance of the fields in Fourier space is commonly called the static structure factor. At equilibrium the Hamiltonian is quadratic in the small fluctuations around the steady state $(\delta\rho, \delta v, \delta c)$, and as we saw in the Section 2.1.4.1 that simplifies the calculation of the covariance. At equilibrium, with periodic boundary conditions, the components of static structure factor are

$$\mathbf{S}_{\rho\rho}(\mathbf{k}) = \langle \delta\hat{\rho}(\mathbf{k})\delta\hat{\rho}^*(\mathbf{k}) \rangle = \frac{\rho_0 k_B T}{c_T^2}, \quad (2.69)$$

$$\mathbf{S}_{vv}(\mathbf{k}) = \langle \delta\hat{v}(\mathbf{k})\delta\hat{v}^*(\mathbf{k}) \rangle = \frac{k_B T}{\rho_0} \mathbf{I}, \quad (2.70)$$

$$\mathbf{S}_{cc}(\mathbf{k}) = \langle \delta\hat{c}(\mathbf{k})\delta\hat{c}^*(\mathbf{k}) \rangle = \frac{Mc_0(1-c_0)}{\rho_0}, \quad (2.71)$$

where ρ_0 and c_0 are the equilibrium values of the density and concentration and c_T is the isothermal speed of sound. It is also possible to calculate cross-correlations between the fluctuating variables $(\delta\rho, \delta v, \delta c)$. Since the expansion of Hamiltonian around the equilibrium state does not have cross terms all the cross-correlations are zero, for example $\mathbf{S}_{v\rho}(\mathbf{k}) = \langle \delta\hat{v}(\mathbf{k})\delta\hat{\rho}^*(\mathbf{k}) \rangle = 0$. Note also that at equilibrium the structure factors are independent of the wavevector \mathbf{k} , this property implies that in the real space the fields are delta correlated, e.g. $\langle \delta v(\mathbf{r})\delta v^*(\mathbf{r}') \rangle = (k_B T/\rho)\mathbf{I}\delta(\mathbf{r} - \mathbf{r}')$, a result due to our assumptions about the stochastic noise terms.

2.1.5 Incompressible limit

The compressible Navier-Stokes equation are very stiff due to the presence of viscous and sound modes with quite different characteristic times. If one is interested in the vorticity diffusion only, the sound modes are not relevant and they can be eliminated from the Navier-Stokes equations to reduce their stiffness. In the incompressible limit the density ρ is constant and the dynamic equation for the conservation of mass reduces to $\nabla \cdot \mathbf{v} = 0$, the condition of null divergence on the velocity field. In this limit the fluid equations of motion become

$$\partial_t \mathbf{v} = -\nabla \pi - \nabla \cdot (\mathbf{v} \mathbf{v}) + \nu \nabla^2 \mathbf{v} + \nabla \cdot \left(\sqrt{2\nu\rho^{-1}k_B T} \widetilde{\mathcal{W}}_v \right), \quad (2.72)$$

$$\rho \partial_t c = -\rho \mathbf{v} \cdot \nabla c + \nabla \cdot (\rho \chi (\nabla c + c(1-c)S_T \nabla T) + \Psi), \quad (2.73)$$

$$\text{s.t. } \nabla \cdot \mathbf{v} = 0, \quad (2.74)$$

where $\widetilde{\mathcal{W}}_v = (\mathcal{W}_v + \mathcal{W}_v^T) / \sqrt{2}$ and \mathcal{W}_v is an uncorrelated random Gaussian tensor with covariance

$$\langle \mathcal{W}_v^{ij}(\mathbf{r}, t) \mathcal{W}_v^{kl}(\mathbf{r}', t') \rangle = \delta_{ik} \delta_{jl} \delta(t - t') \delta(\mathbf{r} - \mathbf{r}'), \quad (2.75)$$

while the stochastic term Ψ in the concentration equation is the same that in the compressible case, given in the Eq. (2.60). In these equations $\nu = \eta/\rho$ is the kinematic viscosity while the pressure is a Lagrange multiplier that ensures the free divergence condition (2.74). Since the density is constant, with an abuse of notation we use π to refer either the pressure or the pressure divided by the density. The divergence free condition modifies the momentum equation in several ways, it allows us to write the advective term as $\nabla \cdot (\mathbf{v} \mathbf{v}) = \mathbf{v} \cdot \nabla \mathbf{v}$. Also, it eliminates the dissipative term associated with the bulk viscosity, since $\nabla \cdot \mathbf{v} = 0$ by construction.

To gain some physical insight about the incompressible limit is useful to eliminate the pressure from the momentum equation using projector operator techniques. To eliminate the pressure we write the momentum equation like

$$\partial_t \mathbf{v} = -\nabla \pi + \mathbf{Q}, \quad (2.76)$$

where \mathbf{Q} collects all the terms not explicitly shown in the equation. Taking the divergence and using the divergence free condition on the velocity a Poisson equation for the pressure is obtained

$$\nabla^2 \pi = \nabla \cdot \mathbf{Q}, \quad (2.77)$$

whose solution is formally written as

$$\pi = \nabla^{-2}(\nabla \cdot \mathbf{Q}). \quad (2.78)$$

Plugging this result into the equation (2.76) one gets an alternative form for the momentum equation where the pressure have been eliminated

$$\partial_t \mathbf{v} = (\mathbf{I} - \nabla(\nabla^{-2})\nabla \cdot) \mathbf{Q} = \mathcal{P} \mathbf{Q}. \quad (2.79)$$

Here we have introduced the projector operator

$$\mathcal{P} = \mathbf{I} - \nabla(\nabla^{-2})\nabla \cdot, \quad (2.80)$$

which projects any field into the divergence free space. In general the construction of \mathcal{P} requires knowledge of the boundary conditions, in the case of periodic boundary conditions (PBC) it takes the simple form

$$\widehat{\mathcal{P}}(\mathbf{k}) = \mathbf{I} - \frac{\mathbf{k} \mathbf{k}^*}{k^2}, \quad (2.81)$$

in the Fourier space. Helmholtz's theorem states that a smooth vector field \mathbf{u} can be written as the sum of a irrotational and a divergence free parts, such as $\mathbf{u} = \mathbf{a} + \mathbf{b}$ with $\nabla \times \mathbf{a} = 0$ and $\nabla \cdot \mathbf{b} = 0$ [Aris 1962]. From the definition of the projector operator and basic calculus identities it can be shown that projector operator eliminates the non-divergence free component of any vector field $\mathcal{P}\mathbf{u} = \mathbf{b}$. Also, from the definition of Laplacian $\nabla^2 = \nabla \cdot (\nabla)$ is easy to see that the projection of any gradient field is zero $\mathcal{P}\nabla\phi = 0$. This is the reason why after projecting the velocity equation with \mathcal{P} , the pressure gradient vanishes. The same happens with the stochastic flux

$$\nabla \cdot \left(\sqrt{\frac{\zeta k_B T}{3}} - \frac{\sqrt{2\eta k_B T}}{3} \right) \text{Tr}(\widetilde{\mathcal{W}}_v) \mathbf{I} = \left(\sqrt{\frac{\zeta k_B T}{3}} - \frac{\sqrt{2\eta k_B T}}{3} \right) \nabla \text{Tr}(\widetilde{\mathcal{W}}_v),$$

which is only present in the compressible equations.

Expanding the term \mathbf{Q} in the Eq. (2.79), the momentum equation becomes

$$\partial_t \mathbf{v} = \mathcal{P} \left[-\mathbf{v} \cdot \nabla \mathbf{v} + \nu \nabla^2 \mathbf{v} + \nabla \cdot \left(\sqrt{2\nu\rho^{-1}k_B T} \widetilde{\mathcal{W}}_v \right) \right]. \quad (2.82)$$

This equation shows that the velocity evolves following the Navier-Stokes equation but with its allowed values restricted to the divergence free space.

From the linearized version of the equation (2.82) and the FDB, Eq. (2.45), it is possible to find the velocity structure factor. One has to use that the divergence and gradient are negative adjoint, which implies $\mathcal{P}^* = \mathcal{P}$, and the fact the divergence and Laplacian commute in systems with PBC. The result is

$$S_{vv}(\mathbf{k}) = \frac{k_B T}{\rho} \widehat{\mathcal{P}}(\mathbf{k}), \quad (2.83)$$

where $\widetilde{\mathcal{P}}$ is given in the Eq. (2.81). Each mode has an amplitude

$$\text{Tr} S_{vv}(\mathbf{k}) = \frac{2k_B T}{\rho}. \quad (2.84)$$

Therefore all the modes have the same amplitude (independent of \mathbf{k}) but due to the lack of the sound mode the amplitude is reduced by one $k_B T / \rho$ when comparing with the compressible case, a result that could have been anticipated from the equipartition theorem.

In section 2.4 the structure factor will be used to check the accuracy of our schemes. To that end the best option is to work with an orthogonal basis for the velocity, formed by one longitudinal (or sound) mode

$$\tilde{\mathbf{v}}^{(1)} = k^{-1}(k_x, k_y, k_z), \quad (2.85)$$

and two vortical (or solenoidal) modes

$$\tilde{\mathbf{v}}^{(2)} = (k_x^2 + k_y^2)^{-1/2}(-k_y, k_x, 0), \quad (2.86)$$

$$\tilde{\mathbf{v}}^{(3)} = k^{-1}(k_x^2 + k_y^2)^{-1/2}(k_x k_z, k_y k_z, -(k_x^2 + k_y^2)), \quad (2.87)$$

which satisfy the divergence free condition $\nabla \cdot \tilde{\mathbf{v}}^{(2,3)} = 0$. Due to the equipartition theorem in this basis the structure factor of the two vortical modes should be the same for all wavenumber $\langle \tilde{\mathbf{v}}^{(2)} \tilde{\mathbf{v}}^{(2)} \rangle = \langle \tilde{\mathbf{v}}^{(3)} \tilde{\mathbf{v}}^{(3)} \rangle = k_B T / \rho$ while the structure factor of the longitudinal mode is zero. Note also that at equilibrium all the cross correlations are zero.

2.2 Spatial discretization

We discretize the Navier-Stokes equations following the so called *method of lines* [Gottlieb 2001], this discretization process consists on two different parts: the discretization of the equations in space and in time. We use different time-stepping for the compressible and incompressible cases, however the spatial discretization is the same for all the algorithms presented in this thesis. In this section we discuss the spatial discretization. Temporal discretization is left for the next Section 2.3.

Although our approach is to construct a discrete version of the dynamic equations starting from the continuum formulation, we want to stress that it is also possible to derive a discrete version of the Navier-Stokes equations from a microscopic description of the fluid [Español 2009]. Roughly speaking, this alternative procedure consists on averaging the microscopic equations of motion over small volumes to derive equations of motion for the coarse-grained variables.

The spatial discretization is done using the finite volume method [Patankar 1980]. The space is divided in cubic cells of volume h^3 and the value of the discrete magnitudes defined at each cell represent the average of the continuum fields over that volume. For example, the density defined at the cell i is

$$\rho_i = \frac{1}{h^3} \int_{V_i} \rho(\mathbf{r}) d^3r,$$

where the integral is over the volume of the cell i . We will use subscripts to denote the spatial location where fluid variables are defined on the grid.

The finite volume method is optimal to solve stochastic differential equations because it naturally deals with the delta correlated fluctuations. The Dirac delta function appearing in the stochastic terms [see Eqs. (2.116)-(2.60)] is averaged over fluid cells of volume h^3 to give

$$\delta(\mathbf{r}_i - \mathbf{r}_j) \rightarrow \frac{\delta_{ij}}{h^3}, \quad (2.88)$$

where δ_{ij} is the Kronecker Delta function. Delta correlations in time are regularized in a similar way. Any scheme solves the Navier-Stokes equations over discrete time steps Δt so fields are obtained at discrete times $t^n = n\Delta t$. This discretization regularizes the delta correlations of the stochastic fluxes whose average over a Δt becomes

$$\delta(t_1 - t_2) \rightarrow \frac{\delta_{t_1 t_2}}{\Delta t}. \quad (2.89)$$

To perform the spatial discretization we employ a staggered or “MAC” (*Marker-and-cell*) grid, which is formed by cubic cells with meshwidth h [Harlow 1965]. In a staggered grid not all the variables are defined at the same cell locations. In our case scalars fields are defined at cell centers, vector fields at cell faces and tensor fields at the edges and centers of the cells. For example, the cells $i = (i_x, i_y, i_z)$ are centered at \mathbf{r}_i and the density, the α -component of the velocity and the $\alpha\beta$ -component of the stochastic stress tensor are respectively defined at

$$\rho_i \rightarrow \mathbf{r}_i, \quad (2.90)$$

$$v_{i+\frac{\alpha}{2}}^\alpha \rightarrow \mathbf{r}_i + \frac{h}{2}\boldsymbol{\alpha}, \quad (2.91)$$

$$\Sigma_{i+\frac{\alpha}{2}+\frac{\beta}{2}}^{\alpha\beta} \rightarrow \mathbf{r}_i + \frac{h}{2}\boldsymbol{\alpha} + \frac{h}{2}\boldsymbol{\beta}, \quad (2.92)$$

Where $\boldsymbol{\alpha}$ and $\boldsymbol{\beta}$ are the unit vectors in those directions. In figure 2.1 we show a schematic view of the staggered grid in 2D. The dots at the center of each cell represent the points where scalar fields (i.e.

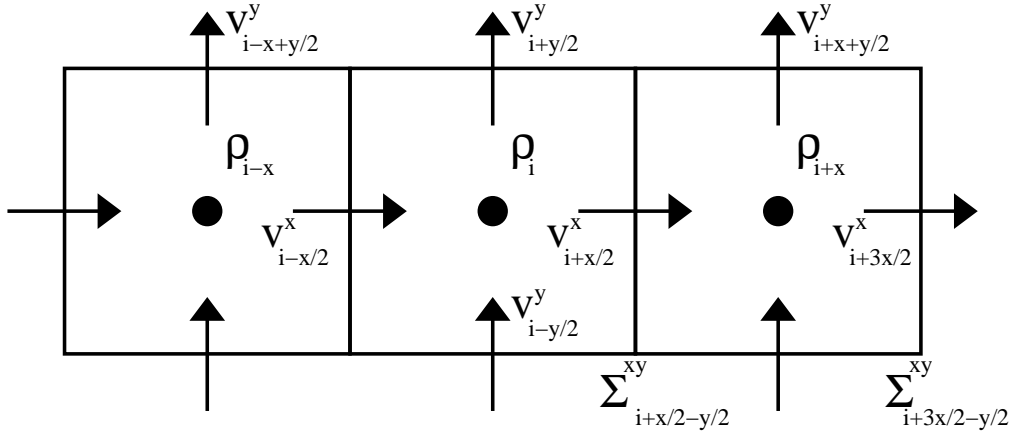


Figure 2.1: 2D grid view. Scalar fields are defined at the cell centers (dots) while the vector fields are defined at the cell faces (arrows). Note that each component of a vector field is defined at a different location. Second rank tensors are defined at the centers and corners of the cells in 2D or at the cell centers and the middle of the edges in 3D. Here we only denote the position of the xy -component of the stress tensor Σ , velocities v^x and v^y and densities ρ .

density, concentration) are defined, while the arrows represent the vector fields (i.e. velocity). Note that each component of the vector field is defined in its own location. An equivalent interpretation of the grid is to consider that each variable ($\rho, v_x, v_y \dots$) is defined in its own grid which may have a shift of half meshwidth respect the others.

To ensure exact conservation of momentum, in the implementation of the compressible scheme we employ the momentum $\mathbf{g} = \rho\mathbf{v}$ rather than the velocity as degree of freedom. The momentum involves a vector and a scalar variable and is defined as

$$g_{i+\frac{\alpha}{2}}^\alpha = \rho_{i+\frac{\alpha}{2}} v_{i+\frac{\alpha}{2}}^\alpha = \frac{1}{2}(\rho_{i+\alpha} + \rho_i) v_{i+\frac{\alpha}{2}}^\alpha.$$

2.2.1 Discrete differential operators

In this section we introduce a discrete version of the differential operators that appear in the Navier-Stokes equations (2.1)-(2.3). In constructing the differential operators for the discrete setting it is necessary to ensure that the FDB is preserved by the discretization. Recall, that in the Section 2.1.4 we were able to show that the FDB holds for the Navier-Stokes equations because the differential operators satisfy the following conditions

- The divergence and gradient are negative adjoint $\nabla = -\nabla^*$.
- The Laplacian is self adjoint and given by the divergence of the gradient $\nabla^2 = \nabla \cdot \nabla$.
- The advection term is skew-adjoint, in the linear setting $\mathbf{v}_0 \cdot \nabla = -(\mathbf{v}_0 \cdot \nabla)^*$.

The first two conditions were used to derive the dissipative terms in the Navier-Stokes equations from the stochastic forcing in the momentum and concentration equations $\mathcal{K}_v = \rho^{-1} \nabla \cdot \Sigma$ and $\mathcal{K}_c = \rho^{-1} \nabla \cdot \Psi$, while the last condition was necessary to obtain the non-dissipative (advective) terms of the Navier-Stokes equations. In this Section we present a second-order accurate version of each operator that

preserves the relations stated above, we use the notation \mathbf{G} , \mathbf{D} and \mathbf{L} to denote the discrete gradient, divergence and Laplacian operators.

The gradient \mathbf{G} maps scalars to vectors while the divergence \mathbf{D} maps vector to scalars. The divergence is defined in the conservative manner

$$\nabla \cdot \mathbf{v} \rightarrow (\mathbf{D}\mathbf{v})_i = \frac{1}{h} \sum_{\alpha} (\mathbf{v}_{i+\alpha/2}^{\alpha} - \mathbf{v}_{i-\alpha/2}^{\alpha}), \quad (2.93)$$

which just means that the divergence is the difference between fluxes at the cell faces. This implies that the integral of a divergence over the whole (periodic) space is always zero. This is of major importance to ensure the conservation laws of the Navier-Stokes equations. Note also that the divergence of a vector (a scalar) its defined at the cell centers, in accordance with our definition of the staggered grid. The second-order accurate gradient is defined as

$$(\nabla \rho)^{\alpha} \rightarrow (\mathbf{G}\rho)_{i+\alpha/2}^{\alpha} = \frac{1}{h} (\rho_{i+\alpha} - \rho_i). \quad (2.94)$$

Note that the gradient of a scalar (a vector) is defined at the cell faces, as any other vector in the staggered grid. We now show that the discrete gradient satisfies $\mathbf{G} = -\mathbf{D}^*$. In the continuum setting the negative adjoint property between divergence and gradient implies

$$\int_{\Omega} c(\nabla \cdot \mathbf{v}) d\mathbf{r} = - \int_{\Omega} \mathbf{v} \cdot \nabla c d\mathbf{r}, \quad (2.95)$$

for a scalar field $c(\mathbf{r})$ and a periodic vector field $\mathbf{v}(\mathbf{r})$ in a domain Ω . It is easy to check that the definitions given above for the gradient and the divergence obey a discrete version of the negative adjoint property (2.95). In one periodic dimension

$$\sum_i c_i (\mathbf{D}\mathbf{v})_i = \frac{1}{h} \sum_i \left(c_i (v_{i+\frac{1}{2}} - v_{i-\frac{1}{2}}) \right), \quad (2.96)$$

and now shifting the index in the second term we obtain

$$- \frac{1}{h} \sum_i v_{i+\frac{1}{2}} (c_{i+1} - c_i) = - \sum_i v_{i+\frac{1}{2}} (\mathbf{G}c)_{i+\frac{1}{2}}, \quad (2.97)$$

which finishes the demonstration.

These two operators are used to construct the Laplacian $\mathbf{L} = \mathbf{D}\mathbf{G}$ and the $\nabla(\nabla \cdot) \rightarrow \mathbf{G}\mathbf{D}$ operator.

$$(\nabla^2 \mathbf{v})^{\alpha} \rightarrow (\mathbf{L}\mathbf{v})_{i+\alpha/2}^{\alpha} = \frac{1}{h^2} \sum_{\beta} \left(v_{i+\alpha/2+\beta}^{\alpha} - 2v_{i+\alpha/2}^{\alpha} + v_{i+\alpha/2-\beta}^{\alpha} \right), \quad (2.98)$$

$$[\nabla(\nabla \cdot \mathbf{v})]^{\alpha} \rightarrow (\mathbf{G}\mathbf{D}\mathbf{v})_{i+\alpha/2}^{\alpha} = \frac{1}{h^2} \sum_{\beta} \left(v_{i+\alpha+\beta/2}^{\beta} - v_{i+\alpha-\beta/2}^{\beta} - v_{i+\beta/2}^{\beta} + v_{i-\beta/2}^{\beta} \right). \quad (2.99)$$

The Laplacian is the divergence of a gradient and therefore it is conservative. Also the operator $\mathbf{G}\mathbf{D}$ is conservative, note that the gradient of a scalar ϕ is equivalent to the divergence of the tensor $\phi\mathbf{I}$. Finally, we have to describe the advective terms $\mathbf{v} \cdot \nabla \rho$ and $\mathbf{v} \cdot \nabla \mathbf{v}$. Since the problem in the two cases is equivalent we just illustrate the first one. In the continuum setting the skew-adjoint property implies

$$\int_{\Omega} c (\nabla \cdot (\rho \mathbf{v})) d\mathbf{r} = - \int_{\Omega} \rho (\nabla \cdot (c \mathbf{v})) d\mathbf{r}, \quad (2.100)$$

for a periodic vector field $\mathbf{v}(r)$ and any scalar fields $c(r)$ and $\rho(r)$. The skew-adjoint property of the advection term can be ensured by using

$$(\mathbf{v} \cdot \mathbf{G}\rho)_{\mathbf{i}} = \frac{1}{2} \sum_{\alpha} \left(\mathbf{v}_{\mathbf{i}+\alpha/2}^{\alpha} (\mathbf{G}\rho)_{\mathbf{i}+\alpha/2}^{\alpha} + \mathbf{v}_{\mathbf{i}-\alpha/2}^{\alpha} (\mathbf{G}\rho)_{\mathbf{i}-\alpha/2}^{\alpha} \right). \quad (2.101)$$

The discrete equivalent of (2.100) can be easily proved with our definition (2.101) as we did for the negative-adjoint property (2.95). Finally, collecting the results derived so far, the discrete Navier-Stokes equations for the conserved variables are

$$\partial_t \rho_{\mathbf{i}} = -(\mathbf{D}\mathbf{g})_{\mathbf{i}}, \quad (2.102)$$

$$\begin{aligned} \partial_t g_{\mathbf{i}+\alpha/2}^{\alpha} &= -(\mathbf{D}(\mathbf{g}\mathbf{v}))_{\mathbf{i}+\alpha/2}^{\alpha} - (\mathbf{G}\pi)_{\mathbf{i}+\alpha/2}^{\alpha} \\ &\quad + \eta(\mathbf{L}\mathbf{v})_{\mathbf{i}+\alpha/2}^{\alpha} + (\zeta + \frac{1}{3}\eta)(\mathbf{G}\mathbf{D}\mathbf{v})_{\mathbf{i}+\alpha/2}^{\alpha} + (\mathbf{D}\Sigma)_{\mathbf{i}+\alpha/2}^{\alpha}, \end{aligned} \quad (2.103)$$

$$\partial_t (\rho_1)_{\mathbf{i}} = -(\mathbf{D}(\rho_1 \mathbf{v}))_{\mathbf{i}} + \chi_0 \rho_0 (\mathbf{L}\mathbf{c})_{\mathbf{i}} + \chi_0 \rho_0 (\mathbf{D}(c(1-c)\nabla T))_{\mathbf{i}} + (\mathbf{D}\Psi)_{\mathbf{i}}, \quad (2.104)$$

where the divergence acts component-wise on the tensor $(\mathbf{g}\mathbf{v})_{\mathbf{i}+\alpha/2+\beta/2}^{\alpha\beta}$ defined as

$$\begin{aligned} (\mathbf{g}\mathbf{v})_{\mathbf{i}+\alpha/2+\beta/2}^{\alpha\beta} &= g_{\mathbf{i}+\alpha/2+\beta/2}^{\beta} v_{\mathbf{i}+\alpha/2+\beta/2}^{\alpha} \\ &= \frac{1}{2} (g_{\mathbf{i}+\alpha+\beta/2}^{\beta} + g_{\mathbf{i}+\beta/2}^{\beta}) \frac{1}{2} (v_{\mathbf{i}+\alpha/2+\beta}^{\alpha} + v_{\mathbf{i}+\alpha/2}^{\alpha}), \end{aligned} \quad (2.105)$$

and the divergence of the momentum $\mathbf{g} = \rho\mathbf{v}$ (or the term $\rho_1\mathbf{v}$) is defined by

$$(\mathbf{D}\mathbf{g})_{\mathbf{i}} = \rho_{\mathbf{i}} (\mathbf{D}\mathbf{v})_{\mathbf{i}} + \frac{1}{2} \sum_{\alpha} \left((\mathbf{G}\rho)_{\mathbf{i}+\alpha/2}^{\alpha} v_{\mathbf{i}+\alpha/2}^{\alpha} + (\mathbf{G}\rho)_{\mathbf{i}-\alpha/2}^{\alpha} v_{\mathbf{i}-\alpha/2}^{\alpha} \right). \quad (2.106)$$

Note that the equations for the mass, momentum and the mass of the first species are written (or can be written) in a conservative form, that is, as the divergence of fluxes, which ensure the exact conservation of the fluid variables ρ , \mathbf{g} and ρ_1 .

2.2.2 Transport coefficients in the discrete formulation

It is useful to write the expressions for the discrete operators in Fourier space. From the equation (2.93), (2.94) and (2.99) and using a discrete Fourier transform one finds the following expressions (see Appendix B for the details)

$$\widehat{\mathbf{G}}_{\mathbf{k}}^{\alpha} = \frac{2i}{h} \sin \left(\frac{k_{\alpha}h}{2} \right), \quad (2.107)$$

$$\widehat{\mathbf{D}}_{\mathbf{k}} = \frac{2i}{h} \sum_{\alpha} \sin \left(\frac{k_{\alpha}h}{2} \right), \quad (2.108)$$

$$\widehat{\mathbf{L}}_{\mathbf{k}} = -\frac{4}{h^2} \sum_{\alpha} \sin^2 \left(\frac{k_{\alpha}h}{2} \right). \quad (2.109)$$

For small wavenumbers the operators tend to the continuum limit given by Eqs. (2.15)-(2.17) as it is expected for any second order discretization (for example, for the Laplacian $\widehat{\mathbf{L}}_{\mathbf{k}} \xrightarrow[k \rightarrow 0]{} -k^2$). However, the deviations become significant for large wavenumbers. A way to see this is through the eigenvalues and normal modes of the linearized discrete equations (2.102)-(2.104). The eigenvalues are physically equivalent to those of the continuum case (2.18)-(2.20), but the transport coefficients depend on the

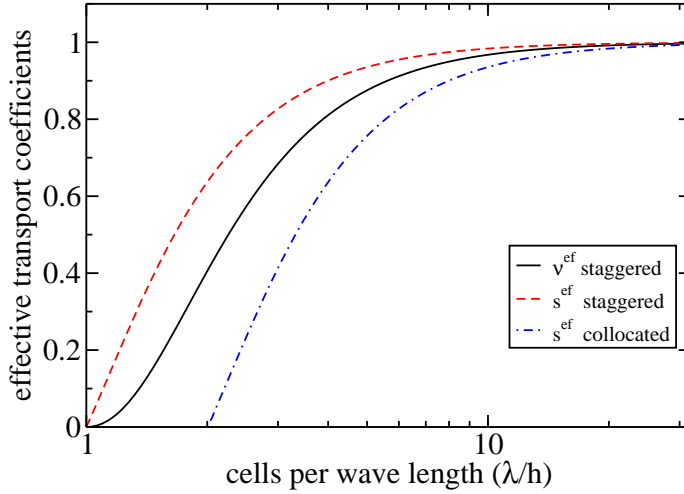


Figure 2.2: Effective transport coefficients [Eqs. (2.111)-(2.114)] versus the number of cells per wave length $\lambda = 2\pi/k$. The transport coefficients are normalized with their values in the continuum setting. We have also included the effective speed of sound for a collocated grid with central differences (dot-dashed line) [Fabritiis 2007] to show that staggered schemes reduce the wavenumber dependence of the transport coefficients.

wavevector. Using Eqs. (2.21)-(2.24) and (2.107)-(2.109) it is easy to show that for our staggered grid this dependence can be written as function of

$$\phi(kh) = \frac{2}{kh} \sin\left(\frac{kh}{2}\right), \quad (2.110)$$

with the discrete version of the transport coefficients being

$$\nu_{\text{ef}} = \phi^2(kh)\nu, \quad (2.111)$$

$$\Gamma_{\text{ef}} = \phi^2(kh)\frac{\nu_L}{2}, \quad (2.112)$$

$$s_{\text{ef}} = \frac{1}{2}\phi(kh)\sqrt{4c^2 - \nu_L^2 k^2 \phi^2(kh)}, \quad (2.113)$$

$$\chi_{\text{ef}} = \phi^2(kh)\chi_0. \quad (2.114)$$

These relations are important when evaluating transport coefficients at small wavelengths. For example, consider a solution of colloids in a Newtonian fluid, it is well known that at low colloid concentrations the viscosity of the fluid can be written like $\eta(\phi) = \eta_0 + \eta_c(\phi)$, where η_0 is the viscosity of the Newtonian solvent and $\eta_c(\phi)$ is an extra contribution due to the colloids [Landau 1987]. This last contribution not only depends on the colloids volume fraction ϕ , but also on wavelength and frequency of the perturbation (k, ω) [Larson 1998, Heemels 1998]. If a finite volume scheme is used to measure the k -dependent viscosity of a complex fluid it is important to be able to discern if the k -dependence comes from the solute particles or it is just a spatial discretization effect. The same kind of issues arise with the other transport coefficients like the sound absorption or the speed of sound [Riese 1999].

In figure 2.2 we represent the effective transport coefficients versus the number of cells per wavelength. The effective transport coefficients remain close to the continuum limit for $kh \lesssim 0.6$, with variations below 10% when the resolution for the mode is 6 cells or more. To illustrate the accuracy of our staggered discretization we include the effective speed of sound obtained for a collocated grid with central differences [Fabritiis 2007]. In the collocated scheme the dependence with k is much stronger (in particular $s_{\text{ef}} = 0$ for $k = \pi/h$). Moreover, Voulgarakis et al. showed that at short times the collocated scheme presents an unphysical transport of mass between neighbor cells due to the sound modes [Voulgarakis 2009]. This is one of the reasons why we have chosen to work with the staggered scheme.

2.2.3 Stochastic fluxes

In order to define the stochastic fluxes one needs to consider the locations where they are defined, their relation with the fluid variables and their regularization. In the discrete setting the delta correlated noises [see Eqs. (2.116)-(2.118)], are regularized by the averaging over a cell of volume h^3 and a time step Δt . This regularization can be represented by the identification rule between the Gaussian field in the continuum setting \mathcal{W} and its counterpart in the discrete setting \mathbf{W} ,

$$\mathcal{W} \rightarrow (h^3 \Delta t)^{-1/2} \mathbf{W}, \quad (2.115)$$

where \mathbf{W} is a collection of normally distributed random numbers with zero mean and unit variance. More explicitly, in the discrete setting the stochastic terms in the Navier-Stokes equations are

$$\Sigma = \sqrt{\frac{2\eta k_B T}{h^3 \Delta t}} \widetilde{\mathbf{W}}_v + \left(\sqrt{\frac{\zeta k_B T}{3h^3 \Delta t}} - \frac{1}{3} \sqrt{\frac{2\eta k_B T}{h^3 \Delta t}} \right) \text{Tr}(\widetilde{\mathbf{W}}_v) \mathbf{I}, \quad (2.116)$$

$$\Psi = \sqrt{\frac{2\chi \rho k_B T}{h^3 \Delta t (\partial \mu / \partial c)}} \mathbf{W}_c = \sqrt{\frac{2\chi \rho M c (1 - c)}{h^3 \Delta t}} \mathbf{W}_c, \quad (2.117)$$

with $\widetilde{\mathbf{W}}_v = (\mathbf{W}_v + \mathbf{W}_v^T) / \sqrt{2}$ and

$$\langle W_v^{\alpha\beta}(\mathbf{r}, n\Delta t) W_v^{\gamma\delta}(\mathbf{r}', n'\Delta t) \rangle = \delta_{\alpha\gamma} \delta_{\beta\delta} \delta_{nn'} \delta_{\mathbf{r}\mathbf{r}'}, \quad (2.118)$$

$$\langle W_c^\alpha(\mathbf{r}, n\Delta t) W_c^\beta(\mathbf{r}', n'\Delta t) \rangle = \delta_{\alpha\beta} \delta_{nn'} \delta_{\mathbf{r}\mathbf{r}'}, \quad (2.119)$$

where \mathbf{r} and \mathbf{r}' represent the discrete location where each random number is defined.

The stochastic term $\Sigma(\mathbf{r}, t)$ depends on the viscosities η and ζ and on the temperature T , here these magnitudes are taken as constants and therefore they do not pose any special difficulty. The tensor \mathbf{W}_v is defined at the centers and edges of the cells (see Eq. (2.92)). In principle, for each cell we should generate 9 random numbers, however in the momentum equation \mathbf{W}_v only enters in the symmetrized form $\widetilde{\mathbf{W}}_v$, this allows us to generate only 6 random number per cell, 3 defined at the cell center $[\widetilde{\mathbf{W}}^{xx}]_i$, $[\widetilde{\mathbf{W}}^{yy}]_i$, $[\widetilde{\mathbf{W}}^{zz}]_i$ with variance 2 and other three at the cell edges $[\widetilde{\mathbf{W}}^{xy}]_{i+\frac{\hat{x}}{2}+\frac{\hat{y}}{2}}$, $[\widetilde{\mathbf{W}}^{xz}]_{i+\frac{\hat{x}}{2}+\frac{\hat{z}}{2}}$ and $[\widetilde{\mathbf{W}}^{yz}]_{i+\frac{\hat{y}}{2}+\frac{\hat{z}}{2}}$ with variance 1. This saving in random numbers reduces the memory allocated by the code and also the computational cost of our schemes.

The stochastic flux $\Psi(\mathbf{r}, t)$ appearing in the concentration equation (2.3) depends on the concentration c . Since $\Psi(\mathbf{r}, t)$ is a vector it should be defined at the faces of the grid while the concentration is defined at the cell centers. To solve this problem we use a linear interpolation for the concentration in the stochastic term. For example, its α -component is

$$\Psi_{i+\frac{\alpha}{2}}^\alpha(c_{i+\frac{\alpha}{2}}) = \Psi_{i+\frac{\alpha}{2}}^\alpha\left(\frac{1}{2}(c_i + c_{i+\alpha})\right). \quad (2.120)$$

The fact that $\Psi(\mathbf{r}, t)$ has a dependency on the concentration is problematic because it requires to deal with a multiplicative noise rather than with an additive noise [Risken 1989]. But because the dynamic of the concentration is slow compared to the stochastic flux (delta correlated in the Markovian approximation) we consider that the stochastic forcing $\Psi(\mathbf{r}, t)$ can be treated as an additive noise which only depends on the stationary field $c(\mathbf{r})$. This approximation is valid for small deviations with respect to the steady state. In general, we do not know how to split the concentration into the small fluctuations and the mean value and we simply use the total concentration $c(\mathbf{r}, t)$ in the stochastic noise. More detailed analyses (see appendix A of [Delong 2013]) shows that our time-stepping will only be first order accurate if the noise is multiplicative. However, since the concentration field evolves very slowly our schemes will show a higher order accuracy in most cases.

2.2.4 Rigid boundaries

Confined systems present important differences with respect systems with open or periodic boundary conditions [Hagen 1997, de Zárate 2004], in this section we explain how to include rigid boundaries in the staggered grid to be able to study such systems.

We consider two walls perpendicular to the y direction and separated by a constant distance. In our implementation the walls are defined exactly at the faces of the cells. Therefore some of the variables are defined on the walls, while others are defined half mesh away. In the other two directions x, z we use periodic boundary conditions.

We explain the necessary modifications to deal with Neumann or Dirichlet boundary conditions. Since both walls are equivalent we focus in only one of them. We assume that the velocity has a no-slip boundary condition at the wall, which slides with the constant velocity $\mathbf{v}^b = (v_x^b, 0, v_z^b)$. The normal component of the velocity to the walls v_y is defined exactly on the walls, therefore we only need to fix $v_y = 0$ for the cells living at the wall. This condition ensures that the flux of mass through the wall is zero as one expects for an impermeable wall. The other velocity components and also cell-center quantities such as density or concentration are defined at half meshwidth from the walls. We use ghost cells to calculate finite difference close to the walls. Labelling the cells in both sides of the wall as 0 and 1 where 0 correspond to the ghost cell, the velocity on the ghost cell to hold the no-slip condition should be

$$v_x^0 = 2v_x^b - v_x^1, \quad (2.121)$$

and similarly for the z component. Where we have used a linear interpolation at the wall $(v_x^0 + v_x^1)/2 = v_x^b$. For the density we use the condition $\rho^0 = \rho^1$ which ensures that pressure gradient vanishes at the walls. For the concentration, depending on the problem, one can use Neumann or Dirichlet boundary condition. For Neumann conditions one gets

$$\left(\frac{\partial c}{\partial y} \right) \Big|_{\text{wall}} = 0, \quad (2.122)$$

which implies $c^0 = c^1$. On the other hand, a Dirichlet boundary condition specifies the concentration on the wall c^b by imposing a concentration on the ghost cell $c^0 = 2c^b - c^1$. Mixed boundary conditions can also be implemented.

In the presence of walls the fluctuation-dissipation balance does not holds with our previous definitions of the differential operators and stochastic fluxes. We will show that some modifications are needed. At the wall, the y -component of velocity is not really a variable since $v_y = 0$, therefore we fix that value without further complications. For the rest of variables (v_x, v_z, ρ or c) we have to define

the differential operators close to the wall. In our discretization, we use the same differential operators that with PBC (Eqs. (2.93), (2.94), (2.98) and (2.99)) but using the fluid values at the ghost cells when they are needed. As we will see shortly this can be understood like a modification of the differential operators, which in turns makes necessary to change the stochastic fluxes to hold the FDB.

Since only the direction perpendicular to the wall is affected, to simplify the discussion we consider here a one dimensional system. Moreover, because all the variables (apart from v_y) are defined half-mesh apart from the wall, we can discuss a general case instead of consider the equation for each variable separately. Lets consider this general equation to be

$$\partial_t c = \mathbf{A}(c) + \chi \mathbf{L}c + \sqrt{2\chi/h} \mathbf{D}\mathbf{W}. \quad (2.123)$$

We want to emphasize that here c plays the role of any of the variables (v_x, v_z, ρ or c). $\mathbf{A}(c)$ represents the advective term, at the wall $\mathbf{A}(c) = 0$ and the FDB implies $\langle cc^* \rangle = 2\chi \mathbf{I}$. Although it is not our case we have to mention that it should be possible to allow for flow entrainment (i.e., $\mathbf{A}(c) \neq 0$) without disturbing the FDB [Thompson 1987, Delgado-Buscalioni 2008b]. Because the advection is zero at the wall, to satisfy the FDB in the linear setting is enough to hold [recall Eq. (2.45)]

$$\mathbf{L} = -\mathbf{D}\langle \mathbf{W}\mathbf{W}^* \rangle \mathbf{D}^*. \quad (2.124)$$

We know that our discrete differential operators already satisfy this condition far away from the wall. However, near the wall the situation may be different because the differential operators change with the boundary condition. We follow the appendix C of [Donev 2010a] since it gives an easy recipe to handle the stochastic fluxes close to the wall. In the one dimensional discrete system the variable c is the array with components $c = (c_1, c_2, c_3, \dots)^T$ where c_1 is closest value to the wall. Using matrix notation the divergence and Laplacian operators that act on this array can be written as

$$\mathbf{D} = \frac{1}{h} \begin{pmatrix} -1 & 1 & 0 & \dots \\ 0 & -1 & 1 & \dots \\ 0 & 0 & -1 & \dots \\ \vdots & \vdots & \vdots & \ddots \end{pmatrix}, \quad \mathbf{L} = \frac{1}{h^2} \begin{pmatrix} -(2-\omega) & 1 & 0 & \dots \\ 1 & -2 & 1 & \dots \\ 0 & 1 & -2 & \dots \\ \vdots & \vdots & \vdots & \ddots \end{pmatrix}. \quad (2.125)$$

Where the parameter ω controls the kind of boundary condition at the wall. For Neumann condition the flux at the wall is zero and a zero flux can be obtained by setting the value of c at the ghost cell to $c_0 = c_1$, which gives at the wall

$$(\mathbf{L}c)_1 = h^{-2}(c_2 - c_1),$$

or in the matrix notation $\omega = 1$. The Dirichlet boundary condition, used for the velocity, fixes the value of the c at the wall to a constant referent value $c_b = 0$. This can be achieved by setting the concentration at the ghost cell to $c_0 = -c_1$, which gives the Laplacian

$$(\mathbf{L}c)_1 = h^{-2}(c_2 - 3c_1),$$

or in the matrix notation $\omega = -1$. Note that a Dirichlet boundary condition with $c_b \neq 0$ does not change the definition of the Laplacian, but rather it introduces a constant forcing term in the equation, since at thermal equilibrium such a perturbation should be zero we do not need to consider that case to obey the FDB. The FDB in the form of Eq. (2.124) can be achieved in both types of boundary conditions by using the following covariance

$$\langle \mathbf{W}\mathbf{W}^* \rangle = \begin{pmatrix} 1-\omega & 0 & 0 & \dots \\ 0 & 1 & 0 & \dots \\ 0 & 0 & 1 & \dots \\ \vdots & \vdots & \vdots & \ddots \end{pmatrix}, \quad (2.126)$$

as can be easily proved by the multiplication of the matrices. This covariance means that one should turn off the noise at the wall for Neumann conditions ($\omega = 1$) or double it for Dirichlet conditions ($\omega = -1$). Finally, we note that our spatial discretization is second order accurate far from the boundaries while it is only first order at the walls. In the deterministic setting it is easy to obtain higher order discretizations at the wall by just determining the concentration at the ghost cell with a higher order interpolation method. Unfortunately, in the stochastic setting such route requires a more complicate expression for the stochastic fluxes at the wall so as to obey the FDB. Hence we decided not to implement them.

2.3 Temporal discretization

In this section we present the different temporal integrators implemented during this thesis to solve the Navier-Stokes equations over discrete times Δt . We use superscripts to denote the time, for example \mathbf{v}^n denotes the velocity at time $t^n = n\Delta t$. All the schemes presented in this section use the spatial discretization of Section 2.2.

An important issue when developing numerical methods for partial differential equations is to determine their accuracy and stability region. In finite volume methods the accuracy and stability are determined by the advective α and viscous β CFL (*Courant-Friedrichs-Lowy*) numbers

$$\alpha_c = \frac{c_T \Delta t}{h}, \quad (2.127)$$

$$\alpha_v = \frac{V \Delta t}{h}, \quad (2.128)$$

$$\beta = \frac{\nu \Delta t}{h^2}, \quad (2.129)$$

$$\beta_c = \frac{\chi \Delta t}{h^2}, \quad (2.130)$$

where $V = \|\mathbf{v}\|_\infty = \max(|v_i^\alpha|)$ is the infinity norm of the velocity field. The nature of the temporal discretization (explicit or implicit) determines the stability limits of the numerical methods. An explicit method for the advective terms imposes the limit $\alpha_c, \alpha_v \lesssim 1$ while for the viscous terms the limit is $\beta, \beta_c \leq 1/2^d$ in a d -dimensional space [Courant 1967, Quarteroni 2000, Gottlieb 2001]. However, implicit or semi-implicit methods can relax these restrictions or even more, they can lead to unconditionally stable schemes.

In the section 2.3.1 we present an explicit solver for compressible flows. This explicit solver is quite useful because can be easily adapted to include nonlinearities in either the equation of state or the chemical potential. However, the stiffness of the Navier-Stokes equations and the stability limits of explicit solvers can make the computational cost of some simulations too high.

A partial solution to the high computational cost of the simulations it is to reduce the stiffness of the equations. At the scale of the meshwidth h , viscous compressible flows have two characteristic times, the viscous time for the diffusion of momentum $\tau_\nu = h^2/\nu$ and the acoustic time $\tau_c = h/c$. The ratio between these two times is the so called cell Reynolds number

$$r = \frac{\alpha_c}{\beta} = \frac{ch}{\nu}. \quad (2.131)$$

In general, the cell Reynolds number is very large. For example, at lengths of $1m\mu$ in water, $r \sim 10^3$. This means that the order of 10^3 time steps are required to simulate a single diffusive time (because $\Delta t \sim \tau_c$). Moreover, the longest viscous time scales with the system's length L , like $\tau = (L/h)^2 \tau_\nu$, thus the separation of time scales can become unfeasible for numerical simulations. A common approach

to reduce the stiffness of the Navier-Stokes equations is to use an artificially small speed of sound while conserving the separation of time scales $\tau_\nu > \tau_c$ [Padding 2006]. However, if the changes in density are assumed to be negligible, a better approach is to employ the incompressible formulation introduced in the Sec. 2.1.5. In the incompressible formulation, which correspond to the limit $c_T \rightarrow \infty$, the sound modes are completely eliminated from the description, and thus the only advective CFL number is α_v . Besides, as we will show later, in the incompressible formulation it is easy to use a semi-implicit method for the viscous terms that eliminates the restrictions $\beta, \beta_c \leq 1/2^d$. In such discretization the time step is only limited by the advective CFL number α_v . In the Section 2.3.2 we present a semi-implicit incompressible solver that allows to use very large time steps.

There are some problems where the density fluctuations can not be neglected but where the limitation imposed by the sonic CFL number for explicit solvers is too strong. To deal with such problems we discuss in Section 2.3.3 a novel time stepping that uses a semi-implicit method for the pressure terms which eliminates the restriction $\alpha_c \lesssim 1$.

We will need also a method to determine the accuracy of our schemes. For deterministic problems it is common to study the convergence of the solution with the time step Δt . If for small enough time steps Δt the solution after a time $T = n\Delta t$ converges like Δt^p the algorithm is said to be of order p [Quarteroni 2000]. In such case an error of order Δt^{p+1} is made over each time step. In stochastic problems it only makes sense to study the convergence of distributions, for example $\langle \rho(\mathbf{r}) \rangle$ or $\langle \delta\mathbf{v}(\mathbf{k}) \delta c^*(\mathbf{k}) \rangle$. An algorithm is called of p -order in the weak convergence sense, when the error in the averages is proportional to Δt^p for small enough time steps [Cao 2002]. In Section 2.4 we will use the static structure factor $S(\mathbf{k})$ to determine the weak convergence for each scheme.

2.3.1 Explicit compressible scheme

Here we present a fully explicit solver for the compressible fluid equations. As we explained in the previous section, the explicit solvers have the limitations in the time step $\alpha \lesssim 1$ and $\beta < (1/2)^d$. However explicit schemes also have advantages, mainly they can handle nonlinear terms without further complications. This fact is useful when working with nonlinear equation of state such as the Van der Waals equation or when including a chemical potential gradient in the Navier-Stokes equations to model non-miscible fluids (e.g. Cahn-Hilliard model [Lowengrub 1998, Vorobev 2010]).

In the compressible formulation we shall work with conserved variables $(\rho, \mathbf{g}, \rho_1)$ to ensure their conservation up to machine precision. The discretized Navier Stokes equations (2.102) can be written as a conservation law for the field $\mathbf{U} = (\rho, \mathbf{g}, \rho_1)^T$, i.e.

$$\partial_t \mathbf{U} = -\nabla \cdot \mathbf{F}(\mathbf{U}, \mathbf{W}, t), \quad (2.132)$$

where $\mathbf{F}(\mathbf{U}, \mathbf{W}, t)$, the flux at time t that depends on both the fluid variables \mathbf{U} and noise tensor \mathbf{W} , can be derived from the equations (2.102)-(2.103). Strict conservation of momentum and mass of each species is guaranteed by the divergence form of the equation and by the discrete operators introduced in Section 2.2. We solve the equation (2.132) using a *strong stability preserving* (SSP) explicit third-order Runge-Kutta scheme [Bell 2007, Gottlieb 2001]. The SSP methods were developed to work with problems with discontinuous solutions like shock waves. Although here we are not dealing with that kind of problems, the SSP methods are usually preferred for their good stability properties. The SSP scheme has three stages in which the following increment is calculated

$$\Delta \mathbf{U}(\mathbf{U}, t) = -\Delta t \nabla \cdot \mathbf{F}(\mathbf{U}, \mathbf{W}, t). \quad (2.133)$$

The three Runge-Kutta stages are,

$$\tilde{\mathbf{U}}^{n+1} = \mathbf{U}^n + \Delta\mathbf{U}(\mathbf{U}^n, \mathbf{W}_1), \quad (2.134)$$

$$\mathbf{U}^{n+\frac{1}{2}} = \frac{3}{4}\mathbf{U}^n + \frac{1}{4}\left[\tilde{\mathbf{U}}^{n+1} + \Delta\mathbf{U}(\tilde{\mathbf{U}}^{n+1}, \mathbf{W}_2)\right], \quad (2.135)$$

$$\mathbf{U}^{n+1} = \frac{1}{3}\mathbf{U}^n + \frac{2}{3}\left[\mathbf{U}^{n+\frac{1}{2}} + \Delta\mathbf{U}(\mathbf{U}^{n+\frac{1}{2}}, \mathbf{W}_3)\right], \quad (2.136)$$

which correspond to approximations of \mathbf{U} at times $(n+1)\Delta t$, $(n+\frac{1}{2})\Delta t$ and the final prediction at time $(n+1)\Delta t$. The random numbers used are

$$\mathbf{W}_1 = \mathbf{W}_A - \sqrt{3}\mathbf{W}_B, \quad (2.137)$$

$$\mathbf{W}_2 = \mathbf{W}_A + \sqrt{3}\mathbf{W}_B, \quad (2.138)$$

$$\mathbf{W}_3 = \mathbf{W}_A, \quad (2.139)$$

$$\langle \mathbf{W}_A(\mathbf{r}_i, t_n) \mathbf{W}_B(\mathbf{r}_j, t_m) \rangle = \delta_{AB} \delta_{ij} \delta_{nm}. \quad (2.140)$$

The scheme with this particular combination of random numbers is third-order weak accurate in the linearized setting [Donev 2010b, Usabiaga 2012]. A more recently work (see Ref. [Delong 2013]) has shown that a second-order weak accuracy can be achieved for the non-linear Navier-Stokes equations if the random numbers are chosen according to

$$\mathbf{W}_1 = \mathbf{W}_A + \frac{(2\sqrt{2} - \sqrt{3})}{5}\mathbf{W}_B, \quad (2.141)$$

$$\mathbf{W}_2 = \mathbf{W}_A + \frac{(-4\sqrt{2} - 3\sqrt{3})}{5}\mathbf{W}_B, \quad (2.142)$$

$$\mathbf{W}_3 = \mathbf{W}_A + \frac{(\sqrt{2} + 2\sqrt{3})}{10}\mathbf{W}_B, \quad (2.143)$$

$$\langle \mathbf{W}_A(\mathbf{r}_i, t_n) \mathbf{W}_B(\mathbf{r}_j, t_m) \rangle = \delta_{AB} \delta_{ij} \delta_{nm}. \quad (2.144)$$

In the problems that we study the perturbations are small and the system remains close to the linear setting, therefore we keep using the weights given by (2.137)-(2.140).

2.3.2 Semi-implicit incompressible scheme

As discussed at the begin of Sec. 2.3, the sound modes are eliminated in the incompressible scheme so that the time step is not limited by the sound CFL number α_c . Rather, in a explicit scheme for an incompressible flow the limiting (fastest) process is momentum diffusion (or advection at large flow rates) so stability is determined by the viscous CFL number $\beta = \nu\Delta t/h^2$. As we explained, we use a semi-implicit discretization of the viscous terms that eliminate the restriction $\beta \leq (1/2)^d$ and therefore it allows to use much larger time steps. The advection terms are solved with an explicit method and therefore the stability limit $\alpha_v \lesssim 1$ still applies.

We have developed a second-order semi-implicit discretization [Usabiaga 2012] based on previous work for the deterministic setting [Griffith 2009] which uses a Crank-Nicolson method for the viscous terms while it uses a explicit method for the remaining terms. A predictor step is needed to forecast the advective terms at the middle of the time-step, so the corrector step can be centered in time to achieve second order accuracy. The predictor step reads

$$\tilde{\mathbf{v}}^{n+1} + \Delta t \mathbf{G} \tilde{\pi} = \mathbf{v}^n + \Delta t \mathbf{A}_v(\mathbf{v}^n) + \frac{\Delta t}{2} \mathbf{L} (\mathbf{v}^n + \tilde{\mathbf{v}}^{n+1}) + \Delta t \rho^{-1} \mathbf{D} \boldsymbol{\Sigma} (\tilde{\mathbf{W}}_v^n), \quad (2.145)$$

$$\tilde{c}^{n+1} = c^n + \Delta t \mathbf{A}_c(\mathbf{v}^n, c^n) + \frac{\Delta t}{2} \chi \mathbf{L} (c^n + \tilde{c}^{n+1}) + \Delta t \rho^{-1} \mathbf{D} \boldsymbol{\Psi} (c^n, \mathbf{W}_c^n) \quad (2.146)$$

$$\text{s.t. } \mathbf{D} \tilde{\mathbf{v}}^{n+1} = 0, \quad (2.147)$$

and the corrector step

$$\mathbf{v}^{n+1} + \Delta t \mathbf{G}\pi = \mathbf{v}^n + \Delta t \mathbf{A}_v^{n+\frac{1}{2}} + \frac{\Delta t}{2} \mathbf{L}(\mathbf{v}^n + \mathbf{v}^{n+1}) + \Delta t \rho^{-1} \mathbf{D}\Sigma(\tilde{\mathbf{W}}_v^n), \quad (2.148)$$

$$c^{n+1} = c^n + \Delta t \mathbf{A}_c^{n+\frac{1}{2}} + \frac{\Delta t}{2} \chi \mathbf{L}(c^n + c^{n+1}) + \Delta t \rho^{-1} \mathbf{D}\Psi(\tilde{c}^{n+\frac{1}{2}}, \mathbf{W}_c), \quad (2.149)$$

$$\text{s.t. } \mathbf{D}\mathbf{v}^{n+1} = 0. \quad (2.150)$$

The advective terms $\nabla \cdot (\mathbf{v}\mathbf{v})$ and $\nabla \cdot (c\mathbf{v})$ are written with the abstract notation \mathbf{A}_v and \mathbf{A}_c . There are several possible choices for the nonlinear terms in the corrector step to ensure second-order weak accuracy. We decided to use the explicit trapezoidal rule

$$\mathbf{A}_v^{n+\frac{1}{2}} = \frac{1}{2} (\mathbf{A}_v(\mathbf{v}^n) + \mathbf{A}_v(\tilde{\mathbf{v}}^{n+1})), \quad (2.151)$$

$$\mathbf{A}_c^{n+\frac{1}{2}} = \frac{1}{2} (\mathbf{A}_c(\mathbf{v}^n, c^n) + \mathbf{A}_c(\tilde{\mathbf{v}}^{n+1}, \tilde{c}^{n+1})). \quad (2.152)$$

In the corrector step the concentration inside the stochastic term $\Psi(\mathbf{r}, t)$ is centered in time

$$\tilde{c}^{n+\frac{1}{2}} = \frac{1}{2} (c^n + \tilde{c}^{n+1}), \quad (2.153)$$

while for the stochastic fluxes we use the same random numbers $\tilde{\mathbf{W}}_v$ and \mathbf{W}_c in both steps. Importantly, although we use a single realization of the random numbers \mathbf{W} per time step, this scheme is still second-order weak accurate for any non-zero background flow. Moreover, in the absence of advection, the Crank-Nicolson method guarantees an infinite order of weak accuracy, that is, the scheme produces the correct thermodynamic averages for any time step [Donev 2010b, Usabiaga 2012, Delong 2013].

2.3.2.1 Projector method

One can see that the predictor and corrector steps have the same structure. Although these set of equations may look challenging, their solution by projector operator techniques becomes a relatively easy task in systems with periodic boundary conditions and uniform grids [Othmer 1997]. We illustrate how to proceed with the velocity equation in the predictor step Eq. (2.145) as the protocol is exactly the same for the concentration and the corrector step. First, we arrange the equations (2.145) and (2.147) like

$$\left(\mathbf{I} - \frac{\Delta t}{2} \nu \mathbf{L} \right) \tilde{\mathbf{v}}^{n+1} + \Delta t \mathbf{G}\tilde{\pi} = \mathbf{Q}, \quad (2.154)$$

$$\text{s.t. } \mathbf{D}\tilde{\mathbf{v}}^{n+1} = 0. \quad (2.155)$$

In the right-hand side \mathbf{Q} represents all the terms of the equation (2.145) that are not explicitly shown. All the terms collected in \mathbf{Q} are all explicit, so they are known a priori. As the equation (2.154) is linear in $\tilde{\mathbf{v}}^{n+1}$, its Fourier modes are uncoupled,

$$\left(\mathbf{I} - \frac{\Delta t}{2} \nu \hat{\mathbf{L}}_{\mathbf{k}} \right) \hat{\tilde{\mathbf{v}}}_{\mathbf{k}}^{n+1} + \Delta t \hat{\mathbf{G}}_{\mathbf{k}} \hat{\tilde{\pi}}_{\mathbf{k}} = \hat{\mathbf{Q}}_{\mathbf{k}}, \quad (2.156)$$

$$\text{s.t. } \hat{\mathbf{D}}_{\mathbf{k}} \hat{\tilde{\mathbf{v}}}_{\mathbf{k}}^{n+1} = 0. \quad (2.157)$$

Thanks to the Fourier transform our differential equation becomes an algebraic one. To find the pressure one just has to apply the divergence to the velocity equation (2.156) and use the fact that the Laplacian and the divergence operators commute (with PBC), therefore one gets

$$\Delta t \hat{\tilde{\pi}}_{\mathbf{k}} = \frac{\hat{\mathbf{D}}_{\mathbf{k}} \hat{\mathbf{Q}}_{\mathbf{k}}}{\hat{\mathbf{D}}_{\mathbf{k}} \hat{\mathbf{G}}_{\mathbf{k}}}. \quad (2.158)$$

Then, using this result in Eq. (2.156)

$$\hat{\tilde{v}}_k^{n+1} = \frac{\left(\hat{Q}_k - \frac{\hat{D}_k \hat{Q}_k}{\hat{D}_k \hat{G}_k}\right)}{\left(\mathbf{I} - \frac{\Delta t}{2} \nu \hat{L}_k\right)}. \quad (2.159)$$

The velocity modes in Fourier space $\hat{\tilde{v}}_k^{n+1}$ are then transformed to real space to finish the predictor step. A subtle point to remember is that one should use the discrete Fourier transform and the discrete version of the gradient, divergence and Laplacian operators, given in Fourier space in the equations (2.107)-(2.109). Finally, consider the special case $k = 0$. For this wavenumber all the operators are zero and the result of equation (2.156) is just $\hat{\tilde{v}}_0^{n+1} = \hat{Q}_0 = \hat{\tilde{v}}_0^n$ which implies the conservation of the total linear momentum. If there are external forces acting on the fluid such that the total momentum is not conserved, \hat{Q}_0 can be set to zero to represent a closed environment where the center of mass is fixed.

The most expensive operation of this scheme is the discrete Fourier transform, however in a regular grid the Fast Fourier Transform (FFT) of \mathbf{Q} (or $\hat{\tilde{v}}_k^{n+1}$) scales almost linearly ($O(n \log n)$) with the number of cells n . This allows for a large speed-up respect iterative schemes, which nonetheless are more versatile, since they can be used with nonuniform grids, without periodic boundary conditions or with variable viscosity [Griffith 2009, Griffith 2012a].

2.3.3 Semi-implicit compressible scheme

In some problems is unavoidable to solve the acoustic modes but the limitations in the time step imposed by explicit solvers are too strong. Inspired by the semi-implicit solvers for incompressible fluids we have developed a family of semi-implicit schemes for compressible flows. These schemes handle the pressure term with semi-implicit methods in an unconditionally stable way, therefore the time step is not longer limited by the speed of sound or the corresponding CFL number $\alpha_c = c\Delta t/h$. The rest of the terms will be, however, handled explicitly so the stability will be ensured only for CFL numbers $\alpha_v = \|\mathbf{v}\|_\infty \Delta t/h \lesssim 1$ and $\beta < (1/2)^d$. To alleviate the notation in this section we omit the equation for the concentration c , nonetheless the equation for a passive tracer can be easily included like we did in the other schemes.

We employ the second order weak accurate semi-implicit Runge-Kutta schemes presented in the reference [Delong 2013] in the context of incompressible flows. These schemes have two parts, a predictor an a corrector substep. The predictor substep update the system from time $t^n = n\Delta t$ to time $\tilde{t} = (n + \omega_2)\Delta t$ and it reads

$$\tilde{\rho} = \rho^n - (\omega_2 - \omega_1)\Delta t \mathbf{D}\mathbf{g}^n - \omega_1 \Delta t \mathbf{D}\tilde{\mathbf{g}}, \quad (2.160)$$

$$\tilde{\mathbf{g}} = \mathbf{g}^n - (\omega_2 - \omega_1)\Delta t \mathbf{G}\pi^n - \omega_1 \Delta t \mathbf{G}\tilde{\pi} + \omega_2 \Delta t \mathbf{D}\sigma^n + (\omega_2 \Delta t)^{1/2} \mathbf{D}\Sigma_1^n, \quad (2.161)$$

where the coefficients ω will be specified later, σ collects the terms that we are going to treat explicitly (in our case the advection and the dissipative terms) and Σ is the fluctuating stress tensor. If $\omega_1 \neq 0$ both equations are semi-implicit since it is necessary to know the state at time $\tilde{t} = (n + \omega_2)\Delta t$ to calculate the increment during the predictor step. We will explain shortly how to solve this kind of system.

The corrector substep update the system from time $t^n = n\Delta t$ to time $t^{n+1} = (n + 1)\Delta t$ and it reads

$$\rho^{n+1} = \rho^n - (1 - \omega_3 - \omega_4)\Delta t \mathbf{D}\mathbf{g}^n - \omega_3 \Delta t \mathbf{D}\tilde{\mathbf{g}} - \omega_4 \Delta t \mathbf{D}\mathbf{g}^{n+1}, \quad (2.162)$$

$$\begin{aligned} \mathbf{g}^{n+1} = & \mathbf{g}^n - (1 - \omega_3 - \omega_4)\Delta t \mathbf{G}\pi^n - \omega_3 \Delta t \mathbf{G}\tilde{\pi} - \omega_4 \Delta t \mathbf{G}\pi^{n+1} \\ & + \omega_5 \Delta t \mathbf{D}\tilde{\sigma} + (1 - \omega_5) \Delta t \mathbf{D}\sigma^n \\ & + (\omega_2 \Delta t)^{1/2} \mathbf{D}\Sigma_1^n + ((1 - \omega_2) \Delta t)^{1/2} \mathbf{D}\Sigma_2^n. \end{aligned} \quad (2.163)$$

Where Σ_1^n and Σ_2^n represent two independent realization of the stochastic stress tensor at time $t^n = n\Delta t$. Again these equations are a semi-implicit system of equations if $\omega_4 \neq 0$. Before providing the values for the coefficients ω we explain how to solve system of equations such as (2.160)-(2.161) or (2.162)-(2.163). Since predictor and corrector substeps are similar, we focus on the predictor substep. Taking the divergence of the momentum equation (2.161) and plugging the result into the density equation we get, after rearrangement,

$$\begin{aligned} \tilde{\rho} - (\omega_1 \Delta t)^2 \mathbf{L} \tilde{\pi} &= \rho^n + \omega_1(\omega_2 - \omega_1) \Delta t^2 \mathbf{L} \pi^n - \omega_2 \Delta t \mathbf{D} \mathbf{g}^n \\ &\quad - \omega_1 \Delta t \mathbf{D} \left(\omega_2 \Delta t \mathbf{D} \sigma^n + (\omega_2 \Delta t)^{1/2} \Delta t \mathbf{D} \Sigma^n \right). \end{aligned} \quad (2.164)$$

The terms in the right hand side are defined at time $t^n = n\Delta t$ and they can be calculated before the predictor update. On the other hand, the terms on the left represent the scheme's implicit part, encoded in $\tilde{\rho}$ via the equation of state $\tilde{\pi} = \pi(\tilde{\rho})$.

In general it is necessary to employ iterative solvers to update equations like (2.164). However, when the equation of state is linear $\pi(\rho) = c_T^2 \rho$ and the system has PBC it is possible to solve the above equation using FFT, just as we did for the viscous terms in the incompressible scheme (see projector method's section 2.3.2.1). Once the density at the end of the predictor step is known, it is possible to calculate the pressure $\tilde{\pi}$ and then update the momentum equation (2.161). The protocol to solve the corrector step is exactly the same.

Now we discuss the optimal values for the coefficients ω . To achieve second order accuracy the values of the coefficients ω should be chosen such as the first five moments of the numerical increment ($x^{n+1} - x^n$) match up to order Δt^2 the moments of the real increment ($x((n+1)\Delta t) - x(n\Delta t)$) which can be calculated by a Taylor expansion of the stochastic differential equation. For details the reader is referred to the work of Delong et al. and the references herein [Delong 2013]. For additive noise the second order accuracy is achieved if the coefficients obey the relations

$$\omega_2 \omega_5 = \frac{1}{2}, \quad (2.165)$$

$$\omega_2 \omega_3 + \omega_4 = \frac{1}{2}. \quad (2.166)$$

In the next sections we discuss the most promising choices to simulate acoustic problems.

2.3.3.1 Semi-implicit midpoint predictor-corrector

After several trials we determined that the best choice of values to work with acoustic problems is

$$\omega_1 = \omega_2 = \omega_4 = \frac{1}{2}, \quad \omega_3 = 0, \quad \omega_5 = 1. \quad (2.167)$$

This scheme has several advantages. In the first place, in the corrector substep (recall Eqs. (2.162)-(2.163)) the semi-implicit terms take the form of a Crank-Nicolson method. This guarantees that in the absence of the explicit terms the scheme produces the correct static structure factor for any time step or sonic CFL number. We note that the explicit terms are never zero, but in general the time step will be small compared with the characteristic times of advective and diffusive process, therefore we expect that this scheme will provide a good accuracy for the physical magnitudes related with those terms.

Despite its advantages this method has also limitation, specially to study the dynamics of the sound modes for large time steps. To see this, lets consider the update of a density mode in Fourier space $\rho_{\mathbf{k}}$. From the equations (2.162)-(2.163) the density mode at time $t^{n+1} = (n+1)\Delta t$ is

$$\left[\mathbf{I} - \left(\frac{c_T \Delta t}{2} \right)^2 \mathbf{L}_{\mathbf{k}} \right] \rho_{\mathbf{k}}^{n+1} = \left[\mathbf{I} + \left(\frac{c_T \Delta t}{2} \right)^2 \mathbf{L}_{\mathbf{k}} \right] \rho_{\mathbf{k}}^n + \mathcal{O}(\Delta t). \quad (2.168)$$

For $c_T \Delta t \rightarrow \infty$ the updated density is just $\rho_{\mathbf{k}}^{n+1} = -\rho_{\mathbf{k}}^n$, these unphysical oscillations are characteristic of the Crank-Nicolson method when it is used with very large time steps. We can estimate how large can be the time step to correctly capture the dynamics of a mode with wavelength λ . From the Eq. (2.168) we hypothesized that the correct dynamic can only be captured if $\left[\mathbf{I} + \left(\frac{c_T \Delta t}{2} \right)^2 \mathbf{L}_{\mathbf{k}} \right] > 0$, which avoids the unphysical oscillations of the density mode. Using the discrete expression for the Laplacian operator [Eq. (2.109)] we get the condition for the time step $\Delta t < h/(c_T \sin(\pi h/\lambda))$, this time step implies a CFL acoustic number

$$\alpha_c = \frac{c_T \Delta t}{h} < \sin^{-1} \left(\frac{\pi h}{\lambda} \right). \quad (2.169)$$

If we want to capture the dynamic of small wavelengths the sonic CFL number can not be very large, for example for $\lambda = 2h$ the above limit gives $\alpha_c = 1$. However, if we only want to recover the dynamic for long wavelengths the maximum acoustic CFL number can be much larger, for example for $\lambda = 32h$, $\alpha_c \approx 10$, which represents a huge speed-up with respect to the explicit compressible solver.

A similar argument could have been done by comparing the time step Δt with the characteristic time of each mode τ_λ , and the non-surprising conclusion is that the correct dynamic of a given mode can only be recovered if $\Delta t < \tau_\lambda$.

2.3.3.2 L-stable method

To finish the discussion of the semi-implicit compressible solver we introduce a method that can correctly handle the limit $c_T \rightarrow \infty$ and which presents a smooth transition between the compressible and incompressible setting.

To handle the incompressible limit we want that the sound modes, or equivalently the longitudinal velocity modes decay to zero for very large speed of sound. A easy method to achieve this property is to use a the density update that obeys $\rho_{\mathbf{k}}^{n+1} \rightarrow 0$ for $c_T \Delta t \rightarrow \infty$ independently of the modes in the previous time step $\rho_{\mathbf{k}}^n$. The kind methods that obeys the above relations are known in numerical analysis as L-stable methods. In this way the scheme is stable for any sonic CFL number $\alpha_c = c_T \Delta t / h$, and the density modes decays to zero for large enough time steps. It possible to have a second order accurate L-stable method by using the coefficients [Delong 2013]

$$\omega_1 = \omega_4 = 1 - \frac{\sqrt{2}}{2}, \quad \omega_2 = \frac{1}{2}, \quad \omega_3 = -1 + \sqrt{2}, \quad \omega_5 = 1. \quad (2.170)$$

The Runge-Kutta scheme with these coefficients damps the density modes for the wave vector \mathbf{k} when $(c_T \Delta t k)^2 \gtrsim 1$. Since the longitudinal velocity modes are coupled with the density, they are damped at the same rate than $\rho_{\mathbf{k}}$. Although the properties of this scheme seem very appealing, we have found that the density modes are damped too fast for the acoustic problems that we present in Chapter 7. Therefore, in general we will prefer the semi-implicit midpoint scheme introduced above. Nonetheless we think this last scheme can be useful for some problems [Kwatra 2009].

2.4 Validation

In this section we present numerical results to assert the accuracy of our schemes. We will study the static structure factor $S(\mathbf{k})$ and the dynamic structure factor $S(\mathbf{k}, \omega)$ for systems at thermal equilibrium [de Zárate 2006]. The results will be presented as function of the dimensionless CFL number introduced in the Eqs. (2.127)-(2.130), since they control the stability and accuracy of the results. In some of the

tests we will include a strong uniform background flow \mathbf{v}_0 to test the behavior of the advective term $\mathbf{v} \cdot \nabla \mathbf{v}$. Note that while the continuous Navier-Stokes equations are Galilean invariant the discrete version of the equations are not, and it is important to check that the numerical artifacts are small.

To better appreciate the numerical errors of the static structure factor the results are normalized with the theoretical covariance [Eqs. (2.69)-(2.71)] for the self correlation like $S_{vv}(\mathbf{k})$ or $S_{\rho\rho}(\mathbf{k})$. For the cross correlations we normalize the results with the square root of the covariance of each variable, for example, for the cross-correlation between the velocity and the density we use

$$S_{v\rho}(\mathbf{k}) = \frac{\langle \delta \hat{\mathbf{v}}_{\mathbf{k}} \delta \hat{\rho}_{\mathbf{k}}^* \rangle}{\sqrt{k_B T / \rho} \sqrt{\rho k_B T / c_T^2}}. \quad (2.171)$$

To compute the static structure factor we use a Discrete Fourier Transform which for a scalar field $\phi(\mathbf{r})$ defined at $\mathbf{r} = (j_1, j_2, j_3)h$ for integers j_1, j_2 and j_3 in a simulation box of side $L = Nh$, it is given by

$$\hat{\phi}_{\mathbf{k}} = \frac{1}{N^3} \sum_{j_1, j_2, j_3=0}^{N-1} e^{-\frac{2\pi i}{N}(m_1 j_1 + m_2 j_2 + m_3 j_3)} \phi_{\mathbf{r}}, \quad (2.172)$$

where $\mathbf{k} = (m_1, m_2, m_3)2\pi/L$ and m_1, m_2 and m_3 are also integer numbers taking values from 0 to $N - 1$. For vector fields the staggered grid introduces a phase shift in the Fourier space that should be taken into account. For example, a factor $\exp(ik_x h/2)$ is introduced during the Fourier transform of the x-component of the velocity field.

2.4.1 Explicit compressible scheme

In figure 2.3 we show some results for the explicit compressible solver presented in section 2.3.1. The simulations were done for a relatively high advective CFL number ($\alpha = 0.25$) with a strong background flow ($\|\mathbf{v}_0\| \simeq 0.23c_T$ or $\text{Ma} \simeq 0.23$). Even in those conditions the errors are relatively small for all the wavenumbers \mathbf{k} . The largest deviations from the theory are observed in the density self-correlation $S_{\rho\rho}$ with errors up to 5% for some wavenumbers (Top left panel of Fig. 2.3). We hypothesize that the error is largest in the density self-correlation because its dynamic equation does not contain diffusive or stochastic terms, and therefore the density fluctuations arise only from its coupling with the velocity field. In the same figure we can see that the numerical errors are smaller for small wavenumbers (which correspond with the center of the cube) and grow with the wavenumbers. This result seems natural since the characteristic times are smaller for larger wavenumbers, and therefore it is expected that the numerical error from the temporal discretization will be more evident for such modes.

For other side, the cross-correlations ($S_{\rho v^x}, S_{v^x v^y}, \dots$) are very close to zero for all wavenumbers as theoretically predicted, although the largest error are observed again for the largest wavenumbers. We repeated this simulation without background flow to find similar results, therefore any possible non-Galilean effect in the discretized equations is very weak. In the left panel of Fig. 2.4 we show the error of the covariance of the fluid variables for several time steps (or CFL numbers). The scheme exhibits a third order convergence for all the covariances even in the presence of a strong background flow, again $\text{Ma} \simeq 0.23$. Therefore these results confirm the theoretical prediction of reference [Donev 2010b].

2.4.2 Semi-implicit incompressible scheme

In figure 2.5 we show the structure factor for the incompressible scheme presented in section 2.3.2. As we explained, at equilibrium, the velocity structure factor is proportional to the divergence free projector operator, $S_{vv} = (k_B T / \rho) \mathcal{P}$. Because of this, the spectra is not white in the cartesian basis (v_x, v_y, v_z) ,

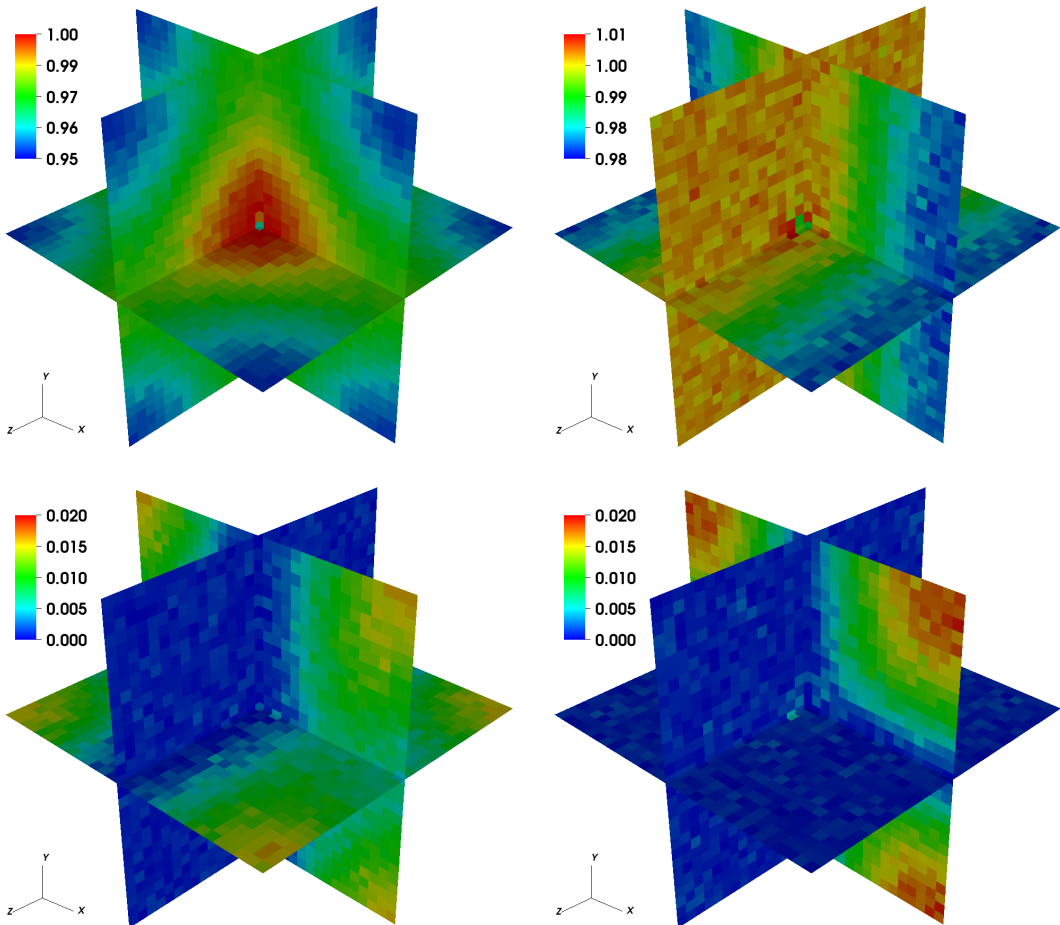


Figure 2.3: **(Explicit compressible scheme)** Normalized structure factors $\tilde{S}_{\rho\rho}$ (top left), $\tilde{S}_{v_x v_x}$ (top right), $\tilde{S}_{\rho v_x}$ (bottom left), and $\tilde{S}_{v_x v_y}$ (bottom right) obtained with the explicit compressible solver of Sec. 2.3.1 in a periodic system with 30^3 cells. In these simulations a strong uniform background flow $v_0 = (0.2, 0.1, 0.05)c_T$ is imposed and the acoustic CFL number is set to $\alpha_c = 0.25$. The rest of the parameters are given in Table 2.1. The density self-correlation presents deviations from the theoretical value ($S_{\rho\rho} = 1$) for large wavenumbers. The deviations do not show a preferred direction although the background flow is stronger along the x axis, this fact proves that the non-Galilean effects of the advective terms are very small. The different structure factors for v_x ($\tilde{S}_{v_x v_x}$, $\tilde{S}_{\rho v_x}$ and $\tilde{S}_{v_x v_y}$) also have larger errors for large wavenumbers but in this case the direction is important because for v_x the direction x is not equivalent to y or z . In the three cases the errors are smaller for the wavevectors $\mathbf{k} = (0, k_y, k_z)$. The structure factors for the other velocity components are similar.

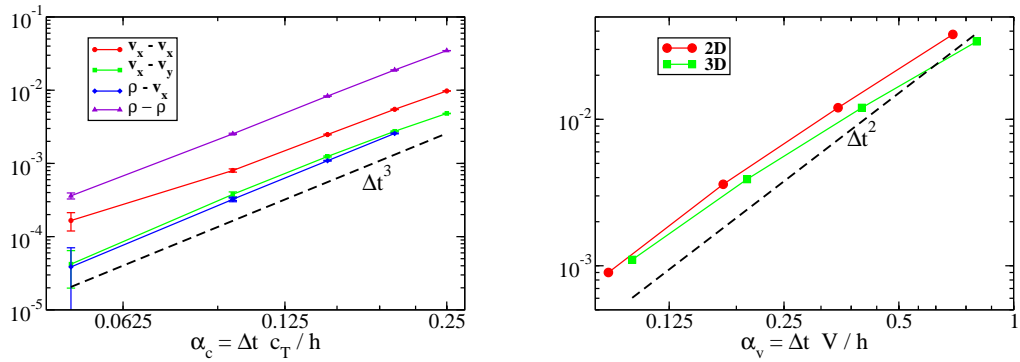


Figure 2.4: Relative error in the cross-correlations versus the time step or advective CFL number α . (Left) Results for the explicit compressible solver with parameters as in Figure 2.3. The error bars represent the statistical errors which are proportional to $N^{-1/2}$, being N the number of independent measures. From the results it is clear that the scheme is third-order weak accurate. (Right) Results for the incompressible solver in 2 and 3 dimensions in a periodic system with 32^2 or 32^3 cells. The background flow was set to $v_0 = (\sqrt{3}, 2)/2$ and $v_0 = (1, 1/3, 1/3)$ in each case, corresponding to cell Reynolds number $r = \sqrt{3}/2$ and $r = 1$. In these cases the scheme is second-order weak accurate as stated in section 2.3.2. The incompressible simulations were done by collaborators with the IBAMR code [Griffith , Usabiaga 2012].

and we rather use the normal basis formed by the longitudinal and vortical modes $(v^{(1)}, v^{(2)}, v^{(3)})$ [see equations (2.85)-(2.87)] to calculate the static structure factor. The structure factor of the longitudinal mode is exactly zero while the two vortical modes presents small errors even for an advective CFL number as high as $\alpha = 0.5$. Also, note that the viscous CFL number ($\beta = 0.5$) is above the stability limit for explicit solvers ($\beta \leq (1/2)^3$ in three dimensions). This excellent result arises from the unconditionally stable behavior of the scheme in solving the linearized Navier-Stokes equations, in which case the correct covariances are reproduced for any time step (or viscous CFL number β) [Donev 2010b, Usabiaga 2012]. However, it is important to note that for a given time step Δt , this scheme only reproduces the correct dynamic for modes with a characteristic time larger than Δt .

In the right panel of figure 2.4 we show the weak convergence order in presence of a background flow $v_0 \neq 0$. As it was expected the scheme shows a clear second-order convergence accuracy.

2.4.3 Semi-implicit compressible solver

To finish the study of the static structure factor we present the results for the two versions of the semi-implicit compressible solver that we described in the section 2.3.3, the midpoint and the L-stable scheme. In figure 2.6 we show the static structure factor for several variables calculated with the midpoint semi-implicit scheme. The first thing to notice is that the advective CFL number $\alpha_c = c_T \Delta t / h$ is well above the stability limit for the explicit solvers ($\alpha_c \lesssim 1$), since we work at $\alpha_c = 2$. In spite of that, the calculated structure factors are nearly perfect for all the correlations considered. In fact, the small deviations from the theory are probably of statistical nature. To obtain these good results it is necessary to employ a small viscous CFL number, since the dissipative terms are treated with an explicit method. However, this is not a strong limitation if we are interested in the sonic modes, normally much faster than the viscous modes. As we explained in the Section 2.3, the ratio between the advective and viscous

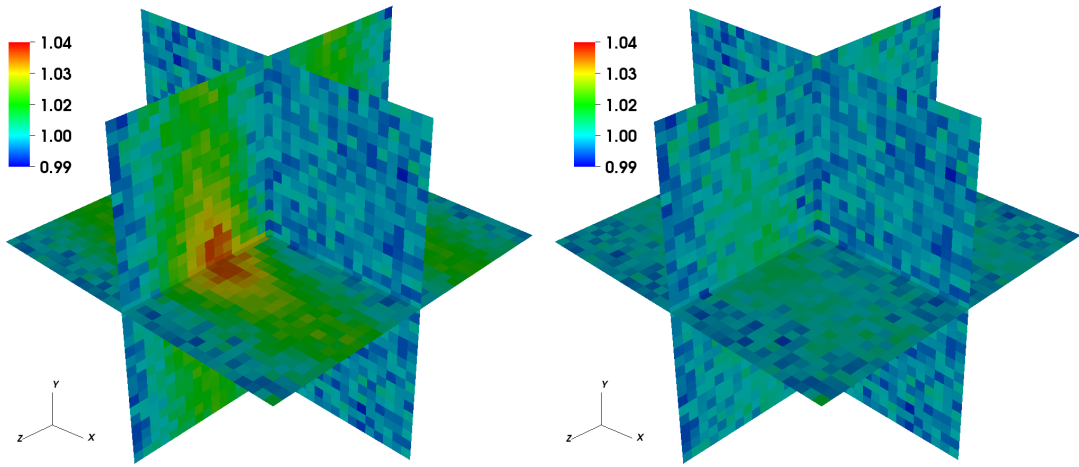


Figure 2.5: (**Semi-implicit incompressible scheme**) Structure factor for the first solenoidal mode ($\tilde{v}^{(2)}$) calculated with the incompressible solver of Sec. 2.3.2 for an advective CFL number $\alpha_v = 0.5$ (left) and $\alpha_v = 0.25$ (right). From the definition of $\tilde{v}^{(2)} = (k_x^2 + k_y^2)^{-1/2}(-k_y, k_x, 0)$, the structure factor dependence on k_x should be equivalent to its dependence on k_y as it is clearly the case for the numerical results. These simulations were done by collaborators with the code IBAMR [Griffith , Usabiaga 2012].

CFL numbers is the so called Reynolds cell number $r = \alpha_c/\beta = ch/\nu$. For water at ambient conditions one gets $r \sim 1(\text{nm})^{-1}h$. As $h > 50$ nm for fluctuating hydrodynamics hypothesis to hold (e.g. [Delgado-Buscalioni 2006]) one concludes that for water $r \gg 1$, or equivalently $\beta \ll \alpha_c$. In fact, for the vast majority of fluids, the time scale separation between sound and viscous modes is so large that in computational approaches it is common to scale down the speed of to reduce the equation's stiffness, what this new scheme allows it is to work with the right separation of time scales or at least close to it.

Figure 2.7 presents the structure factor for the L-stable compressible scheme for different time steps. In this case we focus on the longitudinal velocity mode. For very small CFL number $\alpha_c = 0.02$ (top left panel in Fig. 2.7), the structure factor does not present any appreciable structure and it recovers the theoretical prediction $k_B T / \rho$ for a compressible fluid. However, as the time step is increased to $\alpha = 0.2, 2$ and 50 the longitudinal modes of the velocity decay very fast and for the largest time step considered the scheme behaves practically like an incompressible solver. We tested that the density fluctuations presented a similar behavior with the time step, decaying to zero for $\alpha_c \gg 1$. Therefore, by varying the sonic CFL number the scheme smoothly switches from a compressible to an incompressible behavior, a feature reported also in other schemes [Kwatra 2009]. As for the midpoint semi-implicit compressible solver we remind that the time step is still limited by the conditions $\alpha_v = \|\mathbf{v}\|_\infty \Delta t / h \lesssim 1$ and $\beta < (1/2)^d$ in a d dimensional space.

2.4.4 Dynamic structure factor

The static structure is an important magnitude because it characterizes the steady state, however, it does not provide information about the dynamics. To study the temporal accuracy of our schemes it is convenient to use the dynamic structure factor, which is a measure of the spatio-temporal correlation of the hydrodynamic fields. For any two fields \mathbf{u} and \mathbf{w} their dynamic structure factor is defined by

$$S_{uw}(\mathbf{k}, \omega) = \langle \hat{\mathbf{u}}(\mathbf{k}, \omega) \hat{\mathbf{w}}^*(\mathbf{k}, \omega) \rangle, \quad (2.173)$$

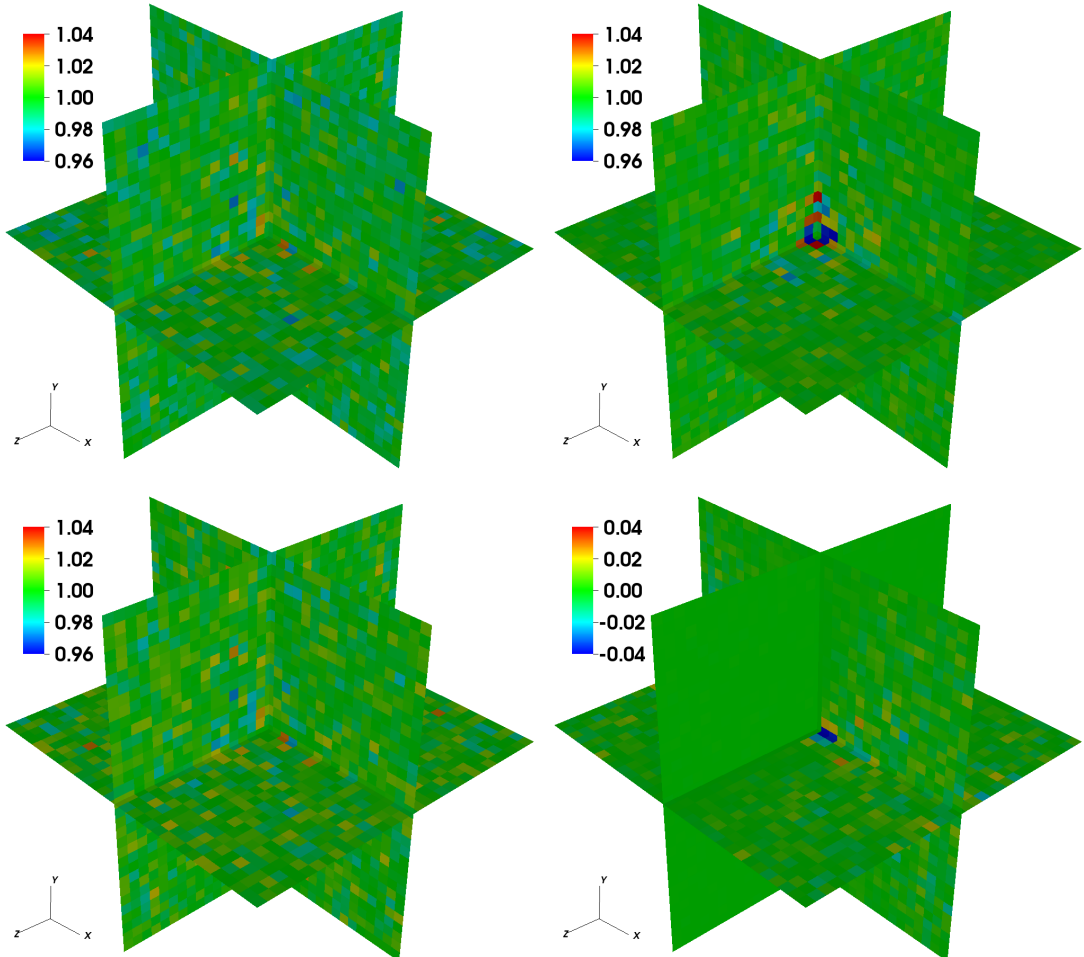


Figure 2.6: (**Semi-implicit midpoint compressible scheme**) Normalized structure factors for the velocity longitudinal mode $\tilde{S}_{v(1)v(1)}$ (top left), first velocity vortical mode $\tilde{S}_{v(2)v(2)}$ (top right), $\tilde{S}_{\rho\rho}$ (bottom left) and $\tilde{S}_{v_x\rho}$ (bottom right) obtained with the semi-implicit midpoint compressible solver in a periodic system with 32^3 cells. The sonic CFL number in these simulation is $\alpha_c = 2$. Besides the very large time step the results are nearly perfect because the scheme uses a Crank-Nicolson discretization for the pressure terms (see Sec. 2.3.3) and the viscous CFL number is small, in these figures $\beta = 0.01$.

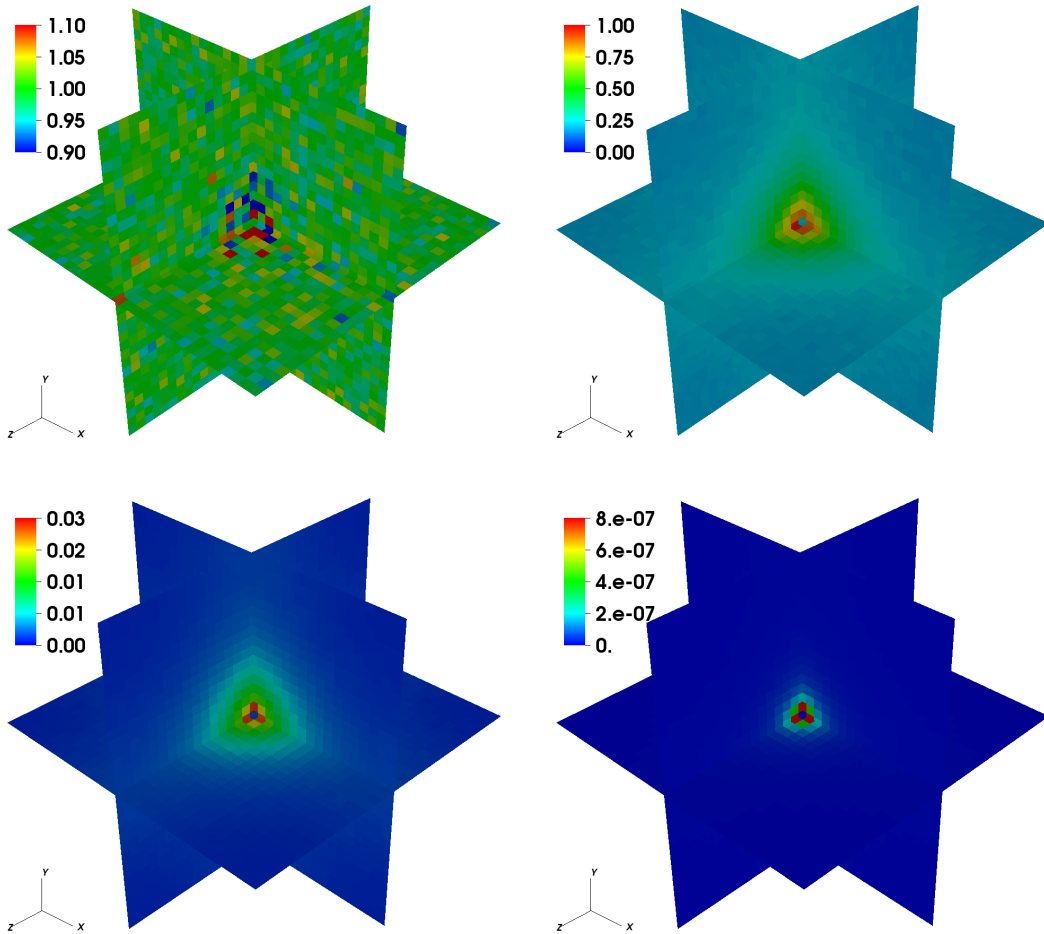


Figure 2.7: **(Semi-implicit L-stable compressible scheme)** Normalized structure factors for the velocity longitudinal mode $\tilde{S}_{v(1)v(1)}$ obtained with the compressible semi-implicit L-stable method of Sec. 2.3.3.2. The sonic CFL number in these figures is $\alpha_c = 0.02$ (top left), $\alpha_c = 0.2$ (top right), $\alpha_c = 2$ (bottom left) and $\alpha_c = 50$ (bottom right). In all the panels $c_T = 4$ expect in the left bottom panel where $c_T = 100$, the rest of the parameters are given in Table 2.1. The amplitude of the longitudinal mode decays very fast with the sonic CFL number. The density mode (not shown) presents a similar behavior while the vortical modes (not shown) are in agreement with the theoretical value because the viscous CFL numbers are small $10^{-4} \leq \beta \leq 2.5 \cdot 10^{-2}$.

where spatio-temporal Fourier transform of the field $\mathbf{u}(\mathbf{r}, t)$ is defined in the continuous case by

$$\hat{\mathbf{u}}(\mathbf{k}, \omega) = (2\pi)^{-4} \int \mathbf{u}(\mathbf{r}, t) e^{-i(\mathbf{k}\mathbf{r} + \omega t)} d^3k dt, \quad (2.174)$$

and in the discrete case by the generalization of the equation (2.172). If a scheme reproduces the correct dynamic structure factor it also reproduces the correct static structure factor, since both magnitudes are related by

$$S_{uu}(\mathbf{k}) = \frac{1}{2\pi} \int_{-\infty}^{\infty} S_{uu}(\mathbf{k}, \omega) d\omega$$

However the opposite is not generally true. The best example is the semi-implicit incompressible scheme. As we said, in absence of advective terms that scheme reproduces the correct static structure factor for any time step thanks to the Crank-Nicolson discretization. However only the modes with characteristic time $\tau > \Delta t$ show the correct dynamic [Delong 2013].

The panels of Figure 2.8 show the dynamic of several variables calculated with the explicit compressible solver of Sec. 2.3.1. Together the numerical results we also show the theoretical curves for the linearized Navier-Stokes equations [Boon 1991, de Zárate 2006]. In the left panel of Fig. 2.8 we show the self correlation $S_{\rho\rho}(\mathbf{k}, \omega)$ and $S_{vv}(\mathbf{k}, \omega)$. The curve $S_{\rho\rho}(\mathbf{k}, \omega)$ has two Brillouin peaks due to the sonic transport of mass while the central peak observed in the experiments is missing because we are working with the isothermal Navier-Stokes equations (i.e. we are not including an equation for the fluid energy). The velocity structure factor presents a central peak at $\omega = 0$ associated the viscous transport of momentum and two Brillouin peaks due to the sonic transport of momentum. In the continuum setting the Brillouin peaks of either $S_{\rho\rho}(\mathbf{k}, \omega)$ or $S_{vv}(\mathbf{k}, \omega)$ are located at $\omega \approx \pm c_T k$, however, in the discrete setting the peaks are located at $\omega \approx \pm s_{\text{ef}} k$ where $s_{\text{ef}} = s_{\text{ef}}(\mathbf{k})$ is the effective speed of sound given in the equation (2.113). Therefore, even in the limit $\Delta t \rightarrow 0$ the spatial discretization introduces a deviation from the continuous setting. These deviations can be explained by the wavelength dependence of the effective transport coefficients (see Sec. 2.2.1). However, for small wavenumbers these effects are small and it is possible to have a perfect agreement between the numerical and theoretical results, just as we show in Fig. 2.8. The good agreement in the density structure factor is specially remarkable because the density equation of motion does not have stochastic terms and the density fluctuations arise only from the velocity-density coupling. To recover these results, the skew-adjoint property of the advective terms is fundamental, since that term couples the velocity and density modes. In the right panel of the same figure (Fig. 2.8) we plot cross-correlations between the density and different velocity components. Again the results from the explicit compressible solver show a perfect match with the theoretical prediction even for a sonic CFL number as high as $\alpha_c = 0.25$.

In Figure 2.9 we show dynamic structure factors calculated with the semi-implicit midpoint compressible solver of Section 2.3.3. In the left panel, the simulations for a moderate sonic CFL number ($\alpha_c = 0.2$) obtain a good agreement between theory and numerical results. In the right panel of the same figure, we maintain all the simulation parameters constant but the time step, increasing the sonic CFL number to $\alpha_c = 2$. The central peak, related to the viscous transport of momentum, is still well solved because the viscous CFL number is small. However, the Brillouin peaks are shifted to lower frequencies. To explain these results we should compare the characteristic time of these modes with the time step. The Brillouin peaks of Figure 2.9 have a characteristic time $\tau = 2\pi/\omega_{\text{peak}} \approx 23$ (arb. units) while in these simulations the time step was $\Delta t = 5$. The semi-implicit scheme can not capture the oscillation of a mode with a time resolution so small, only 4 steps per oscillation. This is a natural result that seems very difficult (or impossible) to overcome. However, as we discussed in Sec. 2.3.3 the semi-implicit solver allows to under-resolve the dynamic for the highest modes while correctly described the lower and slower modes.

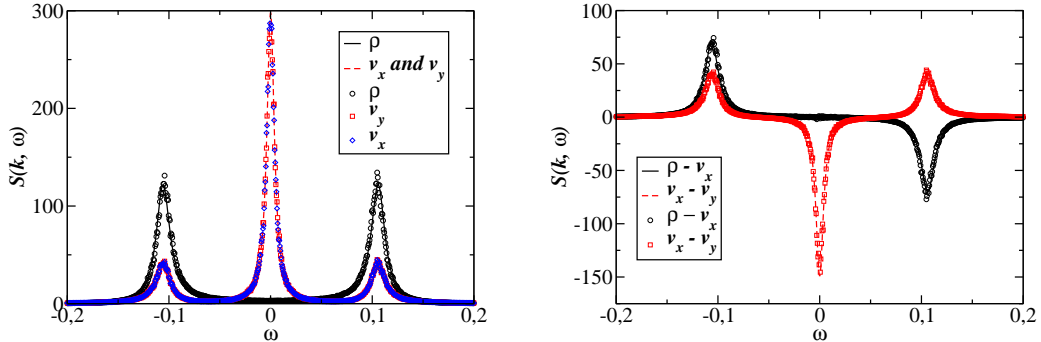


Figure 2.8: (**Explicit compressible scheme**) Numerical data (symbols) and theory (lines) for the real part of the dynamic structure factor in a system of 30^3 cells and volume L^3 for the wavevector $k = (2, 2, 2,)2\pi/L$. The imaginary parts are strictly zero for the self correlations and zero within statistical accuracy for the cross-correlations as predicted by the theory. The rest of the parameters are given in Table 2.1.

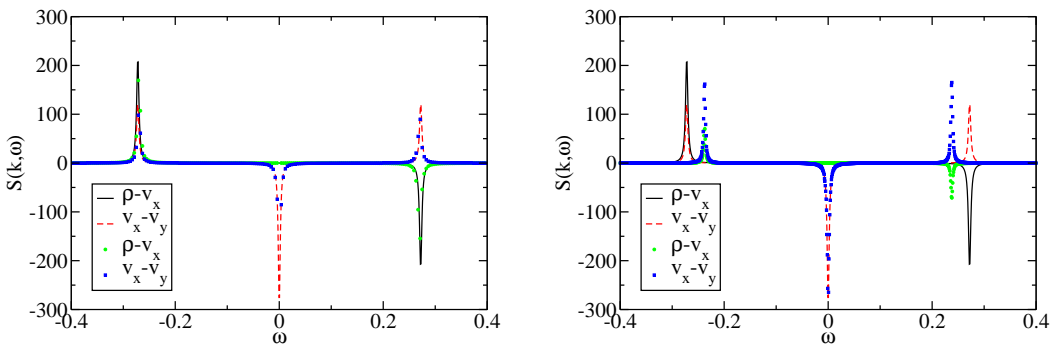


Figure 2.9: (**Semi-implicit midpoint compressible scheme**) Real part of the dynamic structure factor obtained with the semi-implicit midpoint compressible solver (symbols) and predicted by the theory (lines). Left panel, results for a sonic CFL number $\alpha_c = 0.2$. Right panel, results for $\alpha_c = 2$, the rest of the parameters are given in Table 2.1. As one can see large time steps shift the Brillouin to lower frequencies, which should be interpreted as a smaller speed of sound due to numerical errors.

Figure	2.3 & 2.4 & 2.8	2.5 & 2.4	2.6	2.7
grid spacing h	100	1	10	10
number of cells N	30^3	32^3	32^3	32^3
equilibrium density ρ_0	0.632	1	1	1
shear viscosity η	53.71	1	0.5	0.5
bulk viscosity ζ	127.05	-	0.5	0.5
speed of sound c_T	14.67	-	4	4-100
advective CFL α	0.25	0.5-0.25	2	0.02-50
viscous CFL β	0.017	0.5	0.01	0.0001-0.025

Table 2.1: Simulation parameters for the validation tests. The values of the first column (Fig. 2.3, 2.4 and 2.8) are given in units of Å, ps and g/mol to model water [Fabritiis 2007]. The values of the other columns are given in arbitrary units and they were selected to have the appropriate dimensionless numbers for each scheme.

Chapter 3

Inertial coupling method

Contents

3.1	Equations of motion	62
3.2	The blob model	63
3.2.1	Derivation of the Inertial Coupling Method	64
3.3	Equations of the ICM	67
3.3.1	Equivalent forms of the equations of motion	68
3.3.2	Energy conservation	69
3.3.3	Fluctuation dissipation balance	70
3.3.4	Incompressible limit	72
3.4	Spatial discretization	74
3.4.1	Notes for the incompressible case	76
3.5	Temporal discretization	76
3.5.1	First order compressible scheme	76
3.5.2	Compressible scheme	79
3.5.3	Incompressible scheme	80
3.6	Validation	85
3.6.1	Steady flows and hydrodynamic radius R_H	86
3.6.2	Deterministic convergence	89
3.6.3	Hydrodynamic forces	92
3.6.4	Equilibrium distribution	94
3.6.5	Velocity autocorrelation function	96
3.6.6	Diffusion Coefficient	99

In this chapter we introduce an Eulerian-Lagrangian method to solve the dynamic of solute particles embedded in a Newtonian fluid. As stated in the introduction in many problems the difference of particles sizes is so large that it is necessary to use hybrid simulation methods where the solvent formed by small molecules is described by continuous fields while for the larger solute particles (colloids, polymers) an explicit description is used. Therefore, the problem of coupling the dynamic equations of discrete particles and continuous fields arises quite often. Many methods have been developed to simulate soft matter systems, but in general they are constrained to work in a narrow regime of physical conditions. We develop a method able to work in many different regimes with a low computational cost.

Before we describe our method it is useful to review some popular methods and discuss their strengths and disadvantages.

Purely Lagrangian methods like dissipative particle dynamics (DPD) [Español 1995], smoothed particle hydrodynamics (SPH) [Monaghan 1992], smoothed dissipative particle dynamics (SDPD) [Español 2003] or stochastic rotation dynamics (SRD) [Malevanets 1999, Padding 2006] have become quite popular in the soft matter community. These methods describe both the solute particles and the solvent by mean of particles or Lagrangian points. They allow to an easy treatment of complex boundaries or different kind of solute particles. However, these methods also present important drawbacks, typically they have to work at unrealistic Schmidt, Mach or Knudsen numbers. To approach realistic numbers they have to use unfeasible small time steps and an incredible large number of solvent particles [Padding 2006].

To circumvent such problems Eulerian and Eulerian-Lagrangian methods have been employed. These methods use a Eulerian description to solve the hydrodynamic fields, typically described by the fluctuating Navier-Stokes equations, while the solute particles are described in a Lagrangian way and therefore can move freely through the space. These methods allow to use all the machinery developed for deterministic fluid dynamics. However, the problems due to the separation of length and time scales are not totally solved, in part because the details of each method have a profound effect on the process they can accurately recover.

Due to the disparate range of length and time scales usually involved in particle hydrodynamics, computational studies have to reduce the number of degrees of freedom characterizing these systems. This is the *coarse-graining* paradigm. A hierarchical list of simplifications might be envisaged, starting from the elimination of the molecular degrees of freedom of the solvent and following by the gradual simplification of the solute particles structure. One limit to this reductionist approach is the so called *point-particle* model where particles are driven by the flow but do not modify it. Such *one-way* coupling model is valid for small particle radius [Maxey 1983] and has been one of the main tools in turbulent research [Eaton 2009]. In the next description level the fluid-particle force is also transferred to the fluid phase thus allowing for *two-way* coupling [Eaton 2009] (see also Ref. [Lomholt 2001] for further classifications). The two-way coupling permits a fast solution of the hydrodynamic coupling between particles if enough resolution is used (a maximum of one particle per fluid cell [Dünweg 2009]). For this reason this approach has become quite popular in the soft matter community (zero Reynolds), being applied to colloids [Dünweg 2009, Giupponi 2007], polymer chains [Kekre 2010] and membranes [Atzberger 2011]. It is also being used in turbulence, although with a coarser spatial resolution (several particles per cell) [Eaton 2009]. The standard implementation of the fluid-particle force rests on a *frictional coupling* ansatz, based on the form of the Stokes drag [Eaton 2009, Dünweg 2009]. Such a force recovers the perturbative field far from the particle [Dünweg 2009] but does not resolve the near flow, leading to large fluid slip over the particle sites. The fluid force over a real particle is determined by the net fluid stress over the particle surface, however resolving the distribution of fluid stress around the particle requires spatial resolution of the fluid-solid boundary [Uhlmann 2005]. In this finer level of description it is also possible to include elastic forces arising from interface deformations, so as to describe fluid-structure interaction [Peskin 2002, Atzberger 2007, Atzberger 2011]. According to this upgrade, the “particle” interface becomes a 2D *continuum* boundary immersed in a 3D continuum media [Peskin 2002] and technical issues related to the surface spatial discretization need to be considered (meshing, convergence, leaking, area/volume preservation, etc., see Refs. [Griffith 2012a, Bringley 2008, Atzberger 2011] for recent works). A different but interesting approach with intermediate resolution [Nakayama 2005] delimits the *whole* particle domain with a smooth kernel or weighting function which distributes the particle and fluid contribution into a mixed (particle-fluid) velocity field. Imposing the incompressibility constraint in both (fluid and mixed) fields, results in the

impenetrability of fluid across the particle-fluid interface.

Time resolution is the other important aspect in coarse-graining. Colloidal dynamics involves a broad range of times and physical phenomena: from random collisions with solvent molecules (picoseconds) to colloidal diffusion times $\tau_d = R^2/\chi$ (reaching seconds for typical colloidal sizes $R \sim 1\mu\text{m}$). All scaled are intertwined: the diffusion coefficient $\chi = kT/\xi$ is determined by the friction coefficient ξ which, in turn, depends on solvent-surface molecular details [Felderhof 2012]. However, such large separation in time scales permits to derive closed equations for dynamical regimes at different time resolution [Atzberger 2011], the slowest one corresponding to the Brownian limit, where hydrodynamic memory is integrated out and colloid positions are the only relevant variables. Here, we are interested in resolving particle interactions with all hydrodynamic modes. In particular, in a fluid of density ρ and viscosity η , vorticity diffusion (transverse mode) needs a viscous time $\tau_\nu = \rho R^2/\eta$ (microseconds) to reshape the fluid velocity field in response to colloid displacements. In turn, due to friction forces $\xi(\dot{\mathbf{q}} - \mathbf{v})$, a colloid of mass m relaxes its velocity $\dot{\mathbf{q}}$ to the environment velocity \mathbf{v} within a friction time $\tau_f = m/\xi$. From the hydrodynamic relation $\xi \propto \eta R$, it turns out that the ratio of both characteristic times τ_f/τ_ν is just the particle-fluid density ratio $\alpha = \rho_P/\rho$.

Neutrally buoyant particles $\alpha = 1$ gently adapt to the local fluid deformation offering no inertial resistance. This limit is assumed in the vast majority of applications of the Immersed Boundary Method (see Ref. [Mori 2008, Fai 2013] for some exceptions). However, if the fluid is in a gravitational field (Archimedes principle) or under acceleration, any difference between the particle mass and the mass of fluid it displaces leads to inertial forces. Particle inertia constitutes a key component in many applications, ranging from turbulence [Eaton 2009] to microrheology [Franosch 2011]. Interestingly, the problem of resolving the particle inertia is also a problem of spatial resolution. To see this, note that $m/\xi \propto \rho_P R^2$, so one can enhance the particle inertia by either increasing its density ρ_P or its size R . Many computational studies on inertial effects in turbulence or unsteady flow consider very massive but *small* particles which scarcely perturb the hydrodynamic fields (thus allowing for one-way coupling). Albeit, inertial effects arising from large particle *densities* are not equivalent to those induced by *finite particle sizes* [Tanaka 2010]. Understanding how particle volume and stick condition modifies the flow remains an open question [Eaton 2009, Tanaka 2010].

Slow time response is another limitation of frictional coupling. In such scheme, the particle inertia only manifests in response to (time) variations in the flow drag, so any other hydrodynamic force acting faster than the friction rate ξ/m is not captured by the particle. A clear example are thermal forces from the fluid phase which, following Landau and Lifshitz formalism [Landau 1987], can be introduced in the stress tensor of finite volume [Fabritiis 2007] or Lattice Boltzmann [Dünweg 2009, Kaehler 2011] hydrodynamic solver. A dissipative (frictional) particle-fluid coupling requires adding an extra “particle noise” [Dünweg 2009] to thermalize particles, or immersed structures [Atzberger 2011]. While this issue does not precludes frictional coupling from being a valid approach for many soft matter applications [Dünweg 2009, Kekre 2010], a number of interesting phenomena (even at low Reynolds number) require rapidly varying deterministic flows with small characteristic length-scales $\lambda \sim R$ which cannot be captured via frictional coupling. A relevant example is ultrasound, whose technological applications are flourishing [Haake 2005a, Oberti 2007]. Ultrasound forces permits, for instance, to manipulate micron size particles [Bruus 2011]. Simulations of this phenomena are difficult and scarce [Dukhin 2002] because they require full resolution of each particle surface and very small time steps (for micron colloids in liquid, the sound time is $R/c_F \sim 10^{-9}\text{s}$).

This chapter presents a two-way coupling model which aims to be an intermediate coarse-grained level. In terms of spatial resolution, each particle is described by a single position vector but treated as a volume source, in the sense that the no-slip constraint is imposed to the fluid velocity *averaged* over the particle domain (hereby described by a kernel or weighting function). This permits to cap-

ture essential features of the near field but still preserve computational efficiency. Since in the present model the particle has not a well define surface it behaves in some situations like a soft blob rather than a rigid sphere. We will refer to this approximation as the *Blob model*. The form of the fluid-particle force is not assumed *a priori*, but calculated from the no-slip constraint. This constraint ensures *instantaneous* fluid-particle momentum transfer and permits to resolve the inertial response to arbitrarily fast changing forces, beyond the friction rate ξ/m . Accordingly, the scheme will be referred to as *Inertial Coupling* (IC). The approach bears some similarities with “Direct Forcing” [Uhlmann 2005] for immersed surfaces. However, here we focus on the point-wise particle description and show that the precise meaning of the particle effective mass and volume follows from the consistency between Eulerian and Lagrangian momentum balance. To guarantee such a consistency, the kernels used in the Immersed Boundary method (IBM) [Roma 1999] are shown to be a practical tool. Moreover our scheme is quite versatile to work in a broad range of Schmidt, Mach or Reynolds numbers.

In Section 3.1 the equations of motion for a particle immersed in a fluid are introduced. In Section 3.2 the Blob modes is presented and used to derive a simplify set of equations of motion, that we refer as the *Inertial Coupling Method* (ICM). The properties of the ICM are discussed in Section 3.3. The spatial and temporal discretization are presented in sections 3.4 and 3.5. We close the Chapter with the numerical results to validate our schemes in Section 3.6.

3.1 Equations of motion

In this chapter we consider the problem of a rigid sphere of radius R and volume \mathcal{V} moving in a Newtonian fluid. To simplify the notation we will focus on the one particle case except when the generalization to many particles presents some problem. The fluid obeys the laws of conservation of mass and momentum introduced in Chapter 2

$$\partial_t \rho + \nabla \cdot \mathbf{g} = 0, \quad (3.1)$$

$$\partial_t \mathbf{g} + \nabla \cdot (\mathbf{g} \mathbf{v}) = -\nabla \pi + \nabla \cdot \boldsymbol{\sigma} - \mathbf{f}, \quad (3.2)$$

where \mathbf{f} represent the density force exerted by the particle and we have collected in $\boldsymbol{\sigma}$ the dissipative and stochastic components of the stress tensor. The particle position \mathbf{q} , velocity \mathbf{u} and angular velocity $\boldsymbol{\omega}$ are governed by the Newton’s and Euler’s equations [Goldstein 2000],

$$\frac{d\mathbf{q}}{dt} = \mathbf{u}, \quad (3.3)$$

$$m \frac{d\mathbf{u}}{dt} = \mathbf{F}_f + \mathbf{F}_{ext}, \quad (3.4)$$

$$I \frac{d\boldsymbol{\omega}}{dt} = \mathbf{N}_f + \mathbf{N}_{ext}, \quad (3.5)$$

where m and I are the mass and moment of inertia of the particle. Since we are considering spherical particles it is not necessary to include an equation for the particle orientation, although such an equation can be supplied to simulate active matter, patchy colloids, nematics... [Bianchi 2006]. In the particle’s equations (3.3)-(3.5) the force and torque coming from the fluid are denoted by \mathbf{F}_f and \mathbf{N}_f while \mathbf{F}_{ext} and \mathbf{N}_{ext} represent other forces and torques acting on the particle.

The fluid and particle’s equations of motion are connected by the boundary conditions at the particle surface, which arise from the molecular details at the fluid-solid interface. In some cases the fluid slips over the solid surface [Bocquet 2007, Fellerhof 2012], however we restrict our attention to the no-slip

or stick boundary condition, which can be written as [Mazur 1974a, Bedaux 1974a]

$$\mathbf{v}(\mathbf{r}, t) = \mathbf{u}(t) + \boldsymbol{\omega}(t) \times (\mathbf{r} - \mathbf{q}(t)) \quad \|\mathbf{r} - \mathbf{q}(t)\| \leq R, \quad (3.6)$$

$$\rho(\mathbf{r}, t) = 0 \quad \|\mathbf{r} - \mathbf{q}(t)\| < R, \quad (3.7)$$

where the fluid fields have been extended to the particle domain. These boundary conditions determine the fluid-particle force appearing in the Eqs. (3.1)-(3.2) and (3.3)-(3.5). Note that these boundary conditions are usually expressed at the surface of the sphere, however Eqs. (3.6)-(3.7) are equivalent and better suited for numerical implementation.

3.2 The blob model

In the boundary condition Eqs. (3.6)-(3.7) the fluid fields have been extended inside the particle domain. To enforce those conditions we need a mechanism to transfer information between the Eulerian description of the fluid and the Lagrangian description of the particles. To this end we use a soft kernel function $\delta_h(\mathbf{q} - \mathbf{r})$ with finite support that integrates to unity. In the blob model the kernel links the fluid and particle equations of motion, but also it is used to represent all the relevant physical properties of the particle, like its volume, mass or compressibility. The link between the Eulerian and Lagrangian frames is specially delicate in the discrete setting because the fluid variables are defined at a discrete set of points (on the grid) while the particles move on the continuum space, therefore careful construction of the kernel is necessary to overcome the discretization problems.

Before deriving the equations of motion we explain some properties that a kernel should satisfy to correctly model a hard particle. In the continuum setting, all the properties introduced in this section hold for the Heaviside function ($\Theta(\mathbf{q} - \mathbf{r}) = \mathcal{V}^{-1}$ if $\|\mathbf{q} - \mathbf{r}\| < (3\mathcal{V}/(4\pi))^{1/3}$ and zero otherwise). In fact, to simulate spherical particles a Heaviside function seems a natural choice for the kernel. However, it presents some problems in the discrete setting, for example, it is not true that it integrates to unity when the integrals are replaced by sums over the discrete grid. Nonetheless, approximations to a Heaviside function have been used in the literature, and they can give good results if the fluid is resolved to scales a few times smaller than the particle radius [Nakayama 2005, Melchionna 2011]. We will present our kernel, a bell-shaped function, in Section 3.4, for now it is enough to know that it satisfies the properties introduced here.

We use the kernel to build operators that transfer information between the Eulerian and Lagrangian frameworks. The averaging operator \mathbf{J} transfer information from the Eulerian representation of the fluid to the Lagrangian representation of the particles while the spreading operator \mathbf{S} transfer information from the particles to the fluid. In the continuum setting these two operators are defined as

$$\mathbf{J}\mathbf{v}(\mathbf{r}, t) = \int \delta_h(\mathbf{q} - \mathbf{r})\mathbf{v}(\mathbf{r}, t) d^3r, \quad (3.8)$$

$$\mathbf{S}\mathbf{F} = \delta_h(\mathbf{q} - \mathbf{r})\mathbf{F}. \quad (3.9)$$

The first equation represents the fluid velocity averaged at the particle position \mathbf{q} while in the second a force \mathbf{F} in the Lagrangian frame is spread to the fluid as the density force \mathbf{SF} . Note that while \mathbf{J} is a dimensionless operator \mathbf{S} has units of inverse of volume. The averaging and spreading operators are adjoint $\mathbf{J}^* = \mathbf{S}$ in the sense that the dot product in the particle and fluid domains are related by

$$(\mathbf{J}\mathbf{v}) \cdot \mathbf{u} = \int \delta_h(\mathbf{q} - \mathbf{r})(\mathbf{v} \cdot \mathbf{u}) d^3r = \int \mathbf{v} \cdot (\mathbf{S}\mathbf{u}) d^3r. \quad (3.10)$$

We saw in Chapter 2 that the adjoint property of the advective operator was crucial to ensure the fluctuation dissipation balance. In this chapter we prove that the adjoint property between \mathbf{J} and \mathbf{S} is

(once again) fundamental to preserve the energy conservation in the inviscid limit and the fluctuation dissipation balance [Atzberger 2011].

Our kernel does not describe a dimensionless object (a Dirac delta function) but rather a finite size object with a given volume. The construction of $\delta_h(\mathbf{q} - \mathbf{r})$ ensures that the particle volume, independent of the particle position \mathbf{q} , is

$$\mathcal{V} = (\mathbf{J}\mathbf{S})^{-1} = \left(\int \delta_h^2(\mathbf{q} - \mathbf{r}) d^3 r \right)^{-1}. \quad (3.11)$$

Another property that will be important later it is the material derivative of a field following the particle. For example, for the velocity field $\mathbf{v}(\mathbf{r}, t)$

$$\frac{d\mathbf{J}\mathbf{v}}{dt} = \mathbf{J}\partial_t \mathbf{v} + (\mathbf{u} \cdot \nabla_{\mathbf{q}} \mathbf{J}) \mathbf{v}, \quad (3.12)$$

where \mathbf{u} is the particle velocity. Using the definition of the averaging operator [Eq. (3.8)] and integration by parts one can derive the equivalent expression

$$\frac{d\mathbf{J}\mathbf{v}}{dt} = \mathbf{J} (\partial_t \mathbf{v} + \nabla \cdot (\mathbf{u}\mathbf{v})). \quad (3.13)$$

3.2.1 Derivation of the Inertial Coupling Method

To derive the equation of motion we start by simplifying the boundary conditions. In the equations (3.6) and (3.7) we imposed a condition on the density and the velocity fields, it is clear however, that if both conditions are satisfied at the initial state the constraint on the velocity [Eq. (3.6)] is enough to ensure the impermeability condition (3.7), since the flux of mass through the surface of the sphere is proportional to $(\mathbf{v}(R) - \mathbf{u}) \cdot \mathbf{n} = 0$. Since the dynamics of the system is controlled by the boundary condition on the velocity, in the following we will not impose any condition on the density. This choice greatly simplifies the computational complexity of our schemes. As no constraint is imposed on the density (neither by the initial conditions) the fluid fills the whole domain, including the volume nominally occupied by the particles. As crude as it may look this approximation, we note that in the incompressible setting it only redefines the particle mass m

$$m = m_e + \mathcal{V}\mathbf{J}\rho = m_e + \mathcal{V} \int \delta_h(\mathbf{q} - \mathbf{r})\rho d^3 r, \quad (3.14)$$

where $m_f = \mathcal{V}\mathbf{J}\rho$ is the fluid mass carried by the particle and m_e is the excess of mass over the enclosed fluid (i.e. $m_e = 0$ for a neutrally buoyant particle and $m_e < 0$ for particles lighter than the fluid).

To impose the rigid motion of the fluid in the particle domain [Eq. (3.6)], it is necessary to describe the fluid velocity field with a high spatial resolution, something that in the discrete setting we want to avoid for computationally reasons. An equivalent and more convenient approach is to constraint the different *moments* of the velocity field to their appropriate values. The first three velocity moments are

$$\begin{aligned} \int \Theta_h(\mathbf{q} - \mathbf{r}) v_\alpha d^3 r &= \dots, \\ \int \Theta_h(\mathbf{q} - \mathbf{r}) \partial_\alpha v_\beta d^3 r &= \dots, \\ \int \Theta_h(\mathbf{q} - \mathbf{r}) \partial_\alpha \partial_\beta v_\gamma d^3 r &= \dots, \end{aligned}$$

where all the moments are consistently weighted with the Heaviside function $\Theta(\mathbf{q} - \mathbf{r})$, centered at the particle site. The particle resolution can be increased by including constraints on higher velocity

moments, however, good results can be obtained by constraining only the first moments. Besides, the first two (and most important) moments have a clear physical interpretation,

$$\int \Theta_h(\mathbf{q} - \mathbf{r}) \mathbf{v} d^3 r = \mathbf{u}(t), \quad (3.15)$$

$$\frac{1}{2} \int \Theta_h(\mathbf{q} - \mathbf{r}) \nabla \times \mathbf{v} d^3 r = \boldsymbol{\omega}, \quad (3.16)$$

$$\frac{1}{2} \int \Theta_h(\mathbf{q} - \mathbf{r}) (\partial_\alpha v_\beta + \partial_\beta v_\alpha) d^3 r = 0. \quad (3.17)$$

The first constraint [Eq. (3.15)] implies that fluid and particle have the same translational velocity, it is not hard to show that this constraint derives from the no-slip condition (3.6). The nature of the second moment is better understood by splitting the constraint into the antisymmetric the symmetric parts. The antisymmetric part [Eq. (3.16)] is the equivalent no-slip constraint for the angular velocity, meaning that particle and fluid share a rigid rotation. The symmetric part [Eq. (3.17)] or stresslet condition is related to the deformation of the particle (or the enclosed fluid), which should be zero for a rigid body. Note, however, that for a elastic body the strain is related with its internal stress tensor. Since the stresslet term controls the local deformation of the fluid it affects the energy dissipation rate [Landau 1987]. Through the rest of the thesis we will consider only the translational constraint and we will refer to it as no-slip condition. The rotational and stresslet condition are left for future work, as a consequence of not fulfilling Eq. (3.17) our scheme does not recover the dependence of the effective fluid viscosity η_{eff} with the particle concentration ϕ (unlike the force-coupling method [Lomholt 2003]), which arise from the stress created by each individual particle (linear in ϕ)

$$\eta_{\text{eff}} = (1 + \frac{5}{2}\phi)\eta. \quad (3.18)$$

Once we have introduced the averaging and spreading operators and simplified the boundary conditions to the no-slip given by Equation (3.15), we now derive the equations of motion. The force exerted by the fluid on the particle is the surface traction, i.e., the momentum flux through the particle surface $S(t)$ [Landau 1987]

$$\mathbf{F}_f = - \oint_{S(t)} ((\mathbf{v} - \mathbf{u})\mathbf{g} + \pi\mathbf{I} - \boldsymbol{\sigma}) \cdot \mathbf{n} d^2 r. \quad (3.19)$$

Using the Gauss theorem the surface integral can be written as a volume integral over the particle domain

$$\begin{aligned} \mathbf{F}_f &= - \int_V \nabla \cdot ((\mathbf{v} - \mathbf{u})\mathbf{g} + \pi\mathbf{I} - \boldsymbol{\sigma}) d^3 r \\ &= -V \int \Theta(\mathbf{q} - \mathbf{r}) \nabla \cdot ((\mathbf{v} - \mathbf{u})\mathbf{g} + \pi\mathbf{I} - \boldsymbol{\sigma}) d^3 r, \end{aligned} \quad (3.20)$$

where for the second equality we have used the Heaviside function $\Theta(\mathbf{q} - \mathbf{r})$ and integrated over the whole system domain. The essence of the blob model is to substitute the Heaviside kernel in Eqs. (3.15) and (3.20) by the soft kernel $\delta_h(\mathbf{q} - \mathbf{r})$. This leads to the following equation of motion for the particle

$$m \frac{d\mathbf{u}}{dt} = -V \int \delta_h(\mathbf{q} - \mathbf{r}) \nabla \cdot ((\mathbf{v} - \mathbf{u})\mathbf{g} + \pi\mathbf{I} - \boldsymbol{\sigma}) d^3 r + \mathbf{F}_{ext} + \boldsymbol{\varepsilon}_\delta. \quad (3.21)$$

For a rigid sphere the first term in the integral is zero due to the impenetrability condition, $(\mathbf{v} - \mathbf{u}) \cdot \mathbf{n} = 0$ at the particle surface. However, in the blob approximation this is not be generally true, therefore we

will maintain that advective term. The last term in Eq. (3.21), ε_δ , is an extra force due to the use of a soft kernel instead of a Heaviside function,

$$\varepsilon_\delta = \mathcal{V} \int (\delta_h(\mathbf{q} - \mathbf{r}) - \Theta(\mathbf{q} - \mathbf{r})) \nabla \cdot ((\mathbf{v} - \mathbf{u})\mathbf{g} + \pi\mathbf{I} - \boldsymbol{\sigma}) d^3r. \quad (3.22)$$

Doing a Taylor expansion of $\nabla \cdot ((\mathbf{v} - \mathbf{u})\mathbf{g} + \pi\mathbf{I} - \boldsymbol{\sigma})$ around the particle center and using the fact that both $\delta_h(\mathbf{q} - \mathbf{r})$ and $\Theta(\mathbf{q} - \mathbf{r})$ are even functions that integrates to unity it is easy to show that the new term ε_δ is proportional to the second derivatives of the advective and stress tensor around the particle. Since we are not solving the fluid at scales smaller than the particle radius this extra term is a high order correction. Neglecting ε_δ is consistent with our second order accurate description of the fluid and with the number of constraints that we impose to the fluid velocity field, notably the no slip constraint. Therefore in the rest of the equation we just eliminate the contribution from ε_δ .

Using the averaging and spreading operators notation the equation of motion for the particle is

$$m \frac{d\mathbf{u}}{dt} = -\mathcal{V} \mathbf{J} \nabla \cdot ((\mathbf{v} - \mathbf{u})\mathbf{g} + \pi\mathbf{I} - \boldsymbol{\sigma}) + \mathbf{F}_{ext}. \quad (3.23)$$

In principle it would be possible to compute all the terms in Eq. (3.23) to update the particle velocity. However, such an approach is not suited for numerical implementation. The reason is that since the boundary condition does not enter explicitly in Eq. (3.23), any mismatch in the no-slip condition will increase during the simulation to arbitrary values. For this reason we follow another route and start by considering the change in the fluid momentum dragged by the particle

$$\frac{d\mathbf{J}\mathbf{g}}{dt} = \mathbf{J} (\partial_t \mathbf{g} + \nabla \cdot (\mathbf{u}\mathbf{g})). \quad (3.24)$$

Using the equation of the fluid momentum (3.2) to substitute $\partial_t \mathbf{g}$ one gets

$$\frac{d\mathbf{J}\mathbf{g}}{dt} = -\mathbf{J} \nabla \cdot ((\mathbf{g}\mathbf{v}) + \pi\mathbf{I} - \boldsymbol{\sigma}) - \mathbf{J}\mathbf{f}, \quad (3.25)$$

and plugging this result into the particle equation of motion (3.23),

$$m \frac{d\mathbf{u}}{dt} = \mathcal{V} \frac{d\mathbf{J}\mathbf{g}}{dt} + \mathcal{V} \mathbf{J}\mathbf{f} + \mathbf{F}_{ext}. \quad (3.26)$$

To complete the derivation we will assume that the density fluctuations are small compared with the average density. This is a valid approximation for small Mach numbers and it allows us to neglect the fluctuations in the fluid mass dragged by the particle, therefore we approximate the change in the fluid momentum in the particle domain by

$$\mathcal{V} \frac{d\mathbf{J}\mathbf{g}}{dt} \approx \mathcal{V} (\mathbf{J}\rho) \frac{d\mathbf{u}}{dt} = m_f \frac{d\mathbf{u}}{dt}, \quad (3.27)$$

where m_f is the mass of fluid displaced by the particle. Note that in the incompressible setting this expression is exact. This final result allows us to write the particle equation of motion (3.26) as

$$m_e \frac{d\mathbf{u}}{dt} = \boldsymbol{\lambda} + \mathbf{F}_{ext}, \quad (3.28)$$

where the excess mass $m_e = m - m_f$ represents the excess inertia of the particle over the fluid and $\boldsymbol{\lambda}$ is the fluid-particle force

$$\boldsymbol{\lambda} = \mathcal{V} \mathbf{J}\mathbf{f}. \quad (3.29)$$

At this point one can write the force density acting on the fluid [Eq. (3.2)] as

$$-\mathbf{f} = -\mathcal{V}\mathbf{S}\boldsymbol{\lambda}. \quad (3.30)$$

Note that by the properties of the kernel [Eq. (3.11)] $\mathcal{V}\mathbf{J}\mathbf{S}\boldsymbol{\lambda} = \boldsymbol{\lambda}$ which guarantees momentum conservation. Our choice for the force density ($\mathbf{S}\boldsymbol{\lambda}$) is not the only one possible, but it is the most natural at our level of approximation, moreover this choice ensures the conservation of energy in the inviscid limit and the fluctuation dissipation balance as we will show later. So far we have not given any expression for the fluid-particle force $\boldsymbol{\lambda}$, the value of this force has to be obtained from the no-slip constraint $\mathbf{J}\mathbf{v} = \mathbf{u}$, therefore, $\boldsymbol{\lambda}$ is just a Lagrangian multiplier and its evaluation is one of the central objectives of the present method.

3.3 Equations of the ICM

Using the results derived in the previous section and making use of the averaging and spreading operators, the equations of motion for a particle immersed in a Newtonian fluid are

$$\partial_t \rho + \nabla \cdot \mathbf{g} = 0, \quad (3.31)$$

$$\partial_t \mathbf{g} + \nabla \cdot (\mathbf{g}\mathbf{v}) = -\nabla \pi + \nabla \cdot \boldsymbol{\sigma} - \mathbf{S}\boldsymbol{\lambda}, \quad (3.32)$$

$$m_e \dot{\mathbf{u}} = \mathbf{F}(\mathbf{q}) + \boldsymbol{\lambda}, \quad (3.33)$$

$$\text{s.t. } \mathbf{J}\mathbf{v} = \mathbf{u}, \quad (3.34)$$

where $\boldsymbol{\sigma}$ contains the viscous and fluctuating parts of the stress tensor. The above equations are also valid in the incompressible limit by replacing the continuity equation with the condition $\nabla \cdot \mathbf{v} = 0$ and then treating the pressure π as a Lagrangian multiplier to impose the divergence free constraint. In the compressible case the pressure takes the following form

$$\pi(\rho, \mathbf{q}) = p(\rho) + \frac{m_f}{m} \mathbf{S} k_B T. \quad (3.35)$$

The first term is the fluid contribution to the pressure, for simplicity in most cases we will consider a barotropic fluid, $p(\rho) = c_T^2 \rho$, with a constant isothermal speed of sound c_T . The second term is a thermal drift required to recover the fluctuation dissipation balance (FDB), we will discuss the origin of this term in detail in Section 3.3.2.

As discussed earlier these equations can be extended to include the rotation of the particle and the stresslet condition on the fluid. This can be achieved by including an equation for the particle angular velocity

$$I_e \dot{\boldsymbol{\omega}} = \mathbf{N}_{ext} + \boldsymbol{\Omega}, \quad (3.36)$$

and the forcing terms $\boldsymbol{\Omega}/2 \times \nabla \mathbf{S}$ and $\mathbf{E} \cdot \nabla \mathbf{S}$ in the fluid momentum equation. In the previous equations I_e is an *excess Inertia* due to the particle and \mathbf{E} and $\boldsymbol{\Omega}$ are the fluid-particle forcing terms that ensure the stresslet and rigid motion of the fluid [Yeo 2010, Keaveny 2013], in the ICM notation

$$\frac{1}{2} \mathbf{J}(\nabla \times \mathbf{v}) = \boldsymbol{\omega}, \quad (3.37)$$

$$\mathbf{J} \left(\frac{\partial v_i}{\partial x_j} + \frac{\partial v_j}{\partial x_i} \right) = 0. \quad (3.38)$$

During the rest of the chapter we will not consider these terms and we restrict to the equations (3.31)-(3.34).

The no-slip condition stated in the equation (3.34) eliminates the particle velocity as a degree of freedom, leaving only the particle positions and the fluid degrees of freedom. An important consequence of this fact it is the relation between the particle acceleration and the advective derivative

$$\dot{\mathbf{u}} = \frac{d}{dt} (\mathbf{J}(\mathbf{q})\mathbf{v}) = \mathbf{J}(\partial_t \mathbf{v}) + (\mathbf{u} \cdot \nabla_{\mathbf{q}} \mathbf{J}) \mathbf{v}. \quad (3.39)$$

With our definition of averaging operator

$$(\mathbf{u} \cdot \nabla_{\mathbf{q}} \mathbf{J}) \mathbf{v} = \int (\mathbf{u} \cdot \nabla_{\mathbf{q}} \delta_h(\mathbf{q} - \mathbf{r})) \mathbf{v}(\mathbf{r}, t) d^3 r, \quad (3.40)$$

in the limit of a point particle $h \rightarrow 0$ the kernel becomes a Dirac delta function and the particle acceleration is given by the advective derivative

$$\frac{d}{dt} (\mathbf{J}\mathbf{v}) \approx \frac{d}{dt} \mathbf{v}(\mathbf{q}(t), t) = \partial_t \mathbf{v} + (\mathbf{v} \cdot \nabla) \mathbf{v}, \quad (3.41)$$

which is physically consistent with a very small particle that acts as a Lagrangian marker. To recover this limit suggests that the no-slip constraint is a good model for small particles, however, for a finite particle the relative fluid-particle acceleration is in general non-zero

$$\mathbf{a}_{\mathbf{J}} = \frac{d}{dt} (\mathbf{J}\mathbf{v}) - \mathbf{J}(\partial_t \mathbf{v}) \neq 0. \quad (3.42)$$

The finite size of the blob is also important when a particle is advected by a flow with a non-zero curvature. Expanding the fluid velocity $\mathbf{v}(\mathbf{r}, t)$ around the particle center \mathbf{q} , the particle velocity can be approximated by

$$\mathbf{u} \approx \int \delta_h(\mathbf{q} - \mathbf{r}) (\mathbf{v}(\mathbf{q}, t) + \nabla \mathbf{v}(\mathbf{q}, t) \cdot (\mathbf{r} - \mathbf{q}) + \dots) d^3 r \quad (3.43)$$

$$\frac{1}{2} \nabla \nabla \mathbf{v}(\mathbf{q}, t) : [(\mathbf{r} - \mathbf{q})(\mathbf{r} - \mathbf{q})^T] d^3 r \quad (3.44)$$

$$= \mathbf{v}(\mathbf{q}, t) + \frac{1}{2} \nabla \nabla \mathbf{v}(\mathbf{q}, t) : \int \delta_h(\mathbf{r}) \mathbf{r} \mathbf{r}^T d^3 r, \quad (3.45)$$

and for kernels with spherical symmetry [and also for our kernel choice Eq. (3.81)]

$$\mathbf{u} \approx \mathbf{v}(\mathbf{q}, t) + \left(\frac{1}{2} \int r_x^2 \delta_h(r) dr \right) \nabla^2 \mathbf{v}(\mathbf{q}, t) = \mathbf{v}(\mathbf{q}, t) + \frac{a_F^2}{6} \nabla^2 \mathbf{v}(\mathbf{q}, t), \quad (3.46)$$

where the last term is the well known Faxén drag force [Maxey 1983]. Therefore the contribution to the particle's advection by the curvature of the flow is controlled by the second moments of the kernel function. For a Dirac delta function such a term is zero, but for a rigid sphere $a_F = R$. Therefore, kernels with non-zero second moments are better suited to recover the dynamics of a finite size particle.

Before we discuss the discretization of the above equations we study some of their properties in the continuum setting.

3.3.1 Equivalent forms of the equations of motion

We now rewrite the equation of motion for the fluid and the particle in several equivalent forms which allow to better understand the model. Eliminating $\lambda = m_e \dot{\mathbf{u}} - \mathbf{F}$ from the particle velocity equation and using (3.42) to eliminate the particle acceleration, equation (3.32) becomes

$$(\rho + m_e \mathbf{S} \mathbf{J}) \partial_t \mathbf{v} = -(\rho(\mathbf{v} \cdot \nabla) + m_e \mathbf{S}(\mathbf{u} \cdot \nabla_{\mathbf{q}} \mathbf{J})) \mathbf{v} - \nabla \pi + \nabla \cdot \boldsymbol{\sigma} + \mathbf{S} \mathbf{F}. \quad (3.47)$$

This is a generalized Navier-Stokes equation in which the particle contributes to both the fluid inertia with the term $m_e \mathbf{S} \mathbf{J}$ and to the kinetic stress term with $m_e \mathbf{S} (\mathbf{u} \cdot \nabla_{\mathbf{q}} \mathbf{J}) \mathbf{v}$. For neutrally buoyant particles ($m_e = 0$) the system reduces to the standard Navier-Stokes equation with a forcing term \mathbf{SF} [Peskin 2002, Atzberger 2007].

Following similar steps one can rewrite the particle equation of motion as

$$m \dot{\mathbf{u}} = \mathcal{V} \mathbf{J} (-\nabla \pi + \nabla \cdot \boldsymbol{\sigma}) + m_f \mathbf{a}_J + \mathbf{F}, \quad (3.48)$$

where the particle mass is given by $m = m_e + \mathcal{V} \mathbf{J} \rho = m_e + m_f$, with m_f the fluid mass dragged by the particle. Note that this equation is just another form of write Eq. (3.23). The first term in the right hand side represents the integral of the divergence of the stress tensor inside the particle. The second term, $m_f \mathbf{a}_J$, is an inertial force proportional to the relative fluid-particle acceleration and represents the transport of momentum through the particle surface due to the advective terms $[(\mathbf{v} - \mathbf{u}) \mathbf{g}]$, just as in the equation (3.23). Previous works has neglected the \mathbf{a}_J term [Mori 2008] however we will show that it should be conserved to ensure the fluctuation dissipation balance (see below). In any case for small particle Reynolds number we expect this term to be small $\mathbf{a}_J \approx 0$.

3.3.1.1 Momentum formulation

Since hydrodynamics is all about the transport of momentum it is important to ensure that the momentum is conserved by our scheme. In the Eulerian frame of reference the total momentum can be defined as the fluid momentum plus the particle contribution

$$\mathbf{p}(\mathbf{r}, t) = \rho \mathbf{v} + m_e \mathbf{S} \mathbf{u} = (\rho + m_e \mathbf{S} \mathbf{J}) \mathbf{v}. \quad (3.49)$$

The evolution equation for \mathbf{p} is derived by combining the Eqs. (3.32) and (3.33)

$$\begin{aligned} \partial_t \mathbf{p} &= \rho \partial_t \mathbf{v} + m_e \mathbf{S} \dot{\mathbf{u}} + m_e (\mathbf{u} \cdot \nabla_{\mathbf{q}} \mathbf{S}) \mathbf{u} \\ &= -\nabla \pi - \nabla \cdot \boldsymbol{\sigma} - \nabla \cdot (\rho \mathbf{v} \mathbf{v}^T + m_e \mathbf{S} (\mathbf{u} \mathbf{u}^T)) + \mathbf{SF}. \end{aligned} \quad (3.50)$$

In the absence of external forces, the right hand side becomes the divergence of a tensor, meaning that momentum is locally conserved. The term

$$\boldsymbol{\sigma}_{\text{kin}} = (\rho \mathbf{v} \mathbf{v}^T + m_e \mathbf{S} (\mathbf{u} \mathbf{u}^T)), \quad (3.51)$$

is the kinetic stress tensor which contains a contribution from the particle.

3.3.2 Energy conservation

In absence of dissipation the system can be described by the Hamiltonian of an ideal fluid [Morrison 1998] (see Sec. 2.1.4.2) plus the kinetic and potential energy of the particle

$$\mathcal{H} = \int \left(\frac{1}{2} \rho \mathbf{v}^2 + \rho \varepsilon(\rho) \right) d^3 r + \frac{1}{2} m_e \mathbf{u}^2 + U(\mathbf{q}), \quad (3.52)$$

where $U(\mathbf{q})$ is the potential associated with the conservative force $\mathbf{F}(\mathbf{q}) = -\nabla U(\mathbf{q})$ and the fluid contribution was introduced in Sec. 2.1.4.2. We want to show that in the absence of viscous dissipation the postulated equations (3.31)-(3.34) conserve the Hamiltonian (3.52). To that end we calculate the rate of energy change

$$\frac{d\mathcal{H}}{dt} = -\mathbf{F} \cdot \mathbf{u} + m_e \mathbf{u} \cdot \dot{\mathbf{u}} + \int \left(\rho \mathbf{v} \cdot (\partial_t \mathbf{v}) + \left(\frac{1}{2} \mathbf{v}^2 + \varepsilon + \rho^{-1} \pi \right) (\partial_t \rho) \right) d^3 r. \quad (3.53)$$

Making use of the equations of motion for an ideal fluid (i.e. $\nabla \cdot \boldsymbol{\sigma} = 0$)

$$\begin{aligned}\frac{d\mathcal{H}}{dt} &= -\mathbf{F} \cdot \mathbf{u} + \mathbf{u} \cdot (\mathbf{F} + \boldsymbol{\lambda}) - \int \mathbf{v} \cdot (\mathbf{S}\boldsymbol{\lambda}) d^3r \\ &\quad - \int (\mathbf{v} \cdot \nabla \pi + (\varepsilon + \rho^{-1}\pi) \nabla \cdot (\rho\mathbf{v})) d^3r \\ &\quad - \int \left(\rho\mathbf{v} \cdot (\mathbf{v} \cdot \nabla \mathbf{v}) + \frac{1}{2}\mathbf{v}^2 \nabla \cdot (\rho\mathbf{v}) \right) d^3r \\ &= (\mathbf{u} - \mathbf{J}\mathbf{v}) \cdot \boldsymbol{\lambda} \\ &\quad - \int (\mathbf{v} \cdot \nabla \pi - \rho\mathbf{v} \cdot \nabla(\varepsilon + \rho^{-1}\pi)) d^3r \\ &\quad - \int \rho\mathbf{v} \cdot \left((\mathbf{v} \cdot \nabla \mathbf{v}) - \frac{1}{2}\nabla \mathbf{v}^2 \right) d^3r.\end{aligned}\tag{3.54}$$

The first term vanishes due to the no-slip condition, the second vanishes because of the thermodynamic relation $\partial(\rho\varepsilon)/\partial\rho = (\varepsilon + \rho^{-1}\pi)$ (see Sec. 2.1.4.2) and the third due to the properties of the curl operator (recall $\mathbf{v} \cdot \nabla \mathbf{v} = \nabla(v^2/2) + (\nabla \times \mathbf{v}) \times \mathbf{v}$). Therefore, in the absence of viscous terms the scheme conserves the mechanical energy while the particle-fluid coupling remains intact. In other words, the inertial coupling is non-dissipative and conserves the energy, this is in contrast with previous coupling ansatz based on frictional (i.e. dissipative) velocity relaxation [Giupponi 2007, Dünweg 2009].

In a viscous fluid the total energy is not conserved but it can be shown that no energy is created (or destroyed) in the fluid-particle interaction [Peskin 2002]. To see this, consider the power exerted by the particle on the fluid,

$$-\int \mathbf{v} \cdot \mathbf{S}\boldsymbol{\lambda} d^3r = -\boldsymbol{\lambda} \cdot \mathbf{J}\mathbf{v} = -\boldsymbol{\lambda} \cdot \mathbf{u},\tag{3.55}$$

where we have made use of the skew-adjoint property ($\mathbf{J} = \mathbf{S}^*$). Eliminating lambda

$$-\int \mathbf{v} \cdot \mathbf{S}\boldsymbol{\lambda} d^3r = -\frac{1}{2}m_e \frac{d\mathbf{u}^2}{dt} + \mathbf{F} \cdot \mathbf{u}.\tag{3.56}$$

Therefore, the work exerted by the particle on the fluid is equal to its loss of kinetic energy plus the work made by the external force \mathbf{F} . That means that even if the total energy is not conserved in the viscous case, the particle-fluid interaction remains non-dissipative.

3.3.3 Fluctuation dissipation balance

The stochastic terms of the ICM [collected in $\boldsymbol{\sigma}$ in Eqs. (3.31)-(3.34)] are the same that for the fluctuating Navier-Stokes equations without immersed particles. It is not necessary to include additional stochastic terms because the fluid-particle interaction is non-dissipative, as we just proved in Section 3.3.2. In this section we use the Augmented Langevin formalism to show that the ICM obeys the FDB. As primary variables we will use the fluid density ρ , its velocity \mathbf{v} and the particle position \mathbf{q} . Note that the particle velocity is not an independent degree of freedom due to the no-slip condition $\mathbf{u} = \mathbf{J}\mathbf{v}$. To prove that the equations of motion obeys the FDB it is convenient to use the ICM in the form of Eq. (3.47) together with the conservation of mass $\partial_t \rho = -\nabla \cdot (\rho\mathbf{v})$ and the particle equation $d\mathbf{q}/dt = \mathbf{J}\mathbf{v}$. Recall from Section 2.1.4 that the Augmented Langevin formalism requires to define a Hamiltonian \mathcal{H} and its derivatives, a mobility matrix \mathcal{N} and its divergence and a stochastic term \mathcal{K} that obeys the FDB: $\langle \mathcal{K}\mathcal{K}^* \rangle = k_B T(\mathcal{N} + \mathcal{N}^*)\delta(\mathbf{r} - \mathbf{r}')\delta(t - t')$.

The coarse-grained Hamiltonian is given in the Eq. (3.52), however, to calculate its derivatives it is convenient to express it in the form

$$\mathcal{H} = \int \left(\frac{1}{2} \mathbf{v}^T (\rho \mathbf{I} + m_e \mathbf{S} \mathbf{J}) \mathbf{v} + \rho \varepsilon(\rho) \right) d^3 r + U(\mathbf{q}). \quad (3.57)$$

The Hamiltonian derivatives are

$$\frac{\partial \mathcal{H}}{\partial \rho} = \frac{1}{2} \mathbf{v}^2 + \varepsilon(\rho) + \rho^{-1} \pi, \quad (3.58)$$

$$\frac{\partial \mathcal{H}}{\partial \mathbf{v}} = (\rho \mathbf{I} + m_e \mathbf{S} \mathbf{J}) \mathbf{v}, \quad (3.59)$$

$$\frac{\partial \mathcal{H}}{\partial \mathbf{q}} = -\mathbf{F}(\mathbf{q}) + m_e \mathbf{J} (\mathbf{v} \cdot \nabla_{\mathbf{q}} \mathbf{J}) \mathbf{v}. \quad (3.60)$$

To recover the Equation (3.47) (as it can be shown by matrix multiplication) the mobility matrix and the stochastic term should be (recall the Augmented Langevin formalism, Sec. 2.1.4)

$$\mathcal{N} = \begin{bmatrix} 0 & \nabla \cdot \rho (\rho \mathbf{I} + m_e \mathbf{S} \mathbf{J})^{-1} & 0 \\ (\rho \mathbf{I} + m_e \mathbf{S} \mathbf{J})^{-1} \rho \nabla & \mathcal{N}_{vv} & (\rho \mathbf{I} + m_e \mathbf{S} \mathbf{J})^{-1} \mathbf{S} \\ 0 & -\mathbf{J} (\rho \mathbf{I} + m_e \mathbf{S} \mathbf{J})^{-1} & \mathcal{N}_{BD} \end{bmatrix}, \quad (3.61)$$

$$\mathcal{K} = \begin{bmatrix} 0 \\ (\rho \mathbf{I} + m_e \mathbf{S} \mathbf{J})^{-1} \rho \mathcal{K}_v \\ \mathcal{K}_{BD} \end{bmatrix} = \begin{bmatrix} 0 \\ (\rho \mathbf{I} + m_e \mathbf{S} \mathbf{J})^{-1} \nabla \cdot \Sigma \\ \mathcal{K}_{BD} \end{bmatrix}, \quad (3.62)$$

where $\mathcal{N}_{BD} = \mathcal{K}_{BD} = \mathbf{0}$ and

$$\begin{aligned} \mathcal{N}_{vv} = & -(\rho \mathbf{I} + m_e \mathbf{S} \mathbf{J})^{-1} \rho \boldsymbol{\omega} (\rho \mathbf{I} + m_e \mathbf{S} \mathbf{J})^{-1} \\ & + (\rho \mathbf{I} + m_e \mathbf{S} \mathbf{J})^{-1} \rho \mathcal{M}_{vv} (\rho \mathbf{I} + m_e \mathbf{S} \mathbf{J})^{-1}. \end{aligned} \quad (3.63)$$

In the above equations the vorticity $\boldsymbol{\omega}$, the dissipative matrix \mathcal{M}_{vv} and the stochastic tensor Σ are the same that the ones defined in Chapter 2 Section 2.1.4.2 for a compressible fluid without immersed particles.

The last term in the Augmented Langevin formalism is the drift coming from the mobility divergence

$$k_B T \nabla_{\mathbf{U}} \cdot \mathcal{N}^* = \begin{bmatrix} 0 \\ \frac{m_f}{m\rho} \nabla_{\mathbf{q}} \mathbf{S} k_B T \\ \mathbf{0} \end{bmatrix} = \begin{bmatrix} 0 \\ -\frac{m_f}{m\rho} \nabla \mathbf{S} k_B T \\ \mathbf{0} \end{bmatrix}. \quad (3.64)$$

This term should be understood as an extra contribution to the local fluid pressure due to the thermal agitation of the particle. The presence of this term is required in the fluid momentum equation for consistency with the Augmented Langevin formalism, which ensures that the fluid-particle system relaxes to the Gibbs-Boltzmann distribution of the generalized Hamiltonian $P = Z^{-1} \exp(-\mathcal{H}/k_B T)$. More precisely, it is the thermal drift due to the dependence of the dissipative matrix with the particle coordinate, as first derived by Atzberger in the context of neutrally buoyant particles [Atzberger 2011]. Note however that the total contribution to the pressure due to one colloid should be $k_B T / \mathcal{V}$, independently of its mass, since for an ideal fluid $\pi = k_B T N / \mathcal{V}$, where N is the number of particles in the volume \mathcal{V} . The remaining part appears in the total momentum flux like an extra Kirkwood kinetic pressure coming from the particle velocity. The particle terms inside the divergence operator of Eq. (3.50) are $\mathbf{S} [m_e \mathbf{u} \mathbf{u}^T + (m_f/m) k_B T]$. Colloids have very large Schmidt number ($\sim 10^6$) so the particle position $\mathbf{q}(t)$ (and thus \mathbf{S}) can be considered to be fixed in front of the fast velocity fluctuations.

Now, equipartition ensures $\langle \mathbf{u}\mathbf{u}^T \rangle = k_B T \mathbf{I}/m$ so the particle contribution to the kinetic pressure is just $S k_B T$ [Usabiaga 2013a]. Both terms (thermal drift and Kirkwood pressure) have been taken into account in the present formalism. However, their effect is negligibly small: the contribution to the total kinetic pressure of one colloidal particle is $m_f c_T^2/k_B T \sim N$ times smaller than the pressure of the N surrounding solvent molecules.

3.3.3.1 Bare friction and partial slip

It is interesting to consider nonvanishing values of the \mathcal{N}_{BD} and \mathcal{K}_{BD} terms. Note that the inclusion of these terms do not modify the others mobility matrix elements. A possible choice for them is

$$\mathcal{N}_{\text{BD}} = \mu \mathbf{I}, \quad \mathcal{K}_{\text{BD}} = \sqrt{2k_B T \mu} \mathcal{W}_q, \quad (3.65)$$

where $\mathcal{W}_q(t)$ is a white-noise random Gaussian vector. These terms do not modify the fluid equations of motion, but they lead to the particle equation

$$\frac{d\mathbf{q}}{dt} = \mathbf{J} [\mathbf{I} - \mu m_e (\mathbf{v} \cdot \nabla_{\mathbf{q}} \mathbf{J})] \mathbf{v} + \mu \mathbf{F}(\mathbf{q}) + \sqrt{2k_B T \mu} \mathcal{W}_q. \quad (3.66)$$

The new coefficient μ plays the role of an extra mobility that adds a partial slip to the fluid-particle coupling. For a neutrally buoyant particle the balance between the external force \mathbf{F} and the slippage is $\mathbf{F} = \mu^{-1}(\mathbf{u} - \mathbf{J}\mathbf{v})$ as commonly assumed in the Stokes coupling [Dünweg 2009]. Therefore, for these equations we expect that the particle will show a diffusion coefficient $\chi = \chi_H + \mu k_B T$, where χ_H is the diffusion coefficient for $\mu = 0$. However, we have not tested this hypothesis.

3.3.4 Incompressible limit

As discussed in Chapter 2 (Sec. 2.1.5) the incompressible limit can be understood as a projection of the fluid momentum equation onto the divergence free space. This methodology is applied in exactly the same form in the present case. Applying $\mathcal{P} = [\mathbf{I} - \nabla(\nabla^{-2}\nabla \cdot)]$ on Eqs. (3.32) and (3.33) leads to

$$\rho \partial_t \mathbf{v} = \mathcal{P} (-\rho \mathbf{v} \cdot \nabla \mathbf{v} - \nabla \cdot \boldsymbol{\sigma} - m_e \mathbf{S} \dot{\mathbf{u}} + \mathbf{S} \mathbf{F}). \quad (3.67)$$

Then, using Eq. (3.39) to eliminate the particle acceleration one gets

$$\begin{aligned} \rho_{\text{eff}} \partial_t \mathbf{v} &= \mathcal{P} (-(\rho(\mathbf{v} \cdot \nabla) + m_e \mathbf{S} \mathbf{J}(\mathbf{v} \cdot \nabla_{\mathbf{q}} \mathbf{J})) \mathbf{v} - \nabla \cdot \boldsymbol{\sigma}) + \mathcal{P} \mathbf{S} \mathbf{F} \\ &= \mathcal{P} \mathbf{f} + \mathcal{P} \mathbf{S} \mathbf{F}, \end{aligned} \quad (3.68)$$

where the effective density is defined as

$$\rho_{\text{eff}} \equiv \rho \mathbf{I} + m_e \mathcal{P} \mathbf{S} \mathbf{J} \mathcal{P}. \quad (3.69)$$

It is noted that the effective density is an operator (or a field), rather than a constant scalar as ρ . Formally, Eq. (3.68) is solved by

$$\partial_t \mathbf{v} = \rho_{\text{eff}}^{-1} (\mathcal{P} \mathbf{f} + \mathcal{P} \mathbf{S} \mathbf{F}), \quad (3.70)$$

but this route requires to invert the effective density operator. Instead, we search for an analytical expression for ρ_{eff}^{-1} by performing a Taylor expansion,

$$\rho_{\text{eff}}^{-1} = \rho^{-1} (\mathbf{I} - m_e \rho^{-1} \mathcal{P} \mathbf{S} \mathbf{J} \mathcal{P} + (m_e \rho^{-1} \mathcal{P} \mathbf{S} \mathbf{J} \mathcal{P})^2 + \dots). \quad (3.71)$$

Since the projector operator is idempotent $\mathcal{P}^2 = \mathcal{P}$, we have $(\mathcal{P}SJP)^n = \mathcal{P}S(JPS)^{n-1}JP$, where the operator JPS appears for the first time. We will show shortly that if JPS is a constant matrix it is possible to write a closed expression for the inverse of the effective density. In general the operator JPS depends on the particle position through the averaging and spreading operators, however, with periodic boundary conditions (PBC) translational invariance ensures that $JPS = \tilde{\mathcal{V}}^{-1}$ is just a constant matrix independent of \mathbf{q} . Also, since all the directions are equivalent the matrix JPS can only have two different components: a diagonal and an off-diagonal term. To calculate these two values we apply JPS to a vector $\omega = (1, 0, 0)$ and compute the result in Fourier space. Using $\tilde{\mathcal{P}}_k = \mathbf{I} - \mathbf{k}\mathbf{k}^T/k^2$ one gets

$$JPS\omega = \int k^{-2}(k^2 - k_x^2, k_xk_y, k_xk_z)\tilde{\delta}_h^2(\mathbf{k}) d^3k. \quad (3.72)$$

The off-diagonal terms (k_xk_y and k_xk_z) are zero by symmetry. The diagonal term is

$$\begin{aligned} \tilde{\mathcal{V}}^{-1} &= (JPS\omega)_{xx} = \int k^{-2}(k^2 - k_x^2)\tilde{\delta}_h^2(\mathbf{k}) d^3k \\ &= \left(1 - \frac{1}{3}\right) \int \tilde{\delta}_h^2(\mathbf{k}) d^3k = \left(1 - \frac{1}{3}\right) \mathcal{V}^{-1}, \end{aligned} \quad (3.73)$$

where we have used that all axes are equivalent and the Parseval's theorem. This means that JPS is proportional to the identity matrix and to the inverse of the particle volume $\mathcal{V} = (\mathbf{J}\mathbf{S})^{-1}$. In general, in a d-dimensional space with PBC

$$JPS = \tilde{\mathcal{V}}^{-1}\mathbf{I} = \left(1 - \frac{1}{d}\right) \mathcal{V}^{-1}\mathbf{I}. \quad (3.74)$$

If we interpret $\tilde{\mathcal{V}}$ as the effective particle volume in a incompressible fluid, the total particle inertia is then $\tilde{m} = \tilde{m}_f + m_e = \tilde{\mathcal{V}}\rho + m_e$. This implies that in a 3-dimensional space the particle inertia is increased by a term $m_f/2$, which is the well known added mass effect arising from the incompressibility constraint [Zwanzig 1975, Hinch 1975, Landau 1987].

Coming back to the expression (3.71), the result in Eq. (3.74) permits to compute the Taylor series for ρ_{eff}^{-1} and to obtain the closed expression

$$\rho_{\text{eff}}^{-1} = \rho^{-1} \left(\mathbf{I} - \frac{m_e \tilde{\mathcal{V}}}{\tilde{m}} \mathcal{P}SJP \right). \quad (3.75)$$

In the presence of hard walls the system has no longer translational invariance and the above results do not hold. The same happens when a system with PBC contains more than one particle. For many particles the effective density operator reads

$$\rho_{\text{eff}} \equiv \rho\mathbf{I} + \sum_i (m_e)_i \mathcal{P}S_i J_i \mathcal{P}, \quad (3.76)$$

where the summation runs over all the particles. In this case, the Taylor expansion of ρ_{eff}^{-1} contains cross terms of the form $J_i \mathcal{P} S_j$ that depend on the position of the particles i and j . These cross terms prevent us to find a closed form for ρ_{eff}^{-1} as in the case of a single particle. Nevertheless, numerical calculations suggest that $J_i \mathcal{P} S_j$ decays fast with the distance between the particles i and j , we use this fact to use the approximation $J_i \mathcal{P} S_j \approx \tilde{\mathcal{V}}^{-1} \delta_{ij} \mathbf{I}$ which leads to

$$\rho_{\text{eff}}^{-1} \approx \rho^{-1} \left(\mathbf{I} - \sum_i \frac{(m_e)_i (\tilde{\mathcal{V}})_i}{\tilde{m}_i} \mathcal{P}S_i J_i \mathcal{P} \right) \quad (3.77)$$

We will study the accuracy of this approximation working in the discretized space in Sec. 3.4 and in Sec. 3.5.3 we will use it to develop a numerical integrator for the incompressible limit. Also, we want to point out that the incompressible limit in the form of Eq. (3.68) is consistent with the FDB and the Augmented Langevin formalism, as it can be proved following the steps of Sections 2.1.4.2 and 3.3.3 [Usabiaga 2014].

3.4 Spatial discretization

In this section we describe the spatial discretization to solve the equations (3.31)-(3.34). Our description of the particle hydrodynamics contains both Lagrangian and Eulerian degrees of freedom. The solvent, described by the Navier-Stokes equations, is discretized by a staggered grid described in Chapter 2. Here we focus on how to handle the discretization of the particle terms.

As explained in Section 3.2, to connect the fluid and particle descriptions we use the averaging operator \mathbf{J} and its adjoint the spreading operators $\mathbf{S} = \mathbf{J}^*$ [see Eqs. (3.8)-(3.9)]. In the discrete setting the integrals over the fluid domain become sums over the grid points and the structure of the staggered grid should be taken into account when averaging or spreading variables. For example, the density averaged at the particle position \mathbf{q} is

$$\mathbf{J}\rho = \sum_{\mathbf{i} \in \text{grid}} h^3 \delta_h(\mathbf{q} - \mathbf{r}_i) \rho_i, \quad (3.78)$$

where, as in Chap 2, h is the meshwidth; and the x-component of the averaged velocity is

$$\mathbf{J}v^x = \sum_{\mathbf{i} \in \text{grid}} h^3 \delta_h(\mathbf{q} - (\mathbf{r}_i + \frac{h}{2}\hat{\mathbf{x}})) v^x_{i+\frac{\hat{\mathbf{x}}}{2}}. \quad (3.79)$$

Similar care should be taken when spreading centered variables (like the pressure, see Chapter 7) or faced variables (λ or F). For example, the spreading of the x-component of the force is

$$(\mathbf{S}F^x)_{i+\frac{\hat{\mathbf{x}}}{2}} = \delta_h(\mathbf{q} - (\mathbf{r}_i + \frac{h}{2}\hat{\mathbf{x}}))F^x. \quad (3.80)$$

The kernel function $\delta_h(\mathbf{r})$ is based on the tensor product of a one dimensional function for each direction α

$$\delta_h(\mathbf{r}) = h^{-d} \prod_{\alpha}^d \phi_h\left(\frac{r_{\alpha}}{h}\right). \quad (3.81)$$

This splitting simplifies the implementation of the scheme and it makes easier to impose the important conditions for ϕ_h that we state below. It is clear that this splitting breaks the isotropy of the particle, however the underlying grid is not isotropic neither so (3.81) does not introduce any extra limitation. Also, we point out that the anisotropy of the kernel δ_h is small.

For the one dimensional kernel ϕ_h we use the 3 points kernel of Roma and Peskin [Roma 1999, Peskin 2002], which is constructed upon the following properties

1. $\phi_h(r)$ is continuous for all real numbers r . (3.82)

2. $\phi_h(r) = 0$ for $|r| > 3/2$. (3.83)

3. $\sum_i \phi_h(r - i) = 1$ for $\forall r$. (3.84)

4. $\sum_i (r - i)\phi_h(r - i) = 0$ for $\forall r$. (3.85)

5. $\sum_i \phi_h^2(r - i) = \frac{1}{2}$ for $\forall r$, (3.86)

where the sums are taken over the nodes of a one dimensional grid. These properties were introduced by Peskin to recover a Dirac delta function in the limit $h \rightarrow 0$ while reducing the effects of the Eulerian discretization as much as possible. We are not interested in the limit $h \rightarrow 0$, since the size of our particles is slaved to the kernel size, however we have found the IBM kernels to be very well suited for our applications.

The property 1 ensures that the kernel has no jumps and the particle interaction with the underlying grid varies smoothly as the particle moves through the grid. This property is important to avoid instabilities and overshots in the particle dynamics. Note that the Heaviside function is incompatible with this condition.

Property 2 is important for computational efficiency. In three dimensions it implies that each particle interacts with only 27 grid points. The original implementation of the IBM was based on a collocated grid and it used central differences (with support $2h$) to construct the gradient and divergence operators. The null space of the central difference operator not only includes constant functions but also oscillating functions of period $2h$, and it is well known that this null space can lead to strong oscillations when localized forces are applied to the grid [Peskin 2002]. To avoid the excitation of one of these modes the IBM has traditionally used a 4 point kernel which has a wider support. For the 4 point kernel, properties 2 and 3 are replaced by

$$\phi_h(r) = 0 \quad \text{for } |r| > 2, \quad (3.87)$$

$$\sum_{i \text{ even}} \phi_h(r - i) = \sum_{i \text{ odd}} \phi_h(r - i) = \frac{1}{2}, \quad (3.88)$$

which ensures that all the functions of the null space are assigned with an equal weight in the spreading operation. Since we employ a staggered grid we do not suffer from the problems introduced by central differences. Although, tests by other researches [Dünweg 2009] suggest that (even without central differences) the 4 point kernel has a better translational invariance than the 3 points kernel. Such good behavior does not comes for free, since the particle interacts, in 3 dimensions, with 64 grid points. In our GPU implementation of the ICM one of the main bottlenecks is the access to memory; by reducing the number of grid neighbors per particle we hope to reduce the computation time by at least a factor 2 when the particle concentration is sufficiently high.

Property 3 and property 4 ensure that linear and angular momentum do not change during the fluid-particle interaction (see again [Peskin 2002]), note that this does not mean they are conserved, since that will depend on other properties of the scheme. We proved that the linear momentum is conserved in subsection 3.3.1.1, while angular momentum can not be conserved with periodic boundary conditions since the Hamiltonian of the system does not have spherical symmetry [Allen 1991]. Also, property 3 and property 4 ensure that linear functions are interpolated exactly and smooth functions with second order accuracy [$\mathcal{O}(h^2)$]. We have found that for application of soft matter with PBC this accuracy is high enough, but for applications that include complex boundary conditions it falls too short. Other groups have proposed the use of refined grids [Griffith 2005, Griffith 2007] or generalizations of the kernel function to increase the order of accuracy [Bringley 2008, Pinelli 2010]. However, increasing the kernel accuracy is not necessarily good if one wishes to model colloids. For example, to exactly interpolate quadratic functions it is necessary to include the condition

$$\sum_i (r - i)^2 \phi_h(r - i) = 0,$$

but this condition implies that the Faxén radius as defined in Eq. (3.46) becomes zero; something not desirable in modeling a finite size particle.

Property 5 was introduced by Peskin to ensure that the interaction of one Lagrangian point with itself (spreading and averaging) was stronger than with other near points. However, for our blob model property 5 is of central importance since it implies that the particle volume $\mathcal{V} = (\mathbf{J}\mathbf{S})^{-1}$ it is independent of the particle position with respect the underlying grid [recall Eq. (3.11)]. Property five gives, for the 3 points kernel, the volume $\mathcal{V} = 8h^3$ in three dimensions and $\mathcal{V} = 4h^2$ in 2D.

3.4.1 Notes for the incompressible case

In the previous analysis for the continuum setting we found that the matrix $\mathbf{J}\mathbf{P}\mathbf{S}$ was constant and proportional to the identity matrix and the particle volume. However, the discrete kernel we are using was not developed with this operator in mind and it is not guaranteed that its discrete version will conserve the same properties that its continuum counterpart. Here we check how the important relation $\mathbf{J}\mathbf{P}\mathbf{S} = \tilde{\mathcal{V}}^{-1}\mathbf{I}$ in the continuum formulation translates to the discretized space.

The left panel of figure 3.1 shows through numerical experiments the maximum deviation of $\mathbf{J}\mathbf{P}\mathbf{S}$ from the continuum limit. In particular, to measure the discretization errors we employ the matrix

$$\delta\mathbf{I}(\mathbf{q}) = \frac{d}{d-1}\mathcal{V}\mathbf{J}\mathbf{P}\mathbf{S} - \mathbf{I}, \quad (3.89)$$

which in the continuum setting is $\delta\mathbf{I}(\mathbf{q}) = 0$. The left panel of 3.1 shows that the maximum difference is always a few percent for large enough systems ($L \gtrsim 16h$). Also, the same figure shows that the error in the off-diagonal terms is practically zero for all box sizes. Therefore the operator $\mathbf{J}\mathbf{P}\mathbf{S}$ is nearly constant and closely proportional to the identity matrix as desired.

In the right panel of figure 3.1 we investigate the accuracy of our approximation for ρ_{eff}^{-1} in the case of several particles. Recall that to invert the effective density we use the approximation $\mathbf{J}_i\mathbf{P}\mathbf{S}_j = 0$ if $i \neq j$. The figure shows $\mathbf{J}_i\mathbf{P}\mathbf{S}_j$ versus the particle distance $l = |\mathbf{q}_i - \mathbf{q}_j|$ and indicates that for particles at distances $l > 5h$ the maximum error is below 2%. This allows us to employ the approximation (3.77) as the inverse of the effective density operator. Also, it is important to highlight that the errors in this approximation only affect the dynamic at short times, when the particle inertia is important. The reason for this fact is that the density operator ρ_{eff} does not affect the steady states for which $\partial_t \mathbf{v} = 0$. However, to ensure strict momentum conservation special care should be taken when using the approximation to ρ_{eff}^{-1} . We will come back to this issue in Section 3.5.3.

3.5 Temporal discretization

In this section we present different temporal discretizations to solve the equation of the inertial coupling method. The temporal integrators solve the equation of motion for discrete time steps Δt , which, along this section, are denoted by a superscript. For example the particle position at time $t^{n+\frac{1}{2}} = (n + \frac{1}{2})\Delta t$ is denoted by $\mathbf{q}^{n+\frac{1}{2}}$ and \mathbf{J}^n represents the average operator at the particle position $\mathbf{q}^n = \mathbf{q}(n\Delta t)$.

In Section 3.5.1 we present a first order scheme for particles immersed in a compressible fluid. The accuracy of this scheme is not high but the main ideas for the integration of the dynamic equations are presented there. In Section 3.5.2 we present a more accurate scheme for particles immersed in compressible flows and finally in Section 3.5.3 a second order scheme for incompressible flows is presented.

3.5.1 First order compressible scheme

The first order scheme is based on a projection method that was used in the direct forcing method [Uhlmann 2005]. First, fluid and particles are updated independently, so they do not interact with each

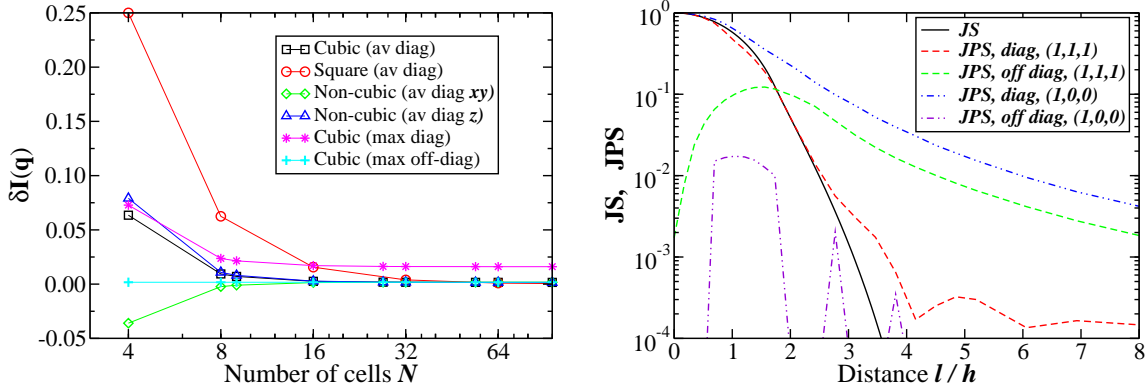


Figure 3.1: Left, discretization errors in the diagonal and off-diagonal terms of the operator $\mathbf{J}\mathbf{P}\mathbf{S}$ as measured by $\delta\mathbf{I}(\mathbf{q})$ [Eq. (3.89)] in two (circles) and three dimensions. The average (av) values of $\delta\mathbf{I}(\mathbf{q})$ decay to zero for moderately sized boxes ($N \approx 16$ cells) while the maximum (max) diagonal values of $\delta\mathbf{I}(\mathbf{q})$ remain non-zero for all box sizes. One can see that the errors are larger for non-cubic boxes in three dimensions and specially for two dimensional systems. Right, maximum diagonal and off-diagonal values of the operator $3\mathcal{V}(\mathbf{J}_i \mathbf{P} \mathbf{S}_j)/2$ for two particles i and j at distance l along the $(1, 0, 0)$ or $(1, 1, 1)$ direction as indicated by legend. To compare the decay of this operator we include the maximum particle overlap $\mathcal{V}(\mathbf{J}_i \mathbf{S}_j)$ for two particles at a distance l apart. All simulations in the right panel were performed in a cubic box with 32^3 cells.

other. Then, the fluid-particle force $\boldsymbol{\lambda}$ is calculated so that at the end of the time step the no-slip constraint $\mathbf{J}^{n+1}\mathbf{v}^{n+1} = \mathbf{u}^{n+1}$ is satisfied.

In general, imposing a constraint at the end of the time step requires iterative solvers but here it is possible to evaluate the coupling force in a single step as we show below. The scheme is divided in the following substeps:

1. Unperturbed flow. Update the hydrodynamic fields from time $t^n = n\Delta t$ to time $t^{n+1} = (n+1)\Delta t$ without including any effect coming from the particle. To solve the Navier-Stokes equations it is possible to use any fluid solver, for example, the explicit compressible solver presented in Section 2.3.1. At the end of the substep one has the density ρ^{n+1} and the unperturbed velocity field $\tilde{\mathbf{v}}^{n+1}$. The density field is no longer modified in the rest of substeps, but the velocity field will be updated to obey the no-slip condition.
2. Update particle position with a first order method.

$$\mathbf{q}^{n+1} = \mathbf{q}^n + \Delta t \mathbf{u}^n. \quad (3.90)$$

3. Calculate coupling force $\boldsymbol{\lambda}$. The force should be such that at the end of the time step the no-slip constraint is satisfied. The coupling force is obtained from the equations

$$\rho^{n+1} \mathbf{v}^{n+1} = \rho^{n+1} \tilde{\mathbf{v}}^{n+1} - \mathbf{S}^{n+1} \boldsymbol{\lambda} \Delta t, \quad (3.91)$$

$$m_e \mathbf{u}^{n+1} = m_e \mathbf{u}^n + \mathbf{F}^{n+1} \Delta t + \boldsymbol{\lambda} \Delta t, \quad (3.92)$$

$$\text{s.t. } \mathbf{J}^{n+1} \mathbf{v}^{n+1} = \mathbf{u}^{n+1}. \quad (3.93)$$

Averaging the first equation around the particle position, using the low Mach number approximation $\mathbf{J}(\rho\mathbf{v}) = (\mathbf{J}\rho)(\mathbf{J}\mathbf{v})$, the kernel property $\mathbf{JS} = \mathcal{V}^{-1}$ and plugging the result into the particle equation, one gets

$$\lambda\Delta t = \frac{m_e m_f}{m_f + m_e} (\mathbf{J}^{n+1} \tilde{\mathbf{v}}^{n+1} - \mathbf{u}^n) - \frac{m_f}{m_e + m_f} \mathbf{F} \Delta t, \quad (3.94)$$

where the fluid mass “inside” the particle domain is $m_f = \mathcal{V} \mathbf{J}^{n+1} \rho^{n+1}$. The term $\lambda\Delta t$ is the impulse exchanged between the particle and the fluid during the time step and it is used in the next substeps to update the particle and fluid velocities.

4. Update particle velocity. Using the coupling force λ , one gets

$$\mathbf{u}^{n+1} = \mathbf{u}^n + \frac{m_f}{m_f + m_e} (\mathbf{J}^{n+1} \tilde{\mathbf{v}}^{n+1} - \mathbf{u}^n) + \frac{\mathbf{F} \Delta t}{m_f + m_e}. \quad (3.95)$$

Recall that the particle mass is $m = m_f + m_e$.

5. Update the fluid velocity. Using the coupling force λ in the Eq. (3.91) the fluid update can be written as

$$\mathbf{v}^{n+1} = \tilde{\mathbf{v}}^{n+1} - \mathcal{V} \mathbf{S}^{n+1} (\mathbf{J}^{n+1} \tilde{\mathbf{v}}^{n+1} - \mathbf{u}^{n+1}). \quad (3.96)$$

If the velocity field is averaged at the particle position \mathbf{q}^{n+1} it is evident by the condition $\mathbf{JS} = \mathcal{V}^{-1}$ that the no-slip condition is obeyed at the end of the time step. In the case of many particles the situation is slight different, if there are many particles in the system, all the substeps are exactly the same but the Eq. (3.96) reads

$$\mathbf{v}^{n+1} = \tilde{\mathbf{v}}^{n+1} - \mathcal{V} \sum_i \mathbf{S}_i^{n+1} (\mathbf{J}_i^{n+1} \tilde{\mathbf{v}}^{n+1} - \mathbf{u}_i^{n+1}), \quad (3.97)$$

where the sum runs over all the particles in the system. Now, if one averages the fluid velocity at the position of a particle j the results is

$$\mathbf{J}_j^{n+1} \mathbf{v}^{n+1} = \mathbf{u}_j^{n+1} - \mathcal{V} \sum_{i \neq j} \mathbf{J}_j^{n+1} \mathbf{S}_i^{n+1} (\mathbf{J}_i^{n+1} \tilde{\mathbf{v}}^{n+1} - \mathbf{u}_i^{n+1}). \quad (3.98)$$

If the kernels of particles i and j do not overlap then $\mathbf{J}_j \mathbf{S}_i = 0$ and the no-slip constraint is recovered. However, if the particles are allowed to overlap a small error in the no-slip condition is introduced. The right panel of Fig. 3.1 shows that the kernel overlap for two particles decays fast with the distance and for distances $l > 2h$ is negligible. Therefore we neglect this small error.

Since the same coupling force has been using in the fluid and particle update the momentum is strictly conserved even if particles overlap.

It is interesting to consider the case of neutrally-buoyant particles ($m_e = 0$). In this case our method reduces to the immersed boundary method of Peskin [Peskin 2002], where the particles are advected by the fluid and driven by the external forces. From Eq. (3.95) one can derive the equation $\mathbf{u}^{n+1} = \mathbf{J}^{n+1} \tilde{\mathbf{v}}^{n+1} + \mathbf{F} \Delta t / m_f$. If there are no external forces acting on the particles ($\mathbf{F} = 0$), the particles do not perturb the flow at all and they can be used as passive tracers. In fact, for neutrally buoyant particles, independently of possible overlaps between them, the no slip constraint $\mathbf{J}^{n+1} \tilde{\mathbf{v}}^{n+1} = \mathbf{u}^{n+1}$ is always satisfied.

3.5.2 Compressible scheme

With small modifications the previous method can transformed into a second order scheme for neutrally buoyant particles. For non-neutrally buoyant particles the scheme is formally first order, but it presents a much better accuracy than the previous algorithm. As before, the method is based in a splitting algorithm that first solves the fluid without including the fluid-particle force and second, it solves the constraint force λ that impose the no-slip condition at the end of the time step. The main differences are that the particle position is updated with a predictor-corrector method and that the external forces F are spread to the fluid before this is updated.

The scheme update the system's state from time $t^n = n\Delta t$ to time $t^{n+1} = (n + 1)\Delta t$ as follows

1. Estimate particle position at time $t^{n+\frac{1}{2}} = (n + \frac{1}{2})\Delta t$

$$\mathbf{q}^{n+\frac{1}{2}} = \mathbf{q}^n + \frac{\Delta t}{2} \mathbf{J}^n \mathbf{v}^n. \quad (3.99)$$

2. Calculate the forces $\mathbf{F}^{n+\frac{1}{2}} = \mathbf{F}(\mathbf{q}^{n+\frac{1}{2}})$ acting on the particles and spread them to the fluid as $\mathbf{S}^{n+\frac{1}{2}} \mathbf{F}^{n+\frac{1}{2}}$. The superscript $n + \frac{1}{2}$ in the spreading operator indicates that the force are spread around the particle position $\mathbf{q}^{n+\frac{1}{2}}$.
3. Solve the density and unperturbed momentum equations for the fluid

$$\begin{aligned} \partial_t \rho + \nabla \cdot \mathbf{g} &= 0, \\ \partial_t \mathbf{g} + \nabla \cdot (\mathbf{g} \mathbf{v}) &= -\nabla \cdot \boldsymbol{\sigma} + \mathbf{S}^{n+\frac{1}{2}} \mathbf{F}^{n+\frac{1}{2}}, \end{aligned}$$

using the third-order Runge-Kutta scheme described in chapter 2, to obtain the density ρ^{n+1} and the unperturbed velocity $\tilde{\mathbf{v}}^{n+1}$. During this step the density force $\mathbf{S}^{n+\frac{1}{2}} \mathbf{F}^{n+\frac{1}{2}}$ is treated as a constant forcing but we do not impose the no-slip constraint. To allow for larger time steps, other fluid solvers can be used, for example the semi-implicit compressible solver described in Section 2.3.3.

4. Calculate the impulse exchanged between particle and fluid during the time step such that at the end of the time step the no-slip condition holds. From the particle equation $\mathbf{u}^{n+1} = \mathbf{u}^n + \Delta t(\lambda + \mathbf{F})/m_e$ and the fluid equation

$$\rho^{n+1} \mathbf{v}^{n+1} = \rho^{n+1} \tilde{\mathbf{v}}^{n+1} - \Delta t \mathbf{S}^{n+\frac{1}{2}} \left(\lambda^{n+\frac{1}{2}} + \mathbf{F}^{n+\frac{1}{2}} \right), \quad (3.100)$$

one can derive the impulse

$$\Delta \mathbf{p} = \Delta t \left(\lambda^{n+\frac{1}{2}} + \mathbf{F}^{n+\frac{1}{2}} \right) = \frac{m_e m_f}{m_e + m_f} \left(\mathbf{J}^{n+\frac{1}{2}} \tilde{\mathbf{v}}^{n+1} - \mathbf{u}^n \right), \quad (3.101)$$

where the dragged fluid mass is

$$m_f = \mathcal{V} \mathbf{J}^{n+\frac{1}{2}} \rho^{n+1}. \quad (3.102)$$

In this derivation we have assumed that the constraint force λ is constant during the time step and that $\mathcal{V} \mathbf{J}^{n+\frac{1}{2}} (\rho^{n+1} \mathbf{v}^{n+1}) = m_f \mathbf{J}^{n+\frac{1}{2}} \mathbf{v}^{n+1}$. When dealing with several particles it is necessary to add a summation over all of them in the equation (3.100), just as in the first order scheme. If the particles do not overlap, that is $\mathbf{J}_i \mathbf{S}_j = \delta_{ij}^{\text{Kronecker}}$, the impulse (3.101) still holds. For overlapping particles we assume that Eq. (3.101) is still valid to avoid solving a large linear system. In doing so we introduce a small error in the no-slip condition but the rest of the properties, like the conservation of momentum, still hold.

5. Update the particle velocity

$$\mathbf{u}^{n+1} = \mathbf{u}^n + \frac{\Delta p}{m_e} = \mathbf{u}^n + \frac{m_f}{m_e + m_f} (\mathbf{J}^{n+\frac{1}{2}} \tilde{\mathbf{v}}^{n+1} - \mathbf{u}^n). \quad (3.103)$$

Note that here the external force acting on the particle does not appear because it was already included in the fluid momentum equation in the first substep.

6. Update the fluid velocity while keeping the density ρ^{n+1} fixed

$$\mathbf{v}^{n+1} = \tilde{\mathbf{v}}^{n+1} - \frac{\mathcal{V}}{m_f} \mathbf{S}^{n+\frac{1}{2}} \Delta p = \tilde{\mathbf{v}}^{n+1} + \mathcal{V} \mathbf{S}^{n+\frac{1}{2}} (\mathbf{u}^{n+1} - \mathbf{J}^{n+\frac{1}{2}} \tilde{\mathbf{v}}^{n+1}). \quad (3.104)$$

If the system has several particles, the above equation should be replaced by

$$\mathbf{v}^{n+1} = \tilde{\mathbf{v}}^{n+1} + \mathcal{V} \sum_j \mathbf{S}_j^{n+\frac{1}{2}} (\mathbf{u}_j^{n+1} - \mathbf{J}_j^{n+\frac{1}{2}} \tilde{\mathbf{v}}^{n+1}),$$

where the sum runs over all the particles. As with the first order scheme, this last equation produces a small error in the no-slip constraint if particles overlap. Since the overlap is always small we neglect this source of error.

7. Finally, update the particle position to time $t^{n+1} = (n + 1)\Delta t$ with a centered method

$$\mathbf{q}^{n+1} = \mathbf{q}^n + \frac{\Delta t}{2} \mathbf{J}^{n+\frac{1}{2}} (\mathbf{v}^n + \mathbf{v}^{n+1}). \quad (3.105)$$

This scheme conserves the momentum and obeys the no-slip condition in the form $\mathbf{u}^{n+1} = \mathbf{J}^{n+\frac{1}{2}} \mathbf{v}^{n+1}$. The first order scheme presented in the previous section used the no-slip condition $\mathbf{u}^{n+1} = \mathbf{J}^{n+1} \mathbf{v}^{n+1}$ which, although it seems more natural, gives a much slower convergence for the particle dynamics. Therefore, we prefer to use the second order scheme presented in this section.

The inertia of the particle is taken into account in the second part of the scheme, during the update from the unperturbed fluid velocity $\tilde{\mathbf{v}}^{n+1}$ to the final velocity \mathbf{v}^{n+1} , therefore neutrally-buoyant particles just spread the external forces \mathbf{F} to the fluid, and in the case in which no external forces are present, the neutrally-buoyant particles are advected by the fluid without disturbing it in any way. Again, this limitation comes from the fact that we are only imposing the no-slip condition in an averaged way, without including rotational and stresslet terms that will disturb the fluid even for neutrally-buoyant particles. This limitation of the present method will be solved in future works.

3.5.3 Incompressible scheme

The time stepping for incompressible flows is close to those presented in the previous sections. To allow for large time steps we use a semi-implicit discretization of the viscous terms (recall Sec. 2.3.2). However, the semi-implicit discretization and the incompressibility constraint introduce some difficulties not present in the compressible schemes.

The scheme, based on the Eq. (3.47), has the following steps

1. Estimate particle position at time $t^{n+\frac{1}{2}} = (n + \frac{1}{2})\Delta t$

$$\mathbf{q}^{n+\frac{1}{2}} = \mathbf{q}^n + \frac{\Delta t}{2} \mathbf{J}^n \mathbf{v}^n. \quad (3.106)$$

2. Update the fluid velocity with a second-order algorithm while keeping the no-slip condition

$$\begin{aligned} \left(\rho \mathbf{I} + m_e \mathbf{S}^{n+\frac{1}{2}} \mathbf{J}^{n+\frac{1}{2}} \right) \frac{\mathbf{v}^{n+1} - \mathbf{v}^n}{\Delta t} + \nabla \pi^{n+\frac{1}{2}} &= -\nabla \cdot (\rho \mathbf{v} \mathbf{v}^T + \boldsymbol{\sigma})^{n+\frac{1}{2}} + \mathbf{S}^{n+\frac{1}{2}} \mathbf{F}^{n+\frac{1}{2}} \\ &\quad - (m_e \mathbf{S} \mathbf{J} (\mathbf{v} \cdot \nabla_{\mathbf{q}} \mathbf{J}) \mathbf{v})^{n+\frac{1}{2}}, \quad (3.107) \\ \text{s.t. } \nabla \cdot \mathbf{v}^{n+1} &= 0. \end{aligned}$$

Note that these equations are equivalent to Eq. (3.68), but instead of use the projector operator \mathcal{P} we include the pressure π and the constraint $\nabla \cdot \mathbf{v} = 0$.

3. Finally, update the particle position to time $t^{n+1} = (n + 1)\Delta t$

$$\mathbf{q}^{n+1} = \mathbf{q}^n + \frac{\Delta t}{2} \mathbf{J}^{n+\frac{1}{2}} (\mathbf{v}^n + \mathbf{v}^{n+1}). \quad (3.108)$$

In the next sections we explain how to discretize each term of Eq. (3.107) and how to integrate it.

3.5.3.1 Particle kinetic stress tensor

A simple choice to discretize the particle kinetic stress contribution in Eq. (3.107) is

$$(\mathbf{J} (\mathbf{v} \cdot \nabla_{\mathbf{q}} \mathbf{J}) \mathbf{v})^n = ((\mathbf{u} \cdot \nabla_{\mathbf{q}} \mathbf{J}) \mathbf{v})^n = \left(\frac{\mathbf{J}^{n+\frac{1}{2}} - \mathbf{J}^{n-\frac{1}{2}}}{\Delta t} \right) \mathbf{v}^n. \quad (3.109)$$

However, the above term is not centered in time and therefore it only gives first order accuracy. To reach second order accuracy we introduce a correction $\Delta \mathbf{u}^{n+\frac{1}{2}}$ in the no-slip constrain

$$\mathbf{u}^{n+1} = \mathbf{J}^{n+\frac{1}{2}} \mathbf{v}^{n+1} + \Delta \mathbf{u}^{n+\frac{1}{2}}. \quad (3.110)$$

The correction $\Delta \mathbf{u}^{n+\frac{1}{2}}$ can be used to obtain a second order accurate discretization of the kinetic stress tensor by using a no-slip condition centered at the time $t^{n+\frac{1}{2}} = (n + \frac{1}{2})\Delta t$

$$\frac{1}{2} \mathbf{J}^{n+\frac{1}{2}} (\mathbf{v}^{n+1} + \mathbf{v}^n) = \frac{1}{2} (\mathbf{u}^{n+1} + \mathbf{J}^n \mathbf{v}^n) = \frac{1}{2} (\mathbf{J}^{n+\frac{1}{2}} \mathbf{v}^{n+1} + \Delta \mathbf{u}^{n+\frac{1}{2}} + \mathbf{J}^n \mathbf{v}^n), \quad (3.111)$$

which yields

$$\Delta \mathbf{u}^{n+\frac{1}{2}} = (\mathbf{J}^{n+\frac{1}{2}} - \mathbf{J}^n) \mathbf{v}^n. \quad (3.112)$$

Then, the second order accurate discretization of the stress tensor is

$$[m_e \mathbf{S} \mathbf{J} (\mathbf{v} \cdot \nabla_{\mathbf{q}} \mathbf{J}) \mathbf{v}]^{n+\frac{1}{2}} = m_e \mathbf{S}^{n+\frac{1}{2}} \left(\frac{\mathbf{J}^{n+\frac{1}{2}} - \mathbf{J}^{n-\frac{1}{2}}}{\Delta t} \mathbf{v}^n + \frac{\Delta \mathbf{u}^{n+\frac{1}{2}} - \Delta \mathbf{u}^{n-\frac{1}{2}}}{\Delta t} \right), \quad (3.113)$$

with $\Delta \mathbf{u}^{n+\frac{1}{2}}$ given in Eq. (3.112).

3.5.3.2 Fluid advection

Other nonlinear term in the momentum equation is the fluid advection. In Chapter 2 we used a predictor-corrector scheme to approximate it at time $(n + \frac{1}{2})\Delta t$, here for computational efficiency we prefer to use the classical Adams-Bashforth method [Quarteroni 2000, Griffith 2012b]

$$\nabla \cdot (\rho \mathbf{v} \mathbf{v}^T)^{n+\frac{1}{2}} = \frac{3}{2} \nabla \cdot (\rho \mathbf{v} \mathbf{v}^T)^n - \frac{1}{2} \nabla \cdot (\rho \mathbf{v} \mathbf{v}^T)^{n-1}, \quad (3.114)$$

which also yields second order accuracy.

3.5.3.3 Viscous terms

We discuss here the viscous and stochastic terms since they are strongly connected through the FDB. To be able to use large time steps we use a semi-implicit discretization for the viscous terms, in particular a Crank-Nicolson method just as we did in Chapter 2 Section 2.3.2

$$[\eta \nabla^2 \mathbf{v}]^{n+\frac{1}{2}} = \frac{\eta}{2} \nabla^2 (\mathbf{v}^{n+1} + \mathbf{v}^n). \quad (3.115)$$

In this case, the discretization of the stochastic term is just

$$[\nabla \cdot \Sigma]^n = \nabla \cdot \left[\sqrt{\frac{k_B T \eta}{h^3 \Delta t}} (\mathbf{W}^n + (\mathbf{W}^n)^T) \right] \quad (3.116)$$

where \mathbf{W} is a collection of normally distributed random numbers with zero mean and unit variance. Note that this discretization is the same that we presented and tested in the Chapter 2 for the incompressible scheme and it is enough to achieve a second order weak accuracy.

3.5.3.4 Velocity splitting

Collecting all the terms discussed in the previous sections the discretization of the velocity update is

$$\begin{aligned} (\rho \mathbf{I} + m_e \mathbf{S}^{n+\frac{1}{2}} \mathbf{J}^{n+\frac{1}{2}}) \frac{\mathbf{v}^{n+1} - \mathbf{v}^n}{\Delta t} + \nabla \pi^{n+\frac{1}{2}} &= \frac{\eta}{2} \nabla^2 (\mathbf{v}^n + \mathbf{v}^{n+1}) + \mathbf{S}^{n+\frac{1}{2}} \mathbf{F}^{n+\frac{1}{2}} - \nabla \cdot (\rho \mathbf{v} \mathbf{v}^T)^{n+\frac{1}{2}} \\ &- m_e \mathbf{S}^{n+\frac{1}{2}} \left[\frac{\mathbf{J}^{n+\frac{1}{2}} - \mathbf{J}^{n-\frac{1}{2}}}{\Delta t} \mathbf{v}^n + \frac{\Delta \mathbf{u}^{n+\frac{1}{2}} - \Delta \mathbf{u}^{n-\frac{1}{2}}}{\Delta t} \right] \\ &+ \nabla \cdot \Sigma^n, \end{aligned} \quad (3.117)$$

$$\nabla \cdot \mathbf{v}^{n+1} = 0. \quad (3.118)$$

Note that in the above equation the operator acting on the updated velocity \mathbf{v}^{n+1} is

$$\left[\rho \mathbf{I} - \frac{\eta \Delta t}{2} \nabla^2 + m_e \mathbf{S}^{n+\frac{1}{2}} \mathbf{J}^{n+\frac{1}{2}} \right]. \quad (3.119)$$

This is a linear constant operator, since the particle is fixed at $\mathbf{q}^{n+\frac{1}{2}}$ during the velocity update. For neutrally-buoyant particles $m_e = 0$, we know how to invert this operator using FFT (always with PBC, recall Sec. 2.3.2.1), however, when the excess mass is not zero this is not possible, since the particle inertia couples all modes. One possibility to invert the operator is to use some iterative method, see for example [Zhu 2002, Mori 2008] for implementations of the IBM for non neutrally-buoyant structures. The iterative solvers, though very versatile, cannot compete in speed with the methods based on FFT. In soft matter applications it is common to need very long simulations to average over thermal fluctuations, thus, we develop a method that only employs FFT.

In the micro-regime the leading effects governing the particle dynamics come from the viscous terms while particle inertial effects usually are small contributions, therefore we split the fluid velocity in two terms, $\tilde{\mathbf{v}}^{n+1}$ which does not have into account particle inertia effects and $\Delta \mathbf{v}^{n+\frac{1}{2}} = \mathbf{v}^{n+1} - \tilde{\mathbf{v}}^{n+1}$ that contains the correction. The equation for $\tilde{\mathbf{v}}^{n+1}$ is

$$\begin{aligned} \left[\rho \mathbf{I} - \frac{\eta \Delta t}{2} \nabla^2 \right] \tilde{\mathbf{v}}^{n+1} + \nabla \tilde{\pi}^{n+\frac{1}{2}} &= \left[\rho \mathbf{I} + \frac{\eta \Delta t}{2} \nabla^2 \right] \mathbf{v}^n + \Delta t \mathbf{S}^{n+\frac{1}{2}} \mathbf{F}^{n+\frac{1}{2}} - \Delta t \nabla \cdot (\rho \mathbf{v} \mathbf{v}^T)^{n+\frac{1}{2}} \\ &- m_e \mathbf{S}^{n+\frac{1}{2}} \left[\left(\mathbf{J}^{n+\frac{1}{2}} - \mathbf{J}^{n-\frac{1}{2}} \right) \mathbf{v}^n + \left(\Delta \mathbf{u}^{n+\frac{1}{2}} - \Delta \mathbf{u}^{n-\frac{1}{2}} \right) \right] \\ &+ \nabla \cdot \Sigma^n, \end{aligned} \quad (3.120)$$

$$\nabla \cdot \tilde{\mathbf{v}}^{n+1} = 0. \quad (3.121)$$

This kind of equations with the incompressible constraint are easily solved by using FFT, in the way we explained in Chapter 2 Section 2.3.2.1. If the particles are not neutrally buoyant ($m_e \neq 0$) we then need to find the velocity correction $\Delta\mathbf{v}^{n+\frac{1}{2}}$. Replacing \mathbf{v}^{n+1} in Equation (3.117) by $(\tilde{\mathbf{v}}^{n+1} + \Delta\mathbf{v}^{n+\frac{1}{2}})$ and using Equation (3.120) one can find the equation for the velocity correction

$$\left[\left(\rho\mathbf{I} - \frac{\Delta t}{2}\eta\nabla^2 \right) + m_e\mathbf{S}\mathbf{J} \right] \Delta\mathbf{v}^{n+\frac{1}{2}} + \Delta t\nabla(\Delta\pi^{n+\frac{1}{2}}) = m_e\mathbf{S}(\mathbf{u}^n - \mathbf{J}\tilde{\mathbf{v}}^{n+1} - \Delta\mathbf{u}^{n+1}), \quad (3.122)$$

$$\nabla \cdot \Delta\mathbf{v}^{n+\frac{1}{2}} = 0. \quad (3.123)$$

However, this equation has the same operator that Eq. (3.117) acting on $\Delta\mathbf{v}^{n+\frac{1}{2}}$. We rewrite it in a more suitable form,

$$\left[\rho\mathbf{I} - \frac{\Delta t}{2}\eta\nabla^2 + m_e\mathbf{S}\mathbf{J} \right] = (\rho\mathbf{I} + m_e\mathbf{S}\mathbf{J}) \left(\mathbf{I} - \frac{\Delta t}{2}\nu\nabla^2 \right) + \frac{m_e\nu\Delta t}{2}\mathbf{S}\mathbf{J}\nabla^2. \quad (3.124)$$

Ignoring the last term the above equation gives an approximation of order $\mathcal{O}(m_e\Delta t)$ which can be solved with FFT. However, we can improve the accuracy if we time-lag the last term, that is, if we evaluate it in the previous time step. With this approximation we can rewrite the equation (3.122) as

$$(\rho\mathbf{I} + m_e\mathbf{S}\mathbf{J}) \left(\mathbf{I} - \frac{\Delta t}{2}\nu\nabla^2 \right) \Delta\mathbf{v}^{n+\frac{1}{2}} = m_e\mathbf{S} \left(\mathbf{u}^n - \mathbf{J}\tilde{\mathbf{v}}^{n+1} - \delta\mathbf{u}^{n+\frac{1}{2}} \right) = \mathbf{S}\Delta\mathbf{p}, \quad (3.125)$$

where we have introduced the term

$$\delta\mathbf{u}^{n+\frac{1}{2}} = \Delta\mathbf{u}^{n+\frac{1}{2}} + \frac{\nu\Delta t}{2}\mathbf{J}^{n-\frac{1}{2}}\nabla^2\Delta\mathbf{v}^{n-\frac{1}{2}}. \quad (3.126)$$

The equation (3.125) can be solved in two steps. First, denote $\Delta\tilde{\mathbf{v}} = (\mathbf{I} - (\nu\Delta t/2)\nabla^2)\Delta\mathbf{v}^{n+\frac{1}{2}}$ and write Eq. (3.125) as

$$(\rho\mathbf{I} + m_e\mathbf{S}\mathbf{J})\Delta\tilde{\mathbf{v}} + \Delta t\nabla\Delta\pi^{n+\frac{1}{2}} = \mathbf{S}\Delta\mathbf{p}, \quad (3.127)$$

$$\nabla \cdot \Delta\tilde{\mathbf{v}} = 0, \quad (3.128)$$

where we have used $\mathcal{P}\Delta\tilde{\mathbf{v}} = \Delta\tilde{\mathbf{v}}$ (valid due to the incompressibility constraint). Then, applying the projector operator to Eq. (3.127) one gets the equation

$$(\rho\mathbf{I} + m_e\mathcal{P}\mathbf{S}\mathbf{J}\mathcal{P})\Delta\tilde{\mathbf{v}} = \mathcal{P}\mathbf{S}\Delta\mathbf{p} \quad (3.129)$$

This is the equation one has to solve to take into account the particle inertia effects on the flow. Note that the operator acting on $\Delta\tilde{\mathbf{v}}$ is just the effective density ρ_{eff} introduced in the Eq. (3.69). Then, using the approximation for ρ_{eff}^{-1} given by the equation (3.77) one can write the velocity correction as

$$\Delta\tilde{\mathbf{v}} = \frac{\tilde{m}_f}{\rho(\tilde{m}_f + m_e)} \mathcal{P} \sum_i^N \mathbf{S}_i \Delta\mathbf{p}_i, \quad (3.130)$$

where $\tilde{m}_f = \tilde{\mathcal{V}}\rho$ and we have assumed that the system contains N particles with excess mass m_e . $\mathbf{S}\Delta\mathbf{p}$ is a field that can be calculated without problems and the projector operator is easily applied in the Fourier space (see Sec. 2.3.2.1). Once $\Delta\tilde{\mathbf{v}}$ is known the velocity correction $\Delta\mathbf{v}^{n+\frac{1}{2}}$ can be calculated. To ensure exact momentum conservation and incompressibility we solve

$$\left(\rho\mathbf{I} - \frac{\Delta t}{2}\eta\nabla^2 \right) \Delta\mathbf{v}^{n+\frac{1}{2}} + \Delta t\nabla\pi^{n+\frac{1}{2}} = \mathbf{S}(\Delta\mathbf{p} - m_e\mathbf{J}\Delta\tilde{\mathbf{v}}), \quad (3.131)$$

$$\nabla \cdot \Delta\mathbf{v}^{n+\frac{1}{2}} = 0. \quad (3.132)$$

In the continuum setting the above equations are equivalent to the simpler $(\mathbf{I} - (\nu \Delta t / 2) \nabla^2) \Delta \mathbf{v}^{n+\frac{1}{2}} = \Delta \tilde{\mathbf{v}}$. However, because we use an approximation for the inverse of ρ_{eff} it is necessary to solve Eqs. (3.131)-(3.132) to ensure exact incompressibility and momentum conservation. This update is consistent with the system of equations (3.31)-(3.34) if we set

$$\Delta t (\boldsymbol{\lambda} + \mathbf{F})^{n+\frac{1}{2}} = m_e \left[\mathbf{J}^{n+\frac{1}{2}} (\tilde{\mathbf{v}}^{n+1} + \Delta \tilde{\mathbf{v}}) + \delta \mathbf{u}^{n+\frac{1}{2}} - \mathbf{u}^n \right], \quad (3.133)$$

which in turns determines the particle velocity update

$$\mathbf{u}^{n+1} = \mathbf{u}^n + m_e^{-1} \Delta t (\boldsymbol{\lambda} + \mathbf{F})^{n+\frac{1}{2}} = \mathbf{J}^{n+\frac{1}{2}} (\tilde{\mathbf{v}}^{n+1} + \Delta \tilde{\mathbf{v}}) + \delta \mathbf{u}^{n+\frac{1}{2}}. \quad (3.134)$$

We should ask if after this rather complex scheme the no-slip constraint has some violation. Using the previous results, the violation in the no-slip constraint is

$$\begin{aligned} \Delta \mathbf{u}^{n+1} &= \mathbf{u}^{n+1} - \mathbf{J}^{n+\frac{1}{2}} (\tilde{\mathbf{v}}^{n+1} + \Delta \mathbf{v}^{n+\frac{1}{2}}) - \Delta \mathbf{u}^{n+\frac{1}{2}} \\ &= -\frac{\Delta t \nu}{2} \left(\mathbf{J}^{n+\frac{1}{2}} \nabla^2 \Delta \mathbf{v}^{n+\frac{1}{2}} - \mathbf{J}^{n-\frac{1}{2}} \nabla^2 \Delta \mathbf{v}^{n-\frac{1}{2}} \right), \end{aligned} \quad (3.135)$$

which is $\mathcal{O}(m_e \Delta t^2)$ if the velocity correction is smooth in time. In Section 3.6 we will present some test to show that this scheme can provide accurate results even with very large time steps.

3.5.3.5 Summary

We give now a summary of the incompressible scheme

1. Estimate the particle position at time $t^{n+\frac{1}{2}} = (n + \frac{1}{2}) \Delta t$

$$\mathbf{q}^{n+\frac{1}{2}} = \mathbf{q}^n + \frac{\Delta t}{2} \mathbf{J}^n \mathbf{v}^n. \quad (3.136)$$

2. Calculate the force $\mathbf{F}^{n+\frac{1}{2}} = \mathbf{F}(\mathbf{q}^{n+\frac{1}{2}})$ acting on the particle and spread it to the fluid as $\mathbf{S}^{n+\frac{1}{2}} \mathbf{F}^{n+\frac{1}{2}}$.

3. Solve the unperturbed fluid equation

$$\begin{aligned} \rho \frac{\tilde{\mathbf{v}}^{n+1} - \mathbf{v}^n}{\Delta t} &= \frac{\eta}{2} \nabla^2 (\tilde{\mathbf{v}}^{n+1} + \mathbf{v}^n) + \nabla \cdot \left(\left(\frac{k_B T \eta}{h^3 \Delta t} \right)^{1/2} (\mathbf{W}^n) + (\mathbf{W}^n)^T \right) \\ &\quad - \left(\frac{3}{2} \nabla \cdot (\rho \mathbf{v} \mathbf{v}^T)^n - \frac{1}{2} \nabla \cdot (\rho \mathbf{v} \mathbf{v})^{n-1} \right) + \mathbf{S}^{n+\frac{1}{2}} \mathbf{F}^{n+\frac{1}{2}}, \end{aligned} \quad (3.137)$$

$$\nabla \cdot \tilde{\mathbf{v}}^{n+1} = 0. \quad (3.138)$$

4. If $m_e = 0$, set $\mathbf{v}^{n+1} = \tilde{\mathbf{v}}^{n+1}$ and skip to step 9.

5. Evaluate the slip correction

$$\delta \mathbf{u}^{n+\frac{1}{2}} = (\mathbf{J}^{n+\frac{1}{2}} - \mathbf{J}^n) \mathbf{v}^n + \frac{\nu \Delta t}{2} \mathbf{J}^{n-\frac{1}{2}} \mathbf{L} \Delta \mathbf{v}^{n-\frac{1}{2}}, \quad (3.139)$$

and the particle impulse

$$\Delta \mathbf{p} = m_e \left(\mathbf{u}^n - \mathbf{J}^{n+\frac{1}{2}} \tilde{\mathbf{v}}^{n+1} - \delta \mathbf{u}^{n+\frac{1}{2}} \right). \quad (3.140)$$

6. Calculate the fluid velocity perturbation due to the excess mass

$$\Delta\tilde{\mathbf{v}} = \frac{\tilde{m}_f}{\rho(\tilde{m}_f + m_e)} \mathcal{P}S\Delta\mathbf{p}, \quad (3.141)$$

where the fluid dragged mass is $\tilde{m}_f = dV\rho/(d-1)$.

7. Account for the viscous dissipation in the velocity correction

$$\left(\rho\mathbf{I} - \frac{\Delta t}{2}\eta\nabla^2\Delta\mathbf{v}^{n+\frac{1}{2}} \right) + \Delta t\nabla\pi^{n+\frac{1}{2}} = \mathbf{S}(\Delta\mathbf{p} - m_e\mathbf{J}\Delta\tilde{\mathbf{v}}), \quad (3.142)$$

$$\nabla \cdot \Delta\mathbf{v}^{n+\frac{1}{2}} = 0. \quad (3.143)$$

8. Update the fluid velocity

$$\mathbf{v}^{n+1} = \tilde{\mathbf{v}}^{n+1} + \Delta\mathbf{v}^{n+\frac{1}{2}}. \quad (3.144)$$

9. Update the particle velocity

$$\mathbf{u}^{n+1} = \mathbf{J}(\tilde{\mathbf{v}}^{n+1} + \Delta\tilde{\mathbf{v}}) + \delta\mathbf{u}^{n+\frac{1}{2}}. \quad (3.145)$$

10. Update the particle position

$$\mathbf{q}^{n+1} = \mathbf{q}^n + \frac{\Delta t}{2}\mathbf{J}^{n+\frac{1}{2}}(\mathbf{v}^n + \mathbf{v}^{n+1}). \quad (3.146)$$

3.6 Validation

Here we validate our schemes in different regimes. The accuracy and stability of the fluid solvers are inherited by the particle-fluid schemes, therefore as in Section 2.4 of Chapter 2 we will make use of the CFL numbers

$$\begin{aligned} \alpha &= \frac{V\Delta t}{h}, \\ \beta &= \frac{\nu\Delta t}{h^2}, \end{aligned}$$

where V represent the speed of sound c in the compressible case and $\|\mathbf{v}\|_\infty$ in the incompressible one. We refer the reader to Section 2.4 for the different stability limits.

As we have explained through the chapter we intend that our model recovers as many features of a hard sphere as possible but always using a cheap description. As the schemes do not resolve the fluid at scales smaller than the particle it is impossible that our particle behaves exactly as a hard colloid with a well defined surface. It is rather a soft blob that perturbs the fluid in the kernel domain (with extension $3h$) and presents different radius for different hydrodynamic interactions; yet always with $R \approx h$.

In Section 3.6.1 we present some results for steady flows. These results depend mainly on the spatial discretization and in the limit $\Delta t \rightarrow 0$, $Mach \rightarrow 0$, both the compressible and incompressible schemes give the same result. In Section 3.6.2 we use deterministic tests to assert the convergence order of our schemes and in Section 3.6.3 results for hydrodynamic interactions beyond the Stokes drag are presented. Thermal fluctuation are included in the remaining sections. In Section 3.6.4 the particles equilibrium distribution are evaluated to show that the ICM obeys the FDB. Finally in section 3.6.5 and 3.6.6 we study the particle velocity autocorrelation function (VACF) and the particle diffusion.

To help the reader Table 3.1 shows the most important variables and parameters that describe our particle or blob, some of them have already appeared and the rest will be discussed in the remaining of the chapter.

Particle position	$\mathbf{q}(t)$
Particle velocity	$\mathbf{u}(t)$
Particle volume	$\mathcal{V} = 8h^3$ (in 3D)
Particle excess mass	m_e
Displaced fluid mass	$m_f = \mathcal{V}\mathbf{J}\rho$
Particle mass	$m = m_e + m_f$
Hydrodynamic radius	$R_H = 0.91h$ (in an infinite system)

Table 3.1: Variables and parameters of the blob model.

3.6.1 Steady flows and hydrodynamic radius R_H

As we pointed early in Section 3.3 the blob has a size linked to the meshwidth h and given by the kernel properties. For example, we saw that the Faxén radius was given by the second moment of the kernel function

$$a_F = \sqrt{3\mathbf{J}(\mathbf{r} - \mathbf{q})^2} \approx 0.945h,$$

with deviations of 5% over the mesh. The particle volume, $\mathcal{V} = 8h^3$, was another measure of the particle finite size. Note that the particle volume gives a different particle radius $(3\mathcal{V}/4\pi)^{1/3} \approx 1.24h$. In this section we want to determine the hydrodynamic radius R_H defined as the ratio between a drag force F_d and the resulting particle terminal velocity u . At small Reynolds numbers $R_H = F_d/(6\pi\eta u)$, where the factor 6π correspond to a particle with a stick surface and it will be 4π for a slip surface.

We start by looking at the flow profile around a particle in a steady flow at $Re \approx 0$. A particle with zero velocity is fixed in a periodic box of size L while a small density force is apply to the fluid. Once the system reaches the steady state we compare the flow profile from our simulation with that of a rigid sphere under a Stokes flow [Landau 1987]. At the top of figure 3.2 we show the radial velocity of the fluid v_r along $\theta = 0$ (the incoming direction of the flow) and $\theta = \pi/4$ versus the distance to the center of the particle. We compare the outcome of our inertial coupling method (ICM) with that obtained by a frictional coupling based on the Stokes drag ($\lambda = -\zeta_0(\mathbf{u} - \mathbf{J}\mathbf{v})$ [Dünweg 2009]).

At short distances the velocity profiles are quite different, in particular the weaker Stokes coupling fails to recover the no-slip condition on any particle site.

As the distance increases both methods converge to the same solution, corresponding to the far field created by a hard sphere. The same figure shows the theoretical prediction for a sphere of radius R_H chosen to mach the numerical results for the radial velocity along $\theta = 0$. Surprisingly, neither the ICM nor the Stokes coupling converge to the theoretical result for $\theta = \pi/4$ even at large distances. The reason is the slow decay of the hydrodynamic interaction ($1/r$) which makes the particle to interact with its periodic images. In fact, the theoretical result corresponds to the $L \rightarrow \infty$ limit.

To avoid the uncontrolled effect of the periodic images we perform a simulation with the particle fixed at the center of a spherical shell of radius $R_{\text{shell}} \gg R_H$, where a fluid velocity \mathbf{v}_0 is imposed. The second and third plots of figure 3.2 show the radial and polar velocities of the flow in this configuration together with the analytical solution [Usabiaga 2013b]. Analytical and numerical results converge at large distances if a radius $R_H \approx 0.9h$ is used in the analytical solution. This gives us the first estimation of the hydrodynamic radius for our blob under the Stokes flow. At distances shorter than about $2R_H$ the numerical solutions start to deviate from the analytical result, and in particular the no-slip is only obeyed at the center of the particle (a singular point) and not at any finite surface. We could have expected a result like this since the no-slip condition was imposed only in an average sense. Nevertheless the no-slip constraint imposed by the ICM permits to correctly reproduce the near field flow (up to $r > 2R_H$).

Moreover, it shall be shown that the no-slip condition is crucial to recover the correct dynamics under fast forces, either acoustic or drags at high Re .

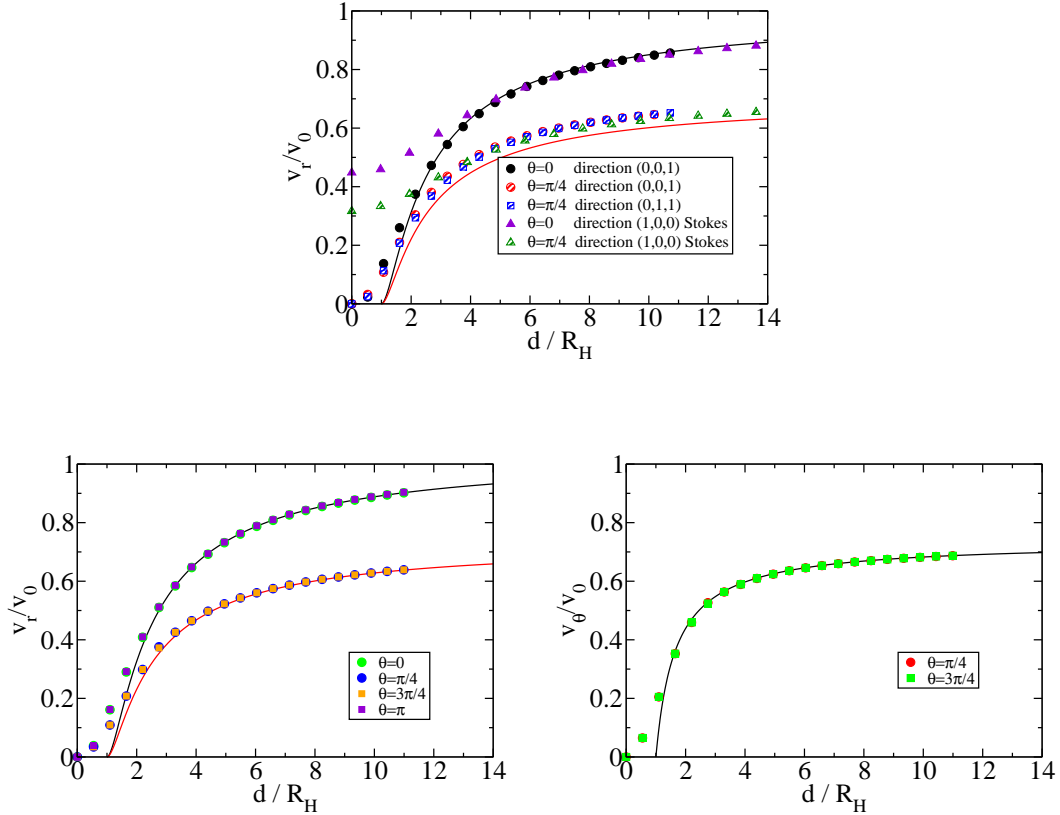


Figure 3.2: Top panel, fluid radial velocity around a particle in a cubic simulation box with periodic boundary conditions for the ICM (circles and squares) and the Stokes coupling (triangles) together the theoretical result for a hard sphere in an infinite system (lines). Results are presented for several flows with different income directions (as indicated by the legend) to test the discretization anisotropy, however, not appreciable difference is observed between the flows. Middle and bottom panels, fluid radial and tangential velocity around a particle enclosed by a shell of radius $R_{\text{shell}} \gg R$ for the ICM (dots) and theory (lines). The good agreement reflects the ability of the ICM to reproduce the near field around a sphere (at least for $r > 2R_H$).

A better method to measure the hydrodynamic radius than to fit velocity profiles is to pull the particle with a constant force \mathbf{F}_d and to measure the terminal velocity \mathbf{u} to get the hydrodynamic radius R_H defined by the Stokes drag force $\mathbf{F}_d = 6\pi\eta R_H \mathbf{u}$. In these tests it is necessary to spread a constant force $-\mathbf{F}_d$ to the fluid in order to conserve the linear momentum of the system. The hydrodynamic radius R_H depends on the spatial discretization as well as on the system size L , as we have seen above. To extract the value of R_H free of the interference of periodic images we use the result of Hasimoto for the drag of an infinite array of falling spheres

$$\frac{R_H(\infty)}{R_H(L)} = \frac{\mathbf{u}(L)}{\mathbf{u}(\infty)} = 1 - 2.84 \frac{R_H}{L} + 4.1887 \left(\frac{R_H}{L} \right)^3 - 27.359 \left(\frac{R_H}{L} \right)^6 + \dots \quad (3.147)$$

where $\mathbf{u}(\infty)$ represent the terminal velocity of a single sphere in an infinite system pulled by a force \mathbf{F}_d

while $\mathbf{u}(L)$ is the terminal velocity of a sphere in a periodic cubic box of size L .

This measure gives a value of $R_H(\infty) = 0.91h$ which in the following we will just call hydrodynamic radius R_H . Using only the two first term in the Hasimoto's formula it is possible to determine the effective hydrodynamic radius for cubic boxes of size L

$$R_H(L) = \frac{R_H}{1 - 2.84 \left(\frac{R_H}{L} \right)}, \quad (3.148)$$

while for noncubic boxes it is possible to use the Ewald summation of the Rotne-Prager force to calculate the tensor \mathbf{R}_H in a periodic box with sides L_x , L_y and L_z [Beenakker 1986].

At the top of figure 3.3 we compare the numerical values of the hydrodynamic radius for cubic boxes of several sizes with equation (3.148) and with the result of summing the hydrodynamic interaction (in a Rotne-Prager approximation) over all the periodic images [Beenakker 1986]. For large enough boxes all the results converge to the same value which means that the ICM correctly capture the far flow around a sphere. For small systems $L < 16R_H$ our numerical results deviate from the predictions of the Rotne-Prager tensor, which in turn are just an approximation for the flow around a sphere. It is also important to note that the equation (3.148) is a very good approximation for systems with size above $L > 10R_H$, and we will make extensive use of it to calculate the effective hydrodynamic radius in the following simulations.

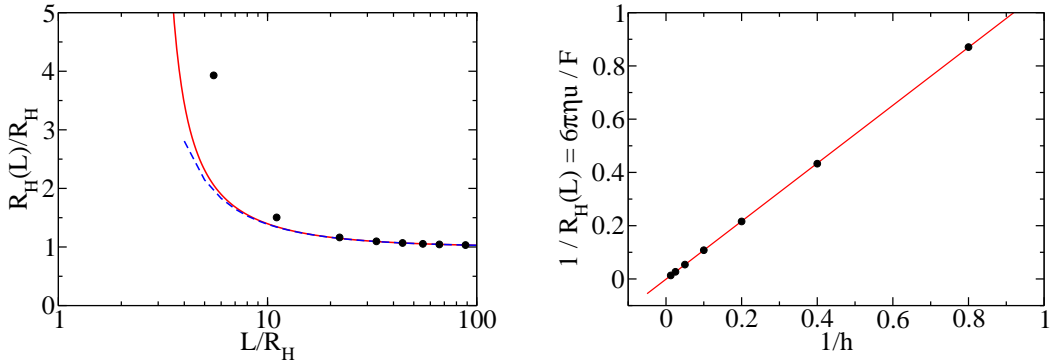


Figure 3.3: Left panel, hydrodynamic radius $R_H(L)$ versus system size L for the ICM (dots), equation (3.148) (continuous line) and the essentially exact result in a Rotne-Prager approximation from the Ewald sum [Beenakker 1986] (dashed line). Right panel, inverse of the effective hydrodynamic radius $R_H(L)$ versus the inverse cell size $1/h$ in a cubic system with $N = 64$ fluid cells per side. The offset is zero which proves that the effective coupling constant is infinity or better $1/\zeta_0 = 0$.

Before we finish this subsection there are two additional results concerning the hydrodynamic radius we should discuss. It is well known that when using the Stokes coupling in the form

$$\boldsymbol{\lambda} = -\zeta_0(\mathbf{u} - \mathbf{J}\mathbf{v}),$$

the particle shows an effective hydrodynamic radius

$$\frac{1}{R_H} = \frac{1}{a_0} + \left(\frac{1}{g} - \frac{2.84}{N} \right) \frac{1}{h},$$

where the input radius is $a_0 = \zeta_0/6\pi\eta$, g is a parameter that depends on the spatial discretization and the last term is just the contribution from the periodic images in a cubic system with $N = L/h$ cells along each direction (see [Giupponi 2007] or the review [Dünweg 2009]). One of our claims about the ICM is that the coupling is *instantaneous*, or in other words, the ICM correspond to the limit $\zeta_0 \rightarrow \infty$ [Atzberger 2011]. Representing the inverse of the hydrodynamic radius vs the cell size, for a constant number of cells N , we can measure our effective ζ_0 or better $1/\zeta_0$. In the second plot of figure 3.3 we see that in fact the ICM provides $1/\zeta_0 = 0$. This is the first numerical prove of the *instantaneous* nature of our coupling.

As final test for this section we study the dependence of the hydrodynamic radius with the particle position on the grid. In the continuum setting translational invariance ensures that the hydrodynamic radius is independent of the particle position, but after the discretization this is not longer true. In the Stokes limit the flow created by a blob pulled by a constant force \mathbf{F} is

$$\mathbf{v}(\mathbf{r}) = \int \mathbf{G}(\mathbf{r}, \mathbf{r}') \mathbf{S} \mathbf{F} d^3 r' = \int \mathbf{G}(\mathbf{r}, \mathbf{r}') \mathbf{F} \delta_h(\mathbf{q} - \mathbf{r}') d^3 r', \quad (3.149)$$

where \mathbf{G} is the Green's function for the Stokes equation $\nabla \pi = \eta \nabla^2 \mathbf{v} + \mathbf{S} \mathbf{F}$ subject to $\nabla \cdot \mathbf{v} = 0$. For example, for an unbounded system \mathbf{G} is the well known Oseen tensor $\mathbf{G}(\mathbf{r}', \mathbf{r}'') = (8\pi r)^{-1} (\mathbf{I} - \mathbf{r}\mathbf{r}^T/r^2)$ where $\mathbf{r} = \mathbf{r}' - \mathbf{r}''$ [Larson 1998]. To write the flow profile we can use also the compact notation

$$\mathbf{v}(\mathbf{r}) = \mathcal{L}^{-1} \mathbf{S} \mathbf{F}, \quad (3.150)$$

where \mathcal{L}^{-1} is the shorthand notation for the Stokes solution operator. The velocity of the blob is given by the averaging of the fluid velocity at the particle site $\mathbf{u} = \mathbf{J} \mathbf{v}$ but in the Stokes limit is also given by the mobility operator $\boldsymbol{\mu}$ by $\mathbf{u} = \boldsymbol{\mu} \mathbf{F}$. These relations define the mobility tensor

$$\boldsymbol{\mu} = \int \delta_h(\mathbf{q} - \mathbf{r}) \mathbf{G}(\mathbf{r}, \mathbf{r}') \delta_h(\mathbf{q} - \mathbf{r}') d^3 r' d^3 r, \quad (3.151)$$

or in shorthand notation

$$\boldsymbol{\mu} = \mathbf{J} \mathcal{L}^{-1} \mathbf{S}.$$

The Peskin's kernel $\delta_h(\mathbf{r})$ was designed to ensure $\mathbf{J} \mathbf{S} = \text{const.}$ but it does not consider the fluid solver at all. Because of this, the mobility $\boldsymbol{\mu} = \mathbf{J} \mathcal{L}^{-1} \mathbf{S}$ is not constant and depends on the particle position relative to the grid. At least, due to the symmetries of the system, $\boldsymbol{\mu}$ is a diagonal matrix just as in the continuum setting. The hydrodynamic radius of a sphere is related to the mobility matrix by

$$\boldsymbol{\mu} = \frac{1}{6\pi\eta R_H} \mathbf{I}, \quad (3.152)$$

therefore the small violations of the translational invariance by $\boldsymbol{\mu}$ are equivalent to a small variations of the hydrodynamic radius R_H . We study the variations of the hydrodynamic radius R_H in Fig. (3.4). As the particle moves along the grid its radius presents some deviations that however are always below 2.5% from the mean, which we consider to be an acceptable error. As we will see over and over the Peskin's kernel function presents in most situations a extremely good behaviour in hiding the effects of the grid discretization to the particle dynamics.

3.6.2 Deterministic convergence

In this section the temporal accuracy of the schemes is studied. The compressible and incompressible schemes are usually employed in different regimes or for different time scales, for this reason we perform

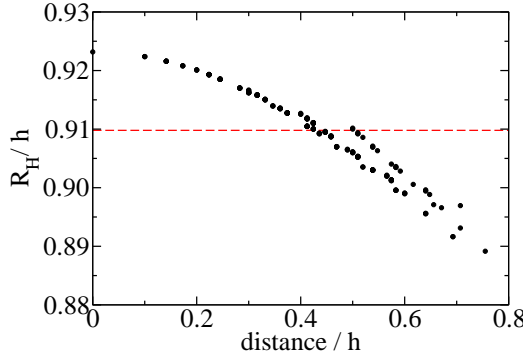


Figure 3.4: Hydrodynamic radius R_H for a particle moving along the x -direction versus $l = |\mathbf{q} - (\mathbf{r}_i + h\hat{x}/2)|$, the distance between the particle and the closest node of the grid where the x -component of the velocity is defined. The deviations from the mean value $R_H = 0.91$ are always smaller than a 2.5%. By using a kernel with a wider support, for example the four points kernel of Peskin [Peskin 2002], the variations can be further reduced.

separate tests to prove the accuracy of each of the schemes. In the compressible case we present the convergence against the sonic CFL number $\alpha_c = c\Delta t/h$ while for the incompressible tests we use the viscous CFL number $\beta = \nu\Delta t/h^2$.

In both cases we look at the error in the particle position $\mathbf{q}(t)$ defined as the difference in the position between time steps Δt and $\Delta t/2$ over a period $T = N_s\Delta t$,

$$E(\Delta t) = \frac{1}{hN_s} \sum_{n=1}^{N_s} \left\| \mathbf{q}_{\Delta t}(n\Delta t) - \mathbf{q}_{\Delta t/2} \left(2n \frac{\Delta t}{2} \right) \right\|. \quad (3.153)$$

This error should decrease as $E(\Delta t) = \mathcal{O}(\Delta t^p)$ for a numerical method of order p .

To test the compressible scheme presented in Sec. 3.5.2 we pull a particle (initially at rest) with a constant force \mathbf{F} , for $t > 0$. To conserve linear momentum in the system the same force with opposite sign is uniformly spread to the flow. In figure 3.5 we show the convergence results for a neutrally buoyant particle as well as for a particle with excess mass $m_e = m_f$. The neutrally buoyant results show the expected second order convergence, while for the non-neutrally buoyant particle the scheme is only first order. However, we note that the scheme presents a good accuracy for a wide range of acoustic CFL numbers and it is also much more accurate than the first order scheme presented in Sec. 3.5.1.

For the incompressible solver tests we choose a fluid parameters such that $\Delta t = \beta$ and $\alpha = \text{Re}\beta$. For small Reynolds numbers (Re) we are interested in regimes close to $\beta = 1$ while for high Reynolds number we are limited by the stability condition $\alpha < 1$. In these tests the particle performs damped oscillations under the influence of an harmonic spring. In Figure 3.6 we show the particle position for a case with an excess mass $m_e = m_f$ and Reynolds number $\text{Re} = u_{\max}h/\nu \approx 0.02$, where u_{\max} is the maximum particle speed during the simulation. We see no visible difference for quite different time steps. It is remarkable that for quite large time steps ($\beta = 8$), the particle recovers the correct dynamics even if the high wavenumber fluid modes are underresolved.

In the left plot of Figure 3.7 we show the convergence of the error for this configuration ($\text{Re} \approx 0.02$). Neutrally buoyant particles clearly show second order convergence, as expected. Particles with excess mass $m_e = m_f$ show second order convergence for moderate and large time steps while for the smaller

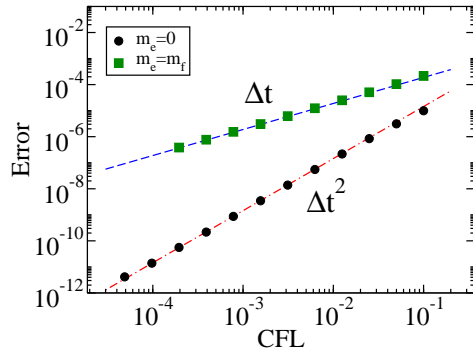


Figure 3.5: Error in particle position defined in Eq. (3.153) versus the CFL number $\alpha = c_T \Delta t / h$, where c_T is the fluid speed of sound. Results correspond to the neutrally buoyant particles (excess mass $m_e = 0$) and particles twice as heavy as the fluid $m = 2m_f$ (i.e. $m_e = m_f$). By the definition of the Error Eq. 3.153 and the particle radius $R_H \sim h$ we can see that the error in the position is very small compared with the particle dimensions even for the largest time steps. In these simulations the viscous CFL number is $\beta = \alpha$, therefore the compressible scheme is accurate even close to its stability limit $\beta = (1/2)^3$.

time steps considered the convergence reduces to first order. We believe this is due to the approximation of considering JPS as translational invariant: with our discretization this is accurate up to a few percent (see Fig. 3.1). For a very large excess mass $m_e = 10m_f$, the scheme shows first order convergence for a wider range of time steps.

In the right panel of Figure 3.7 we study the scheme behavior when the inertia effects are more important, large excesses of mass $m_e = 10m_f$ and moderate Reynolds number $Re \approx 2$ and $Re \approx 20$. Also, we study the following alternatives to the no-slip correction $\delta\mathbf{u}^{n+\frac{1}{2}}$ derived in Section 3.5.3 [Eq. (3.139)]

$$\delta\mathbf{u}^{n+\frac{1}{2}} = 0, \quad (3.154)$$

$$\delta\mathbf{u}^{n+\frac{1}{2}} = \frac{\nu \Delta t}{2} \mathbf{J}^{n-\frac{1}{2}} \mathbf{L} \Delta \mathbf{v}^{n-\frac{1}{2}}, \quad (3.155)$$

$$\delta\mathbf{u}^{n+\frac{1}{2}} = (\mathbf{J}^{n+\frac{1}{2}} - \mathbf{J}^n) \mathbf{v}^n + \frac{\nu \Delta t}{2} \mathbf{J}^{n-\frac{1}{2}} \mathbf{L} \Delta \mathbf{v}^{n-\frac{1}{2}}. \quad (3.156)$$

The first option, Eq. (3.154), is the least expensive but the other two including the viscous and the viscous and centering correction may be more accurate. Note that the third option, Eq. (3.156), was the slip correction derived in Section 3.5.3.

To achieve higher Reynolds number we employ stronger spring constants ($k = 1$ and $k = 500$) while keeping the rest of the parameter like in Figure 3.6. For $Re = 2$ the three options show similar results, only for very large time steps the $\delta\mathbf{u}^{n+\frac{1}{2}} = 0$ choice is worst than the others. However, for the highest Reynolds $Re = 20$, the third correction Eq. (3.156) [or Eq. (3.139)] gives better convergence. In the rest of the chapter we will use Eq. (3.156) if the Reynolds is high while if the Reynolds number is small we will use sometimes the other (less expensive) options.

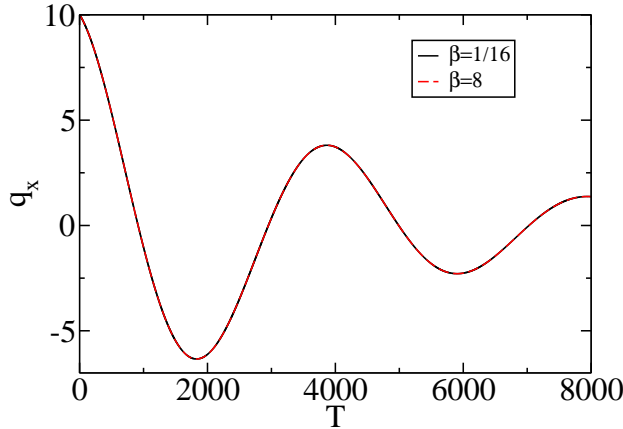


Figure 3.6: Particle damped oscillations in an harmonic potential for two very different time steps ($\beta = \Delta t$) at a low Reynolds number $\text{Re} \approx 0.02$. In these simulations the meshwidth is $h = 1$, the viscosity $\eta = 1$, the fluid density $\rho = 1$ and the spring constant $k = 0.01$.

3.6.3 Hydrodynamic forces

In this section the ability of the blob model to recover different kinds of hydrodynamic forces is further studied. We start by looking at the hydrodynamic force between two particles approaching along the line of collision. To do this we apply a force \mathbf{F}_0 on one particle and $-\mathbf{F}_0$ on the other. While the particles approach at slow velocity ($\text{Re} < 10^{-3}$) we measure the hydrodynamic forces through their relative speed u_r and normalize the result with the Stokes force for a isolated particle,

$$\frac{F}{F_{\text{Stokes}}} = -\frac{2F_0}{6\pi\eta R_H u_r}. \quad (3.157)$$

In the left panel of figure 3.8 we compare the results obtained with the incompressible solver for several time steps and excesses mass with the theoretical result for two particles in an periodic system interacting through the Rotne-Prager tensor [Beenakker 1986]. We can see that the Rotne-Prager mobility correctly describes the mutual hydrodynamic friction for distances $d > 3R_H$. It is well known that when two rigid bodies approach to very small distances the incompressible fluid between them has to be squeezed which gives rise to the lubrication forces. For two rigid spheres of radius R this force can be modeled by the expression [Nguyen 2002, Dünweg 2009]

$$\mathbf{F}_{\text{lubrication}} = \frac{3}{2}\pi\eta R^2 \left(\frac{1}{d-2R} - \frac{1}{d_{\text{cutoff}}} \right) \mathbf{u}_r \cdot \hat{\mathbf{q}}_r, \quad (3.158)$$

where d_{cutoff} is a free parameter of the model that measures the interaction range. The key property of the lubrication force is its divergence at the contact distance $d = 2R$. The hydrodynamic force between blobs does not diverge at any finite distance because they do not have a well define surface, however, increases monotonically as the distance is decreased because of the no-slip constraint and to some extend the lubrication force due to the squeezed fluid is recovered.

As second test in this section we present results for the drag force at high Reynolds number, defined here as $\text{Re} = 2R_H u / \nu$. We pull a particle with a constant force \mathbf{F}_0 and estimate the drag from its average velocity $\langle \mathbf{u} \rangle$ at long times. As in Section 3.6.1 we ensure conservation of mometum by

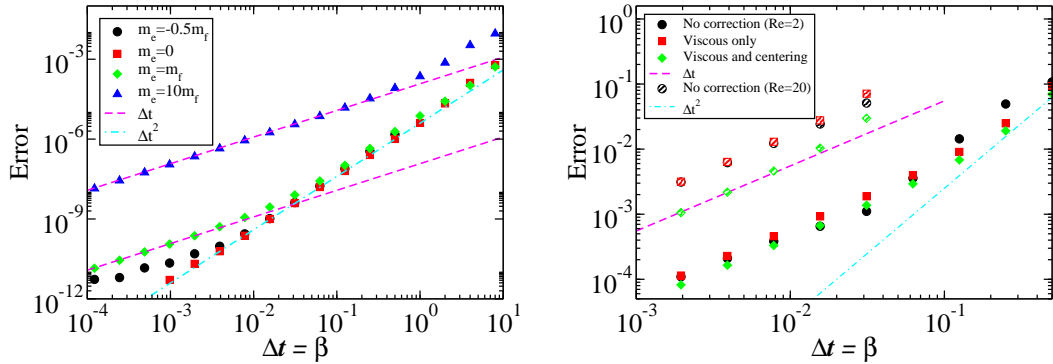


Figure 3.7: Convergence rate for the incompressible scheme for small Reynolds number (left panel) and moderate Reynolds number $Re = 2$ and $Re = 20$ (right panel). Even when the scheme shows first order accuracy the error in the particle position is rather small. Note that the error in the right panel is always $E \lesssim 0.1$ even for the largest time step for which the advective CFL number is practically in the stability limit ($\alpha = Re\beta \approx 1$).

uniformly spreading a force $-F_0$ to the fluid. Since we have not implemented open boundaries in the code [Poinsot 1992, Delgado-Buscalioni 2008b], we use long simulation boxes to allow that the wake created by the particle relaxes before it crosses the simulation box. A particle advected by a velocity $\langle u \rangle$ interacts with its periodic image after a time $\tau \sim L/\langle u \rangle$, while the wake created by the particle requires times larger than $\tau_\nu = R_H^2/\nu$ to relax. Therefore to correctly model the drag of a isolate particle we need to use simulation boxes for which $\tau/\tau_\nu > 1$ or equivalently $L/R_H > Re$.

In the right panel of figure 3.8 we compare the results from the compressible and incompressible solver with the commonly used fit to experiments for hard spheres [Clift 1978], valid for $Re < 800$. The incompressible ICM method provides remarkably good results for all the Reynolds number considered $0 < Re < 350$. The compressible scheme presents similar results up to $Re \approx 30$. As the Reynolds number increases it is necessary to increase the speed of sound to remain in the low Mach number limit and this fact makes larger Re simulations prohibitively expensive for the explicit compressible solver. If one wants to keep the Mach and sonic CFL numbers constant the time step have to be reduced accordingly to

$$\Delta t = \frac{2R_H h}{\nu} \frac{\text{Ma}}{Re} \alpha_c,$$

while the characteristic time $\tau_\nu = R_H^2/\nu$ does not change. However, we do not expect any fundamental problem provided the necessary computational power.

In the figure 3.9 we show some snapshots for the vorticity field around the particle. The evolution of the vorticity field with the Reynolds number is similar to the case of a rigid sphere. For $Re \approx 0$ (not show) the flow is symmetric respect to the particle trajectory and tends to the Stokes flow, a result consistent to those of Section 3.6.1 and figure 3.2. For moderate Reynolds number $Re \approx 1.5$ (first panel of Fig. 3.9) the symmetry of the flow is broken and its form resembles the contour lines of the Oseen flow [Lomholt 2001], although we have not made a detail comparison. As the Reynolds grows the wake created by the particles becomes more elongated and aligned with the particle direction of motion. Up to the Reynolds number considered $Re \approx 350$ (see bottom panel of Fig. 3.9 for $Re \approx 140$) the wake remains stable and it does not present vortex shedding. For a rigid sphere, a transition to vortex shedding

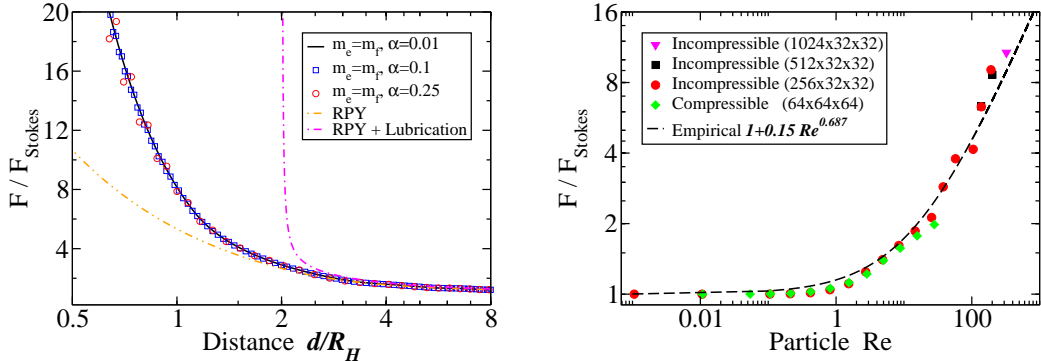


Figure 3.8: Left panel, hydrodynamic force between two particles approaching along the line of collision versus the interparticle distance. The numerical results are independent of the excess mass m_e as predicted by the theory and they only show a weak dependence with the time step. Together the numerical results we show the Rotne-Prager prediction (RPY) and the Rotne-Prager plus lubrication [Eq. (3.158)] result. Right panel, drag force versus Reynolds number, the dimensions of the simulation box are given in the figure legend in units of the meshwidth $h \approx R_H$.

is experimentally observed around $\text{Re} \approx 270$. For the Reynolds number considered we only observe such a transition if the blob is subject to an additional perturbation. For example, in the second panel of Fig. 3.9 we show the vortex shedding of a blob interacting with its periodic images.

Results like these are impossible to reproduce with a Stokes coupling which creates a weaker perturbative flow with substantial velocity slip (see Fig. 3.2). By using instead the no-slip condition we recover the correct drag for a wide number of Reynolds numbers. This is certainly a useful property to study particulate flows in turbulence [Balachandar 2010].

3.6.4 Equilibrium distribution

We now consider the effects of thermal fluctuations on the particle distribution function, showing that the system is indeed at thermal equilibrium. Because the Hamiltonian is separable in the particle variables \mathbf{q} and \mathbf{u} it is possible to consider their distribution functions separately. For a collection of N particles interacting through a conservative potential $U(\mathbf{Q}) = U(\{\mathbf{q}_1, \mathbf{q}_2, \dots, \mathbf{q}_N\})$ the configurational part of the particles distribution function should be

$$P(\mathbf{Q}) \sim \exp\left(-\frac{U(\mathbf{Q})}{k_B T}\right). \quad (3.159)$$

A simple method to verify that the schemes reproduce the correct distribution $P(\mathbf{Q})$ is to compute the radial distribution function $g(r)$ and compare the results with a well established method, for example Monte Carlo. In the figure 3.10 we present the results for the radial distribution function of $N = 1000$ particles (volume fraction $\phi = 0.128$) interacting through a purely repulsive Lennard-Jones (WCA) potential

$$U(\mathbf{r}) = \begin{cases} 4\varepsilon \left(\left(\frac{\sigma}{r}\right)^{12} - \left(\frac{\sigma}{r}\right)^6 \right) + \varepsilon & \text{if } r < 2^{1/6}\sigma, \\ 0 & \text{if } r > 2^{1/6}\sigma. \end{cases} \quad (3.160)$$

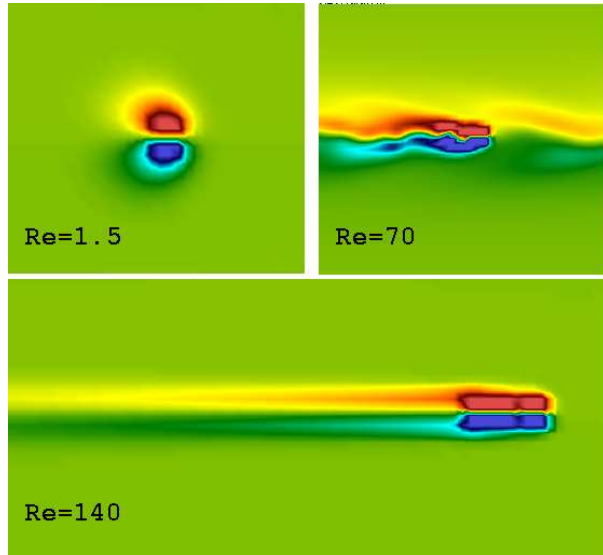


Figure 3.9: Vorticity plots at the particle plane. Colours red and blue represent positive and negative vorticity values respectively. The scale of colors is different in each snapshot to make visible the variations of the vorticity field.

We can see that there is a perfect agreement between the Monte Carlo and the ICM results for either heavy or neutrally buoyant particles. This is consistent with the general result stating that the hydrodynamics can not affect structural properties at equilibrium. It is interesting to point out that the incompressible scheme gives the correctly particles distribution even for a large time step $\beta = 1$, implying that not all the fluid modes are resolved. Results for the compressible scheme (not shown) are equivalent, but the simulations are much more expensive due to the stability limits on the time step.

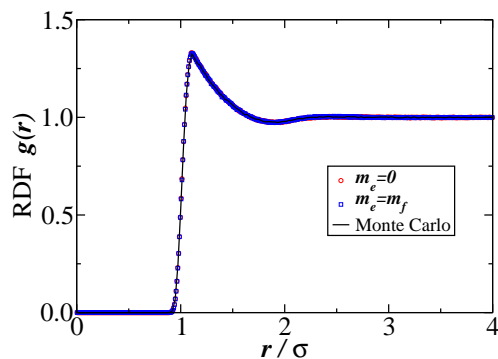


Figure 3.10: Radial distribution function $g(r)$ for $N = 1000$ particles interacting with a purely repulsive potential [Eq. (3.160)] in a simulation box with $m_x = 32$ fluid cells per side. The viscous CFL number used in these simulation is $\beta = 1$.

The other part of the particle distribution function is the velocity distribution. For particles in a

compressible fluid, statistical mechanics predicts

$$P(u_x) \sim \exp\left(-\frac{mu_x^2}{2k_B T}\right), \quad (3.161)$$

with similar results for the y and z components. In the left panel of figure 3.11 we compare the numerical results with the theoretical prediction to find a perfect agreement. For compressible fluids the results are independent of the fluid compressibility (speed of sound) and the only dependence on the particle mass m is the one collected by Eq. (3.161), where $m = m_e + m_f$ is the total particle mass.

The results for the incompressible fluid deserves a more detailed explanation. The right panel of figure 3.11 presents results for the incompressible scheme with particles with different excesses of mass. In these cases, the velocity distribution does not follow a Gaussian distribution with variance $k_B T/m$ but rather a Gaussian distribution with variance $k_B T/\tilde{m} = k_B T/(m + m_f/2)$ (in 3D). This difference can be interpreted in several ways. First, the incompressibility constraint eliminates the longitudinal velocity (sound) modes, and such reduction on the velocity degrees of freedom is translated to the particle fluctuations, since $\mathbf{u} = \mathbf{Jv}$. A second interpretation of this effect, complete equivalent to the previous one, is that due to the added mass effect the particle inertia is $\tilde{m} = m + m_f/2$ and this inertia is reflected in the velocity distribution [Zwanzig 1975, Hinch 1975]. Those ideas can be developed more formally. From the equation (3.68) or from the Hamiltonian (3.57) (quadratic in \mathbf{v}) it can be shown that the fluid velocity field has covariance $\langle \mathbf{v} \mathbf{v}^* \rangle = k_B T \rho_{\text{eff}}^{-1}$, with the effective density defined by the Eq. (3.69). Therefore the particle velocity covariance in a d -dimensional space is

$$\begin{aligned} \langle u^2 \rangle &= \text{Tr} [\mathbf{J} \langle \mathbf{v} \mathbf{v}^* \rangle \mathbf{S}] = k_B T \text{Tr} [\mathbf{J} \rho_{\text{eff}}^{-1} \mathbf{S}] \\ &= \frac{k_B T}{\rho} \text{Tr} \left[\mathbf{J} \left(\mathbf{I} - \frac{m_e \mathcal{V}}{\tilde{m}} \mathcal{P} \mathbf{S} \mathbf{J} \mathcal{P} \right) \mathbf{S} \right] \\ &= d \frac{k_B T}{\tilde{m}}, \end{aligned} \quad (3.162)$$

a result consistent with our above arguments. It is very important to note that, however, the particles spatial distribution is always the same for both compressible and incompressible schemes.

The inset of Fig. 3.11 shows the error in the variance of the particle velocity as function of the viscous CFL number β for the case $m_e = m_f$. To obtain an accurate result it is necessary to use a small time step able to solve the dynamic of every fluid mode. Nonetheless, we repeat that the structural distribution is recovered even for time steps as large as $\beta = 1$, this is directly related to the fact that the particle diffusion is much slower than the momentum diffusion and that $P(\mathbf{Q})$ is determined by the particle diffusion.

3.6.5 Velocity autocorrelation function

The velocity distribution function is just a static property, to validate the dynamic accuracy of our schemes we devote this section to study the velocity autocorrelation function (VACF) for a particle immersed in a compressible or incompressible fluid. The VACF is defined by

$$C(t) = \langle u_x(t) u_x(0) \rangle = \frac{1}{d} \langle \mathbf{u}(t) \cdot \mathbf{u}(0) \rangle. \quad (3.163)$$

The left panel of figure 3.12 presents results for the VACF of a particle immersed in fluids with different compressibilities (different speeds of sound c_T) including the limit $c_T \rightarrow \infty$ which we calculate with the incompressible solver. The VACF has several regimes in which different transport of momentum mechanisms determine its decay. At very short times ($t \rightarrow 0^+$) the VACF tends to the value determined

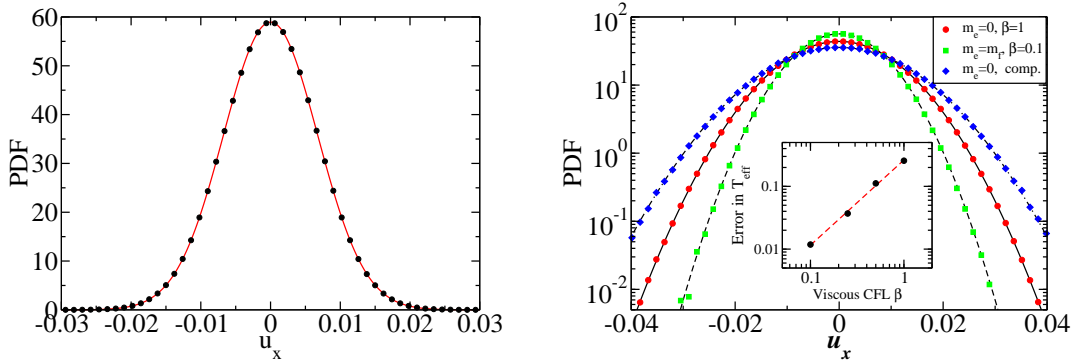


Figure 3.11: Left panel, velocity probability distribution function (PDF) for particles immersed in a compressible fluid. The line correspond to the Boltzmann distribution [Eq. (3.161)] with no fitting parameters and the dots to the numerical results for heavy particles ($m = 16m_f$) in a concentrate suspension (volume fraction $\phi = VN/L^3 = 0.5$). Right panel, velocity distribution for particles with different excess mass m_e immersed in a incompressible fluid. To appreciate the added mass effect on the particle velocity PDF we include the curve for a particle immersed in a compressible fluid with otherwise the same conditions. The inset shows the numerical error in the variance of the particle velocity PDF versus the time step. Only when all the fluid modes are resolved the theoretical result is recovered.

by the energy equipartition theorem, $C(0^+) = k_B T/m$ or $C(0^+) = k_B T/\tilde{m}$ in the compressible and incompressible case respectively.

The next regime is governed by the acoustic transport of momentum. For times $t < t_c = 2R_H/c_T$ sound waves carry away part of the particle momentum while the viscosity effects are still negligible [Zwanzig 1975]. As shown in Figure 3.12 the VACF decays to $k_B T/\tilde{m}$ (horizontal line) at times $t \sim t_c$ (vertical lines). Therefore, as the speed of sound increases this decay is faster. In the incompressible limit a fraction of energy is lost at time $t \rightarrow 0$ due to the absence of longitudinal or sonic modes (which effectively propagate infinitely fast). These results are directly related with the reduction of the variance of the velocity distribution discussed for incompressible fluids in Sec. 3.6.4.

Together with the numerical results, the left panel of figure 3.12 shows the VACF decay for a rigid sphere of radius R_H and density $\rho_s = \rho + m_e/V$ [Hinch 1975]. After the sonic time both compressible and incompressible scheme present a similar behavior, with the VACF decaying as $t^{-d/2}$ (in d dimensions) due to the diffusion of momentum via the vortical modes. At long times, numerical results converge to the trend expected for a rigid sphere. At short times a clear difference is observed between our blob and a rigid sphere. Short times are more sensible to the finer spatial resolution of the particle and our model is closer to a soft, permeable particle than to a rigid one. A way to improve this result within the ICM formalism is to ensure higher order constraints on the velocity field and in particular to introduce a stresslet term (see Sec. 3.3).

In the right panel of figure 3.12 we study with more detail the diffusive decay of the VACF at long times, when the particle diffusion coefficient χ is not very large. The Schmidt number $\text{Sc} = \nu/\chi$ measures how much faster the fluid momentum perturbation diffuses compared with the particle. In colloidal systems the Schmidt number is always larger than 10^3 and typically $\text{Sc} \sim 10^6$, however, low Schmidt numbers are interesting for a number of reasons. It is a stringent numerical limit because the fluid does not have time to relax during the particle translations, both process having similar characteristic times.

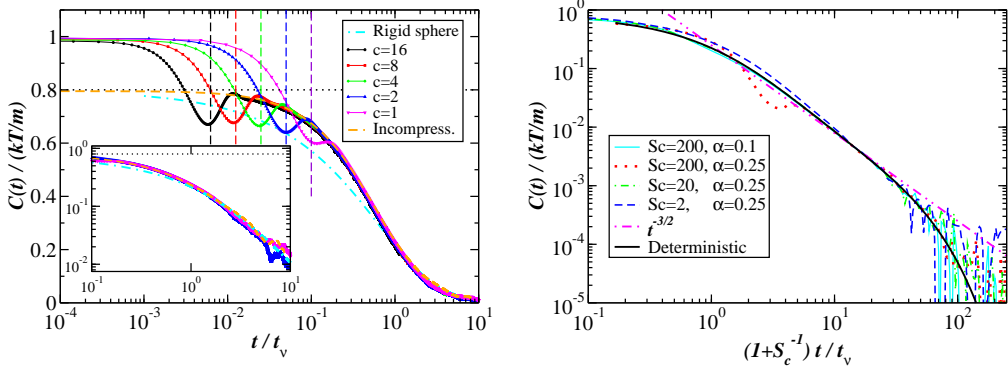


Figure 3.12: Left, VACF for a particle immersed in compressible fluid with different speeds of sound c and also in an incompressible fluid. At short times $C(0^+) = k_B T/m$ for compressible fluids. Around the sonic time, represented by the vertical lines, the VACF has decayed to $C(t_c) = k_B T/\tilde{m}$ represented by the horizontal dot line. After the sound has decayed the VACF presents an algebraic tail due to the diffusion of momentum. Right, VACF for a particle immersed in an incompressible fluid for several Schmidt numbers Sc . All parameters are given in Table 3.2.

It is also an interesting limit for particle-based methods such as DPD/SDPD or SRD which are limited to work at low Schmidt number even when they are trying to model colloids immersed in a liquid. The low Sc limit has also interest in establishing purely hydrodynamic effects on molecular diffusion [Schmidt 2003, Lee 2004]. Therefore we now study the hydrodynamics in the low Schmidt number limit.

Since in our schemes the particle diffusion coefficient χ is an output rather than an input we present our result versus the Stokes-Einstein Schmidt number

$$\text{Sc}^{\text{SE}} = \frac{\nu}{\chi_{\text{SE}}} = \frac{6\pi\rho\nu^2 R_H}{k_B T}, \quad (3.164)$$

which uses the particle diffusion coefficient in the Stokes limit $\chi_{\text{SE}} = k_B T/(6\pi\eta R_H)$. Recall that the hydrodynamic radius should have to take into account the finite size effects [Eq. (3.148)].

To study the behaviour at long times we use the incompressible scheme because it allows to use much larger time steps. For large Schmidt number, the maximum time step that produces accurate results corresponds to $\beta \approx 1$, however, for small Schmidt numbers the stability condition $\alpha < 1$ limits the viscous CFL number. Note that using the thermal velocity $v_{\text{th}} = \sqrt{k_B T/\rho h^3}$ the advective and viscous number are related by $\alpha = \sqrt{6\pi/\text{Sc}^{\text{SE}}}\beta$. To present consistent results we use in most of the simulations $\alpha = 0.25$ which means that in average a particle moves a quarter of cell per time step.

It is commonly assumed that at long times the VACF shows the algebraic decay $(\nu t)^{-d/2}$ [Hinch 1975, Padding 2006] but this does not account for the fact that while the momentum diffuse the particle itself is moving. Taking into account the diffusion of the particle, a self-consistent mode coupling theory predicts a decay of the form $((\chi + \nu)t)^{-d/2}$ [Pomeau 1975]. This suggests that the VACF for different Schmidt number should collapse for long times if they are plotted as function of $(1 + \text{Sc}^{-1})(t/\tau_\nu)$. In the right panel of figure 3.12 we show that is the case for a wide range of Sc .

After the VACF has decayed below 10^{-3} of its initial value strong fluctuations are present due to the difficulty of averaging over long enough times, even with the incompressible scheme. Despite the strong fluctuations it seems clear that the results depart from the power law decay $t^{-3/2}$. This deviation comes

Parameter	Fixed Sc runs	Variable Sc
excess mass m_e	$m_e = m_f$	$m_e = m_f$
grid spacing h	10.543	1
grid size N	41^3	32^3
fluid density ρ	1	1
shear viscosity η	0.5	variable
bulk viscosity ζ	0.5	-
speed of sound c	$1 - \infty$	-
temperature $k_B T$	1	0.1
viscous CFL β	$10^{-5} - 10^{-3}$	$\beta = \alpha \sqrt{\text{Sc}/6\pi}$
sound CFL $\alpha_s = c\Delta t/h$	$0.05 - 0.1$	-
Schmidt number Sc	48.2	variable

Table 3.2: Figure 3.12, left and right panels.

from the fact that in a periodic box the number of fluid modes in the system is finite and each of them follows an exponential decay, as it can be seen from the linearized Navier-Stokes equations (see Chap. 2 Sec. 2.1.3). It is the contribution or interplay between all the modes what produces the power law tail $t^{-3/2}$ but at the time scale of the slowest mode $\tau = L^2/\nu$ all the other modes have decayed to zero and the particle VACF follows an exponential decay with the characteristic time $\tau = L^2/\nu$. A detailed explanation of the phenomenon can be found in the work by Atzberger [Atzberger 2006]. We show that this result is independent of the thermal fluctuations by plotting also in figure 3.12 the velocity decay $\mathbf{u}(t)/\mathbf{u}(0)$ in the deterministic setting.

3.6.6 Diffusion Coefficient

As it is well known in three dimensional systems (and also in 2D for finite systems), at long enough time scales a particle presents a diffusive motion that can be characterized by its mean square displacement (MSD)

$$\Delta q^2(t) = \langle |q_x(t) - q_x(0)| \rangle = \frac{1}{d} \langle \|\mathbf{q}(t) - \mathbf{q}(0)\| \rangle. \quad (3.165)$$

Since at long times $\Delta q^2(t) \approx 2\chi t$ the diffusion coefficient χ can be measured through the slope of the MSD. An equivalent approach is to integrate the VACF, since [Pomeau 1975, Padding 2006]

$$\chi = \lim_{t \rightarrow \infty} \chi(t) = \lim_{t \rightarrow \infty} \int_0^t C(t') dt'. \quad (3.166)$$

To measure the particle diffusion coefficient we employ this second method but replacing the upper limit in the integral by a finite time $\tau_L = L^2/(4\nu) \approx 250\tau_\nu$ chosen to balance the statistical errors present in the VACF a long times with the bias introduced by truncating the integral. In the left panel of Figure 3.13 one can see that the time-dependent diffusion coefficients converge to a finite value for long times but that the results are not free of statistical errors.

In the right panel of figure 3.13 we present the estimation for the diffusion coefficient for several Stokes-Einstein Schmidt numbers. We can see that for large Sc^{SE} the Stokes-Einstein diffusion coefficient is a good approximation to the numerical results, while for moderate and small Sc^{SE} large deviations appear. We should notice that the Stokes-Einstein relation is only well justified for $\text{Sc} \rightarrow \infty$, a limit that we successfully tested by integrating the (equivalent) deterministic decay $\mathbf{u}(t)/\mathbf{u}(0)$ (see Fig. 3.12).

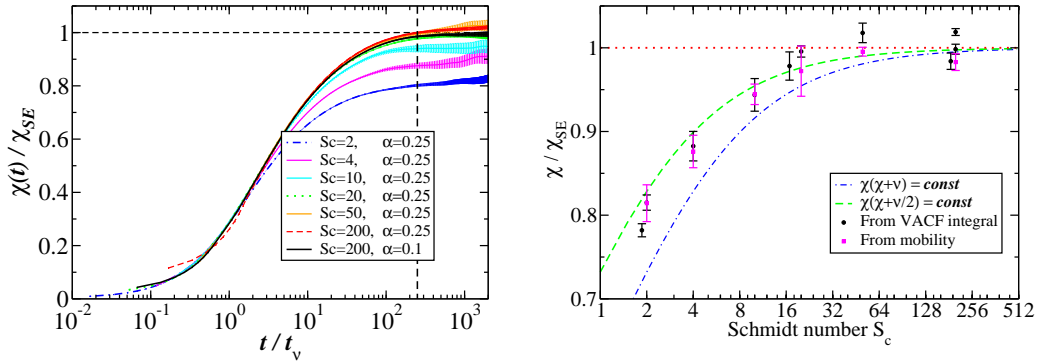


Figure 3.13: Left, diffusive coefficient versus time. The plateau at long times shows that the particle has reached the diffusive regime. Right, diffusive coefficient versus the Schmidt number calculated with the integral of the VACF and with the Einstein formula $\chi = k_B T \mu$. Lines represent the predictions of Eqs. (3.169) and (3.169)

A more general expression for the diffusion comes from the Einstein relation $\chi = k_B T \mu$ where μ is the mobility [Kubo 1966]. In Section 3.6.1 we defined the mobility in the deterministic setting like $\mu = \mathbf{J} \mathcal{L}^{-1} \mathbf{S}$, however the mobility must be measured as the average velocity under a small applied force in the presence of thermal fluctuations

$$\mu = \frac{\langle u \rangle}{F_0}. \quad (3.167)$$

In the right panel of figure 3.13 we plot together the diffusion coefficient obtained from the integral of the VACF and the diffusion coefficient obtained from the mobility, and one can see a very good agreement between both results for all the Sc^{SE} considered. Remarkably, both calculations (diffusion and mobility) consistently predict a significant deviation from the Stokes-Einstein relation for $Sc < 20$. The observed mobility μ is lower than the Stokes value, indicating some form of "thermal drift". This result is a nice example of the importance of the nonlinearities in stochastic systems, usually too difficult to solve analytically. In a linear system the thermal fluctuations are expected to average to zero, but if the system has some nonlinear terms the fluctuations can produce nonzero contributions.

In our system there are two major sources of nonlinearities: the advective term in the fluid equation $\mathbf{v} \cdot \nabla \mathbf{v}$ and the no-slip constraint $d\dot{\mathbf{q}}/dt = \mathbf{J}\mathbf{v}$ which is nonlinear because the averaging operator depends on the particle position \mathbf{q} . In microflows the Reynolds numbers are usually very small and therefore the advective term $\mathbf{v} \cdot \nabla \mathbf{v}$ tends to be negligible. However, we can define a *thermal Reynolds number* based on the particle thermal velocity

$$u_{\text{th}} \approx \sqrt{\frac{k_B T}{\mathcal{V} \rho}},$$

which define the Reynolds number

$$\text{Re} = \frac{u_{\text{th}} R_H}{\nu} \approx \frac{1}{2} \sqrt{\frac{3\pi}{Sc^{SE}}} \sim (Sc^{SE})^{-1/2}. \quad (3.168)$$

This result shows that at low Schmidt number the Reynolds number becomes $\text{Re} \sim 1$. At finite Reynolds number the friction coefficient deviates from the Stokes prediction as we saw in Sec. 3.6.3 and this

effect might be translated to the particle diffusion. To test this hypothesis, we turn off the term $\mathbf{v} \cdot \nabla \mathbf{v}$ in the fluid equations and perform simulations for neutrally buoyant particles. The obtained results do not show any deviation from the results presented in the Figure 3.13, therefore we conclude that the advective terms only play a minimal role (if any) in the particle diffusion.

Once we have discarded the possible effects of the advective terms we assume that the deviation in the particle diffusion coefficient arise because the particle and momentum diffusion take place in similar time scales. The same phenomenon produces the scaling of the tail of the VACF that we saw in Sec. 3.6.5. Since χ is just the integral of the VACF we conjecture the following scaling for the diffusion coefficient [Bedeaux 1974b, Mazur 1974b]

$$\chi(\chi + \nu) = \chi_{SE}\nu. \quad (3.169)$$

This prediction can also be explained by assuming a particle friction coefficient $\zeta = 6\pi\rho(\chi + \nu)R_H$ instead of the usual Stokes friction $\zeta_S = 6\pi\rho\nu R_H$. In turn, this interpretation will explain why the diffusion coefficient obtained from the integral of the VACF and the mobility match. However, this scaling is based on the scaling of the long time tail of the VACF, since the integral of the VACF at short times also contributes to χ we can not be sure that the scaling proposed by the Eq. (3.169) is correct. In Reference [Donev 2011b] a self-consistent theory of diffusion based on a renormalization of the diffusion coefficient was proposed. This theory suggests that the leading effect of a finite Schmidt number in the diffusion coefficient is

$$\chi \left(\frac{\chi}{2} + \nu \right) = \chi_{SE}\nu, \quad (3.170)$$

although at very low Schmidt numbers higher order corrections to this trend are expected. In the right panel of Fig. 3.13 we compare both theoretical predictions, Eqs. (3.169) and (3.170), with the numerical data. One can see that the numerical results lie between the two theoretical prediction although somewhat closer to the Eq. (3.170).

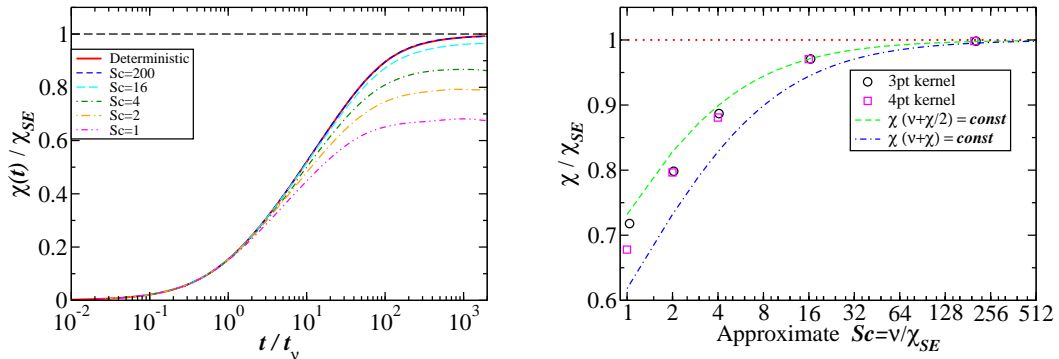


Figure 3.14: (2D). Left, diffusive coefficient versus time, the plateau for long times shows that the particle has reached the diffusive regime. Right, diffusive coefficient versus the Schmidt number calculated with the integral of the VACF and with the Einstein formula.

To further clarify the effect of low Schmidt numbers on the particle diffusion we consider the same problem in a 2 dimensional system. In the limit $Sc^{SE} \rightarrow \infty$, a 2-dimensional disk in a periodic square

box of size L has the following mobility and diffusion coefficient

$$\boldsymbol{\mu} = \frac{1}{4\pi\eta} \ln \left[\frac{L}{3.708R_H} \right] \mathbf{I}, \quad (3.171)$$

$$\chi_{SE} = \frac{k_B T}{4\pi\eta} \ln \left[\frac{L}{3.708R_H} \right], \quad (3.172)$$

where R_H is the disk radius. We use Eq. (3.171) to determine the hydrodynamic radius of a 2D blob and we find $R_H = (0.72 \pm 0.01)h$. Then, in the right panel of Fig. 3.14, we compare the numerical results for the particle diffusion to the predictions (3.169) and (3.170) where we use the value of χ_{SE} given by Eq. (3.172). As in the 3D case we can see that the leading order correction in Sc^{-1} is given by the Eq. (3.170) but that for smaller Schmidt numbers the prediction is not totally accurate.

The low Sc corrections for χ discussed here arise because there is not separation of time scale between the particle and the momentum diffusion. Therefore, we expect this result to be quite general and that it should apply also to methods based on a frictional coupling and even to Lagrangian (or particle) methods. In many of these methods the particle presents an additional non-hydrodynamic contribution χ_0 to its diffusion coefficient due to the details of the fluid-particle interaction [Giupponi 2007, Dünweg 2009]. In those cases the self-consistent theory of Ref. [Donev 2011b] predicts the scaling

$$\chi_H \left(\frac{\chi_H}{2} + \chi_0 + \nu \right) = \chi_{SE}\nu, \quad (3.173)$$

where the total particle diffusion is $\chi = \chi_H + \chi_0$.

Chapter 4

Blob thermomechanical properties

Contents

4.1	Blob compressibility	104
4.2	Numerical implementation	106
4.3	Energy conservation and equilibrium fluctuations	106
4.3.1	Energy conservation	106
4.3.2	Equilibrium fluctuations	107
4.4	Concluding remarks	109

In Chapter 3 we introduced the blob model and the Inertial Coupling Method (ICM). As we explained, the soft kernel $\delta_h(\mathbf{q} - \mathbf{r})$ used in the blob model serves to link the fluid and particle equations of motion but also to represent the relevant physical properties of the particle. As a first step to correctly capture the dynamic of solute particles immersed in a fluid, in Chapter 3 we restricted our attention to the fluid-particle velocity coupling and to the mechanical properties of the blob, such as its mass, volume and hydrodynamic radius. Here we show that the kernel can also be used to include thermodynamic or thermomechanical properties in our model.

A common approach in the literature to describe thermomechanical particle properties has been to represent the particles like a collection of smaller bonded constituents. For example, a polymer can be described like a number of beads connected by springs. However, this kind of approach increases by at least one order of magnitude the number of degrees of freedom of each particle, incurring in a higher computational cost.

There are, however, some previous works which include internal degrees of freedom in simple particle models as we do here. Ripoll et al. [Ripoll 2002, Ripoll 2005] considered the heat transfer in a DPD model where particles, in addition to their positions and velocities, possess an internal energy whose evolution was given by a Langevin equation. This model allowed to study heat conduction. In the SDPD framework (SPH with fluctuations) similar ideas have been used to describe polymer solutions. For instance, Vazquez-Quesada et al. [Vázquez-Quesada 2009] extend the degrees of freedom of each SDPD particle with a conformation tensor characterizing an average polymer state within the SDPD particle and its contribution to the stress tensor. That work is related to previous methods that combine finite elements with effective polymer models evolving under the strain of each Eulerian fluid node [Laso 1993].

In the realm of immersed boundary methods (IBM), very recently it has been published a work that modifies the viscosity of the carrier fluid in the domain occupied by the structure [Fai 2013]. However,

in this case, the immersed structure was described by a large number of Lagrangian markers and not just a single one as we do here.

In this chapter we illustrate the potential of our minimally resolved particle model by adding a far from trivial mechanical property: an arbitrary particle compressibility (speed of sound). The method outlined here can be also generalized to provide particle-fluid or particle-solid wettability, an important property already implemented in Fluid Particle Dynamics methods [Furukawa 2013]. Controlling the particle compressibility is essential to investigate the sound matter interaction, as we will show in Chapter 7. To the best of our knowledge this is the first computational work that considers solute particles with finite compressibility in a low resolution model.

The chapter is divided as follow. We start by explaining how to implement the particle compressibility in Sec. 4.1 and showing in Section 4.3.1, that the model preserves the energy in the inviscid limit. In Section 4.2 we explain how to integrate the equations of motion (we advance that the scheme is essentially the same that the compressible scheme presented in Chapter 3). In Section 4.3.2 it is numerically shown that equilibrium fluctuations (of fluid velocity and particle density) are consistent with thermodynamics. Finally, some concluding remarks are given in Sec. 4.4.

4.1 Blob compressibility

In this chapter the idea of adding physical properties to the blob, via the kernel, is extended to provide a finite blob compressibility. To that end we use the kernel to include a local particle contribution to the pressure equation of state. The method is thus quite general and can be applied to any type of particle-fluid coupling and fluid equations.

Here we consider the inertial coupling (Chap. 3) and the isothermal fluctuating Navier-Stokes equations (Chap. 2). The pressure of the fluid phase is barotropic $p = p(\rho)$ and for simplicity we consider $p(\rho) = p_0 + c_f^2(\rho - \rho_0)$, with constant speed of sound c_f . This approximation is valid for any (single phase) fluid, provided variations of ρ are small enough. For an ideal fluid $p_0 = c_f^2\rho_0$ and $c_f^2 = k_B T/m_s$ (where m_s is the mass of the solvent molecules). To take into account the effect of a compressible particle in the fluid we propose a modification to the pressure field based on the following functional,

$$\pi(\rho, \mathbf{q}) = p(\rho) + S\Omega(\rho; \mathbf{q}). \quad (4.1)$$

The extra particle contribution $S\Omega$ only affects the kernel domain. Recall that the spreading function $S = S(\mathbf{q} - \mathbf{r})$ has units of inverse volume [see Chap. 3, Eq. (3.9)], so Ω has dimensions of energy. The field $S\Omega$ can be related to the chemical potential for particle-fluid interaction (see Sec. 4.4). It determines the energetic cost for fluid entrainment into the kernel domain. There are however two distinct contributions to Ω which can be cast into ideal (“id”) and excess (“ex”) parts,

$$\Omega = \Omega_{ex} + \Omega_{id}. \quad (4.2)$$

The ideal contribution to the local *fluid* pressure, discussed in Chapter 3, is due to the thermal agitation of the colloidal particle and it is

$$\Omega_{id} = \frac{m_f}{m} k_B T, \quad (4.3)$$

where $m_f = \mathcal{V}\mathbf{J}\rho$ is the fluid mass displaced by the particle and m is the colloidal mass.

The form of the thermal drift (4.3) inspired us in choosing a simple, yet efficient, form for Ω_{ex} . It consists of assuming that the particle contribution to the local pressure is a linear function of the averaged local density,

$$\Omega_{ex} = \varepsilon_{pf} \mathcal{V} (\mathbf{J}\rho - \rho_0), \quad (4.4)$$

where ρ_0 is the fluid equilibrium density and the auxiliary parameter ε_{pf} is the particle-fluid interaction energy per unit of fluid mass. Note that Ω_{ex} depends on \mathbf{q} through the average operator $\mathbf{J} = \mathbf{J}(\mathbf{q})$. From (4.1) it is clear that we are modeling the particle compressibility by locally varying the fluid compressibility in the kernel. An interpretation in terms of fluid mass can be also given. We interpret the kernel volume \mathcal{V} as a fixed volume enclosing the “particle” and moving along with it. The particle mass can be generally expressed as $m_p = m_e + \rho_0 \mathcal{V}$, where m_e is the particle *excess mass* measured with respect the mass of fluid it displaces in equilibrium. At any given time, the total mass in the kernel is $m = m_e + \mathbf{J} \rho \mathcal{V} = m_p + (\mathbf{J} \rho - \rho_0) \mathcal{V}$ so Ω_{ex} in (4.4) is proportional to the extra mass of fluid in the kernel $\mathcal{V}(\mathbf{J} \rho - \rho_0)$ due to any displacement from equilibrium. But \mathcal{V} is fixed, so increasing the kernel density is equivalent to “compress the particle”. The prefactor ε_{pf} in (4.4) determines the extra work required to increase the kernel density, compared with that of a fluid parcel in the bulk. As shown below, ε_{pf} controls the particle compressibility.

One can evaluate the compressibility $\kappa(\mathbf{r})$ and the speed of sound $c(\mathbf{r})$ of the fluid, which are scalar fields. To that end we evaluate the pressure variation $\delta\pi(\mathbf{r})$

$$\delta\pi(\mathbf{r}) = \int \frac{\delta\pi(\mathbf{r})}{\delta\rho(\mathbf{r}')} \delta\rho(\mathbf{r}') d^3 r', \quad (4.5)$$

where the functional derivative $\delta\pi(\mathbf{r})/\delta\rho(\mathbf{r}')$ provides change of the pressure field at \mathbf{r} due to a density perturbation $\delta\rho(\mathbf{r}')$. The total pressure functional can be written as

$$\pi(\mathbf{r}) = \int p[\rho(\mathbf{r}')] \delta^{\text{Dirac}}(\mathbf{r}' - \mathbf{r}) d^3 r' + \varepsilon_{pf} \mathcal{V} \delta_h(\mathbf{q} - \mathbf{r}) \int \delta_h(\mathbf{q} - \mathbf{r}') (\rho(\mathbf{r}') - \rho_0) d^3 r', \quad (4.6)$$

where $\delta^{\text{Dirac}}(\mathbf{r})$ and $\delta_h(\mathbf{r})$ are the Dirac delta function and the kernel function introduced in Chapter 3. The functional derivative is given by

$$\frac{\delta\pi(\mathbf{r})}{\delta\rho(\mathbf{r}')} = c_f^2 \delta^{\text{Dirac}}(\mathbf{r} - \mathbf{r}') + \varepsilon_{pf} \mathcal{V} \delta_h(\mathbf{q} - \mathbf{r}) \delta_h(\mathbf{q} - \mathbf{r}'), \quad (4.7)$$

where, c_f is constant for the fluid equation of state used hereby (in general $c_f^2(\mathbf{r}) = \partial p(\rho(\mathbf{r}))/\partial\rho$ is a density dependent field). In terms of the spreading and average operators, the pressure first variation is then

$$\delta\pi(\mathbf{r}) = c_f^2 \delta\rho(\mathbf{r}) + \varepsilon_{pf} \mathcal{V} \mathbf{S} \mathbf{J}(\delta\rho). \quad (4.8)$$

A sound velocity field $c(\mathbf{r})$ can be defined as

$$c^2(\mathbf{r}) = \int \frac{\delta\pi(\mathbf{r})}{\delta\rho(\mathbf{r}')} d^3 r' = c_f^2 + \mathbf{S} \varepsilon_{pf} \mathcal{V}. \quad (4.9)$$

Averaging in (4.8) gives the overall variation of pressure inside the kernel which, for constant fluid sound velocity c_f is equal to,

$$\mathbf{J}[\delta\pi] = (c_f^2 + \varepsilon_{pf}) \mathbf{J}[\delta\rho], \quad (4.10)$$

where we have used $\mathbf{J}\mathbf{S} = \mathcal{V}^{-1}$. Equation (4.10) can be understood as the blob equation of state, which justify our identification of c_p with the speed of sound inside the particle. It is given by,

$$c_p = \sqrt{c_f^2 + \varepsilon_{pf}}. \quad (4.11)$$

The input parameter ε_{pf} can be then either positive or negative (with the obvious condition $c_p \geq 0$). For instance, taking $\varepsilon_{pf} \simeq -c_f^2$ permits to simulate very compressible particles (gas bubbles). Equivalently,

one can introduce $\kappa_p = \kappa_f + \kappa_e$ where $\kappa_p \equiv 1/(\rho_0 c_p^2)$ and $\kappa_f = 1/(\rho_0 c_f^2)$ provide the particle and fluid compressibility, respectively. Then using (4.11), the “excess particle compressibility” is just

$$\kappa_e = -\frac{\varepsilon_{pf}}{c_p^2} \kappa_f. \quad (4.12)$$

From (4.8) one can also infer a bulk modulus operator which applied to any density perturbation field $\delta\rho(\mathbf{r})$ provides the resulting variation in the pressure field $\delta\pi(\mathbf{r}) = \mathcal{B}\delta\rho(\mathbf{r})/\rho_0$,

$$\rho_0^{-1} \mathcal{B} \equiv c_f^2 \mathbf{1} + \varepsilon_{pf} \mathcal{V} \mathbf{S} \mathbf{J} \quad (4.13)$$

Its inverse $\boldsymbol{\kappa} = \mathcal{B}^{-1}$ is the compressibility operator, which applied to some pressure field $\delta\hat{p}(\mathbf{r})$ provides the resulting density perturbation $\delta\hat{\rho}(\mathbf{r}) = \rho_0 \boldsymbol{\kappa}[\delta\hat{p}(\mathbf{r})]$. To invert 4.13 one can use the same formal Taylor expansion used in Section 3.3.4 of Chapter 3 and get,

$$\boldsymbol{\kappa} = \kappa_f + \kappa_e \mathcal{V} \mathbf{S} \mathbf{J}. \quad (4.14)$$

4.2 Numerical implementation

The spatial discretization of the equations is the same that the one presented in Chapter 3. The only small difference is that the particle pressure contribution Ω has to be spread to the cell centers

$$(\mathbf{S}\Omega)_i = \delta_h(\mathbf{q} - \mathbf{r}_i)\Omega(\mathbf{q}, \rho), \quad (4.15)$$

unlike the forces \mathbf{F} and $\boldsymbol{\lambda}$ that are spread to the cell faces (see Section 3.4).

To integrate the equation we use the compressible scheme presented in Section 3.5.2 with again a small modification. During the fluid update (substep 3 in the scheme of Section 3.5.2) the particle contribution to the pressure has to be taken into account. Therefore, the three pressures used during the Runge-Kutta update of the fluid are

$$\pi^n = c_f^2 \rho^n + \varepsilon_{pf} \mathcal{V} \mathbf{S}^{n+\frac{1}{2}} \left(\mathbf{J}^{n+\frac{1}{2}} \rho^n - \rho_0 \right), \quad (4.16)$$

$$\tilde{\pi}^{n+1} = c_f^2 \tilde{\rho}^{n+1} + \varepsilon_{pf} \mathcal{V} \mathbf{S}^{n+\frac{1}{2}} \left(\mathbf{J}^{n+\frac{1}{2}} \tilde{\rho}^{n+1} - \rho_0 \right), \quad (4.17)$$

$$\pi^{n+\frac{1}{2}} = c_f^2 \rho^{n+\frac{1}{2}} + \varepsilon_{pf} \mathcal{V} \mathbf{S}^{n+\frac{1}{2}} \left(\mathbf{J}^{n+\frac{1}{2}} \rho^{n+\frac{1}{2}} - \rho_0 \right), \quad (4.18)$$

where we have assumed that during this substep the particle is fixed at $\mathbf{q}^{n+\frac{1}{2}}$, exactly as in Chap. 3. Because the extra pressure only enters in the fluid update and their equations are solved with a third order accurate Runge-Kutta scheme the pressure contribution $\mathbf{S}\Omega$ does not alter the convergence order of the temporal discretization. Therefore, our numerical discretization is second order accurate for neutrally-buoyant particles and first order accurate for particles with an excess mass $m_e \neq 0$.

4.3 Energy conservation and equilibrium fluctuations

4.3.1 Energy conservation

In a previous Chapter (3) we demonstrated that that the no-slip constraint $\mathbf{J}\mathbf{v} = \mathbf{u}$ does not insert energy into the system. A necessary condition for this result is the adjoint relation between \mathbf{J} and \mathbf{S} [Eq. (3.10)]. It is not difficult to show that the modified pressure field $\pi(\rho)$ does not introduces energy either. The total energy field per unit mass can be written as $e(\mathbf{r}) = v^2/2 + \varepsilon$ where the field ε is the

specific internal energy $\varepsilon = \varepsilon_0 - \pi/\rho$. We do not consider exchange of heat in this work and the energy ε_0 , of entropic origin, is constant. The differential form of the First Law is then $d\varepsilon = (\pi/\rho^2)d\rho$ and only includes the reversible work done by the pressure field π . The rate of total energy production can be shown to be (see e.g. [de Groot 1984]),

$$\frac{d}{dt} \int \rho e dr^3 = \int \rho \frac{de}{dt} dr^3 = - \int \nabla \cdot (\mathcal{P} \cdot \mathbf{v}) d^3r + \int \mathbf{f}^{ext} \cdot \mathbf{v} d^3r. \quad (4.19)$$

Using the Gauss integral theorem $\int \nabla \cdot (\mathcal{P} \cdot \mathbf{v}) d^3r = \oint \mathbf{v} \mathcal{P} \cdot \mathbf{n} d^2r$ (with \mathbf{n} the outwards surface vector). Hence, a way to introduce energy into the system consists of moving its boundaries ($\mathbf{v} \neq 0$ at the boundary). For an ideal fluid (inviscid limit, $\mathcal{P} = (p + S\Omega)\mathbf{1}$), the input power would equal the rate of reversible work $-\oint p \mathbf{v} \cdot \mathbf{n} d^2r$ on the system's boundaries. The particle contribution would then be zero, $-\oint S \mathbf{v} \cdot \mathbf{n} \Omega d^2r = 0$ because S has compact support. In any case, in a periodic system the total surface integral vanishes identically and the only way to introduce energy is to apply an external volume force \mathbf{f}^{ext} , as explained in Chap. 7.

4.3.2 Equilibrium fluctuations

The contribution $-\nabla(S\Omega)$ to the fluid momentum equation is non-dissipative. However, to numerically verify this statement one needs to show that the equipartition of energy remains unaltered upon adding the particle compressibility term. To do so we evaluated the static structure factor of the longitudinal velocity $S_{v,v}(\mathbf{k})$ in an ensemble of $N = 1000$ compressible particles ($c_p = 2c_f$) interacting with repulsive Lennard-Jones potential with strength $\varepsilon = k_B T$ and volume fraction $\phi = 0.244$. As expected, the structure factor is k -independent $S_{v,v}(\mathbf{k}) = k_B T / \rho_0$, showing that the added particle compressibility term does not affect the fluctuation dissipation balance, see left panel of Figure 4.1.

Further we measured the radial distribution function (RDF) of “colloids” with different compressibilities. Results, in the left panel of Fig. 4.2 show that the RDF is not essentially affected by the particle compressibility. This result is however not as general as energy equipartition. Acoustic Casimir forces could, in principle, alter the structure of a colloidal dispersion. The thermo-acoustic Casimir forces are however small [Bschorr 1999], although larger acoustic Casimir forces can be triggered by *forced* white noise of strong amplitude [Larraza 1998] or by the presence of temperature gradients [Kirkpatrick 2013].

In the present approach the particle kernel can be sought as a small domain of fixed volume \mathcal{V} which encloses the particle and it is open to the fluid. As expressed in Eq. (4.10), the particle compressibility is here translated as an excess in the isothermal compressibility of the fluid in the kernel. The mass of fluid in the kernel $m_f = \mathcal{V} \mathbf{J} \rho$ fluctuates and in equilibrium ($\langle \Omega \rangle = 0$ and $\langle \mathbf{J} \rho \rangle = \rho_0$) its variance should coincide with the grand canonical ensemble prescription $\text{Var}[m_f] = m_f k_B T / c_p^2$. The kernel-density variance should then be,

$$\text{Var}[(\mathbf{J} \rho)] = \frac{\rho_0 k_B T}{c_p^2 \mathcal{V}}. \quad (4.20)$$

In the weak fluctuation regime (assumed by the fluctuating hydrodynamics formulation [Landau 1987]) the density probability distribution should then be Gaussian,

$$P(\mathbf{J} \rho) = \left(\frac{\mathcal{V} c_p^2}{2\pi \rho_0 k_B T} \right)^{1/2} \exp \left(-\frac{\mathcal{V} c_p^2}{2\rho_0 k_B T} (\mathbf{J} \rho - \rho_0)^2 \right). \quad (4.21)$$

Figure 4.2 shows the numerical results obtained for $P(\mathbf{J} \rho)$ for particles with different compressibilities, immersed in a fluid at thermal equilibrium. Results are compared with the grand-canonical distribution

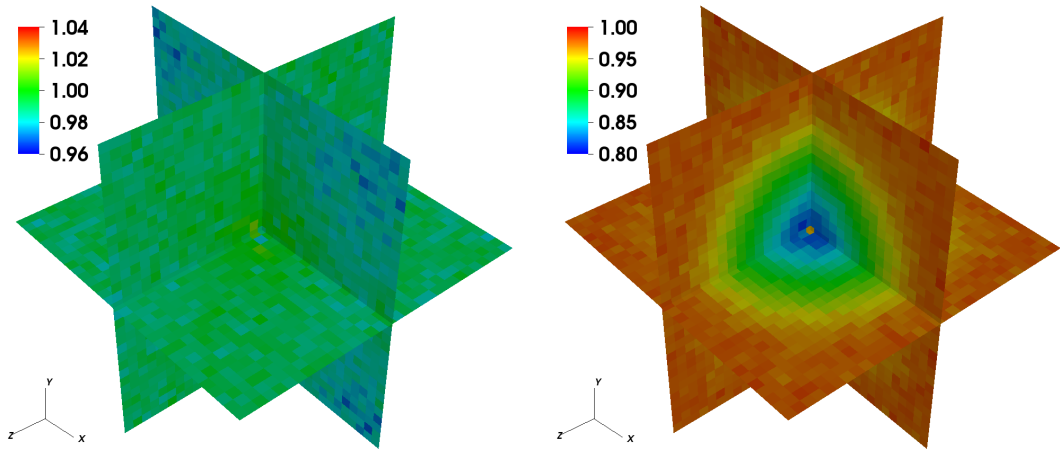


Figure 4.1: Normalized static structure factor of the longitudinal velocity mode $S_{vv}(\mathbf{k})$ (see definition on Chapter 2) in the left panel and the density field $S_{\rho\rho}$ on the right. The velocity structure factor is independent of the wavenumber \mathbf{k} and it recovers the thermodynamic prediction $S_{vv} = k_B T / \rho_0$, independently of the particles compressibility (in this case $c_p = 2c_f$). However, density fluctuation are reduced by the higher incompressibility of the particles. As the right panel shows, the density fluctuation are greatly reduced for small wavenumbers while for high wavenumbers the particles presence seems to play no role. Note that the density fluctuation are directly related with the compressibility of the fluid and for a pure phase fluid $S_{\rho\rho} = \rho_0 k_B T / c_f^2$. All the simulation parameters are given in table 4.1.

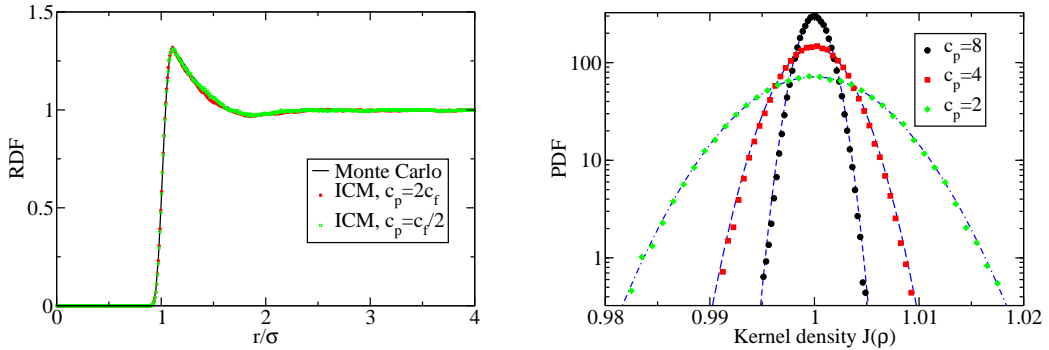


Figure 4.2: Left, radial distribution of a set of particles at volume fraction $\phi = 0.244$ interacting through a repulsive (truncated and shifted) Lennard-Jones potential with strength $\varepsilon = k_B T$, excess mass $m_e = 0$ and diameter $\sigma = 2 h$. Comparison is made between standard Monte-Carlo simulations (i.e. without added particle compressibility) and the hydrodynamic code with two different particle compressibilities. Simulation parameters are like in Fig. 4.1. Right, probability density function (PDF) of the average fluid density inside the particle kernel, with varying particle compressibilities $\kappa_p = 1/(\rho_0 c_P^2)$. Lines corresponds to the normal distribution with the grand canonical ensemble variance in Eq. (4.21) and symbols to numerical results. In all cases the fluid speed of sound is $c_f = 4$. Simulation parameters are given in table 4.1.

Figure	4.1	Right panel of Fig. 4.2
grid spacing h	10	10
number of cells	32^3	32^3
fluid density	1	1
shear viscosity η	0.5	0.5
bulk viscosity ζ	0.5	0.5
fluid speed of sound c_f	4	4
hydrodynamic radius R_H	9.9	9.9
particle excess of mass m_e	0	0
particle speed of sound c_p	8	2-40
number of particles	1000	1

Table 4.1: Variables and parameters of the fluid and particle (arbitrary units). In all cases the particle volume is $\mathcal{V} = 8 h^3$.

of Eq. (4.21). We find excellent agreement, for particles with either larger or smaller compressibility than the surrounding fluid (in Fig. 4.2 $c_f = 4$, see Table 4.1. for the rest of simulation parameters).

We have found that the variance of the kernel density can be used as a sensible measure of the convergence of the numerical scheme. The probability density function (PDF) of the interpolated density $\mathbf{J}\rho$ follows a Gaussian distribution for all the considered cases. However, its variance presents some numerical deviation if large time steps are used. In figure 4.3 we present the relative error between the input particle speed of sound $c_p = \sqrt{c_f^2 + \varepsilon_{pf}}$ and the numerical measure obtained from the variance $\text{Var}[(\mathbf{J}\rho)] = \rho_0 k_B T \mathcal{V}^{-1} / c_p^2$. For neutrally buoyant particles the scheme is second order accurate, as we anticipated. It is interesting to note that when the cell Reynolds number $r = ch/\nu$ is large, the errors are larger for a given speed of sound and time step. The cell Reynolds number measures the importance of the advection relative to the viscous terms and it seems that high advective terms reduce the accuracy of the present scheme.

4.4 Concluding remarks

In this chapter we have extended the ideas of the Blob model to implement an arbitrary particle compressibility by embedding a small domain with a different equation of state (4.10). Alternatively, the particle compressibility can be justified from a free energy functional constructed from the particle-fluid (potential) interaction. Here, such functional would have the form,

$$\mathcal{F}[\rho, \mathbf{q}] = \frac{\mathcal{V}\varepsilon_{pf}}{2\rho_0} [\mathbf{J}(\rho - \rho_0)]^2, \quad (4.22)$$

providing a local fluid chemical potential arising from the particle presence,

$$\mu = \frac{\delta \mathcal{F}}{\delta \rho} = \frac{\mathcal{V}\varepsilon_{pf}}{\rho_0} \mathbf{S} (\mathbf{J}\rho - \rho_0). \quad (4.23)$$

Any variation in this chemical potential would then induce a force density field $\rho \nabla \mu$ in the fluid. A Boussinesq-type approximation, valid at low Mach number $\rho \nabla \mu \simeq \rho_0 \nabla \mu$ leads to the present model equations. In particular, the fluid momentum equation can then be written in a conservative form $\nabla \rho_0 \mu = \nabla \mathbf{S} \Omega$ [see Eqs. (4.4) and (4.1)].

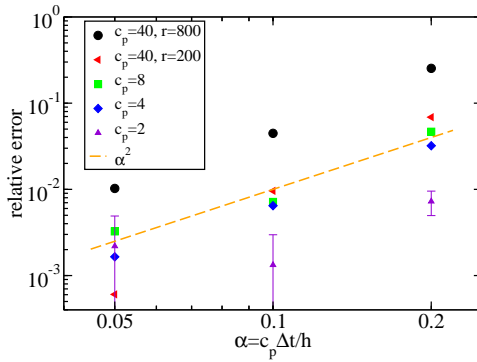


Figure 4.3: Deviation between the input particle speed of sound $c_p = \sqrt{c_f^2 + \varepsilon_{pf}}$ and that obtained from the best fit of the kernel density $J\rho$ PDF to the grand-canonical Gaussian distribution of Eq. (4.21) (see Fig. 4.2). The abscissa correspond to the CFL number $\alpha = c\Delta t/h$ where the speed of sound c is the maximum value between the fluid and particle speed of sound. The simulation parameters are like in the right panel of Fig. 4.2 except in the simulations with cell Reynolds number $r = 200$ where the viscosities are $\eta = \zeta = 2$.

Also, the augmented Langevin formalism can be used to derive the equations of motion of this chapter just as we did in the Section 3.3.3 of Chapter 3. The functional (4.22) can be added to the Hamiltonian (3.57) to yield the total energy of the system

$$\mathcal{H} = \int \left(\frac{1}{2} \mathbf{v}^T (\rho \mathbf{I} + m_e \mathbf{S} \mathbf{J}) \mathbf{v} + \rho \varepsilon(\rho) \right) d^3r + U(\mathbf{q}) + \frac{\mathcal{V} \varepsilon_{pf}}{2\rho_0} [\mathbf{J}(\rho - \rho_0)]^2. \quad (4.24)$$

In this case the Hamiltonian derivatives are

$$\frac{\partial \mathcal{H}}{\partial \rho} = \frac{1}{2} \mathbf{v}^2 + \varepsilon(\rho) + \rho^{-1} p(\rho) + \frac{\mathcal{V} \varepsilon_{pf}}{\rho_0} \mathbf{S} (\mathbf{J}\rho - \rho_0), \quad (4.25)$$

$$\frac{\partial \mathcal{H}}{\partial \mathbf{v}} = (\rho \mathbf{I} + m_e \mathbf{S} \mathbf{J}) \mathbf{v}, \quad (4.26)$$

$$\frac{\partial \mathcal{H}}{\partial \mathbf{q}} = -\mathbf{F}(\mathbf{q}) + m_e \mathbf{J} (\mathbf{v} \cdot \nabla_{\mathbf{q}} \mathbf{J}) \mathbf{v} + \frac{\mathcal{V} \varepsilon_{pf}}{\rho_0} \mathbf{J} ((\rho - \rho_0) \nabla_{\mathbf{q}} \mathbf{J}) (\rho - \rho_0). \quad (4.27)$$

By using the same mobility and stochastic terms that in Sec. 3.3.3 one can see that neither the dynamic equation of the density field ρ or the particle position \mathbf{q} change. However, for the fluid velocity field we recover the Eq. (3.47) with some extra terms

$$\begin{aligned} (\rho + m_e \mathbf{S} \mathbf{J}) \partial_t \mathbf{v} &= [-(\rho(\mathbf{v} \cdot \nabla) + m_e \mathbf{S} (\mathbf{u} \cdot \nabla_{\mathbf{q}} \mathbf{J})) \mathbf{v} - \nabla p + \nabla \cdot \boldsymbol{\sigma} + \mathbf{S} \mathbf{F}] \\ &\quad + [\text{Extra compressibility terms}]. \end{aligned} \quad (4.28)$$

The new terms are given by

$$[\text{Extra compressibility terms}] = -\mathcal{V} \varepsilon_{pf} \nabla \mathbf{S} \mathbf{J} (\rho - \rho_0) + [\text{h.o.t.}] . \quad (4.29)$$

The first term in the right hand side of Eq. (4.29) is the extra contribution to the pressure that we included in our equation of motion along this chapter and that we have used to model compressible particles. The

other term is a high order correction that we have neglected to simplify the algorithm. This neglected term is of the form

$$\begin{aligned} [\text{h.o.t.}] &= \frac{\mathcal{V}\varepsilon_{pf}}{\rho_0} [\mathbf{J}(\rho - \rho_0)] [(\rho - \rho_0) (\nabla_{\mathbf{q}} \mathbf{S}) - \mathbf{S} (\nabla_{\mathbf{q}} \mathbf{J}) (\rho - \rho_0)] \\ &= \frac{\mathcal{V}\varepsilon_{pf}}{\rho_0} [\mathbf{J}(\rho - \rho_0)] \int [\delta^{\text{Dirac}}(\mathbf{r} - \mathbf{r}') - \delta_h(\mathbf{q} - \mathbf{r}')] [\nabla_{\mathbf{q}} \delta_h(\mathbf{q} - \mathbf{r}') (\rho(\mathbf{r}') - \rho_0)] d^3 r'. \end{aligned} \quad (4.30)$$

A rigorous connection between our blob-model (based on a mean field approach) and a first-principle derivation of the coupled fluid-particle equations is beyond the scope of the present work. We believe however that such connection is possible and will provide clues to the interaction free energy functional which ultimately, stems from molecular interactions. This would certainly open many other applications (wettability) to the present mean field approach [Furukawa 2013]. For us, one the main target is to model the sound-particle interaction for which the finite blob compressibility is a key element, as it will be explained in Chapter 7.

Chapter 5

Brownian dynamics

Contents

5.1	Introduction to the equations of Brownian dynamics	114
5.1.1	Free draining limit	116
5.2	Some Lagrangian methods for Brownian dynamics	116
5.2.1	Cholesky decomposition	117
5.2.2	Fixman's method	117
5.3	Eulerian-Lagrangian Brownian hydrodynamics	119
5.4	Benchmark: dynamics of a colloidal cluster	120

This chapter introduces the equations of motion for Brownian particles. The Brownian limit has been treated and analyzed in an extremely large number of works, even before the pioneer computational papers by Ermak and McCammon [Ermak 1978] and up to *Stokesian dynamics* [Brady 1988] and recent developments of *Accelerated Stokesian dynamics* [Banchio 2003]. These formulations generally describe mutual friction coupling between colloids translation, rotation and stresslet, coded in the so called the grand mobility matrix, and also include (pairwise) approximations to lubrication forces near the colloidal contact. In their origin, these methods are based on a fully Lagrangian approach, where the fluid velocity contribution enters only via some suitable analytical approximation of the mobility tensor, which describes how hydrodynamics affect the linear relationship between the colloidal (non-hydrodynamic) forces and their mutual velocities.

Our intention here is to open a new route to Brownian hydrodynamics based on our Eulerian-Lagrangian scheme, equipped with the (instantaneous) no-slip constraint to couple particles and fluid velocities. The description of Brownian motion using Eulerian-Lagrangian methods is not new, and has proved to provide significant computational benefits, thoroughly discussed in the literature [Dünweg 2009]. However, many of these previous Eulerian-Lagrangian schemes used for Brownian dynamics, are based on Langevin-type dynamics as they use a bare (non-hydrodynamic) friction coefficient ζ_0 to relax (in time) the particle velocity to the local fluid velocity. In other words, they include some particle inertia which requires resolving times of order $1/\zeta_0$ [Dünweg 2009]. The true Stokes dynamics would then correspond to the stiff $\zeta_0 \rightarrow \infty$ limit, which has also been considered in a recent work [Atzberger 2011]. Our no-slip constraint formulation avoids this added “numerical friction”, by directly solving the *real* $Sc \rightarrow \infty$ limit. This approach permits to substantially increase the time step, whose stability limit will be given by the much larger h^2/χ colloidal diffusion time. It has to be said, that quite often, the stability limit of colloidal dynamics is however restricted by their hard-core colloidal

repulsion. This is not the case in polymer modeling, where excluded volume interactions among chain blobs are usually described with softer (coarse-grained) interactions [Jendrejack 2002].

In Section 5.1 we present the basic Brownian hydrodynamic (BHD) equations describing particles translations (but not rotation neither stresslet, which can be implemented following the lines mentioned in previous chapters). We then justify why the Eulerian-Lagrangian method, based on a complete numerical solution of the perturbative fluid velocity, can substantially reduce the computational cost when compared with standard fully Lagrangian BHD. We describe two popular Lagrangian BHD methods in Sec. 5.2 and in Section 5.3 introduces our Eulerian-Lagrangian solution of the BHD. Finally we present a benchmark (collapse of a group of attracting colloids) to compare both (Lagrangian and Eulerian-Lagrangian) methods.

5.1 Introduction to the equations of Brownian dynamics

The motion of a solute particle in a fluid can be described by the Brownian or Stokes limit if its diffusion is exceedingly slow compared with the slowest process for fluid momentum transport. Under moderately slow flow (creeping or low Reynolds flow), where all forms of fluid inertia (either unsteady $\partial\mathbf{v}/\partial t$ or convective inertia $\mathbf{v} \cdot \nabla \mathbf{v}$) are negligible, the slowest fluid process is the viscous transport of vorticity. Under these conditions, most (probably all) colloidal molecules move according to the Brownian picture as, the ratio of colloidal diffusivity and fluid kinetic viscosity (the Schmidt number $Sc = \chi/\nu$) is always a very large number. As shown in Chapter 8, the Brownian limit $Sc \rightarrow \infty$ also applies for the different motions (center of mass diffusion and inner modes) of polymeric chains.

An additional requirement for the Brownian dynamics to hold is that the particle inertial time has to be much smaller than the diffusion time $\tau_D = R^2/\chi$. The particle inertial time is $\tau_B = M/\zeta$ with $\zeta \propto \eta R$ (self-friction coefficient) and $M = \rho_p V$ its mass. But $\tau_D/\tau_B \sim (\rho_f/\rho_p)Sc$ so particle inertia can be also neglected, unless the solute is extremely dense. Gold is about 20 times more dense than water, but typical values of Sc are in the range $\sim 10^{[4-6]}$, so even very dense colloids can be treated as Brownian particles.

Under these conditions one can neglect *all* forms of inertia (in particle and fluid). Under no external forces, particles will just follow the underlying local fluid velocity, which, if one neglects stresslet terms, will be completely unperturbed by the particles presence. It is then convenient to decompose the total velocity field as $\mathbf{v}_0 + \mathbf{v}$, where \mathbf{v}_0 is the *unperturbed* (given) part and \mathbf{v} is the perturbative flow arising from any (non-hydrodynamic) forces acting on the particles. In fact, since the particle inertia is negligible the particles equation of motion simplifies to

$$0 = \boldsymbol{\lambda} + \mathbf{F}_{ext}, \quad (5.1)$$

where $\boldsymbol{\lambda}$ is the force exerted by the fluid to the particles (and viceversa, with opposite sign) and $\mathbf{F}_{ext}(\mathbf{Q})$ represents other forces on colloidal particles, which depend on the particles coordinates $\mathbf{Q} = \{\mathbf{q}_i\}$. Thus $\boldsymbol{\lambda} = -\mathbf{F}_{ext}$ and the Stokesian limit of the Navier-Stokes equation for the perturbative flow becomes,

$$\nabla \pi - \eta \nabla^2 \mathbf{v} = \mathbf{f}(\mathbf{r}, t), \quad (5.2)$$

$$\text{s.t. } \nabla \cdot \mathbf{v} = 0, \quad (5.3)$$

where $\mathbf{f}(\mathbf{r}, t) = \mathbf{S}\mathbf{F}_{ext}$ represents the force density exerted by the particles or immersed structures on the fluid. The solution of Eqs. (5.2)-(5.3) shall be referred later as $\mathbf{v} = \mathcal{L}^{-1}\mathbf{f}$, where \mathcal{L}^{-1} is the Green function associated with the Stokes equations. In our formulation, the field $\mathbf{S}(\mathbf{r})$ is modeled by a sum over each blob kernel $\mathbf{S} = \sum_i \mathbf{S}_i(\mathbf{q}_i)$. The solution of these linear equations representing the

Brownian limit provides a linear relation between the particles velocities and the external forces \mathbf{F}_{ext} . Velocities and forces are related by a tensorial quantity, the mobility tensor $\boldsymbol{\mu}(\mathbf{Q})$ which depends on the all particles coordinates $\mathbf{Q} = \{q_i\}$ [Ladd 1990, Jendrejjack 2000, Banchio 2003]. Introducing the base flow, the deterministic dynamics of one particle is then described by,

$$\frac{d\mathbf{q}}{dt} = \boldsymbol{\mu}(\mathbf{Q})\mathbf{F}_{ext}(\mathbf{Q}) + \mathbf{v}_0(\mathbf{q}). \quad (5.4)$$

Where in most applications the base flow is time-independent (this is not a restriction though) and it is usually expressed as $\mathbf{v}_0(\mathbf{q}) = \dot{\gamma}(\mathbf{q} - \mathbf{q}_0)$ where the velocity gradient matrix $\dot{\gamma}$ describes either shear, elongational or mixed flows [Jendrejjack 2002].

In summary, since all the inertia has been neglected the fluid velocity can be eliminated as an independent degree of freedom. The Stokes equations (5.2)-(5.3) would then only be required to evaluate the mobility operator $\boldsymbol{\mu}(\mathbf{Q})$ either using an analytical approximation [Jendrejjack 2000, Kekre 2010] or by direct numerical solution of the Stokes equations [Lomholt 2003, Atzberger 2011]. This later case is the approach we use in the Inertial Coupling Method (ICM) (see Chapter 3, Section 3.6.1). In our approach $\dot{\mathbf{q}}_i = \mathbf{J}_i \mathbf{v} + \mathbf{v}_0(\mathbf{q})$ and applying \mathbf{J}_i to the solution of (5.2), it is not difficult to see that the element ij of the mobility tensor results [Usabiaga 2014, Delong 2014]

$$\boldsymbol{\mu}_{ij} = (\mathbf{J}_i \mathcal{L}^{-1} \mathbf{S}_j) = \boldsymbol{\mu}_{ji}, \quad (5.5)$$

where \mathcal{L}^{-1} represent the solution operator of the Stokes equations (5.2)-(5.3). As we saw in Chap. 3 the averaging and spreading operators employed by our blob model produce a very good approximation to the mobility of rigid spheres (see Sections 3.6.1 and 3.6.3); therefore, it is possible to calculate the mobility tensor on the fly without relying on analytical approximations.

It might seem beneficial to eliminate the fluid velocity as a degree of freedom and take the analytic route for $\boldsymbol{\mu}$ to solve a set of equations with just N solute particles, instead of solving a 3D fluid system with N_f^3 fluid cells. We shall soon show that the addition of thermal fluctuations in the plot, radically changes this view. Once the set of deterministic equations (5.4) are known, it is possible to use the Augmented Langevin formalism (see Sec. 2.1.4) to derive the stochastic dynamics of N Brownian particles under thermal fluctuations. These can be written in the Ito form as [Jendrejjack 2002, Dünweg 2009],

$$\dot{\mathbf{q}} = \mathbf{v}_0(\mathbf{q}) + \boldsymbol{\mu}\mathbf{F}_{ext} + k_B T \nabla_{\mathbf{q}} \cdot \boldsymbol{\mu} + \sqrt{2k_B T} \mathbf{K} \mathbf{W}, \quad (5.6)$$

where \mathbf{W} is a collection of uncorrelated Gaussian random numbers with zero mean and unit variance and \mathbf{K} is a matrix which satisfies

$$\mathbf{K} \mathbf{K}^T = \boldsymbol{\mu} \quad (5.7)$$

to ensure the fluctuation dissipation balance.

Analytical approximations for the mobility tensor permits to forecast $\boldsymbol{\mu}$ for any given configuration $\mathbf{Q}(t)$. Then, to update the particles positions in Eq. (5.6) one needs to solve Eq. (5.7) for \mathbf{K} . The raw computational cost of this matricial problem is however, quite large $\mathcal{O}(N^3)$ (although as shown below, clever algorithmic permits to reduce it to $\mathcal{O}(N^{2.25})$). One of the key aspects of the Eulerian-Lagrangian approach, as the one used hereby, is to bypass this complicated matricial problem by working with the fluid velocity degrees of freedom, i.e. by numerically solving the stochastic version of Eq. (5.2), presented in Section 5.3. The mobility tensor is thus implicitly obtained in the solution of (5.2) (i.e. in solving \mathcal{L}^{-1} and then using Eq. (5.5)). The whole operation (including particle update) scales almost linearly with the number of particles N , in fact as $\mathcal{O}(N \log N)$ if one uses FFT to solve the Stokes equation.

The mixed Eulerian-Lagrangian approach to Brownian dynamics is also very useful when one needs to deal with complex geometries [Zhang 2012] and boundary conditions, which substantially complicate the analytical treatment of μ . However, analytical expressions for the mobility have been (and still are) frequently used in simple geometries. One of the most popular approximations for the mobility of spherical particles of radius R in an unbounded domain is the Rotne-Prager (-Yamakawa) tensor [Rotne 1969]

$$\boldsymbol{\mu}_{ii} = \frac{1}{6\pi\eta R} \mathbf{I}, \quad (5.8)$$

$$\boldsymbol{\mu}_{ij} = \frac{1}{8\pi\eta r_{ij}} \left(\left(1 + \frac{2R^2}{3r_{ij}^2} \right) \mathbf{I} + \left(1 - \frac{2R^2}{r_{ij}^2} \right) \frac{\mathbf{r}_{ij}\mathbf{r}_{ij}}{r_{ij}^2} \right) \quad \text{if } i \neq j \text{ and } r_{ij} \geq 2R, \quad (5.9)$$

$$\boldsymbol{\mu}_{ij} = \frac{1}{6\pi\eta R} \left(\left(1 - \frac{9r_{ij}}{32R} \right) \mathbf{I} + \frac{3}{32} \frac{\mathbf{r}_{ij}\mathbf{r}_{ij}}{Rr_{ij}} \right) \quad \text{if } i \neq j \text{ and } r_{ij} < 2R. \quad (5.10)$$

This mobility includes all the long range terms (r^{-1} and r^{-3}) and it has the additional advantage that $\nabla_Q \cdot \boldsymbol{\mu} = 0$ which simplifies considerably the particles equation (5.6). Also, unlike the simpler Oseen approximation [Kim 2005], it is positive definite for all particles configuration allowing for the fluctuation-dissipation balance in equation (5.7) (note that the product of a matrix with its transpose is always positive definite) [Rotne 1969]. However, it is important to recall that the Rotne-Prager tensor is a pairwise approximation (it only include two-body hydrodynamic interactions) and therefore it is not a good approximation to study solutions with a high particle concentration [Beenakker 1982].

If the system geometry is more complex, for example there are boundaries or the immersed particles are not spheres, it is not possible to use the Rotne-Prager tensor given above. One possible solution for simple geometries is to find an analytic approximation to the mobility tensor, this has been done for a systems confined between two infinite planes, see Refs. [Jones 2004, Kekre 2010]. For other geometries it may be necessary to directly solve the Stokes equations (5.2)-(5.3) with the proper boundary conditions [Kekre 2010, Atzberger 2010, Zhang 2012] (as we do here for periodic systems). This second approach can be followed by introducing the necessary modifications in the fluid solvers introduced in the Chap. 2.

5.1.1 Free draining limit

The simplest Brownian dynamics formulation is to assume that the fluid drains free across the collection of colloidal obstacles. In other words, it just neglects the hydrodynamic interaction between particles in Eq. (5.6). The mobility tensor becomes diagonal, $\boldsymbol{\mu}_{ij} = (\delta_{ij}/\zeta_i) \mathbf{I}$ (with ζ_i being the self-friction coefficient of each particle) making trivial the solution of the matrix $\mathbf{K}_{ij} = (\delta_{ij}/\sqrt{\zeta_i}) \mathbf{I}$. This “free draining” assumption is valid in some problems where hydrodynamic interactions are screened by the presence of obstacles (many particles, walls, etc.). Another example, treated in Chapter 8, is the tumbling motion of polymeric chains under strong shear, which is mainly determined by the interplay between the external forcing and the chain extension. In some of these cases the hydrodynamic interactions do not modify the main features of the dynamic process and it might be convenient to use free draining simulations to save a substantial computational time [Schroeder 2005b, Winkler 2006].

5.2 Some Lagrangian methods for Brownian dynamics

The most difficult challenges posed by equation (5.6) are the evaluation of the stochastic force $\sqrt{2k_B T} \mathbf{K} \mathbf{W}$ and the thermal drift $k_B T \nabla_Q \cdot \boldsymbol{\mu}$. For the Rotne-Prager tensor the thermal drift is zero

for any particle configuration, therefore one only has to calculate the stochastic force. As we said in the introduction the matrix \mathbf{K} should satisfy the equation (5.7) to obey the fluctuation-dissipation theorem, however the matrix \mathbf{K} is not univocally determined by the Eq. (5.7). Several methods have been developed to calculate this matrix, most of them applied in the polymer literature. In the following subsections we will introduce the Cholesky decomposition, an exact method that, however, has a very large computational cost and the Fixman's method, an approximation with a lower cost. We will then present in Section 5.3 the Eulerian-Lagrangian Brownian limit, based on our coupling method.

To update the Brownian equation (5.6) we employ a explicit Forward Euler scheme, which although it requires small time steps, it avoids the use of complicated implicit solvers for non-linear equation. Moreover in the simulations of Chapter 8 the time step stability limit comes from the stretching forces, explicit higher order schemes do not improve this limit much, especially for divergent potentials (like the FENE spring). For these reasons, it is not especially useful to employ higher order schemes, at least in our simulations of Chap. 8. Implicit schemes involving sub-iterative steps, as those proposed by Jendrejack [Jendrejack 2000], can be very useful to increase the stability limit but as we said we did not try to implement any of them.

5.2.1 Cholesky decomposition

For any positive definite matrix, like the Rotne-Prager tensor μ , the Cholesky decomposition finds a lower triangular matrix \mathbf{K} such as $\mathbf{K}\mathbf{K}^T = \mu$. The elements of \mathbf{K} can be found with the following algorithm

$$K_{jj} = \sqrt{\mu_{jj} - \sum_{k=1}^{j-1} K_{jk}^2}, \quad (5.11)$$

$$K_{ij} = \frac{1}{K_{jj}} \left(\mu_{ij} - \sum_{k=1}^{j-1} K_{ik} K_{jk} \right) \quad \text{for } i > j, \quad (5.12)$$

where the indices run from 1 to $3N$. The problem of the Cholesky decomposition is that it is computationally expensive. The number of operation scales with the number of particles N as N^3 so the algorithm becomes impracticable even for small number of particles. Actually, the Cholesky decomposition is mainly used to test the accuracy of faster approximating methods [Schmidt 2011]. This is the case of the present work, as in fact we have not used Cholesky decompostion for any production run.

5.2.2 Fixman's method

Instead of Cholesky decomposition, the algorithm proposed by Fixman [Fixman 1986] has been used in the context of polymer simulations by Jendrejack et al. [Jendrejack 2000, Jendrejack 2002]. We also took this route and used this method in the study of polymer chain dynamics under flow, presented in Chapter 8. The Fixman's method consists of the following steps. First, consider an alternative choice for the matrix \mathbf{K} , namely $\mathbf{K} = \mathbf{S}$ such that $\mathbf{S}^T = \mathbf{S}$ and $\mathbf{S}\mathbf{S} = \mu$. The matrix \mathbf{S} is usually called the square-root of the mobility matrix. The symmetric matrix \mathbf{S} can be calculated with a computational cost that scales like N^3 (as the Cholesky decomposition) by solving an eigenvalue problem. However, it is possible to reduce the computational cost by noting two things. First, to solve the Brownian equation it is enough to use an approximation to \mathbf{S} and second that we really do not require the matrix \mathbf{S} but rather the vector $\mathbf{S}\mathbf{W} = \mathbf{K}\mathbf{W}$. With these considerations a solution of cost $N^{2.25}$ it is possible. This scaling does not seem much better than the scaling of Cholesky method, however, even with a moderate number of beads the speedup becomes non-negligible. For example, for a chain with $N = 30$ beads the

Fixman's method speedup the simulations by a factor $(30)^{0.75} \approx 13$ and for longer chains the difference in computational cost soon becomes very large.

We outline the algorithm to solve the stochastic forcing in the Brownian limit. First, we consider the Chebyshev polynomial approximation $s^{(m)}$ to the square root function \sqrt{m} over the range $[\lambda_{\min}, \lambda_{\max}]$

$$s^{(m)} = \sum_{l=0}^L a_l C_l, \quad (5.13)$$

where L is the degree of the polynomial, the terms

$$C_0 = 1, \quad (5.14)$$

$$C_1 = m_a m + m_b, \quad (5.15)$$

$$C_{l+1} = 2(m_a m + m_b)C_l - C_{l-1} \quad \text{for } l \geq 1, \quad (5.16)$$

are obtained from the recursion relation of the Chebyshev polynomials and

$$m_a = \frac{2}{\lambda_{\max} - \lambda_{\min}}, \quad (5.17)$$

$$m_b = -\frac{\lambda_{\max} + \lambda_{\min}}{\lambda_{\max} - \lambda_{\min}}. \quad (5.18)$$

The coefficients a_l in the Eq. (5.13) can be obtained from the orthogonality relation of the Chebyshev polynomials (see Ref. [Arfken 1985]). The Fixman's method applies the above Chebyshev approximation to obtain a matrix S^μ that approximates the square root of the mobility matrix. The only required modifications of the above equations are to substitute the scalar function m by the matrix μ in the equations (5.14)-(5.16) and to choose λ_{\min} and λ_{\max} such that all the eigenvalues of the mobility matrix lie in the interval $[\lambda_{\min}, \lambda_{\max}]$. However, as we said we do not really need an approximation to the matrix K but rather an approximation to the vector KW . Using the Chebyshev polynomials one can write an approximation to the stochastic forcing as

$$\mathbf{y} = S^\mu \mathbf{W} = \sum_{l=0}^L a_l \mathbf{x}_l, \quad (5.19)$$

with

$$\mathbf{x}_0 = \mathbf{W}, \quad (5.20)$$

$$\mathbf{x}_1 = (m_a \mu + m_b \mathbf{I}) \mathbf{W}, \quad (5.21)$$

$$\mathbf{x}_{l+1} = 2(m_a \mu + m_b \mathbf{I}) \mathbf{x}_l - \mathbf{x}_{l-1} \quad \text{for } l \geq 1. \quad (5.22)$$

Given the upper and lower eigenvalue bounds of the mobility matrix the above calculation can be carried out in LN^2 operations. To achieve a given level of accuracy the degree of the Chebyshev polynomial L should scales as $(\lambda_{\max}/\lambda_{\min})^{1/2}$, and the ratio between the lower and upper eigenvalues scales with the number of beads as $N^{1/2}$ [Fixman 1986, Jendrejack 2000]. Therefore, it follows that the computational cost of the Fixman's method scales as $N^{2.25}$, which represents a considerable saving over the Cholesky decomposition. Finally, the upper and lower eigenvalues of the mobility matrix can be obtained with a N^2 cost using the Arnoldi method, this algorithm has been already implemented in the ARPACK library [Lehoucq 1997], and we just link our Brownian code to that library. Despite the complex order of the Arnoldi method $\mathcal{O}(N^2)$, the computation of the eigenvalues is computationally expensive, therefore, following Jendrejack [Jendrejack 2000] we do not calculate the eigenvalues every

time step. The Chebyshev expansion given above is valid if λ_{\min} and λ_{\max} delimit the eigenvalues of the mobility matrix μ . Therefore, we calculate the upper and lower eigenvalues for a given configuration and keep using that values while it is possible. To estimate the error committed in the Chebyshev expansion we compute the error

$$E_\lambda = \sqrt{\frac{|\mathbf{y} \cdot \mathbf{y} - \mathbf{W} \cdot \mu \mathbf{W}|}{\mathbf{W} \cdot \mu \mathbf{W}}}. \quad (5.23)$$

This expression is zero for an exact solution of the equation (5.7). When this error is larger than the desired accuracy (typically $\sim 10^{-3}$) the eigenvalue range ($[\lambda_{\min}, \lambda_{\max}]$) and the polynomial degree (L) are recalculated with a N^2 cost using the ARPACK library [Lehoucq 1997].

5.3 Eulerian-Lagrangian Brownian hydrodynamics

We explain in this section the Eulerian-Lagrangian method to solve the Eq. (5.6) with a $\mathcal{O}(N \log N)$ computational cost for N particles. This method is not only computational efficient but also allows to include complex boundaries for which the mobility tensor is not correctly described by the Rotne-Prager tensor. A key element of our algorithm is that it is valid even when $\nabla_Q \cdot \mu \neq 0$, however, to simplify the exposition let us start with the simpler case in which the divergence of the mobility tensor is zero. In this case the equations of motion for N particles can be written as

$$\nabla \pi - \eta \nabla^2 \mathbf{v} = \sum_j^N \mathbf{S}_j \mathbf{F}_j + \sqrt{2k_B T \eta} \nabla \cdot \mathbf{W}, \quad (5.24)$$

$$\text{s.t. } \nabla \cdot \mathbf{v} = 0, \quad (5.25)$$

$$\frac{d\mathbf{q}_i}{dt} = \mathbf{J}_i \mathbf{v}, \quad (5.26)$$

where \mathbf{W} is a symmetric tensor field with mean zero and covariance $\langle \mathcal{W}_{ij}(\mathbf{r}, t) \mathcal{W}_{kl}(\mathbf{r}', t') \rangle = (\delta_{ik}\delta_{jl} + \delta_{il}\delta_{jk})\delta(\mathbf{r} - \mathbf{r}')\delta(t - t')$. In the case of periodic boundary conditions (PBC) we can solve the fluid equations (5.24) and (5.25) with the projector methods of Sec. 2.1.5, and the particle coordinates can be updated by a simple forward Euler scheme $\mathbf{q}_i^{n+1} = \mathbf{q}_i^n + \Delta t \mathbf{J}_i \mathbf{v}$. The above system of equations is equivalent to Eq. (5.6) when $\nabla_Q \cdot \mu = 0$. As before we denote the Stokes solution operator by \mathcal{L} , therefore the velocity field that satisfies the Eqs. (5.24) and (5.25) is $\mathbf{v} = \mathcal{L}^{-1} \left(\sum_j \mathbf{S}_j \mathbf{F}_j + \sqrt{2k_B T \eta} \nabla \cdot \mathbf{W} \right)$ and combining this result with the particle Eq. (5.26) we obtain the expressions for the mobility μ and stochastic matrix \mathbf{K} in the Eulerian-Lagrangian approach

$$\mu_{ij} = \mathbf{J}_i \mathcal{L}^{-1} \mathbf{S}_j, \quad (5.27)$$

$$\sqrt{2k_B T} \mathbf{K}_i = \mathbf{J}_i \mathcal{L}^{-1} \sqrt{2k_B T \eta} \nabla \cdot \mathbf{W}. \quad (5.28)$$

By simple matrix multiplication one can show that the fluctuation dissipation balance is indeed recovered

$$\mathbf{K}_i \mathbf{K}_j^T = \mathbf{J}_i \mathcal{L}^{-1} \sqrt{\eta} (\nabla \cdot) (-\nabla) \sqrt{\eta} \mathcal{L}^{-1} \mathbf{S}_j \quad (5.29)$$

$$= \mathbf{J}_i \mathcal{L}^{-1} \mathbf{S}_j \quad (5.30)$$

$$= \mu_{ij}. \quad (5.31)$$

In the above equation we have used $(\nabla \cdot) \nabla = \nabla^2$ and $-\mathcal{L}^{-1} \nabla^2 \mathcal{L}^{-1} = \eta^{-1} \mathcal{L}^{-1}$ a property that can be proved by considering the equation (5.2) [note that from Eq. (5.2) follows $-\mathcal{L}^{-1} \nabla^2 \mathcal{L}^{-1} \mathbf{f} = -\mathcal{L}^{-1} \nabla^2 \mathbf{v} = \eta^{-1} \mathcal{L}^{-1} (-\nabla \pi + \mathbf{f}) = \eta^{-1} \mathcal{L}^{-1} \mathbf{f}$].

However, when the mobility matrix has a nonzero divergence the above scheme becomes useless. Therefore, we need to modify the scheme to include the effect of the thermal drift. A common approach in the literature to include the thermal drift effect without explicitly evaluating the derivative of μ has been to use the Fixman's method (see for example Refs. [Fixman 1986, Hütter 1998]). The Fixman's method by using a predictor-corrector step and evaluating the mobility matrix at two different configurations correctly includes the effect of the thermal drift $k_B T \nabla_Q \cdot \mu$. However, these methods require to evaluate the inverse of the mobility matrix (or the square root of μ) which can be a expensive calculation. We follow another route. To obtain a scheme with first order weak accuracy the first 3 moments of the numerical increment ($\mathbf{q}^{n+1} - \mathbf{q}^n$) should match to first order the increment of the continuum Eq. (5.6) [Delong 2013, Milstein 2004]. To this precision the divergence of μ can be reconstructed by

$$\nabla_Q \cdot \mu(\mathbf{Q}) = \lim_{\varepsilon \rightarrow 0} \varepsilon^{-1} \langle \mu(\mathbf{Q} + \varepsilon \widetilde{\mathbf{W}}) \widetilde{\mathbf{W}} - \mu(\mathbf{Q}) \widetilde{\mathbf{W}} \rangle = \nabla_Q \cdot \mu(\mathbf{Q}) \langle \widetilde{\mathbf{W}} \widetilde{\mathbf{W}} \rangle, \quad (5.32)$$

where $\widetilde{\mathbf{W}}$ is a vector of $3N$ independent random numbers with zero mean and unit variance. Numerically one can approximate Eq. (5.32) by means of “random finite differences”, in which case ε is a small finite spacing, for example $\varepsilon = 10^{-6} h$ with h being the meshwidth. Because we know how to evaluate the mobility matrix ($\mu = \mathbf{J} \mathcal{L}^{-1} \mathbf{S}$) we can use Eq. (5.32) to include the thermal drift in the particle equations of motion. However, that route will require an additional Stokes solver (because the presence of \mathcal{L}^{-1} in the definition of μ). As in general the Stokes solver is the most computationally demanding task in our scheme we do not want to increase the number of Stokes solvers per time step. To avoid increasing its number we note the following relation

$$\begin{aligned} \partial_j \mu_{ij}(\mathbf{Q}) &= \partial_j (\mathbf{J}_{ij}(\mathbf{Q}) \mathcal{L}_{kl}^{-1} \mathbf{S}_{lj}(\mathbf{Q})) \\ &= (\partial_j \mathbf{J}_{ik}(\mathbf{Q})) \mathcal{L}_{kl}^{-1} \mathbf{S}_{lj}(\mathbf{Q}) + \mathbf{J}_{ik}(\mathbf{Q}) \mathcal{L}_{kl}^{-1} (\partial_j \mathbf{S}_{lj}(\mathbf{Q})), \end{aligned} \quad (5.33)$$

where here \mathbf{J}_{ik} is the average velocity in the k-direction at the site of the particle “i”, \mathbf{S}_{lj} is the spreading in the l-direction by the particle “j” and μ_{ij} is the entry “ij” of the tensor μ . The two terms in the right hand side of Eq. (5.33) can be handled independently. To include the first term, containing $\partial_j \mathbf{J}_{ik}(\mathbf{Q})$, we employ a predictor-corrector scheme as in the Euler-Heun integrator for stochastic equations. To evaluate the second term we make use of “random finite differences” as introduced previously. Collecting all the different pieces our temporal integrator is

$$\begin{aligned} \nabla \pi - \eta \nabla^2 \mathbf{v} &= \mathbf{S}^n \mathbf{F}^n + \sqrt{\frac{2\eta k_B T}{\Delta t h^3}} \nabla \cdot \mathbf{W}^n \\ &+ \frac{k_B T}{\varepsilon} \left[\mathbf{S} \left(\mathbf{q}^n + \frac{\varepsilon}{2} \widetilde{\mathbf{W}}^n \right) \widetilde{\mathbf{W}}^n - \mathbf{S} \left(\mathbf{q}^n - \frac{\varepsilon}{2} \widetilde{\mathbf{W}}^n \right) \widetilde{\mathbf{W}}^n \right], \end{aligned} \quad (5.34)$$

$$\mathbf{q}^{n+\frac{1}{2}} = \mathbf{q}^n + \frac{\Delta t}{2} \mathbf{J}^n \mathbf{v}, \quad (5.35)$$

$$\mathbf{q}^{n+1} = \mathbf{q}^n + \Delta t \mathbf{J}^{n+\frac{1}{2}} \mathbf{v}. \quad (5.36)$$

This scheme is first order weak accurate as can be proved by showing that the first 3 moments of the numerical increment ($\mathbf{q}^{n+1} - \mathbf{q}^n$) match to first order the increment of the continuum Eq. (5.6) [Delong 2014].

5.4 Benchmark: dynamics of a colloidal cluster

Solvers for the Stokes limiting equations are, in principle, the most appropriate ones to study colloidal gelation, a process taking place at very large Schmidt number. The recent literature offers contradictory

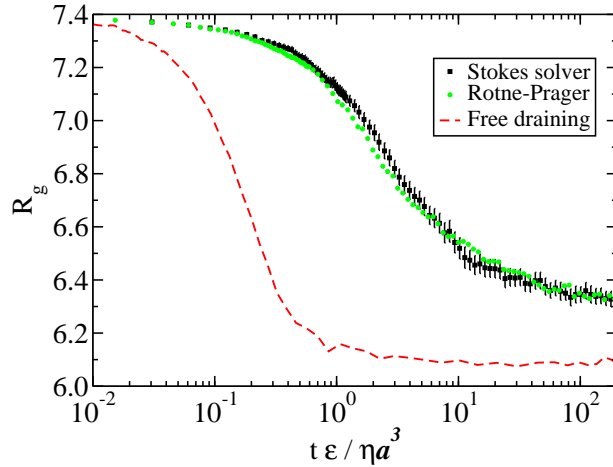


Figure 5.1: Cluster collapsing following the Ref. [Furukawa 2010]. Results for free draining simulations (red dashed line), Lagrangian simulations using the Rotne-Prager tensor (green circles) and the Eulerian-Stokes solver (black squares). Error bars (shown for one curve) show the statistical errors obtained after averaging over 64 simulations. The potential, parameter and initial configurations are described in Ref. [Furukawa 2010].

results, while some works concluded that hydrodynamic interactions only play a minimal role if any in the gelation process [Lu 2008, Yamamoto 2008] others works assert the key role of hydrodynamic interactions in the gelation process [Furukawa 2010, Cao 2012].

As a simple test problem to prove the capabilities of our Stokes solvers we reproduce the results of Fig. 4 in Ref. [Furukawa 2010]. In this test 13 colloids interacting through an Asakura-Oosawa potential (with a smoothed repulsive part) are initially placed at the vertices and center of an icosahedron. When the colloids are released from the initial positions the cluster collapses due to the attractive interaction between colloids at those distance. However, the collapsing process is quite different depending on the hydrodynamic interactions presented in the system. In Fig. 5.1 we show the average gyration radius of the cluster over 64 simulations calculated with schemes for Brownian dynamics without hydrodynamic interaction (free draining limit), Brownian dynamics with hydrodynamic interaction included by using the Rotne-Prager tensor and finally results for our Eulerian-Lagrangian solvers. The free draining results show a fast decay, moreover, the cluster does not change its symmetry during the decay. In the presence of hydrodynamic interaction our Lagrangian (Rotne-Prager) and Eulerian-Lagrangian schemes present similar results as we expected. With hydrodynamics the collapse is slowed down by several orders of magnitude with respect to the free draining simulations. Moreover, the cluster symmetry is broken and the colloids tend to form elongate structures in agreement with the results of Furukawa and Tanaka (see Fig. 4 of Ref. [Furukawa 2010]). It has been argued the formation of this kind of elongate threads favours the gelation of colloidal systems [Whitmer 2011].

Chapter 6

Application of fluctuating hydrodynamics: Giant fluctuations

Contents

6.1 Simplified theory	124
6.2 System modeling	126
6.3 Results	128

In this chapter we employ the numerical methods developed in Chapter 2 in a challenging nonequilibrium problem that span many time scales and makes use of nonperiodic boundary conditions. We try to reproduce the experimental results of Vailati et al. [Vailati 2011] for the diffusive mixing process in microgravity. In particular, we reproduce the giant concentration fluctuations in a nonequilibrium steady state. It is well known that nonequilibrium fluctuations are much larger than equilibrium fluctuations, moreover, they grow with the system size and, if they are not suppressed by some physical constraint, can become macroscopic both in the length scales and in amplitude [Vailati 1998, de Zárate 2004].

The experimental setup of the work we try to reproduce consist of two collinear parallel discs with diameter $D = 25$ mm separate by a short distance, $L = 1$ mm. A dilute solution of polystyrene in toluene is confined between the two discs. At equilibrium, the average concentration of polystyrene c is constant across the sample and the concentration fluctuations are small and independent of the wavenumber $S_{cc} = Mc_0(1 - c_0)/\rho_0$ (see Chap. 2). In the experimental setting the discs allow to an optical access to the sample in a direction perpendicular to them. By using quantitative shadowgraphy technique, one variant of the several light scattering experimental methods, it is possible to record the concentration of polystyrene average though the sample

$$c_{\perp}(x, z) = \frac{1}{L} \int_0^L c(x, y, z) dy, \quad (6.1)$$

where we have assumed that the discs are perpendicular the y -axis.

The discs also allow to create a constant temperature gradient $|\nabla T| = \Delta T/L$ along the y -axis. In the presence of a temperature gradient the polystyrene molecules move to the cold region due to the Soret forcing term $\nabla \cdot (\rho\chi S_T c(1 - c)\nabla T)$ [see Eq. (2.3)]. This implies that for polystyrene molecules (molecular mass $M = 9100\text{g mol}^{-1}$) immersed in toluene (molecular mass $M = 92.14\text{g mol}^{-1}$) the Soret coefficient is positive, as usually happens for large molecules immersed in a molecular fluid for not well understood reasons [Römer 2013]. In the steady state the concentration gradient equals the

Soret term and in the low concentration approximation [$c(1 - c) \approx c$] the Eq. (2.3) allows to obtain the concentration profile

$$c(y) = \frac{c_0 S_T \Delta T}{1 - e^{-S_T \Delta T}} e^{-S_T \Delta T y / L}, \quad (6.2)$$

where c_0 is the average concentration in the sample.

Although this profile is not directly accessible by the experimental setting of Vailati et al. [Vailati 2011] the advective coupling between the concentration gradient and the velocity fluctuations will lead to the giant concentration fluctuations observed in the experiments. These fluctuations are much larger than at equilibrium and more important, they present a strong dependence with the wavelength. The fluctuations amplitude diverge for small wavevectors as k^{-4} , a signature of diffusive processes. However, other transport mechanisms can become dominant and suppress this scaling law. For example, under gravity, buoyancy forces dominate the transport of concentration fluctuations for wavevectors smaller than the cutoff

$$k_c = \left(\frac{\beta \mathbf{g} \cdot \nabla c}{\nu \chi} \right)^{1/4}, \quad (6.3)$$

where \mathbf{g} is the gravity acceleration and $\beta = \rho^{-1}(\partial \rho / \partial c)$ the solutal expansion coefficient. For this reason, previous experiments on giant concentration could not validate this scaling law up to macroscopic length scales [Segrè 1993, Vailati 1998]. This limitation was overcome by the microgravity experiment that we try to reproduce here. By performing the diffusion experiments in an unmanned capsule set into orbit around the Earth the effective gravity was reduced to a value as small as $g \approx 7 \cdot 10^{-6} \text{ m/s}^2$ and therefore negligible [Vailati 2011].

In Section 6.1 we present two simplified theories for the problem of giant fluctuations that recover the correct scaling with the fluid transport coefficients and the system size. Then, in Section 6.2 we explain how we model the experimental setup of Vailati et al. and the parameters that we use to perform the simulations. Finally, in Section 6.3 we compare the results of the theory, simulations and experiments.

6.1 Simplified theory

In this section we present a simplified theory to predict the concentration fluctuations in the steady nonequilibrium state. Since the discs diameter D is much larger than the distance between them L , we consider that the system is periodic in the directions parallel to the plates (x and z). Moreover, for large wavenumbers the effect of the walls should be negligible, therefore we consider that the system is also periodic in the y -axis. We will see later that the presence of the walls has a profound effect on the small wavenumbers modes but this approximation predicts the correct scaling for wavelengths $\lambda \ll L$.

To analytically solve the equations we need to neglect all the nonlinearities in the system. First, in our simplified theory we consider that the fluid is incompressible. This is a reasonable assumption because at the characteristic lengths of the experiment the sonic transport of momentum is many orders of magnitude faster than the viscous diffusion. Using the parameters of toluene the difference between the viscous and the acoustic time is $(L^2/\nu)/(L/c_T) \approx 2 \cdot 10^6$. Besides, it has been argued that compressibility effects do not modify the concentration fluctuations, at least, in most fluid mixtures [de Zárate 2004, de Zárate 2006]. Second, we assume that neither the fluid density ρ or its transport coefficients (viscosity η , concentration diffusion χ ...) depends on the concentration. For the low concentrations of polystyrene employed in the experiments of Vailati et al. ($c \approx 0.02$) this is a reasonable assumption, although it is known that for large variations of the concentrations these dependence of

the fluid parameters can be essential to accurately predict the mixture behavior [Donev 2012]. With the approximations explained above the system can be described by the linearized equations (see also Chap. 2)

$$\partial_t \delta \mathbf{v} = \mathcal{P} \left(\nu \nabla^2 \delta \mathbf{v} + \nabla \cdot \left(\sqrt{2\nu\rho^{-1}k_B T} \tilde{\mathcal{W}}_v \right) \right), \quad (6.4)$$

$$\partial_t \delta c = -\nabla \bar{c} \cdot \delta \mathbf{v} + \chi \nabla^2 \delta c + \nabla \cdot \left(\sqrt{2\chi\rho^{-1}Mc_0(1-c_0)} \tilde{\mathcal{W}}_c \right), \quad (6.5)$$

where the velocity and concentration fields are $\mathbf{v} = \delta \mathbf{v}$ and $c = c_0 + \delta c$, being c_0 the average concentration. In principle, in our simplified periodic description the concentration gradient cannot have a finite value. However, it is well known that the origin of the giant fluctuations is the coupling between the velocity fluctuations $\delta \mathbf{v}$ and the nonequilibrium concentration gradient ∇c [Brogoli 2000]. To mimic this coupling we linearize $\delta \mathbf{v} \cdot \nabla c$ as $\delta \mathbf{v} \cdot \nabla \bar{c}$ where $\nabla \bar{c} = -c_0(1-c_0)S_T \nabla T$ is a constant vector that takes the same value that the average concentration gradient in the nonperiodic case. This term should not be confused with the concentration gradient $\nabla c = \nabla \delta c$.

Since the equations 6.4 and 6.5 are linear and the space is periodic it is possible to transform the equation to Fourier space where the modes become uncoupled

$$\partial_t \delta \mathbf{v}_k = \nu \mathbf{L}_k \delta \mathbf{v}_k + \sqrt{2\nu\rho^{-1}k_B T} \tilde{\mathcal{P}} \mathbf{D}_k \tilde{\mathcal{W}}_v^k, \quad (6.6)$$

$$\partial_t \delta c_k = -\nabla \bar{c} \cdot \delta \mathbf{v}_k + \chi \mathbf{L}_k \delta c_k + \sqrt{2\chi\rho^{-1}Mc_0(1-c_0)} \mathbf{G}_k \tilde{\mathcal{W}}_c^k. \quad (6.7)$$

Fourier transform the equations also in time allows to solve for the velocity and concentration fields. For example, the velocity modes in Fourier space are

$$\delta \mathbf{v}_k(\omega) = \sqrt{2\nu\rho^{-1}k_B T} [i\omega \mathbf{I} - \nu \mathbf{L}_k]^{-1} \mathcal{P}_k \mathbf{D}_k \tilde{\mathcal{W}}_v^k. \quad (6.8)$$

From these equations and using the correlation of the stochastic terms it is possible to find the dynamic structure factor $S(\mathbf{k}, \omega)$ and after integrating for all frequencies the static structure factor (see Sec. 2.4.4). The concentration structure factor $S_{cc}(\mathbf{k}) = \langle c_k c_k^* \rangle$ is the best magnitude to characterize the system outside equilibrium because it is accessible in the shadowgraphy experiments [Vailati 2011]. From Eqs. (6.6)-(6.7) and Eq. (2.45) it is possible to derive the static structure factor for our quasi-periodic (QP) theory

$$S_{cc}^{QP}(\mathbf{k}) = \rho^{-1} Mc_0(1-c_0) + \frac{k_B T}{\rho \chi (\nu + \chi) k^4} \sin^2 \theta (\nabla \bar{c})^2 \quad (6.9)$$

The first term in Eq. (6.9) is independent of the wavenumber and it is present even at equilibrium. The second term, where θ is the angle between the concentration gradient $\nabla \bar{c}$ and the wavevector \mathbf{k} , has its origin in the nonequilibrium perturbation $\nabla \bar{c} = -S_T c_0(1-c_0) \nabla T$ and it presents a strong divergence for small wavevectors k . In the experiments, the use of a shadowgraph technique allows to measure these fluctuations in the plane parallel to the discs through the changes in the refraction index following the changes in concentration. The accessible wavevectors are those with $k_{\parallel} = k_y = 0$ or $\sin \theta = 1$.

The effect of boundaries can be included by a single-mode or a Galerkin approximation for the velocities [de Zárate 2004], its effect is to suppress the large fluctuation for wavelengths comparable to the system size L . For wavevectors parallel to the discs $k_{\parallel} = k_y = 0$ the single-mode approximation predicts, for the non-periodic (NP) system, the structure factor

$$\frac{S_{cc}^{NP}}{S_{cc}^{QP}} \approx \frac{q_{\perp}^4}{q_{\perp}^4 + 24.6 q_{\perp}^2 + 500.5} \quad (6.10)$$

where $q_\perp = Lk_\perp = L\sqrt{k_x^2 + k_z^2}$ is a nondimensional wavevector orthogonal to $\nabla\bar{c}$. On Earth, gravity effects become dominant at lengths smaller than the typical system size and it results difficult to validate the theory given by Eqs. (6.9) and (6.10). The advantage of microgravity experiments is that they allow to observe if the fluctuations can grow with the system size and reach macroscopic values.

6.2 System modeling

In this section we explain how to model the experimental setup in a convenient form to perform numerical simulations. Because many length and time scales are spanned in this problem it is not possible to employ for the system size or the fluid properties the experimental values. However, the modeling have to be done carefully to allow a comparison between experimental data, theory and simulations. In our model the fluid is described by the fields density ρ , velocity v and concentration c and they evolve according to the fluctuating Navier-Stokes equations presented in Chapter 2. As we did then, we consider the concentration to be a passive scalar that does not perturb the density or the velocity fields, because the polystyrene concentration is low $c \approx 0.02$ this seems to be a reasonable assumption.

In the experiments, the sample has a thickness of $L = 1\text{mm}$ and a diameter of $D = 25\text{mm}$. For this system size the light scattering experiment is able to recover the static structure factor $S_{cc}(\mathbf{k}) = \langle \delta c_\perp(\mathbf{k}) \delta c_\perp^*(\mathbf{k}) \rangle$ for wavevectors between $k \sim 20\text{cm}^{-1}$ and $k \sim 200\text{cm}^{-1}$. Those wavevectors correspond to wavelengths between $\lambda \sim 3\text{mm}$ and $\lambda \sim 0.3\text{mm}$. To perform the simulations we need to discretize the sample in a way that allows us to have the same or a better spatial resolution. In the y direction we use a sample of thickness $L = 1\text{mm}$ with periodic or hard boundary conditions depending on if we want to compare the numerical results with the quasi-periodic theory of Sec. 6.1 or with the experimental data [Vailati 2011]. In the directions parallel to the discs we set the length of the sample to $L_\parallel = 4L$ and use periodic boundary conditions to mimic the large size of the experimental system in those directions. We discretize the space with cubic cells of side $h = 31.25\mu\text{m}$, therefore, we have access to wavevectors in the range $\sim 16\text{cm}^{-1} - 2000\text{cm}^{-1}$ which allows us to compare our numerical results with all the range of experimental data.

The numerical simulations of this problem were first performed with the explicit compressible solver for the Navier-Stokes equations presented in Chap. 2. From a computational point of view it is much more difficult to model the system across all the different time scales (from the sonic time $\tau_c = h/c_T$ to the diffusive time $\tau_\chi = h^2/\chi$) than to model the spatial dimensions. Using the experimental values for the transport coefficients and the meshwidth $h = 31.25\mu\text{m}$, the ratio between the two transport times (τ_c and τ_χ) is of the order of 10^8 , therefore, it is complete impossible to track with any numerical method. To solve this problem we reduce the separation of time scales while conserving their hierarchy to correctly resolve the different physical phenomenon involved. First, the momentum is spread via sound waves and diffusion. The ratio between these two processes is given by the cell Reynolds number $r = c_T h / \nu$, experimentally $r \approx 6 \cdot 10^4$, however, to recover the correct physical behaviour it is enough to maintain a separation of one order of magnitude [Padding 2006]. Therefore we use $r \geq 10$. It is interesting to point out that the time scale separation between these two transport mechanisms grows with the length scale, therefore, at length scales comparable with the sample thickness the sonic and viscous characteristic times are separated by at least a factor 300. Second, in the system there are two diffusive process, the diffusion of momentum and the diffusion of concentration, the ratio between their times is given by the Schmidt number, $\text{Sc} = \nu/\chi \approx 3 \cdot 10^3$ in the experiments. However, from eq. 6.9 one can see that the amplitude of the concentration fluctuations is controlled by $(\chi + \nu)\chi = (1 + \text{Sc})\chi^2$, therefore, to recover the experimental results is enough to set $(1 + \text{Sc})\chi^2$ to the experimental value while using $\text{Sc} > 1$. Table 6.1 gives a summary of the parameters using during the simulations.

Parameter	Value	Notes
L	1mm	
h	$31.25\mu\text{m}$	
m_y	32	
$m_x = m_z$	128	
ρ	0.858 gr/cm^3	Constant for incompressible
$\chi(\nu + \chi)$	$1.20 \cdot 10^{-8} \text{ cm}^4/\text{s}^2$	Like in the experiment
ν	$1.96 \cdot 10^{-4} \leq \nu \leq 4.77 \cdot 10^{-4} (\text{cm}^2/\text{s})$	Physical value $\nu = 6.07 \cdot 10^{-3} \text{ cm}^2/\text{s}$
χ	$2.39 \cdot 10^{-5} \leq \chi \leq 4.89 \cdot 10^{-5} (\text{cm}^2/\text{s})$	Physical value $\chi = 1.97 \cdot 10^{-6} \text{ cm}^2/\text{s}$
$\text{Sc} = \nu/\chi$	$4 \leq \text{Sc} \leq 20$	Physical value $\text{Sc} = 3080$
ζ	0	None for incompressible
$k_B T$	$4.18 \cdot 10^{-14} \text{ gr cm}^2/\text{s}^2$	$T = 303 \text{ K}$
M	$1.51 \cdot 10^{-20} \text{ gr}$	Not important for results
S_T	$0.0649 K^{-1}$	
ΔT	4.35, 8.70 and $17.40 K$	Like in the experiments
c_0	0.018	
c_T	1.11 cm/s	Physical value $c_T \approx 1.3 \cdot 10^5 \text{ cm/s}$

Table 6.1: Physical parameters using in the simulations of giant fluctuations. The values are chosen to mimic the experimental system of Vailati et al. [Vailati 2011] while reducing the stiffness of the hydrodynamic equations. Note that the hierarchy between timescales is always satisfied, $r = c_T h / \nu \geq 10$ and $S_c > 1$.

The stability limits of the compressible solver ($\alpha_c < 1$ and $\beta < (1/2)^d$) forced us to use a time step corresponding to a sonic CFL number of $\alpha_c = 0.2$. Numerical errors are then very small (note that, moreover, $\beta, \beta_\chi < 0.02$). However, small values of Δt implies a larger number of sampling steps to reduce statistical “errors” arising from thermal fluctuations. It then proves convenient to employ an incompressible solver. Our implementation of the incompressible equations, based on FFT, does not allow the use of nonperiodic boundary conditions, however, we include results for the incompressible limit performed by collaborators using the code IBAMR [Griffith] and presented in Ref. [Usabiaga 2012]. With the incompressible solver most of the simulations use a time step corresponding to a viscous CFL number $\beta = 1$ or $\beta = 2$, with some simulations using a time step as large as $\beta = 5$. These much larger time steps allow the incompressible solver to obtain a better statistical accuracy even if the IBAMR implementation is significantly slower than our implementation for GPUs.

To represent the walls we use special boundary conditions at $y = 0$ and $y = L$. For the velocity we use no-slip boundary conditions while for the concentration we employed a Robin boundary condition

$$\frac{\partial c}{\partial n} = -c S_T (\mathbf{n} \cdot \nabla T), \quad (6.11)$$

which ensures the vanishing of the concentration flux at the wall and therefore the conservation of concentration (or more precisely mass density $\rho_1 = c\rho$) in the system. The Robin boundary condition can be implemented by setting the concentration in the ghost cells to

$$c_g = c_n \frac{2 \pm S_T (\nabla T)_\perp h}{2 \mp S_T (\nabla T)_\perp h} \quad (6.12)$$

where c_n is the concentration in the neighbor cell across the wall and the signs correspond to the left and right walls (see Sec. 2.2.4 for more details about the implementation of hard walls). As we said

we also perform simulations for periodic boundary conditions (in those cases we set the forcing term to $\nabla \bar{c} = -c_0(1 - c_0)S_T \nabla T$) to compare with the nonperiodic simulations and to observe the effect of the rigid walls.

6.3 Results

The first result we want to discuss is the steady concentration profile $c(y)$ in the nonequilibrium case ($\nabla T \neq 0$). Fig. 6.1 presents the values of $c(y)$ from the numerical simulations together with the theoretical prediction of Eq. (6.2). One can see the perfect agreement between both results but we should note that this only happens because $c \ll 1$, remember that we employed the low concentration approximation $c(1 - c) \approx c$ to obtain the concentration profile given by Eq. (6.2). Figure 6.1 does not include experimental results because this profile is not experimentally accessible, the experiments only can access the concentration averaged c_\perp defined in Eq. (6.1).

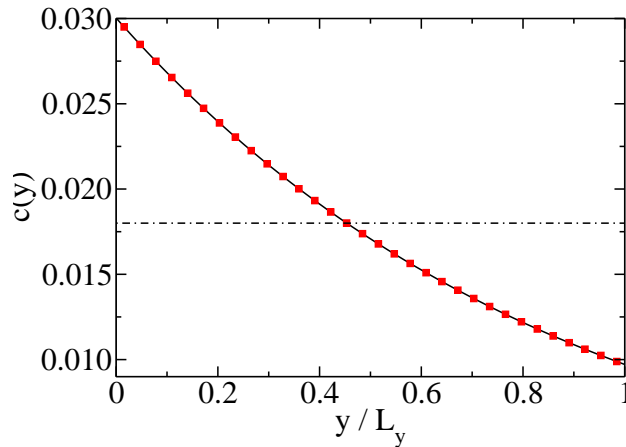


Figure 6.1: Concentration profile through the sample under a temperature gradient $\|\nabla T\| = 17.4K/mm$. Simulation results (squares) and theory Eq. (6.2) (continuous line) show a perfect agreement. We show also the equilibrium profile corresponding to $c = 0.018$ (dash-dotted line). This last line is also the concentration profile for periodic systems even when the forcing term $\nabla \bar{c}$ is nonzero.

The next result to discuss is the concentration static structure factor $S_{cc}^\perp(\mathbf{k}) = \langle \delta c_\perp(\mathbf{k}) \delta c_\perp^*(\mathbf{k}) \rangle$. Before any quantitative analysis of S_{cc}^\perp is illuminating to observe and discuss the snapshots of Fig. (6.2). As we discussed the temperature gradient not only produces concentration profiles like the one presented in Fig. 6.1 but also enhances the concentration fluctuations for wavevectors perpendicular to the steady state gradient ∇c . These fluctuations evolve with a characteristic time $\tau = \lambda^2/(\pi^2 \chi)$ with λ the length-wave of the fluctuation. Fig. 6.2 shows snapshots of the concentration c_\perp in a system with $\Delta T = 17.4K$ at times $\sim 0.1L^2/(\pi^2 \chi)$, $L^2/(\pi^2 \chi)$ and $5L^2/(\pi^2 \chi)$ after starting with no concentration fluctuations at $t = 0$. The panels of Fig. 6.2 shows how the concentration fluctuations evolve during macroscopic times ($L^2/(\pi^2 \chi) \sim 500s$) along macroscopic lengths, as it was announced in the introduction. The reader can compare these results with the Fig. 1 of Ref. [Vailati 2011].

The results of $S_{cc}^\perp(\mathbf{k})$ as function of the wavenumber $k_\perp = \sqrt{(k^x)^2 + (k^z)^2}$ are plotted in figs. 6.3 and 6.4. Figure 6.3 shows a good agreement between experimental, numerical and theoretical results for all the wavenumbers available to the experiment. The spectrum shows the strong dependence with the

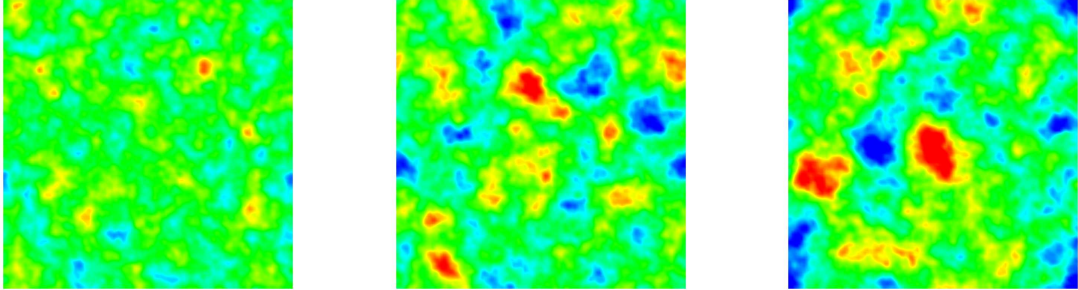


Figure 6.2: Snapshots of the concentration c_{\perp} in a nonperiodic system under a temperature difference between walls $\Delta T = 17.40K$. The size of the sample is $L_{\parallel} = 4L = 4\text{mm}$, therefore the fluctuations are of macroscopic size. The three snapshots correspond to times $\sim 0.1L^2/(\pi^2\chi)$, $L^2/(\pi^2\chi)$ and $5L^2/(\pi^2\chi)$ after starting with no concentration fluctuations at $t = 0$.

wavenumber up to length scales comparable with the sample thickness, $kL \sim 2\pi$. At those scales the amplitude of the fluctuations is about 8 orders of magnitude larger than at thermal equilibrium ($S_{cc}^{\text{Eq.}} = M\rho^{-1}c_0(1 - c_0) \approx 3 \cdot 10^{-22}$), larger samples will lead to even larger fluctuations. Figure 6.3 also illustrates the effects of discretization artifacts. The numerical data (black dots) deviates from the power law scaling at high wavenumbers for which the modes are just a few meshwidth long ($k \sim 2\pi/h$). It is well known that this kind of errors appear because of the limited resolution of the finite volume method, in fact, similar discretization errors have been reported in other works, see for example Figs. 2 and 4 of Ref. [Shang 2011]. One possible solution to reduce these errors is to increase the spatial resolution in which case the deviation will start at larger wavenumbers. However, a better approach is possible. To obtain a good agreement between the numerical and theoretical results it is important to consider the effect of the discretization in the transport coefficients ($\nu, \chi \dots$), because, as we saw in sections 2.1.3 and 2.2.2 after the discretization they are not longer independent of the wavevector \mathbf{k} . Therefore, the correct theoretical prediction for our numerical results is obtained by including the wavevector dependence in the two transport coefficients $\nu_{\text{ef}} = \nu_{\text{ef}}(\mathbf{k})$ and $\chi_{\text{ef}} = \chi_{\text{ef}}(\mathbf{k})$. Equivalently, we can write the denominator of Eq. (6.9) like $\rho\chi_{\text{ef}}(\mathbf{k})(\nu_{\text{ef}}(\mathbf{k}) + \chi_{\text{ef}}(\mathbf{k}))k^4 = \rho\chi(\nu + \chi)\tilde{k}^4$ with the effective discrete wavevector $\tilde{\mathbf{k}}_{\perp} = (\tilde{k}^x, \tilde{k}^z)$ where its two components are defined by

$$\tilde{k}^{\alpha} = \phi(k^{\alpha}h)k^{\alpha} = \frac{\sin(k^{\alpha}h/2)}{k^{\alpha}h/2}k^{\alpha}. \quad (6.13)$$

When the numerical results are plotted against the modified wavevector $\tilde{\mathbf{k}}_{\perp}$ (see red dots in Fig. 6.3) the numerical and theoretical results present a perfect agreement at high wavenumbers. This shows that an understanding of the spatial discretization allows to reabsorb some of the discretization errors into the transport coefficients without needlessly increasing the spatial resolution.

The results of $S_{cc}^{\perp}(\mathbf{k})$ as function of the discrete wavenumber $\tilde{k}_{\perp} = \sqrt{(\tilde{k}^x)^2 + (\tilde{k}^z)^2}$ are plotted in Fig. 6.4 for the quasi-periodic and nonperiodic systems in both 2 and 3 dimensions. The 3 dimensional simulations are necessary to compare our results with the experimental data, however, because there are not essential differences between the 2 and 3 dimensional cases we can obtain a good idea of the physical

process by using the much faster 2 dimensional simulations. The strong dependence of the structure factor with the wavenumber (k^{-4}) makes difficult to discern the possible differences between numerical and theoretical predictions, for this reason we normalize the numerical results with the prediction of Eqs. (6.9) and (6.10) for periodic and nonperiodic simulations respectively. The experimental results are also normalized by the prediction of Eq. (6.10). This normalization also allows us to average over nearby wavenumbers to reduce the statistical error in the spectra in the numerical results. In fig. 6.4 the discretization errors have been absorbed in the modified wavenumber \tilde{k}_\perp . Once this correction has been taken into account one can see in Fig. 6.4 the perfect agreement between the periodic numerical results and the quasi-periodic theory of Eq. (6.9) in both 2 and 3 dimensions for all wave numbers. These results show that the origin of the giant fluctuations is the coupling between the velocity fluctuations δv and the concentration gradient $\nabla \bar{c}$ (which in the quasi-periodic simulations is an additional forcing term and not the real concentration gradient $\nabla c = \nabla \delta c$).

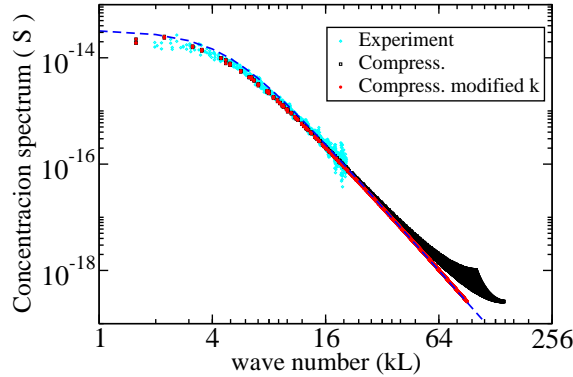


Figure 6.3: Results for the concentration structure factor $S_{cc}^\perp(\mathbf{k}) = \langle \delta c_\perp(\mathbf{k}) \delta c_\perp^*(\mathbf{k}) \rangle$ as given by the theoretical prediction of Eq. (6.10) (dashed line) experimental data (open symbols) and numerical results obtained with the compressible solver (solid symbols). The black dots present large deviations from the power law at high wavenumbers due to the discretization errors. These errors can be controlled by representing $S_{cc}^\perp(\mathbf{k})$ versus the modified wavenumber [see text and Eq. (6.13)] as we have done for the red dots.

The situations is different in the nonperiodic case. The left panel of Fig. 6.4 shows the numerical results normalized with the single mode theory [Eq. (6.10)] in the 2 dimensional case. Even if the agreement is in general good, the deviations at small wavenumbers are of about 30%. The situation in the 3 dimensional case (right panel of Fig. 6.4) is similar. In this case we include also the experimental results of Vailati et al. [Vailati 2011]. The difference, of about 50% between theory and experimental results is not negligible but it has been passed unobserved by the use of a *log-log* representation of the results (see Fig. 2 of Ref. [Vailati 2011]). Also, even if the statistical error of the numerical results (shown as error bars) difficult the comparison, it is clear that the amplitude for the small wavenumbers decrease with the Schmidt number. In fact, the agreement between the experimental values ($Sc \approx 3 \cdot 10^3$) and our numerical results are better for the highest Schmidt number employed, $Sc = 20$. We conjecture that in the limit $Sc \rightarrow \infty$ numerical and experimental results should collapse into a master curve.

The effect of finite Schmidt numbers is not clear at this stage and it is difficult to address it analytically. However, in the related problem of a single particle diffusion (see Sec. 3.6.6 or Ref. [Usabiaga 2013c]) we observe that finite values of the Sc number have a profound effect on the sys-

tem behavior. We think that a similar effect is present here. This will suggest that the separation of time scales between the momentum and the concentration diffusion that we have employed falls somewhat short. The role of the Schmidt number remains, however, an open question.

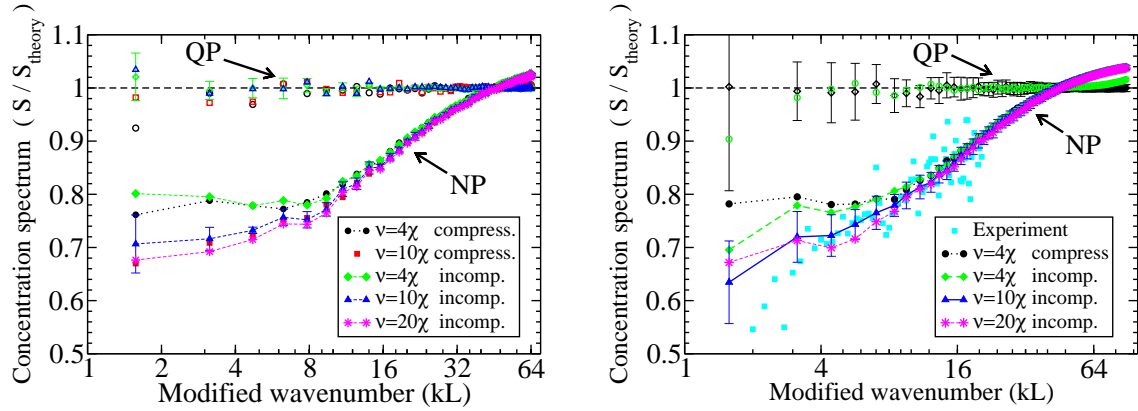


Figure 6.4: Concentration structure factor $S_{cc}^{\perp}(k) = \langle \delta c_{\perp}(k) \delta c_{\perp}^*(k) \rangle$ versus the modified wave number [Eq. (6.13)]. The results are normalized with the theoretical prediction of Eqs. (6.9) and (6.10) for quasi-periodic (QP, empty symbols) and nonperiodic (NP, full symbols) systems respectively. Error bars, shown for some curves, indicate the typical amplitude of the statistical errors. Results for 2 and 3 dimensional systems are presented in the left and right panels. The main features do not change with the space dimensionality. The experimental data (right panel) shows a good agreement with the numerical results, specially for the simulations with the largest Schmidt number, $Sc = 20$.

In this chapter we have studied a complex problem by means of two simplified theories [de Zárate 2004] and the numerical methods of Chapter 2. The simplified theories have been very successful predicting the concentration profile in the steady state and scaling of the fluctuation amplitudes with the fluid transport coefficients and the system size. Therefore, they are incredible useful to obtain a deep understanding of the physical processes involved in the diffusive mixing process. Also, they have shown a good agreement over several orders of magnitude ($k \sim 16 - 2000 \text{ cm}^{-1}$), however, their predictions show deviations of up to a 50% when compared with the experimental results and therefore, their applicability to produce quantitative predictions are limited. We have shown here that numerical methods can improve the predictions by including nonlinear terms or complex boundary conditions which are very difficult to include in analytical calculations.

Chapter 7

Applications of ICM: acoustic forces

Contents

7.1	Acoustic forces: theory	135
7.1.1	Monopolar acoustic forces	137
7.1.2	Dipolar acoustic forces	137
7.1.3	Standing planar waves	138
7.1.4	Acoustic forces in the blob model	138
7.2	Acoustic forces: simulations	139
7.2.1	Monopolar acoustic forces	139
7.2.2	Dipolar acoustic forces	140
7.2.3	Finite size effects: secondary radiation forces	140
7.2.4	Boltzmann distribution and standing waves	142
7.3	Concluding remarks	144

In this chapter we use the Inertial Coupling Method (ICM) with particles with arbitrary compressibility (see Chaps. 3 and 4) to study the fast ultrasound-particle interaction or acoustic forces. Such force, known as acoustic radiation force [Settnes 2012], was theoretically predicted for rigid objects in a fluid by King [King 1934] in 1934 and two decades later extended to compressible particles by Yoshioka and Kawashima [Yoshioka 1955]. In the sixties, Gor'kov [Gor'kov 1962] published an elegant approach in the soviet literature, showing that in the inviscid limit (large enough frequencies) the radiation force for standing waves can be derived from the gradient of an effective potential energy $\mathbf{F}_{ac} = -\nabla U_{ac}$; a result that has been quite useful for subsequent engineering applications. The (sometimes called [Wang 2011]) Gor'kov potential, scales with the particle volume \mathcal{V} and has contributions from the time-averaged pressure p_{in} and velocity v_{in} of the incoming wave,

$$U_{ac} = -\frac{\mathcal{V}}{2} \left[\kappa_e \langle p_{in}^2 \rangle + \frac{3m_e}{2m + \rho_0 \mathcal{V}} \rho_0 \langle v_{in}^2 \rangle \right], \quad (7.1)$$

where ρ_0 is the fluid density and $\langle x \rangle = (1/\tau) \int_0^\tau x(t) dt$ and $\tau = 2\pi/\omega$ is the oscillation period. These two contributions to the acoustic potential (7.1) are proportional to particle excess-quantities relative to the fluid values. In particular, $m_e = m - \rho_0 \mathcal{V}$ denotes the excess of particle mass (m) over the mass of fluid it displaces $\rho_0 \mathcal{V}$ (see Chap. 3) and $\kappa_e = \kappa_p - \kappa_f$ is the excess in particle compressibility ($\kappa = (1/\rho) \partial \rho / \partial \pi$) relative to the fluid (see Chap. 4). Despite their relevance, the early papers on acoustic radiation were rather scarce in explanations and recent theoretical works revisiting this phenomenon

have been most welcome (see [Settnes 2012] and citations thereby). Bruus [Settnes 2012] used a perturbation expansion in the (small) wave amplitude to show that both terms in Eq. (7.1) are in fact related to the monopole and dipolar moments of the flow potential, which are uncoupled in linear acoustics. He also extended the analysis to the viscous regime (smaller frequencies) generalizing previous studies by Doinikov [Doinikov 1994, Doinikov 1997] and others (see [Settnes 2012]).

The first application of ultrasound forces were carried out in the eighties by Maluta *et al.* [Dion 1982]. They used standing waves to trap and orient wood pulp fibers diluted in water into the equidistant pressure planes. The idea was used by the paper industry to measure the fiber size. Recently the usage of ultrasound for manipulation of small objects is flourishing and offering many promising applications for material science, biology, physics, chemistry and nanotechnology. An excellent review of the current state-of-art can be found in the monographic issue on the journal *Lab on a chip* [Volume 12, (2012)] and also in the review of Ref. [Friend 2011] which focuses on applications, cavitation and more exotic phenomena. Trapping extremely small objects (reaching submicron-sizes) using ultrasound, in what has been called “acoustic tweezers” [Ding 2012], is explored by several groups [Oberti 2007, Ding 2012] and used for many different purposes, such as to move and capture colloids [Oberti 2007] or even individual living cells without even damaging them [Haake 2005b, Ding 2012].

Despite the increase in theoretical and experimental works, there are not too many numerical simulations on ultrasound-particle interaction. Its cause might be the inherent difficulties this phenomenon poses to numerical calculations. The acoustic force arises as a non-linear coupling between two fast-oscillating signals and only manifests after averaging over many oscillations. This means a tight connection between the fastest hydrodynamic mode (sound) and the much slower viscous motion of the particle, at a limiting velocity dictated by the viscous drag. The situation, from the numerical standpoint, is even worse if one is interested in studying the dispersion of many small colloids around the loci of the minima of the Gor’kov potential, because dispersion is a diffusion-driven process and requires much longer time scales. Colloidal dispersion around the accumulation loci is certainly important and a nuisance for many applications. It was first studied by Higashitani *et al* [Higashitani 1981], who worked with the hypothesis that the particles follow a Boltzmann distribution based on the acoustic potential energy. Simulation of a swarm of particles diffusing under acoustic radiation involve solving an intertwined set of mechanisms acting over time-scales spanning over many decades. As a typical example, in a liquid, sound crosses a micron-size colloid in $R/c_F \sim 10^{-9}$ seconds, while the colloid diffuses its own radius in $R^2/D \sim 10^0$ seconds. Such wide dynamic range is certainly impossible to tackle for any numerical method involving a detailed resolution of each particle surface.

An important task for numerical studies in the realm of acoustic force applications is the determination of the pressure pattern in resonant cavities [Skafte-Pedersen 2008, Dual 2012]. The main objective of these calculations, which solve the Helmholtz wave equation (but do not involve any particle) is to forecast the pressure nodes inside the chamber, where colloidal coagulation is expected to occur. Using a *one-way-coupling* approach [Maxey 1983], it is also possible to get some insight on the particle trajectories, by directly applying the theoretical acoustic forces together with the (self-particle) viscous drag [Muller 2012]. This leads however to uncontrolled approximations [Skafte-Pedersen 2008] which neglect significant non-linear effects such as the hydrodynamic particle-particle interactions and the effect of multiple particle scattering on the wave pattern [Feuillade 1996].

Another group of numerical studies explicitly calculate the acoustic force on objects although, to the best of our knowledge, have been so far restricted to single two-dimensional spheres (or, more precisely axially projected “cylinders”) [Wang 2009]. These works were based on finite element or finite volume discretizations of the fluid and the immersed object, with explicit resolution of its surface (no-slip and impenetrability conditions). The effect of viscous loss has been studied in a recent work [Wang 2011]. There are also some calculations using Lattice Boltzmann solvers [Barrios 2008] also involving single

2D cylinders and an ideal fluid. It has to be mentioned that all these works considered rigid particles. In fact, implementing a finite particle compressibility is not straightforward for this type of surface-resolved approach as it would demand implementing elastic properties to the solid and couple it to the dynamics of the particle interior [Hasegawa 1979]. Another downside of fully fledged resolution is the large computational cost per particle which limits feasible simulations to few particles at most.

We show in this chapter how the ICM together with blobs with controlled compressibility can accurately model the acoustic forces acting of particles with arbitrary contrast factor (any excess in particle compressibility and/or mass). Any numerical method aiming at a correct representation of acoustic radiation forces requires two key ingredients: First, an instantaneous particle-fluid coupling to capture the extremely fast momentum exchange. Second, it should be able to model particles with compressibility different from that of the carrier fluid. Our method is one of the few models satisfying both requirements.

We start by reviewing the theory of acoustic forces in Sec. 7.1. In Sec. 7.2 this theory is shown to agree with the numerical results. A study of the dispersion of a small colloid under a standing wave is also presented (Sec. 7.2.4). Finally, concluding remarks are given in Sec. 7.3.

7.1 Acoustic forces: theory

We now briefly explain the origin of acoustic forces but for a more comprehensive theoretical description please see Refs. [Gor'kov 1962, Settnes 2012] (also [Landau 1987, Doinikov 1997, Bruus 2010]). We start by considering a fluid under otherwise quiescent condition, which is submitted to an oscillatory mechanical perturbation (maybe through one of its boundaries) which creates a standing acoustic wave. The force exerted on the particle by the fluid is the average flux of momentum across the particle surface. Viscous forces are only important near the particle surface $r = a$, where the oscillating fluid velocity field is enforced to match the particle velocity. At a distance $\delta = \sqrt{2\nu/\omega}$ from the particle surface, called viscous penetration length or sonic boundary layer, the fluid inertia (transient term) $\rho\partial_t v \sim \rho\omega v$ becomes of the same order than viscous forces $\eta\nabla^2 v \sim \eta\delta^{-2}v$. For $|r - a| > \delta$ the fluid can be treated as ideal (inviscid) so the ratio δ/a determines the relevance of the viscous regime [Settnes 2012]. Here we focus on the inviscid regime ($\delta \ll a$) where we expect that the inertial (instantaneous and energy conserving) coupling will *quantitatively* capture the acoustophoretic forces on small particles with arbitrary acoustic contrast. In the inviscid regime bulk forces vanish and the force exerted on the particle can be calculated as the momentum flux across any surface S that encloses the particle

$$\mathbf{F} = - \oint_S \langle \rho \mathbf{v} \mathbf{v} + \pi \mathbf{I} \rangle \cdot \mathbf{n} d^2 r. \quad (7.2)$$

The amplitude of the sound wave is assumed very small, so a standard approach consists on expanding the hydrodynamic fields with respect the equilibrium state in terms of a series of perturbative fields (ρ_n , \mathbf{v}_n) whose amplitude decrease like ε^n , where $\varepsilon \equiv \Delta\rho/\rho_0$ is the *small* incoming wave amplitude (see [Settnes 2012] for details). To second order,

$$\rho = \rho_0 + \rho_1 + \rho_2, \quad (7.3)$$

$$\pi = \pi_0 + c_f^2 \rho_1 + \pi_2 \quad (7.4)$$

$$\mathbf{v} = \mathbf{v}_1 + \mathbf{v}_2, \quad (7.5)$$

where c_f is the fluid isothermal speed of sound. The time dependence of any hydrodynamic perturbative field (say Φ_i with $i > 0$) should have a fast oscillatory contribution with the same frequency as the forced sound wave, i.e. $\Phi_i(\mathbf{r}, t) = \phi(\mathbf{r}) \exp(i\omega t)$. The average $\langle \Phi \rangle = (1/\tau) \int_0^\tau \Phi(\tau) d\tau$ over the wave period $\tau = 2\pi/\omega$ vanishes. Inserting this expansion into the mass and momentum fluid equations leads to a

hierarchy of equations at each order in the wave amplitude. Of particular importance in this expansion is the equation for the second order pressure term π_2 , from the Euler equations (Navier-Stokes equations for $\eta, \zeta = 0$) one can find the average [Bruus 2010, Settnes 2012]

$$\langle \pi_2 \rangle = \frac{1}{2} \kappa_f \langle \pi_1^2 \rangle - \frac{1}{2} \rho_0 \langle \mathbf{v}_1^2 \rangle. \quad (7.6)$$

When used the expansion of Eqs. (7.3)-(7.5) in Eq. (7.2) the time-average of the first-order momentum change rate yields no resulting mean force. However, at second order, the average of non-linear terms (such as $\langle \rho_0 \mathbf{v}_1 \mathbf{v}_1 \rangle$) do not vanish ($\langle \cos(\omega t)^2 \rangle = 1/2$) and create the so called radiation force. The lower order nonzero contributions to the force are

$$\begin{aligned} \mathbf{F} &= - \oint_S [\langle \pi_2 \rangle \mathbf{n} + \rho_0 \langle (\mathbf{n} \cdot \mathbf{v}_1) \mathbf{v}_1 \rangle] d^2 r \\ &= - \oint_S \left[\left(\frac{\kappa_f}{2} \langle \pi_1^2 \rangle - \frac{\rho_0}{2} \langle \mathbf{v}_1^2 \rangle \right) \mathbf{n} + \rho_0 \langle (\mathbf{n} \cdot \mathbf{v}_1) \mathbf{v}_1 \rangle \right] d^2 r. \end{aligned} \quad (7.7)$$

To calculate the acoustic force one has to determine the velocity and pressure to first order in the perturbation. In the inviscid limit $\mathbf{v}_1 = \nabla \phi$ and $\pi = -\rho_0 \partial_t \phi$ where the velocity potential $\phi(\mathbf{r}, t)$ can be expressed as the sum of the incoming (in) and scattered (sc) waves

$$\phi(\mathbf{r}, t) = \phi_{\text{in}}(\mathbf{r}, t) + \phi_{\text{sc}}(\mathbf{r}, t). \quad (7.8)$$

The incoming wave $\phi_{\text{in}}(\mathbf{r}, t)$ and the particle properties (inertia and compressibility) determine the scattered wave $\phi_{\text{sc}}(\mathbf{r}, t)$ which in turn determines the acoustic force. When the particle is much smaller than the wavelength of the incoming wave the scattered field can be written as a time-retarded multipole expansion. At large distance from the particle (note that to calculate the force we can use the flux of momentum across any surface that encloses the particle) the expansion is dominated by the monopole and dipole terms. Therefore, the scattered field is of the form $\phi_{\text{sc}} = b(t - r/c_f)/r - \nabla \cdot (\mathbf{B}(t - r/c_f)/r)$, where the first and second terms correspond to the monopole and dipole terms respectively and $b(t)$ and $\mathbf{B}(t)$ are a scalar and a vector functions to be determined. In the low amplitude approximation ($\Delta\rho/\rho_0 \ll 1$) the scattered wave ϕ_{sc} has to be proportional to the first order fields of the incoming wave; this reduces the possible scalar and vector functions that appear in ϕ_{sc} to the density ρ_1 and the velocity \mathbf{v}_1 up to constant factors. Therefore, one can write

$$\begin{aligned} \phi_{\text{sc}}(\mathbf{r}, t) &= \phi_{\text{mp}}(\mathbf{r}, t) + \phi_{\text{dp}}(\mathbf{r}, t) \\ &= -f_1 \frac{a^3}{3\rho_0} \frac{\partial_t \rho_{\text{in}}(t - r/c_0)}{r} - f_2 \frac{a^3}{2} \nabla \cdot \left[\frac{\mathbf{v}_{\text{in}}(t - r/c_0)}{r} \right], \end{aligned} \quad (7.9)$$

where f_1 and f_2 are two (yet) unknown constants that may depend on the particle and fluid properties. When substituting the incoming and scattered fields in the Eq. (7.7) one finds products of the form ϕ_{in}^2 , $\phi_{\text{in}} \phi_{\text{sc}}$ and ϕ_{sc}^2 . The product of terms ϕ_{in}^2 do not have information about the scattered wave and therefore can not contribute to the acoustic force. Only the product of terms $\phi_{\text{in}} \phi_{\text{sc}}$ effectively contributes to the acoustic forces (more exactly, the terms ϕ_{sc}^2 also contribute but they effect is negligible small). Therefore, the acoustic force to first order in the acoustic field can be written (after some algebra) as

$$\mathbf{F} = - \int \rho_0 \langle \mathbf{v}_{\text{in}} \left(\nabla^2 - \frac{1}{c_f^2} \partial_t \right) \phi_{\text{sc}} \rangle d^3 r. \quad (7.10)$$

For a incoming standing wave, the spatial dependence of ϕ_{in} is real and that allows us to write the acoustic force in the form (see Ref. [Settnes 2012] for details)

$$\mathbf{F} = -\nabla U_{\text{ac}}, \quad (7.11)$$

$$U_{\text{ac}} = \mathcal{V} \left[\text{Re}[f_1] \frac{\kappa_f}{2} \langle \pi_{\text{in}} \rangle - \text{Re}[f_2] \frac{3\rho_0}{4} \langle v_{\text{in}}^2 \rangle \right], \quad (7.12)$$

where only the two coefficients f_1 and f_2 , related to the monopole and dipole parts of the scattered wave, remain to be determined. Both coefficients can be found by matching the far field with the boundary conditions at the particle surface. To simplify the expressions we will assume that close to the particle the fields \mathbf{v}_1 and $\pi_1 = c_f^2 \rho_1$ depends on the instantaneous argument t instead of $t - r/c_f$. In doing so a small error $\sim a/\lambda$ is introduced. We derive the expression for f_1 and f_2 in the next two sections.

7.1.1 Monopolar acoustic forces

Conservation of mass allows us to find the expression for f_1 . Under the local pressure variations of an incoming sound wave a compressible particle pulsates and in doing so it ejects fluid mass in the form of a spherical scattered wave. If the particle and fluid compressibilities do not match, the scattered fluid mass is ejected at a rate which differs from the flux of the incoming wave. This difference creates variations in the Archimedes force which is expressed as a (monopolar) radiation force [Crum 1975, Settnes 2012]. The mass ejected by the particle is

$$\partial_t m = \oint_S (\rho_0 \mathbf{v}_{\text{sc}}) \cdot \mathbf{n} d^2r = f_1 \mathcal{V} \partial_t \rho_{\text{in}}, \quad (7.13)$$

where $\mathcal{V} = 4\pi a^3/3$ is the particle volume and $\mathbf{v}_{\text{sc}} = \nabla \phi_{\text{mp}} = -f_1(a^3/(3\rho_0)) \partial_t \rho_{\text{in}} \nabla(1/r)$. is the scattered velocity. The mass ejected can also be written to first order in the perturbed fields as

$$\partial_t m = \partial_t [(\rho_0 + \rho_{\text{in}})\mathcal{V}] = \left(1 - \frac{\kappa_p}{\kappa_f}\right) \mathcal{V} \partial_t \rho_{\text{in}}, \quad (7.14)$$

where we have used the fluid and particle compressibilities κ_f and κ_p , with $\kappa = -(1/V)(\partial V / \partial \pi)$ and the relation $\partial_t \pi_{\text{in}} = \kappa_f^{-1} \partial_t \rho_{\text{in}}$. Combining the Eqs. (7.13) and (7.14) one can find

$$f_1 = 1 - \frac{\kappa_p}{\kappa_f} = -\frac{\kappa_e}{\kappa_f}. \quad (7.15)$$

7.1.2 Dipolar acoustic forces

The dipole term is related to the particle inertia. To find f_2 one should match the fluid and particle velocity at the particle surface. Assuming the particle is small $a \ll \lambda$ and that around the particle site that incoming wave propagates in the z direction, the velocity matching can be written in spherical coordinates as

$$\hat{\mathbf{e}}_r \cdot \mathbf{u} = \hat{\mathbf{e}}_r \cdot (\mathbf{v}_{\text{in}} + \nabla \phi_{\text{dp}}) = \left(1 - f_2 \frac{a^3}{r^3}\right) \cos \theta v_{\text{in}}, \quad (7.16)$$

where \mathbf{u} is the particle velocity. Note that in the inviscid limit only the normal component of the velocity to the particle surface has to be continuous. To effectively find an expression for f_2 we need an additional equation. For example, using the Newton's third law and assuming that the particle velocity is of the form $\mathbf{u}(t) = \mathbf{u} \exp(i\omega t)$ one gets

$$i\mathcal{V} \rho_p \omega \mathbf{u} \cdot \hat{\mathbf{e}}_z = \oint_{\partial\mathcal{V}} \mathbf{n} \cdot (-(\pi_{\text{in}} + \pi_{\text{dp}}) \mathbf{I}) \hat{\mathbf{e}}_z d^2r, \quad (7.17)$$

where this time the integral is taken in the particle surface and ρ_p is the particle density. By using the pressure at the particle surface $\pi_{\text{in}} + \pi_{\text{dp}} = -\rho_0 \partial_t (\phi_{\text{in}} + \phi_{\text{dp}}) = -i\rho_0 \omega a (1 + f_2/2) \cos \theta v_{\text{in}}$ and combining the Eqs. (7.16) and (7.17) one can find

$$f_2 = \frac{2(\rho_p - \rho_0)}{2\rho_p + \rho_0} = \frac{2m_e}{2m_e + 3\rho_0 \mathcal{V}}. \quad (7.18)$$

This result was found by Gor'kov [Gor'kov 1962] and recently extended to the viscous regime ($\delta = \sqrt{2\nu/\omega} \sim a$) by Settnes and Bruus [Settnes 2012]. However, in most applications the sound frequency is very high and the equation (7.18) can be safely used.

7.1.3 Standing planar waves

Using the expression for the acoustic potential U_{ac} [Eq. (7.12)] and the monopole and dipole coefficients f_1 and f_2 [Eqs. (7.15) and (7.18)] one can derive the Gor'kov potential written at the begin of the chapter [Eq. (7.1)]. For a sinusoidal wave along the z axis with wavenumber $k = 2\pi/\lambda$ (angular frequency $\omega = kc_f$) the expression for the force can be simplified to,

$$\mathbf{F}_1 = \frac{c_f^2 \Delta \rho^2 \mathcal{V} k}{4\rho_0} \left(f_1 + \frac{3}{2} f_2 \right) \sin(2kz). \quad (7.19)$$

This force is usually called the primary acoustic force [Haake 2004, Haake 2005a].

7.1.4 Acoustic forces in the blob model

It is interesting to consider the acoustic forces on the framework of the blob model to discern, before perform any numerical simulation, if the blob model can correctly capture the acoustic forces.

For one side, the dipole force term arise from the difference between particle and fluid inertia. In Chapter 3 it was shown that the blob model indeed captures the inertial effects of the particle. Moreover, because the fluid particle coupling is instantaneous we expect that the dipole acoustic forces will be correctly described by our model.

For other side, the monopole force term appears when the finite compressibility of the particle affect the density fluctuations in the particle domain. The mass of fluid in the kernel is $m_f = \mathcal{V}\mathbf{J}\rho$ so the mass ejected by pulsation of the particle volume, can be equivalently expressed in terms of changes in the local fluid density. Consider an incoming pressure wave p_{in} which is scattered by the particle. The incoming density wave satisfies $\rho_{in} = \rho_0 \kappa_f p_{in}$, so if the particle were absent, the mass of fluid in the kernel would be $\mathcal{V}\mathbf{J}\rho_{in} = \mathcal{V}\rho_0 \kappa_f \mathbf{J}p_{in}$. However, the particle modifies the local density according to Eq. (4.14) and the total mass inside the kernel is then $\mathcal{V}\mathbf{J}\rho = \mathbf{J}(\rho_0 \kappa p_{in})\mathcal{V}$ with,

$$\mathbf{J}\rho = \left(1 + \frac{\kappa_e}{\kappa_f} \right) \mathbf{J}\rho_{in}, \quad (7.20)$$

where we have used the compressibility $\kappa = (\kappa_f + \kappa_e \mathcal{V} \mathbf{S} \mathbf{J})$ introduced in Chap. 4 [see Eq. (4.14)]. The scattered mass

$$m_{sc} = -\mathcal{V} \frac{\kappa_e}{\kappa_f} \mathbf{J}\rho_{in}, \quad (7.21)$$

is then ejected at a rate,

$$\dot{m}_{sc} = -\mathcal{V} \frac{\kappa_e}{\kappa_f} \frac{d}{dt} \mathbf{J}\rho_{in} = -\mathcal{V} \frac{\kappa_e}{\kappa_f} [\mathbf{J}(\partial_t \rho_{in}) + \mathbf{J}(\nabla \cdot \rho_{in} \mathbf{u})], \quad (7.22)$$

where the prefactor $f_1 = -\kappa_e/\kappa_f = 1 - \kappa_p/\kappa_f$ is in agreement with Gor'kov theoretical result [Gor'kov 1962, Settnes 2012]. It is noted that the advective term $\mathbf{J}(\nabla \cdot \rho_{in} \mathbf{u})$ is a second order quantity neglected in theoretical analyses [Settnes 2012] for low Reynolds numbers (recall that we assumed that at the particle surface $\rho_{in}(t - r/c_f) \approx \rho_{in}(t)$). However, particle-advective terms need to be included in studies of larger bubbles at non-vanishing Reynolds [Pelekasis 2004, Garbin 2009].

7.2 Acoustic forces: simulations

In this section we show that the ICM and the blob model are able to recover the acoustic forces discussed in the previous section. To create a standing wave in a periodic box we employ a simple method that resembles the experimental setups [Haake 2005a]. We include a periodic pressure perturbation in all the cells at the plane with coordinate $z = z_0$. The pressure perturbation has the form,

$$p^{ext}(t) = \Delta p_0 \sin(c_f k_0 t) h \delta^{\text{Dirac}}(z - z_0) \quad (7.23)$$

where $k_0 = 2\pi/L$ is (in general) the smallest wave number that fits into the simulation box of length L . In the discrete setting the delta function should be understood as a Kronecker delta $h \delta^{\text{Dirac}}(z - z_0) = \delta_{zz_0}^K$ so only the cells at the plane $z = z_0$ are forced.

A solution for the density modes can be analytically obtained by inserting the forcing pressure (7.23) into the linearized Navier-Stokes equations and transforming the problem into the Fourier space. This leads to,

$$\rho_k = \Delta \rho_k \sin(c_f k_0 t + \phi) = \frac{k^2 \Delta p_0}{\sqrt{4\Gamma^2 k^4 (c_f k_0)^2 + ((c_f k)^2 - (c_f k_0)^2)^2}} \sin(c_f k_0 t + \phi). \quad (7.24)$$

Where $\Gamma = \nu_L/2$ is the sound absorption coefficient (which, in absence of heat diffusion, equals half of the longitudinal viscosity). The singular pressure perturbation $\delta^{\text{Dirac}}(z - z_0)$ excites all the spatial modes of the box. However, since $c_f \gg \Gamma k$, the resonant mode $k = k_0$ is by far the dominant one and it is safe to assume that the incoming wave is just a standing wave with wavenumber k_0 ,

$$\rho_{in}(z, t) = \rho_0 + \Delta \rho_0 \cos(k_0 z) \sin(c_f k_0 t + \phi) \quad (7.25)$$

where $\Delta \rho_0 = \Delta p_0 h / (2\pi \Gamma c_f)$. The validity of this approximation requires working in the linear regime $\Delta \rho_0 \ll \rho_0$ (i.e. low Mach number) which is also satisfied in experiments.

We checked the validity of the present model against the theoretical expression for the (primary) radiation force in Eq. (7.19), by measuring the acoustic force felt by particles with different mass $m_e \neq 0$ or compressibility $\kappa_e \neq 0$ than the carrier fluid. To measure the acoustic force at a given location, particles were bounded to an harmonic potential $U_{\text{spring}} = -(1/2)k_{\text{spring}}(z - z_{eq})^2$ with a given spring constant and equilibrium position z_{eq} . The acoustic force displaces the equilibrium position of the spring to an amount Δl and its average gives the local acoustic force $F(\hat{z}) = k_{\text{spring}} \langle \Delta l \rangle$ where $\hat{z} = z_{eq} + \langle \Delta l \rangle$. In order to conserve the total linear momentum of the system, we place two particles at equal but opposite distances from the pressure perturbation plane $z = z_0$ (a wave antinode). In this way the momentum introduced by each harmonic force cancels exactly. Moreover to minimize the effect of secondary forces, particles were placed at different positions in the x, y plane. In most simulations the particles positions were at $\mathbf{r}_1 = (1/2, 1/2, 3/8)L$ and $\mathbf{r}_2 = (0, 0, -3/8)L$. Using these set of harmonic springs we were able to measure monopolar and dipolar acoustic forces as a function of the distance to the pressure wave node. Results are presented in the next sections.

7.2.1 Monopolar acoustic forces

According to the acoustic potential in Eq. (7.1), neutrally buoyant particles ($m_e = 0$) can only feel monopole acoustic forces proportional to the deficiency in particle compressibility $-\kappa_e$ with respect to the carrier fluid. [see f_1 in Eq. (7.15)]. The left panel of figure 7.1 represents the acoustic force observed in numerical simulations at different positions in the plane of the standing wave z . The particle speed of sound is $c_p = 2c_f$, which corresponds to a particle less compressible than the fluid [$\kappa_e = -(3/4)\kappa_f$,

see Eq. (4.12)]. Simulations of Fig. 7.1 were performed in a cubic periodic box of size $L = 32 h$ (see Table I for the rest of simulation parameters). Numerical results exactly recover the dependence of the radiation force with z given by the theoretical expression of the primary radiation force in Eq. (7.19). However, the force amplitude presents deviations of up to about 10 percent. These deviations tend to zero as the box size is increased, indicating the presence of hydrodynamic finite size effects which, as explained in Sec. 7.2.3, scale like secondary acoustic forces between particles [Crum 1975].

The right panel of figure 7.1 shows the maximum value of the acoustic force for different particle compressibilities (here, in terms of the ratio $c_p/c_f = (\kappa_f/\kappa_p)^{1/2}$). It is noted that while the dipole scattering coefficient is bounded $f_2 \in (-2, 1)$, the monopole scattering coefficient is not [$f_1 \in (-\infty, 1)$, see (7.15)]: for incompressible particles $f_1 = 1$ but f_1 diverges if particles are infinitely compressible $c_p/c_f \rightarrow 0$. This explains why ultrasound is an outstanding tool to manipulate bubbles [Garbin 2009]. As shown in Fig. 7.1, the present method correctly describes the divergence of the acoustic force in the limit of large particle compressibility, $\kappa_p \rightarrow \infty$.

7.2.2 Dipolar acoustic forces

In the left panel of figure 7.2 we plot the acoustic force along the coordinate z felt by a particle with excess of mass $m_e = m_f$ and equal compressibility than the fluid $\kappa_e = 0$. A perfect agreement is found between the numerical results and Eq. (7.19). In the right panel of the same figure we show the dependence of the maximum acoustic force with the particle-fluid density ratio ρ_p/ρ_0 . Again, a quasi-perfect agreement (1.5% deviation) is observed when compared with the theoretical expression for primary radiation force (7.19).

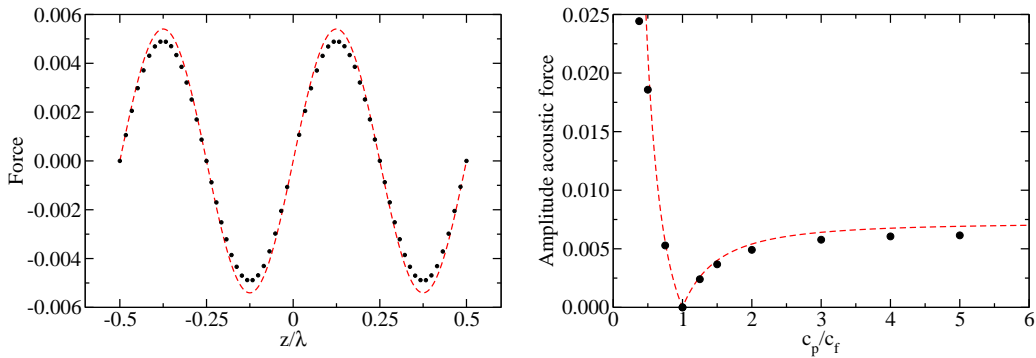


Figure 7.1: Left panel, acoustic force along the pressure wave for a neutrally-buoyant particle with $c_p = 2c_f$ (symbols). The acoustic force predicted by Eq. (7.19) (line), with no fitting parameters, is shown for comparison. Right panel, maximum acoustic force versus the ratio c_p/c_f obtained from simulation (symbols) and theory (lines). All the simulation parameters are given in table 7.1.

7.2.3 Finite size effects: secondary radiation forces

To understand the discrepancies observed between numerical and theoretical expressions for the primary radiation force in Sec. 7.2.1, we performed simulations with different box sizes L . Results, in Fig. 7.3, show that discrepancies between the numerical and theoretical forces vanishes as L increases and indicate that these deviations are not algorithmic or discretization errors but rather *finite size* effects of

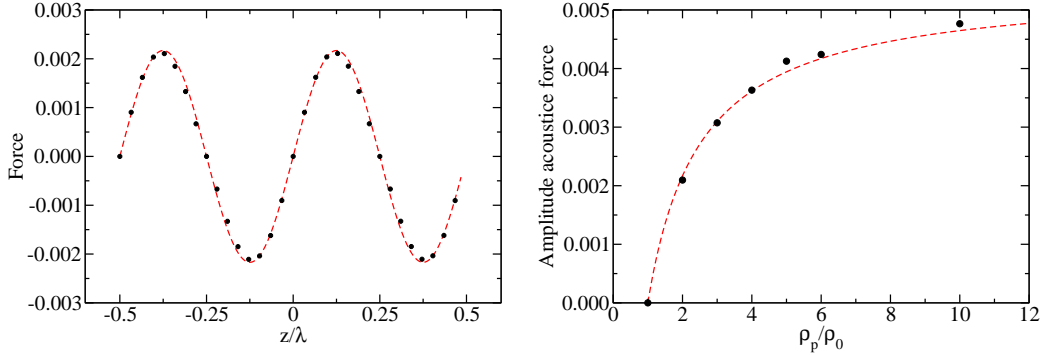


Figure 7.2: Left panel, numerical data (symbols) and theory without fitting parameters (line) for the acoustic force along the pressure wave for a non-neutrally buoyant particle with speed of sound $c_p = c_f$. Right, maximum acoustic force versus the particle fluid density ratio ρ_p/ρ_0 for $c_p = c_f$. Points represent the numerical results and red lines the theoretical prediction [Eq. (7.19)]. All the simulation parameters are given in table 7.1.

hydrodynamic origin. Notably, in a periodic box, particles can interact via secondary radiation forces [Crum 1975] arising from the scattered waves, irradiated by each particle pulsation [Garbin 2009]. We now analyze the observed deviations to show that they have the signature of secondary radiation forces.

Secondary radiation forces, also called Bjerknes secondary forces, depend on the particles' spatial configuration. The problem of elucidating the secondary forces from-and-to an array of scatters is certainly a difficult one [Feuillade 1995], but approximate expressions have been proposed for a couple of interacting particles at distance d , under certain conditions. In particular, for $R \ll d \ll \lambda$, Crum [Crum 1975], Gröschl [Gröschl 1998] and others derived the following analytical expression for the secondary forces for two particles at distance d forming at angle θ with the incident wave,

$$\mathbf{F}_2^{(p)} = -\frac{9}{4\pi} \mathcal{V}^2 \langle p_{in}^2(z) \rangle \left[\frac{\omega^2 \rho_0 \kappa_e^2}{9d^2} \right] \mathbf{e}_r \quad (7.26)$$

$$\mathbf{F}_2^{(v)} = \frac{3}{4\pi} \frac{m_e^2}{2\rho_0 d^4} \langle v_{in}^2(z) \rangle [(3 \cos^2 \theta - 1) \mathbf{e}_r + \sin(2\theta) \mathbf{e}_\theta] \quad (7.27)$$

In general, however, the secondary forces depend on the phase difference between the field scattered from particle 1 (at the particle 2 location) and the vibration of particle 2 [Crum 1975, Mettin 1997]. This phase relation is neglected in the derivation of Eqs. (7.26) and (7.27), which assumes that $p_{in}(z + d) = p_{in}(z)$ (same for the velocity field) and that both particle oscillates in phase. Details of Bjerknes secondary forces are still under research [Garbin 2009, Pelekasis 2004], for instance, in the case of bubbles, this phase difference might even lead to secondary force reversal (it is attractive for zero phase difference, see Eq. 7.26).

Let us first analyze secondary forces resulting from an imbalance in the particle density with respect the fluid density, $m_e \neq 0$, when particles have similar compressibility as the fluid $\kappa_e = 0$. In this case, the scattered field has the form of a dipole and decays with the square of the distance [Settnes 2012]. Therefore, secondary forces (dipole-dipole interaction) should decay as the fourth power of the distance, as expressed in Eq. (7.27). These type of secondary forces are thus short-ranged (and small in magnitude) so they do not induce finite size effects. Consistently, we do not observe any trace of finite size effects in simulations on dipolar acoustic forces, as shown in Fig. 7.2.

By contrast, particles with some excess in compressibility $\kappa_e \neq 0$ vibrate in response to the primary wave, acting as point-sources (monopoles) of fluid mass and creating scattered density waves. These monopolar scattered fields decays like $1/r$ so the secondary interaction between two particles decays with the square of their distance (see Eq. 7.26). This means that secondary compressibility forces are long ranged and reach image particles beyond the primary box of the periodic cell. Although the exact form of the multiple scattering problem leading to finite size effects in periodic boxes is not easy to solve, it is possible to elucidate some of their essential features. In our setup, due to symmetry, secondary forces are directed in z direction (as the primary one) so the total radiation force on one particle (say $i = 1$) should be (summing up to pair reflections in the scattering problem), $F = F_1(z_i) + \sum_{j \neq i} F_2(r_{ij})$, with j running over all particles (including periodic images) and F_1 given by Eq. (7.19).

For any particle pair, the magnitude of F_2 is proportional to the product of the fluid mass ejected by each particle, i.e. to κ_e^2 (see Eq. 7.26). Thus, for a given external wave amplitude $\Delta\rho$, the difference between the force F from simulations and the theoretical primary force F_1 should be proportional to,

$$\Delta F \equiv F - F_1 \propto \left(\frac{\mathcal{V}\omega}{c_f}\right)^2 \left(\frac{\kappa_e}{\kappa_f}\right)^2 \quad (7.28)$$

We have measured ΔF for several compressibilities ratios $|\kappa_e/\kappa_f|$ and frequencies ω . The left side panel of figure 7.3 shows ΔF against $|\kappa_e/\kappa_f| = |f_1|$ for a set of force measures which only differ in the value of κ_e . As predicted by the scaling of secondary forces (7.28), we get a quadratic dependence $\Delta F \propto |\kappa_e/\kappa_f|^2$. A slight deviation from this trend is observed for the smallest value of $|\kappa_e|$ considered (see Fig. 7.3). Near $\kappa_e = 0$ both forces (primary F_1 and secondary force) tend to zero (see Fig. 7.1) and the evaluation of ΔF becomes more prone to numerical errors. Values of ΔF for $\kappa_e > 0$ (more compressible particles) and $\kappa_e < 0$ (less compressible) were found to differ in a factor 2; the reason might come from some change in the phase difference of the interacting particles taking place at $f_1 = 0$.

In the right panel of figure 7.3 we show the relative difference $\Delta F/F_1$ obtained in simulations at different forcing frequencies ω . The primary force scales linearly with ω [see Eq. (7.19)] so, according to Eq. 7.28, the relative difference $\Delta F/F_1$ should also scale linearly in frequency, as observed in Fig. 7.3 (left). Although an analysis of the total effect of multiple scatterings of secondary forces (Edwald summation) is beyond this work, the inset of this figure shows that the effect of scattered waves from periodic images decreases with the system size.

To further check the resolution of secondary acoustic forces we performed some tests with two neutrally buoyant particles and compressibilities $\kappa_p = \kappa_f/2$. Particles were located at $\mathbf{r}_1 = (0, 0, z_0)$ and $\mathbf{r}_2 = (d, 0, z_0)$, where z_0 is the plane of the pressure antinode where the primary force vanishes. As predicted by the theory (see Eq. 7.26) the radial secondary forces were found to be attractive. At close distances $d = [2 - 3] h$, we found them to be in very good agreement with Eq. (7.26) although, at larger distances we found that they decay significantly slower than d^{-2} , probably due to the effect of secondary forces coming from the periodic images. In any case, for most practical colloidal applications the effect of secondary forces is small and quite localized. It tends to agglutinate close by colloids to form small clusters, but only after the main primary force collects them in the node-plane of the sound wave. Simulations showed that this *local* effect of the secondary forces is captured by the present method.

7.2.4 Boltzmann distribution and standing waves

Most of the experimental works on acoustophoresis employ particles with diameters above one micrometer or at least close to that size. The reason is that the acoustic force decays strongly with the particles radius and below diameters of one micrometer other forces become equally important in the

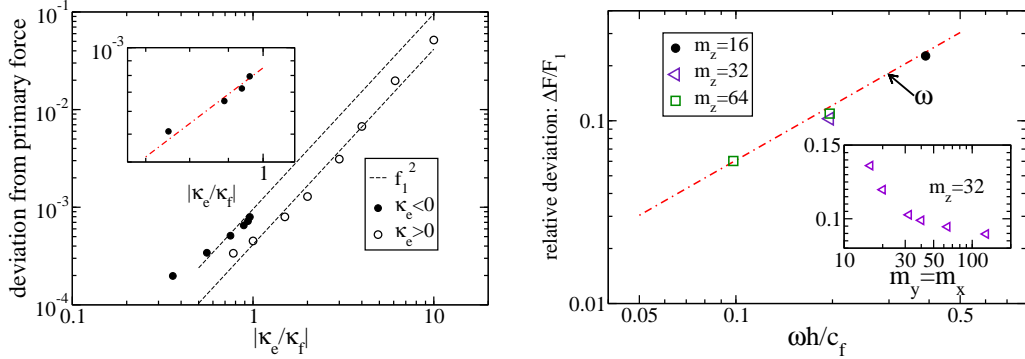


Figure 7.3: Left panel, deviation of the numerical force from the theoretical primary radiation force $\Delta F = F - F_1$ versus the ratio κ_e/κ_f with $\kappa_e = \kappa_p - \kappa_f$. All parameters as in figure 7.1. Right panel, relative deviation $\Delta F/F_1$ versus the wave frequency ω . Main figure: simulations in cubic periodic boxes with m_z cells per side; inset figure: rectangular boxes with $m_z = 32$ and varying $m_x = m_y$ showing that the effect of the periodic images decreases with the system size.

nano-particle dynamics. As stated previously, one of these forces is the streaming force [Nyborg 1965], whose nature and structure is more difficult to control [Bruus 2011]. Advances in miniaturized devices and in experimental techniques makes easy to guess that acoustophoresis will be soon extended to smaller scales (see the recent work [Johansson 2012]). An intrinsic limitation for this miniaturization process comes, however, from thermal fluctuations which strongly affect the dynamics of nanoscopic particles. Here we study how thermal fluctuations disperse sonicated particles around the minimum of the acoustic potential energy.

A standing waves exert a first-order force that oscillate with the same frequency ω than the primary wave and averages to zero [Bedeaux 1974a]. Since the diffusion of the particles is much slower than the wave period, the first-order force should not have any effect in the slow (time-averaged) dynamics of the particle, which is driven by the second-order radiation force. If the particle mass is not very large (typical particles-fluid density ratio $m/m_f \sim O(1)$) the particle inertia, acting in times of $m/\xi = (2/9)(m/m_f)R^2/\nu$, is also negligible in the time scale of Brownian (diffusive) motion (R^2/χ). This indeed is only true provided a large value of the Schmidt number $S_c = \nu/\chi \sim \nu^2 \rho R/k_B T \gg 1$ such as those found in solid colloid - liquid dispersion (here $\chi = k_B T/(6\pi\rho\nu R)$ is the Stokes-Einstein diffusion coefficient). Thus, in the Brownian time scale, the relevant forces are the radiation force F_1 , resulting from the acoustic potential Eq. (7.1), the Stokes friction (which, assuming $\langle \mathbf{v} \rangle = 0$, is equal to $6\pi\eta Ru$) and dispersion forces from fluid momentum fluctuations. Assuming there are no other momentum sources, such as secondary forces from other particles, and that there is no temperature rising from conversion of acoustic energy into heat, the resulting time-averaged motion can be described by the Brownian dynamics of a particle in an external field, given by the acoustic potential (7.1). The resulting particle spatial distribution should then follow the Gibbs-Boltzmann distribution,

$$P(\mathbf{r}) \propto e^{-U_{ac}(\mathbf{r})/k_B T} \quad (7.29)$$

This rationale was proposed in an early work by Higashitani *et al.* [Higashitani 1981], who found a good agreement with experiments in very dilute colloidal suspensions. For validation purposes, the simulations presented hereby are done within the range of validity of these approximations. Figure 7.4

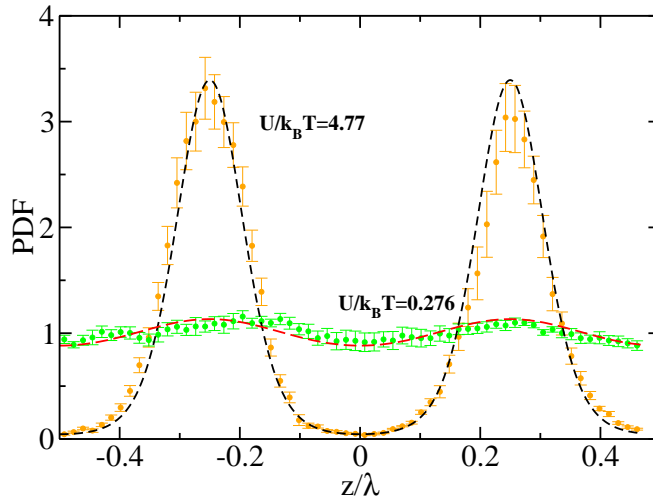


Figure 7.4: PDF for particles inside an acoustic field. Lines Boltzmann distribution. Circles PDF for a single particle (volume concentration $2.4 \cdot 10^{-4}$). Temperature $k_B T = 1$, the rest of the parameters are given in table 7.1.

shows the probability density function of the position of a single particle in a standing wave, where different wave amplitudes have been chosen so as to vary the depth of the acoustic potential well (7.1). The agreement between the numerical result and the Gibbs-Boltzmann distribution is remarkably good and illustrates the difficulty in collecting particles as soon as dispersion forces dominate, $U < k_B T$. The present method offers the possibility to investigate what happens if any of the above approximations fail; notably, in situations where non-linear couplings might become relevant, such as the effect of colloidal aggregation, secondary forces between particles or advection by thermal velocity fluctuations [Donev 2011a].

7.3 Concluding remarks

Our target in this chapter has been to assert the validity of the ICM and the blob model to study the acoustic forces acting on microparticles under sound waves. The present method can be used to resolve micron particles under several MHz, using for instance, water as carrier fluid $\nu \simeq 10^{-6} \text{m}^2/\text{s}$. It is also suited to sub-micron particles $O(0.1\mu\text{m})$, where the thermal drift [Higashitani 1981] becomes significant and one needs to include hydrodynamic fluctuations. Methods for the acoustophoretic control of sub-micron particles are now appearing and indeed require larger frequencies (up to 40MHz range) [Johansson 2012]. Another potential problem in controlling submicron particles is the drag created by the streaming velocity (the second-order average velocity field $\langle v_2 \rangle$) which at these scales, becomes comparable to the radiation force [Bruus 2011]. The streaming field $\langle v_2 \rangle$ spreads over the acoustic boundary layer of any obstacle (e.g. walls) creating, by continuity, an array of vortices [Nybørg 1965]. Streaming can be certainly resolved using the present scheme (see Chapter 2 for a description on how to add boundaries in the fluctuating hydrodynamic solver) although, for validation purposes here we use periodic boxes ($\langle v_2 \rangle = 0$) and avoid this effect.

Figure	7.1	7.2	7.4
grid spacing h	10	10	10
number of cells	32^3	32^3	32^3
fluid density	1	1	1
shear viscosity η	0.5	0.5	0.5
bulk viscosity ζ	0.5	1	0.5
fluid speed of sound c_f	4	4	4
wave frequency ω	0.0784134	0.0784137	0.0784134
pressure forcing Δp	0.005	0.005	0.005 - 0.025
density perturbation $\Delta \rho$	0.00339202	0.00240249	0.00339202 - 0.0140955
hydrodynamic radius R_H	9.9	9.9	9.9
particle excess of mass m_e	0	8000	0
particle speed of sound c_p	8	4	8

Table 7.1: Variables and parameters used in the simulations (arbitrary units). The particle volume is $\mathcal{V} = 8 h^3$ and the forcing frequency is $\omega = 2\pi c_f / L$ with $L = m_z h$ the box size.

As in any *coarse-grained* description, the present model introduces some artifacts which has to be taken into account when analyzing simulation results. In particular, acoustic forces are proportional to the particle volume \mathcal{V} which, in principle, could be used to define a particle *acoustic radius* $R_a = (6/\pi)^{1/3} h \approx 1.2407 h$. This “acoustic radius” however is *not* the particle hydrodynamic radius, which for the present surface-less, soft-particle model takes a somewhat smaller value $R_H = 0.91 h$ (see Chap. 3).

The present model cannot properly resolve viscous effects related to the acoustic boundary layer $\delta = \sqrt{2\nu/\omega}$. The radius R of the present one-kernel-particle model is similar to mesh size h , so for $\delta \sim R \sim h$ the flow inside the viscous layer is ill-resolved. We observe a limited sensitivity of the resolved dipolar forces to the size of the acoustic layer. For instance, the primary force in Fig. 7.2 corresponds to $\delta \simeq 0.28 R_a$ and it is found to be about 2% larger than the inviscid limit result ($\delta \rightarrow 0$), however Settnes and Bruus [Settnes 2012] predict that viscous effects should increase this force in about 10%. Nevertheless, the present approach offers a route to describe these finer details by adding more computational resources to the particle description (larger object resolution, in the spirit of fluid-structure interaction [Peskin 2002, Fai 2013]). We believe the save in computational cost would be still large compared with fully-Eulerian (particle remeshing) schemes and would allow to resolve the acoustic boundary layer (around “arbitrary” 3D objects) and provide more accurate descriptions of secondary acoustic forces and multiple scattering interaction in multiparticle flows.

Comparison with theoretical expressions shows that the present generalization of the IC method accurate resolves acoustic forces in particles with arbitrary acoustic contrast (any excess in particle compressibility and/or mass). The benefit of this minimally-resolved particle model is that although it has a very low computational cost, it naturally includes the relevant non-linear hydrodynamic interactions between particles: mutual hydrodynamic friction, history forces [Garbin 2009] convective effects and secondary forces. Interesting non-trivial effects such as changes in the wave pattern due to multiple scattering [Feuillade 1995] or sound absorption by colloids or bubbles [Kinsler 2000, Riese 1999] can also be simulated, in this later problem, the rate of momentum dissipation inside a droplet or a bubble can be also generalized by embedding a local particle viscosity inside the kernel.

Chapter 8

Application of Brownian dynamics: Polymers in shear flow

Contents

8.1	Polymer structure and dynamics: overview	148
8.1.1	Polymer structure	148
8.1.2	Polymer dynamics: the Rouse chain	149
8.1.3	Hydrodynamic effects: the Zimm chain	151
8.1.4	Flow time scales	152
8.2	Polymers in shear flow	152
8.3	Polymer models	154
8.4	Results	155

Over the last two decades the advance in experimental techniques, like fluorescence microscopy, have allowed the direct observation of single polymer chains in equilibrium or under creeping flows [LeDuc 1999, Smith 1999]. These experiments have boosted the interest in single polymer dynamics as a way to understand the microscopic rheology of dilute polymer melts since, for example, the intrinsic viscosity and the normal stress coefficient of the melt are directly related with the polymer configuration [Larson 2005, Schroeder 2005b].

The high number of degrees of freedom of the polymer molecules give rise to a complex dynamics, however, its rheological properties are controlled by the slowest modes that can be studied by coarse-grained methods and simple models such as the FENE dumbbell [Hsieh 2003]. From a computational point of view, this supposes a huge advantage because low resolution discretization can be employed in the study of flexible polymers.

In this chapter we study the dynamics of single polymer chains under shear flow using simple general models. We will show that the dynamic of flexible chains can be understood in terms of three characteristic times related with the internal polymer relaxation and the response to shear flow. We start with a brief overview of the theory for single chain structure and dynamics in Section 8.1. Section 8.2 introduces the problem of polymer tumbling under shear flow and Section 8.3 presents the computational models used. Results and conclusions are given in Section 8.4.

8.1 Polymer structure and dynamics: overview

In this work we have considered linear polymers in the dilute regime, where chains do not overlap or interact. In fact, we consider the limit of single chain dynamics. For completeness, this section presents a fast overview of the main results of polymer theory concerning the average shape and size and dynamics of a single chain in solution. The reader is referred to some of the abundant books on this subject [Doi 1994, Rubinstein 2003, Strobl 1997]. Apart from recalling the main scaling laws of polymeric chains in solution, this introduction serves to justify the need for treating the polymer dynamics in the Brownian limit (5.6). Along the rest of this chapter we will consider infinitely dilute polymeric chains in unbounded domains, for which the Rotne-Prager tensor provides a fairly good approximation.

8.1.1 Polymer structure

Polymeric chains are usually very large molecules formed by the repetition of one or several types of covalently bonded molecular units (called monomers), which can be ordered in many different ways [Rubinstein 2003]. The polymer microstructure (radicals, tacticity, heterogeneity, architecture) provides many of the polymer properties; however one of the great success of polymer science has been to unveil that their main features can be understood in an universal sense, independently on the molecular and chemical details. This fact permits to use simplified, or “coarse-grained” models to derive general conclusions which can be applied to some of the polymer universal families. One of the first concepts in theory of polymer coarse-graining is the *Kuhn length* which measures the size of statistically independent portions of the chain. By definition, the relative orientation of successive Kuhn segments is completely uncorrelated (i.e. freely jointed) [Rubinstein 2003]. Coarse-grained models, such as the freely jointed chain are constructed with effective monomers or beads, which correspond to a succession of Kuhn segments with the same polymer end-to-end distance as the real polymer. A related quantity is the *persistence length* l_p , defined as the length over which correlations in the direction of the tangent of the chain line are lost. The persistence length is a mechanical property related to its Young modulus which quantifies the chain stiffness. Chains can be very stiff $l_p \gg L$, semiflexible $l_p \sim L$ or flexible $l_p \ll L$. This means that the behaviour of a chain depends on its maximum length L , as for any given l_p , a long enough chain $L \gg l_p$ behaves like an ideal freely jointed chain [Rubinstein 2003]. This thesis presents results for linear flexible chains formed by $N + 1$ monomers (or more generally Kuhn segments of size b) placed at positions $\mathbf{q}_n(t)$ (with $n \in [0, N]$). The maximum chain length being $L = N b$. Consecutive monomers are bonded, with either linear (fully extensible) or non-linear (finite extension) springs.

Universal scaling laws for the polymer size and dynamics are independent on these statistical units and do have predictive power (if properly defined). A standard quantity to measure the chain dimension is the gyration radius R_g which measures the polymer width around its center of mass $\mathbf{q}_G = \sum_n^N \mathbf{q}_n$,

$$R_g^2 = \frac{1}{N} \sum_{n=0}^N \langle (\mathbf{q}_n - \mathbf{q}_G)^2 \rangle. \quad (8.1)$$

Here the brackets denote average over many polymer configurations. Another common measure of the polymer size is the end-to-end vector $\mathbf{P}(t) = \mathbf{q}_N(t) - \mathbf{q}_0(t)$.

The effective monomer-monomer interaction is essential to determine the relation between R_g (or \mathbf{P}) with N . The potential interaction between monomers $U(q_{ij})$ is mediated by the solvent and can be attractive (bad solvent) or repulsive (good solvent) respectively if the monomers “like” each other more than the solvent or not. At a mean-field level of description, such interaction can be measured by the excluded volume (proportional to the second virial coefficient) $v = -\int (1 - \exp[-\beta U(r)]) d^3 r$.

For a good solvent $v > 0$, while poor or bad solvents $v < 0$ (the limits being $-b^3 < v < b^3$). The case $v = 0$ corresponds to the so called Theta solvent [Doi 1994], where the chain approaches the ideal (Gaussian) chain (see below). Here we mimic the excluded volume interactions using purely repulsive Lennard-Jones potentials ($v > 0$) and also considered the ideal case $v = 0$ (non-bonded interactions are absent).

Flory theory [Flory 1949] was one of the first sucessfull predictions for the gyration radius scaling law, leading to a universal power law of the form,

$$R_g \sim N^\nu b$$

where ν is the so called Flory exponent. In the ideal chain, where there is no interaction between non-bonded monomers, the chain path is a pure random walk, whose variance (mean square displacement) scales like $N^{1/2}$. Thus $\nu = 1/2$ for the ideal chain. Flory used a quite simple mean field theory to predict that if the monomers interact in a good solvent, they expand or swell with $\nu = 3/5$. Interestingly, (provided $v > 0$) this scaling law is independent on the excluded volume parameter v which just enters in the prefactor. Finally, a bad solvent yields $\nu = 1/3$ indicating that the monomers collapse to a dense (globular) shape. The exact evaluation of ν and its effect on the polymer configuration is a long standing problem which expands even to recent times. More sophisticated theories for the Flory exponent in good solvent predict $\nu \simeq 0.588$ [Doi 1994], and agree reasonably well with experiments and simulations.

8.1.2 Polymer dynamics: the Rouse chain

The simplest description of the single chain dynamics is the Rouse model which assumes that consecutive monomers in the chain are bonded with harmonic potentials and do not interact by any other means. In particular, in the Rouse chain the non-conservative forces arising from the mutual hydrodynamic friction between parts of the chain is completely neglected. In practice, each bead is just subject to its self-friction force which is complete independent of the configuration of the rest of the chain. This might seem a crude approach, but it works quite well at large enough polymer concentration, when the hindrance of many chains actually screen the hydrodynamic interactions [Dünweg 2009].

The Eq. (5.6) describes a Rouse chain of $N + 1$ beads by using the following mobility μ and force F ,

$$\boldsymbol{\mu}_{ij} = \frac{\delta_{ij}}{\zeta} \mathbf{I}, \quad (8.2)$$

$$\mathbf{F}_i = -\frac{\partial U_{\text{bonded}}}{\partial \mathbf{q}_i}, \quad (8.3)$$

$$U_{\text{bonded}} = \frac{k}{2} \sum_{i=1}^N (\mathbf{q}_i - \mathbf{q}_{i-1})^2, \quad (8.4)$$

where ζ is the bead friction coefficient and U_{bonded} the potential energy of the chain related to bonded interactions. It is noted that this linear spring model allows for an arbitrary chain elongation ($L = N b$ is not bounded), so it will not recover the finite extensibility of real polymers. Invoking the equipartition theorem it is not difficult to show that in this model the spring constant k is related to the temperature and the mean bond length b by

$$k = \frac{3k_B T}{b^2}. \quad (8.5)$$

An equivalent description of the polymer dynamics can be made using the Fokker-Planck equation for the density of states $\Psi(Q)$, where $Q = \{\mathbf{q}_n\}$ represents the whole set of monomer positions (see e.g.

[Doi 1994]),

$$\partial_t \Psi(\mathbf{Q}) = \nabla_{\mathbf{Q}} \cdot (\boldsymbol{\mu} (k_B T \nabla_{\mathbf{Q}} \Psi + \Psi \nabla_{\mathbf{Q}} U)). \quad (8.6)$$

For the mobility and potential energy introduced above, it can be shown that at equilibrium, the bond extension \mathbf{r} follows a Gaussian distribution

$$\Psi(\mathbf{r}) = \left(\frac{3}{2\pi b^2} \right)^{3/2} \exp \left(-\frac{3r^2}{2b^2} \right). \quad (8.7)$$

Indicating that the Rouse model is an example of *Gaussian chain* which is indeed in Theta solvent. Its gyration radius can be exactly calculated $R_g = (N/6)^{1/2}b$. Any portion of a Gaussian chain is a Gaussian chain and, in particular, the end-to-end distribution function satisfies,

$$\Phi(\mathbf{P}, N) = \left(\frac{3}{2\pi Nb^2} \right)^{3/2} \exp \left(-\frac{3\mathbf{P}^2}{2Nb^2} \right). \quad (8.8)$$

The extensional free energy of the chain is obtained from the end-to-end distribution and for the Gaussian chain results to be,

$$F(\mathbf{P}) = -k_B T \ln \Phi(\mathbf{P}, N) = k_B T \frac{3\mathbf{P}^2}{2Nb^2} + F_0. \quad (8.9)$$

The extensional chain free energy has then the form of an harmonic spring with constant,

$$k_N = \frac{3k_B T}{Nb^2},$$

For this reason it is said that a polymeric chain is a *entropic spring*. However, the effective spring of real polymers under large elongations (e.g. under strong shear) becomes non-linear and can be non-isotropic [Hatfield 1999].

The Rouse theory for single chain dynamics dissects the complicated chain fluctuation in its normal modes, the so-called Rouse modes. For a Gaussian chain the normal modes dynamics \mathbf{R}_p are easily derived from the beads configuration. The Rouse modes are given by [Doi 1994]

$$\mathbf{R}_p = \frac{1}{N+1} \sum_{n=0}^N \mathbf{q}_n \cos \left(\frac{p\pi}{N+1} (n + \frac{1}{2}) \right). \quad (8.10)$$

Introducing this expansion into the equation of motion (5.6) and using the discrete orthogonal properties of the trigonometric basis one gets an (uncoupled) set of equation for each mode of the Gaussian chain,

$$\partial_t \mathbf{R}_p = -\frac{1}{\tau_p} \mathbf{R}_p + \mathbf{f}_p \quad (8.11)$$

where the relaxation times τ_p and random forces \mathbf{f}_p for each mode satisfy,

$$\tau_p = \frac{\zeta}{4k} \left[\sin \left(\frac{p\pi}{2(N+1)} \right) \right]^{-2} \approx \frac{\zeta(N+1)^2}{k\pi^2 p^2}, \quad (8.12)$$

$$\langle f_p^\alpha(t) \rangle = 0, \quad (8.13)$$

$$\langle f_0^\alpha(t) f_0^\beta(t') \rangle = \delta_{pq} \delta_{\alpha\beta} \frac{2k_B T}{\zeta(N+1)} \delta(t - t'), \quad (8.14)$$

$$\langle f_p^\alpha(t) f_q^\beta(t') \rangle = \delta_{pq} \delta_{\alpha\beta} \frac{k_B T}{\zeta(N+1)} \delta(t - t') \quad \text{for } p > 0. \quad (8.15)$$

The mode $p = 0$ represents the motion of the center of mass, while $p > 0$ provide the amplitude of the convolutions of the chain configuration with “wavelenght” L/p in the chain path coordinate. The chain center of mass performs a diffusive motion with a mean-square-displacement given by

$$\langle (R_0^\alpha(t) - R_0^\beta(0))^2 \rangle = \delta_{\alpha\beta} \frac{2k_B T}{\zeta(N+1)} t, \quad (8.16)$$

Thus the diffusion coefficient of the Rouse chain is thus $\chi = k_B T / (\zeta N)$. This simple dependence reflects the fact that the friction of the Rouse chain is just the sum of the (self) friction of N beads moving together due to their cohesive bonds. In other words, there is no contribution to the hydrodynamic drain of the chain coming from the mutual hydrodynamic friction between its parts. In this sense, it is said that the chain is in the *free draining* limit.

On the other hand, the Rouse chain configurational modes $p > 1$ decorrelate exponentially,

$$\langle R_p^\alpha(t) R_p^\beta(0) \rangle = \delta_{\alpha\beta} \frac{k_B T \exp(-t/\tau_p)}{8(N+1) \sin^2(p\pi/(2(N+1)))} \quad \text{for } p = 1, 2, \dots \quad (8.17)$$

The relaxation times in Eq. (8.12) indicate that the longest relaxation time correspond to the first mode $p = 1$, while the others decorrelate much faster, proportionally to $1/p^2$. Moreover, Eq. (8.17) tells that the amplitude of the lower modes is also much larger than the amplitude of the higher modes (as $\sin^2[p\pi/(N+1)] \sim 1/p^2$, for $p/(N+1) \ll 1$). This means that the polymer configurational dynamics are governed by the lowest modes and, in fact, a valid description of the chain tumbling under shear flow can be made just in terms of the first Rouse mode dynamics. In passing, we note that this fast decay of higher modes permits to use quite simple models for qualitative chain descriptions. In particular the dumbbell model, consists on two bonded monomers so it just has one non-trivial mode.

Also, the end-to-end vector in the Rouse model can be approximately expressed in terms of a mode expansion [Doi 1994]

$$\mathbf{P}(t) \approx -4 \sum_{p \text{ odd integer}} \mathbf{R}_p(t). \quad (8.18)$$

The highest modes have a much smaller contribution due to their lower amplitude and to some extent the end-to-end vector is controlled by the first mode. Experimentally it is possible to record the dynamics of $\mathbf{P}(t)$ and in fact, the polymer relaxation time is usually defined in terms of the decoration time of the end-to-end vector. This is close (but not equal) to the first mode relaxational time τ_1 but in any case the relation is useful because normal modes are better suited for theoretical analyses.

8.1.3 Hydrodynamic effects: the Zimm chain

When the scaling laws of the Rouse model are confronted with experimental results at low polymer concentrations the agreement is, in general, very poor. To improve the model predictions it is necessary to include the hydrodynamic interactions along the polymer chain. The Zimm model introduce the hydrodynamic interactions in the chain dynamics using Oseen tensor approximation to the mobility matrix. Due to the nonlinear nature of hydrodynamic interactions, it is not possible to solve (close) the full set of stochastic equations. Zimm’s approach (see Ref. [Doi 1994] for detailed derivation) is based on using a pre-averaged form of the friction matrix which in practice substitutes the random variable $1/q_{nm}$ (the inverse of the distance between monomers) appearing in the Oseen hydrodynamic tensor by its average value $1/\langle q_{nm} \rangle$. On introducing the available statistical information about chain configuration, a key point is the assumption that the chain is a fractal object with (one only) fractal dimension $1/\nu$; so all the chain portions satisfy the same scaling law $|\mathbf{q}_n - \mathbf{q}_m| \sim |n - m|^\nu$ (where

ν is the Flory exponent for a general solvent quality). Zimm's preaveraing approach proved to be quite sucessful in predicting the scaling laws of polymers in dilute suspensions In particular, the diffusion coefficient and the relaxation time result,

$$\chi_{cm} \approx \frac{k_B T}{\eta R_g}, \quad (8.19)$$

$$\tau_p \approx \frac{\eta R_g^3}{k_B T p^{3\nu}} \approx \tau_b (N/p)^{3\nu}, \quad (8.20)$$

where we have avoided the prefactors (see [Doi 1994]). It is not difficult to understand the physics of these relations: in Eq 8.19, the diffusion of the chain center of mass is now dictated by the gyration radius. Using the Einstein relation $\chi_{cm} = k_B T / \zeta_{cm}$ this means that the overal chain friction $\zeta_{cm} \propto \eta R_g$ scales like that of a rigid body of size R_g (indeed with different prefactor). In other words, the fluid does not drain free across the polymer, which statically acts as an hydrodynamic "obstacle" dragging fluid with its motion.

On the other hand, Eq. 8.20 is generalized for an arbitrary solvent including the Flory exponent ν appearing in the mode index p . Note also that $R_g \sim N^\nu b$, so the relaxation time of the p -mode scales like that of a chain of lenght N/p . This self-similarity in dynamics (and configuration) reflects again one of the main characteristics of polymers. The relaxation time $\tau_b = b^2 / \chi_b \propto \eta b^3 / k_B T$ is the monomer relaxation time. For an ideal chain $\nu = 1/2$, $\chi_{Rouse} \sim 1/N$ while $\chi_{Zimm} \sim 1/N^{1/2}$, in other words, hydrodynamics enhance the overall chain diffusion. This is consistent with the relaxation times: in a general solvent the Rouse model predicts $\tau_p \approx \tau_b (N/p)^{2\nu+1}$ which is slower than the Zimm prediction $\tau_p \sim \tau_b (N/p)^{3\nu}$ for any $\nu < 1$.

8.1.4 Flow time scales

The Schmidt number related to any of the chain mode dynamics is a very large number for any standard polymer (maybe not for an oligomer). In particular, for the Zimm chain it is given by $Sc_p = Sc_b (N/p)^{3\nu}$ where $Sc_b = \nu \eta b / (k_B T)$ is related to the monomer, whose size ranges from $b = 2\text{nm}$ in polystyrene to 100nm in double helical DNA. This means that polymer dynamics evolve in the Stokes limit, where inertia is not important.

A chain under flow will however tend to affinely deform with the fluid at a rate given by the local average velocity gradient $\dot{\gamma} \equiv |\nabla \mathbf{v}|$. If the flow deformation is faster than the polymer relaxation time τ_0 (here we take that of the slowest mode $\tau_0 = \tau_{p=1}$) the chain will not recover its equilibrium (average) configuration; it will elongate and start offering a different resistance (stress) due to the elongated entropic spring. The nondimensional parameter governing this phenomena is the Weissenberg number $Wi = \dot{\gamma} \tau_0$ so not unexpectedly $Wi > 1$ is the starting point of all the viscoelastic behaviour of polymers, which otherwise ($Wi < 1$) behave in a purely diffusively (viscous) way, as they do in equilibrium. At large Wi the chain reaches its maximum lenght at some point and, the finite chain extensibility becomes an important issue. This obviously alters the chain dynamics (as it cannot be further deformed, the chain tilts and rotates) and more generally the polymer rheology. This fact is clearly observed in the study on flexible polymer under shear flow presented in next sections.

8.2 Polymers in shear flow

In this section we consider the dynamics of flexible polymer chains under pure shear flow. A set-up of the problem is shown in Fig. 8.1, we will refer to the three directions of the problem as: x (flow direction), y (velocity gradient direction) and z (neutral or vorticity direction). Under shear, a polymeric

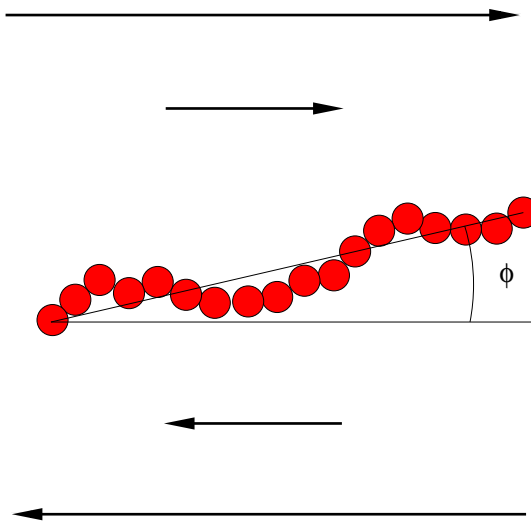


Figure 8.1: Schematic view of a polymer in the flow-gradient plane of a shear flow. The unperturbed flow is $v_0 = (\dot{\gamma}y, 0, 0)$ where $\dot{\gamma}$ is the shear rate. In our setup the x -axis correspond to the flow direction, the y -axis to the gradient direction and the z -axis to the vortical or neutral direction.

chain has no stable configuration and it continuously rotates in the flow-gradient xy -plane. The polymer is stretched along the flow but due to its finite extensibility, at large flow strength, it also tilts in the gradient direction, due to an effective flow compression. In fact, the flow drag on the chain acts like a pair of forces which elongates in x and compress in y directions. This mechanism generates a tumbling cycle. The pair of forces is proportional to the width of the polymer in the gradient direction $F_y \sim \zeta \dot{\gamma} Y$, so once the polymer is fully extended in x (i.e. $Y \sim 0$), drag forces are small, and the chain is there governed by thermal fluctuations. Any thermal chain excursion along Y direction will however push the polymer back to an unstable configuration where the shear drag forces are dominant once again and force the polymer to rotate or tumble in the flow-gradient plane, following the flow rate $\dot{\gamma}$. Just after tumbling, the polymer is stretched by the flow and the process starts all over again [Puliafito 2005, Celani 2005]. A schematic view of a polymer stretched by a shear flow is given in Fig. 8.1. Note that if a thermal fluctuation drives the angle ϕ to negative values, the flow will force the polymer to rotate very fast (at the flow rate),

First experiments on tumbling dynamics were believed to be aperiodic, that is, even if the cyclic motion repeats the same sequence over and over, two consecutive tumbling processes were supposed to be complete uncorrelated [Hur 2000]. Later experiments studied the polymer orientation in the flow-gradient plane and found a clear peak in its power spectral density (PDS) [Schroeder 2005a] proving that the tumbling process has some characteristic time scale. This result was later confirmed by experimental and theoretical works [Gerashchenko 2006, Celani 2005, Teixeira 2005]. The quality factor of the chain-elongation power-spectra decreases with decreasing flow strength (i.e. with Wi) making it difficult to observe the tumbling peak in experimental set-up which are usually limited to moderate values of $Wi < 40$.

A similar cyclic motion has been observed for a single flexible polymer chain tethered to a hard wall [Delgado-Buscallioni 2006, Lueth 2009] and in fact there has been some discussions about if this cyclic motion can be considered periodic or not [Zhang 2009]. In this chapter we only consider the dynamic of free polymers, but most part the same analysis could be applied to the tethered case.

As stated above, the main governing parameter in the system is the Weissenberg number $Wi = \dot{\gamma}\tau_0$,

defined as the product of the shear rate $\dot{\gamma}$ and the polymer relaxation time τ_0 . Although the time between two tumbling processes is a stochastic variable, its average, the tumbling time, has a well defined dependence with the Weissenberg number, $\tau_{\text{tumb}} \sim \text{Wi}^{-2/3}$ [Schroeder 2005a, Celani 2005]. This dependence has been explained by reasoning in terms of the monomer probability function (i.e. concentration). The average chain conformation under shear, should balance the convection of monomers along the flow direction with their diffusion in the vorticity-gradient plane [Gerashchenko 2006]. Other works have focused in structural [Chertkov 2005, Celani 2005] and dynamic aspects, like the distribution of tumbling times [Celani 2005, Gerashchenko 2006, Das 2008]. However, we found that there were still missing pieces of information in the characterization of flexible polymers in shear flow, in particular in the connection between structural and dynamical properties of the chain. In this chapter we will determine three characteristic times to describe the tumbling process for flexible polymers. The tumbling time τ_{tumb} that measures the average time between consecutive tumbling, a diffusive time τ_{diff} that measures the reorganization of the polymer chain in the gradient direction and finally the lag time τ_{lag} that represent the time needed for the chain to response in x direction (elongate) upon a fluctuation in its width over gradient direction.

We will show that the dynamics of polymer chains under a shear flow is a dissipative process driven by external forcing and with a well defined characteristic time. These are the characteristic features of narrowband processes [Nigam 1983] such as the damped oscillator under a random forcing. In the analysis of the results we will use this analogy to characterize the chain dynamics.

8.3 Polymer models

The present analysis is based on a coarse-grained model, i.e. we are not trying to reproduce results for any particular polymer but general (universal) features of flexible chains under shear flow. For the reasons stated above, an important feature of the model is however the finite extensibility of the chain which is modeled using finite extensible non-linear (FENE) springs between adjacent monomers, whose potential is given by,

$$U_F(r) = -\frac{1}{2}Hr_0^2 \ln \left(1 - \left(\frac{r}{r_0} \right)^2 \right), \quad (8.21)$$

where r_0 is the extensibility limit and H is the potential strength. At low Wi , the chain behaviour obtained by harmonic and FENE springs is similar. Note however that in the limit $r \rightarrow r_0^-$ the stretching energy of the FENE model diverges, providing a finite extensibility, like those of real polymer chains. This property is key to model polymers under strong elongational flows. We have performed some simulations with harmonic springs which corresponds to the Gaussian chain (denoted as GC). Results for the FENE potential are labelled with “F”.

We consider chains in good solvent $\nu \simeq 3/5$ and chains in Theta conditions $\nu = 1/2$ [Doi 1994]. Good solvent conditions are modeled by a purely repulsive Lennard-Jones potential

$$U_{EV} = \begin{cases} 4\varepsilon \left(\left(\frac{\sigma}{r} \right)^{12} - \left(\frac{\sigma}{r} \right)^6 \right) + \varepsilon & \text{for } r < 2^{1/6}\sigma, \\ 0 & \text{for } r \geq 2^{1/6}\sigma, \end{cases} \quad (8.22)$$

which provides a positive excluded volume $v > 0$. Although v might depend on the flow strength (thermal blob dimensions are reduced [Rubinstein 2003]) we will not consider this effect in the present work. Theta conditions (ideal chain) are modeled with $v = 0$, i.e. by just switching-off the non-bonded monomer interaction. We use the notation (+EV) to denote chains with excluded volume interaction and

(-EV) to denote chains without any effective excluded volume interactions. Thus, for instance, “F+EV” means a FENE chain with excluded volume. Most results corresponds to chains with $N = 2$ (dumbbell), $N = 30$ and $N = 60$ beads. The persistence length is $l_p/L \sim \sigma/(Nr_0) \sim 1/N$, corresponding to the limit of flexible polymers.

As stated, the dynamics of single flexible chains in shear can be safely captured by Brownian dynamics simulation, where inertia is vanishingly small. We performed simulations with hydrodynamic interaction along the chain, using the Rotne-Prager mobility introduced in Chap. 5 [see Eq. (5.8)] and also in the free draining limit where each monomer friction is independent (hydrodynamically uncoupled). More precisely, in the free draining limit, the hydrodynamic interactions along the chain are not included and the $3N \times 3N$ mobility matrix is just a diagonal matrix with elements $\mu_{ii} = 1/\zeta$ where ζ is the bead friction coefficient. This fact significantly reduces the computational cost, particularly for long chains since it becomes linear with the number of beads. Although we have found that hydrodynamics alter some of the effective chain properties in flow (e.g. its overall friction coefficient) the results of this chapter, concerning tumbling dynamics, are not seriously affected by hydrodynamic interactions. This is a known fact, already reported in some works (e.g. [Delgado-Buscalioni 2006]).

In the following the lenght, energy and time units are the Lennard-Jones monomer diameter σ , ε and monomer diffusive time $\tau_a = 3\pi\eta a^3/k_B T$, where the monomer hydrodynamic radius is set to $a = \sigma/2$ and the FENE extensibility to $r_0 = 1.5\sigma$. The FENE spring constant is $H = 30\varepsilon/\sigma^2$ and the reduced temperature $k_B T/\varepsilon = 1$. Finally, the fluid viscosity is set to $\eta = 0.8488$ in our reduced units.

8.4 Results

We analyze the tumbling dynamics using the first Rouse mode \mathbf{R} [in Eq. (8.10)] and the end-to-end vector $\mathbf{P} = \mathbf{q}_N - \mathbf{q}_0$. As stated, our working ansatz is that the tumbling dynamics can be understood by analogy with a damped oscillator. Thus, to characterize the tumbling dynamics we fit the autocorrelation function (ACF) of the first Rouse mode along flow $\langle X(t)X(0) \rangle$ and gradient directions $\langle Y(t)Y(0) \rangle$ to the following general function,

$$C(t) = A^2 \cos(\omega_d t + \psi) e^{-\Gamma t}. \quad (8.23)$$

This provides a natural frequency ω_0 , which is obtained from the damped frequency ω_d and the damping rate Γ by $\omega_0^2 = \omega_d^2 + \Gamma^2$. It also provides a phase constant ψ which can calculated from slope of the ACF at the origin

$$\dot{C}(0) = (1 + \alpha)\Gamma C(0), \quad (8.24)$$

$$\text{with } \alpha = (\omega_d/\Gamma) \tan \psi. \quad (8.25)$$

Another useful magnitude that one can derive from the ansatz is the phase lag $\Delta\psi = \psi_Y - \psi_X$ between the ACF of the Y and X components of the Rouse mode. The phase lag and the damped frequency provide the time lag $\tau_{\text{lag}} = \Delta\psi/\omega_d$. This time measures the delay in the response of the X component after a fluctuation of the polymer in the Y direction.

In Fig. 8.2 we present the ACF of the Rouse modes together with the fitting ansatz. The excellent agreement found over a broad range of Weissenberg numbers ($0 < \text{Wi} < 6000$) and all chain models considered (both with and without excluded volume interaction and for any number of beads) indicates that the parameters ω_0 , Γ and τ_{lag} have some relevant physical meaning concerning the tumbling process.

Figure 8.2 also gives a clear picture of the tumbling process. For long chains with excluded volume (left panel of Fig. 8.2), there is a clear succession of negative and positive peaks, reflecting the

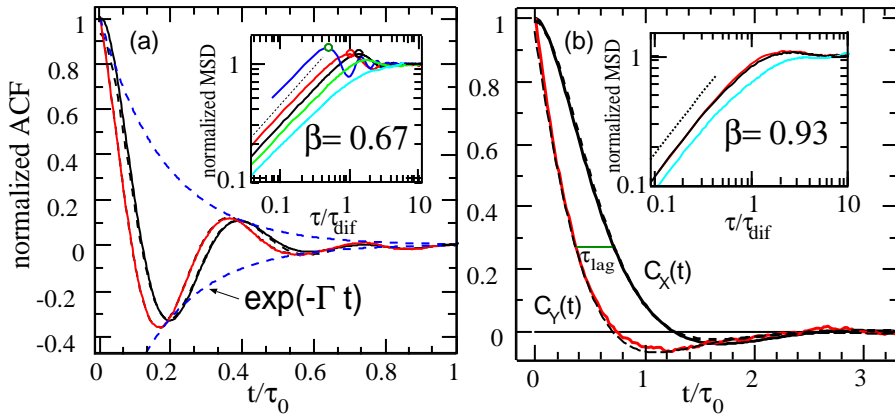


Figure 8.2: Normalized autocorrelation function (ACF) of the first Rouse mode in flow C_X and gradient direction C_Y for: (a) a FENE+EV chain with $N = 60$ at $\text{Wi} = 240$ and (b) a FENE-EV dumbbell at $\text{Wi} = 49.9$. Fits to the damped oscillator ACF are shown in dashed lines. The decay envelope $\pm \exp(-\Gamma t)$ and lag time τ_{lag} are also indicated. Insets show the end-to-end transverse MSD $\langle \delta Y_e^2 \rangle(t) \equiv \langle (Y_e(t) - Y_e(0))^2 \rangle$ normalized with $(2\langle Y_e^2 \rangle)$ versus the diffusion-scaled time ($\tau_{\text{dif}} \equiv 3Y_g^2/D_{CM}$, see text). Circles indicate the average tumbling time and lines (from bottom to top) corresponds to: (a) $\text{Wi} = \{0, 6, 90, 240, 6000\}$ and (b) $\text{Wi} = \{0, 49.9, 198\}$.

correlation between successive rotations of the chain and the periodic nature of the tumbling process. A full cycle consists in two polymer rotations, therefore a single tumbling takes a time $\tau_{\text{tumb}} \simeq \pi/\omega_0$. (more precisely $\tau_{\text{tumb}} = \pi/\omega_d$). The scaling law for the tumbling frequency has been reported to be $\omega_0 \approx \text{Wi}^{2/3}$ [Teixeira 2005, Celani 2005, Gerashchenko 2006]. We recover this scaling law for any finitely extensible chain model, independently of the excluded volume or the hydrodynamic interaction (see Fig. 8.3). The finite extensibility of the chain is thus the origin of the observed tumbling frequency scaling. A somewhat similar power law (with slightly smaller exponent) occurs in the specific polymer shear viscosity, indicating that this broadly observed shear-thinning behaviour is a result of the single chain non-linear spring dynamics. By contrast, in Gaussian chains (results not shown), the tumbling frequency converges to a finite constant value for $\text{Wi} \rightarrow \infty$ [Das 2008]. This (unrealistic) Gaussian chain behaviour is due to the lack of coupling between the chain extension in gradient direction and its overall extension (see e.g. [Das 2008]). Because of the finite extensibility of the chain, in a real polymer, the stretching along the flow direction is always followed by a compression in the other two (gradient and vorticity) directions.

One can already get some interesting conclusion. If the tumbling frequency (ω_d) is not sensible to excluded volume or hydrodynamic effects, then it should be essentially controlled to by the dynamics of the orientation angle $\phi = \arctan(Y/X)$ (see Fig. 8.1). An equation for the orientation angle ϕ can be derived [Chertkov 2005, Gerashchenko 2006] from the Rouse mode equations,

$$\dot{\phi} = -\dot{\gamma} \sin^2 \phi + \varepsilon_\phi, \quad (8.26)$$

where ε_ϕ is the random force acting in the orientation coordinate. The Langevin equation for ϕ is equivalent to the Fokker-Planck equation

$$\partial_t P(\phi) = \frac{\partial}{\partial \phi} J = \frac{\partial}{\partial \phi} \left(-\dot{\gamma} \sin^2(\phi) P(\phi) + \frac{\partial}{\partial \phi} D_\phi P(\phi) \right), \quad (8.27)$$

where D_ϕ is the rotational diffusion coefficient. When the shear is strong $\langle \phi \rangle \ll 1$ the probability

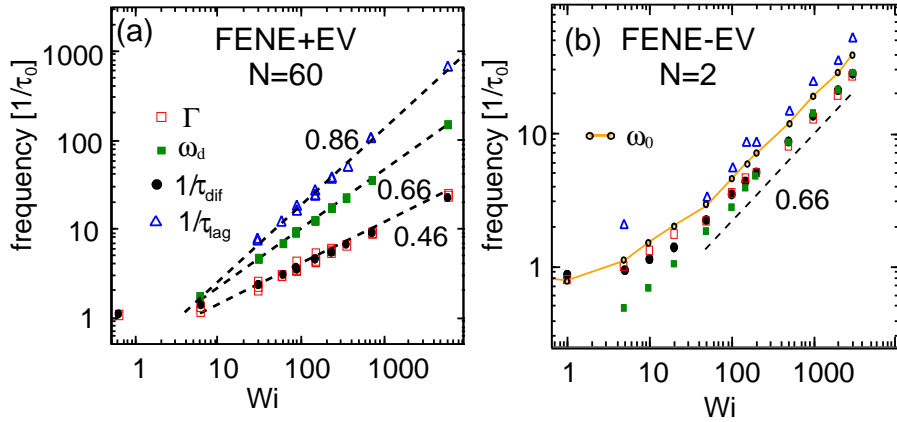


Figure 8.3: Values of ω_d , Γ and $1/\tau_{lag} = \omega_d/\Delta\psi$ obtained from fits to the elongation ACF's for two chain models (ω_d and Γ obtained from $C_X(t)$ and $C_Y(t)$ coincide within error bars). The natural frequency $\omega_0 = \sqrt{\omega_d^2 + \Gamma^2}$ is shown for the dumbbell (for the FENE+EV chain $\omega_0 \simeq \omega_d$) and $\tau_{dif}^{-1} \equiv D/(3Y_g^2)$. All frequencies scaled with the equilibrium relaxation time τ_0 . Scaling exponents are not significantly altered by chain lenght or HI.

distribution function $P(\phi)$ is sharply peaked around $\langle\phi\rangle$. Then, a scaling analysis of the Fokker-Planck equation in the steady state ($\partial J/\partial\phi = 0$) suggest that $\langle\phi\rangle \propto \text{Wi}^{-1/3}$, where we assume the angular diffusion coefficient D_ϕ is constant. Note that for a rigid rod one has $D_\phi = 1/(2\tau_0)$ [Doi 1994]. Also, at high Weissenberg numbers the dominant contribution to the tumbling time is the diffusive random walk of the orientation angle in the region $(0, \langle\phi\rangle)$ where the shear effect is small (almost horizontal chain). Therefore one gets that $\tau_{tumb} \approx \langle\phi\rangle^2/D_\phi \sim \text{Wi}^{-2/3}$. From the above arguments we conclude that the tumbling frequency scales as $\omega_d \approx \text{Wi}^{-2/3}$ and this scaling is robust against other (flexible) chain properties [Kobayashi 2010].

However, as the ansatz indicates ω_d^{-1} , is not the only characteristic time of the system. To have a complete characterization of the tumbling dynamics it is necessary to include the times $1/\Gamma$ and τ_{lag} . From the ansatz 8.23 one can see that Γ is a damping coefficient. As it is shown in Fig. 8.2 the signal's strength decays with Γ and after a few “relaxation times” (i.e. several times $1/\Gamma$) the signal becomes flat. The damping coefficient is a relevant magnitude because it determines the correlation between successive tumbling events. Since a tumbling process takes a time $\tau_{tumb} = \pi/\omega_d$ there are about ω_d/Γ correlated tumbling processes.

Since Γ is related with a relaxation rate, one can expect that it has to be related with the reorganization of the chain internal structure. The chain reorganizes its configuration in the y -direction after a time $\tau_{dif} \approx 3Y_g^2/\chi$ where Y_g^2 is the variance of the monomers y -coordinates and χ is the polymer center of mass diffusion coefficient (note that at thermal equilibrium $\tau_{dif} \approx R_g^2/\chi$). The inset of Fig. 8.2 shows the polymer end-to-end mean square displacement (MSD) in the gradient direction (Y_e) and how it reaches its equilibrium value ($2Y_e^2$) after a few diffusive times τ_{dif} . We found that in the free draining limit $\Gamma = 1/\tau_{dif}$, as shown in Fig. 8.3 for different kinds of chain models.

The results of figures 8.2 and 8.3 give a clear idea of the tumbling process and its dependence with the Weissenberg number. At small Weissenberg numbers $\text{Wi} < 1$ the polymer is coiled and because its relaxation time is faster than the flow deformation time ($1/\dot{\gamma}$) the flow only has a minor effect on the polymer. When the flow strength increases to $\text{Wi} > 1$, the polymer starts to be stretched along the flow direction x and due to its finite extensibility at the same time it is compressed in the other two directions,

and in particular in the gradient direction y . At large Weissenberg number the chain is confined in a tube of width Y along the gradient direction and it needs a time τ_{diff} to reorganize its internal configuration. At the same time, the chain is tumbling with a characteristic time τ_{tumb} . Whenever $\tau_{\text{tumb}} < \tau_{\text{diff}}$ the chain configuration maintains a correlation between successive tumblings and that explains the negative and positive peaks in the left panel of Fig. 8.2. However, if the two times are similar, the chain renews its configuration after each tumbling process and the correlation between successive tumblings is very weak, as it can be seen in the right panel of Fig. 8.2. Extensive simulations suggest that the excluded volume interaction is a key element to increase the diffusive time along the gradient direction τ_{diff} , since it tends to maintain the relative distance between beads. Figure 8.3 predicts that chains with excluded volume will maintain its configuration along $\tau_{\text{tumb}}/\tau_{\text{diff}} \approx \text{Wi}^{0.2}$ tumbling events while for chains without excluded volume the polymer renews its configuration with every tumbling. These results mean that the tumbling process become more deterministic as the Weissenberg number increases, at least for chains with excluded volume interaction.

It is possible to give an explanation of the results presented in Fig. 8.3 using a Graetz-Lévêque balance as other authors did in previous works [Hur 2000, Teixeira 2005]. These analysis argue that in the gradient direction the polymer extension Y is ruled by the diffusion-convection balance of the monomers in the shear flow. Then, the Graetz-Lévêque balance predicts the average chain extension Y is determined by the balance

$$v_x \frac{\partial Y}{\partial x} \sim D_{ef} \frac{\partial^2 Y}{\partial y^2}, \quad (8.28)$$

where D_{ef} is an effective diffusion coefficient that in general will depend on the hydrodynamic interaction and also in the monomer interaction forces. The advective velocity has a simple scaling with the polymer extension and the shear rate $v_x \sim \dot{\gamma}Y$, while the other terms scale like $\partial Y / \partial x \sim \langle \phi \rangle$ and $\partial^2 Y / \partial y^2 \sim 1/Y$. The scaling analysis of this equation suggests the relation $Y_{ex}^2 \sim D_{ef} \tau_{\text{tumb}}$ (because for a stretched polymer $\tau_{\text{tumb}} \sim 1/(\dot{\gamma}\langle \phi \rangle)$). Since the polymer under shear can be considered to be confined into a tube of width Y , one has the approximate relation $Y_{ex}^2 \approx Y^2$, from where it follows

$$D_{ef} \tau_{\text{tumb}} \sim D \tau_{\text{dif}}. \quad (8.29)$$

The scaling of the effective diffusion coefficient can be obtained from the insets of Fig. 8.2 with the relations $\langle \delta Y_e^2 \rangle \sim D_{ef} t \sim t^\beta$ for a fixed time $t < \tau_{\text{tumb}}$. One deduces the scaling $D_{ef} \sim Y^{2(\beta-1)/\beta}$. Therefore we expect that the polymer's width along the gradient direction scales as

$$Y \sim \text{Wi}^{-\beta/3}, \quad (8.30)$$

and the damping coefficient as

$$\Gamma = \tau_{\text{dif}}^{-1} \sim \text{Wi}^{-2\beta/3}. \quad (8.31)$$

These scaling laws agree well with our numerical results. Chains with excluded volume interaction show $\beta \approx 0.75$ which yield $\Gamma \sim \text{Wi}^{-0.5}$, a result in good agreement with the results of Fig. 8.3. On the other hand, the FENE dumbbell without excluded volume interaction we find the exponent $\beta \approx 1$ which yield the scaling $\Gamma \sim \text{Wi}^{-2/3}$, again in agreement with the results of figure 8.3. Therefore we conclude that the internal interaction forces of the polymer chains give raise to a non-universal exponent β that in turn it has a profound effects in the tumbling dynamics and likely the polymer rheology.

This last observation suggests that EV interactions may have some effect on the distribution of tumbling times $P(\tau)$; a revealing quantity studied by several groups [Celani 2005, Gerashchenko 2006,

[Das 2008]. To effectively measure the distribution of tumbling events it is necessary to define what is a tumbling event. In the experimental literature [Gerashchenko 2006] it has been defined as the transition between a stretched and a coiled state, however, this definition requires defining an arbitrary radius of gyration that difference the two states. We prefer to define a tumbling event as a zero-crossing of the end-to-end distance in the flow direction $X_e = 0$ (equivalently by $\phi = \pm\pi/2$) [Puljafito 2005, Das 2008]. The distribution of zero-crossings of a random signal is an extremely difficult and long-standing problem [Nigam 1983, Celani 2005], so far only analytically solved for Gaussian, Markovian processes. In this case successive crossings are completely uncorrelated and can be ascribed to a Poisson process of random arrivals [Nigam 1983]: $P(\tau) = \nu \exp(-\nu\tau)$ with $\nu = 1/\tau_{\text{tumb}}$. We have verified that (despite non-Markovian) linear chains satisfy the Poisson prediction $\nu\tau_{\text{tumb}} = 1$ at all Wi ¹. Also, FENE-EV chains are quite close to the Poissonian prediction $\nu\tau_{\text{tumb}} = 1$ (see Fig. 8.4a) and experiments with DNA strands (for a moderate $\text{Wi} < 40$) were found to agree with FENE-EV dumbbells [Gerashchenko 2006]. One may think, as implicitly assumed in previous theoretical analyses [Celani 2005, Chertkov 2005] and preaveraged models [Winkler 2010], that the Poissonian behaviour is inherent to the chain tumbling. However results in Fig. 8.4 show that this is not really true. In the overdamped regime $\text{Wi} < 1$ all chains have a Gaussian-like, Poissonian behaviour [Das 2008]. Around $\text{Wi} > 10$, FENE-EV chains deviate from the Gaussian trend but remain Poissonian, $\nu = \omega_0/\pi \sim \text{Wi}^{2/3}$. By contrast, FENE+EV chains soon abandon the Gaussian behaviour ($\text{Wi} > 1$) and then present a significantly steeper, non-Poissonian, exponent $\nu \sim \text{Wi}^{0.8(5)}$.

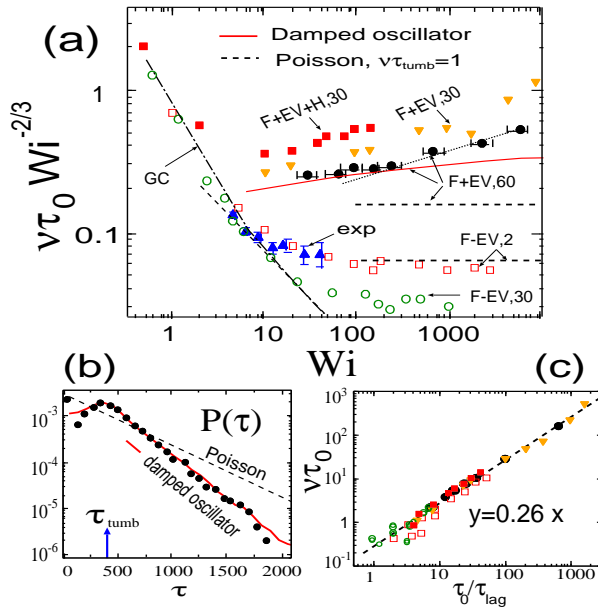


Figure 8.4: (a) The limiting decay rate ν of the tumbling time distribution $P(\tau)$ scaled with the relaxation time τ_0 and $\text{Wi}^{-2/3}$. Figures means chain length N , and labels: F=FENE, $\pm\text{EV}$ with/without excluded volume, $+H$ with hydrodynamic forces, GC=Gaussian chain [Das 2008] and “exp” experiment [Gerashchenko 2006]. The Poisson prediction $\nu\tau_{\text{tumb}} = 1$ at large Wi is indicated for some chains. The result for a damped random oscillator (red solid line) with similar Q as the F+EV $N = 60$ chain is shown in (a) and also in (b) where $P(\tau)$ (at $\text{Wi} = 90$) is compared with the Poisson distribution. (c) The master curve $\nu\tau_{\text{lag}} \simeq 0.26$ [symbols corresponds to the chains in (a).]

¹A recent analytical study [Das 2008] report $\nu\tau_0 = 0.325$ at large Wi . Our simulations yield $\tau_{\text{tumb}} = \tau_0/0.34$

It is well known that the Poisson assumption of random arrivals is particularly poor to explain the zero-crossing distribution of slightly damped narrowband processes [Nigam 1983], because crossing events are correlated. Tumbling is in a similar scenario as the chain configuration remains correlated over a number of cycles $\tau_{\text{dif}}/\tau_{\text{tumb}} \propto Q$. In absence of EV, $Q \sim \text{Wi}^{0.0(3)} \sim 1$ and the assumption of “uncorrelated tumblings” is roughly valid. However, memory might be responsible for the non-Poissonian behaviour of FENE+EV chains ($Q \sim \text{Wi}^{0.2(0)}$). To quantify this effect we calculated the zero-crossing distribution $P_{z=0}(\tau)$ of a stochastic damped oscillator satisfying $\ddot{z} + 2\Gamma\dot{z} + \omega_0^2 z = F$, where F is a Gaussian noise with $\langle F(t)F(0) \rangle = 4\Gamma\omega_0^2\delta(t)$ ensuring $\langle z^2 \rangle = 1$ [Nigam 1983]. We use Γ and ω_0 from the chain analysis so that $z(t)$ reproduces the power spectral density (PSD) of $X(t)$ (and its Q in particular, see Fig. 8.5). As shown in Fig. 8.4b, $P_{z=0}(\tau)$ is in excellent quantitative agreement with the chain’s $P(\tau)$ for a relatively wide range of $1 < \text{Wi} < 100$. Although $z(t)$ is Gaussian, $X(t)$ becomes extremely non-Gaussian as Wi increases indicating that non-Poissonian behaviour in FENE+EV chains is initially due to non-Markovian effects. Non-Gaussianity might affect $P(\tau)$ for $\text{Wi} > 100$.

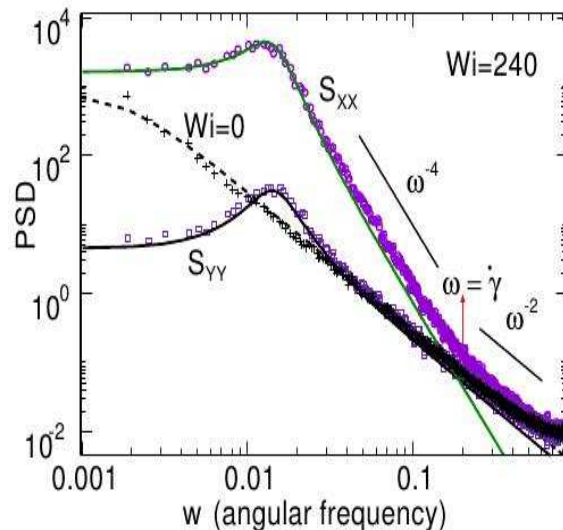


Figure 8.5: The power spectral density (PSD) of the first Rouse mode components in flow ($S_{XX}(\omega)$) and gradient ($S_{YY}(\omega)$) directions for a FENE+EV chain with $N = 60$ at $\text{Wi} = 240$. The spectra for $\text{Wi} = 0$ is also shown. Dashed line is the Lorentzian PSD for $\text{Wi} = 0$, $S(\omega) = 2\Gamma_0/(\omega^2 + \Gamma^2)$ with $\Gamma_0 = 1/\tau_0$. Solid lines for $\text{Wi} = 240$ come from the Fourier transform of the ansatz ACF (forced and damped oscillator, see text): namely, $S_{RR}(\omega) = (2\langle R^2 \rangle \Gamma / \pi)(1 + \alpha_R)\omega_0 + (1 - \alpha_R)\omega^2 / D(\omega)$ where $D(\omega) \equiv (\omega_0 - \omega) + 4\Gamma\omega$ and $R = \{X, Y\}$ where ω_0 , Γ and Ψ_R are obtained by fitting the chain extensions ACF, while $\alpha_R \equiv (\omega_d/\Gamma) \tan \Psi$ (see Eq. 8.25). Scalings for the intermediate frequency regime ($S \sim \omega^{-4}$) and large frequencies ($S \sim \omega^{-2}$ for $\omega > \dot{\gamma}$) are indicated. All units given in the standard Lennard-Jones system m , σ , ε with time unit $\sigma\sqrt{m/\varepsilon}$. The chain relaxation time is $\tau_0 = (1200 \pm 50)$.

Although an analytical derivation of the tumbling time distribution $P(\tau)$ is an extremely difficult problem [Nigam 1983, Chertkov 2005], our results in Fig. 8.4c unambiguously indicate that the decay rate ν and τ_{lag} are related by a simple master curve $\nu\tau_{\text{lag}} \simeq 0.26$. Interestingly, τ_{lag} also determines the standard deviation of $P(\tau)$, which is found to be $\sigma_P \simeq 4\tau_{\text{lag}}$ so that $\nu/\sigma_P = 1$ (within 5% error). The physical picture is however easily understood. A tumbling trial starts with a transversal fluctuation Y

which exposes the chain to the shear flow. The subsequent retraction of the chain elongation X is not instantaneous but requires a *response time* τ_{lag} . Random (uncorrelated) tumbling observed in chains with no EV corresponds to the limit of slow response time $\tau_{\text{lag}} \simeq \tau_{\text{tumb}}$ (for a Poisson process $\sigma_P = \tau_{\text{tumb}}$). By contrast, as one should expect, chains with faster response time tumble more regularly. In the case of expanded (EV) chains $\tau_{\text{lag}}/\tau_{\text{tumb}} \sim \text{Wi}^{-0.2}$ so tumbling becomes more and more regular as the shear rate is increased. We thus find that the mean and variance of $P(\tau)$ are respectively controlled by τ_{tumb} and τ_{lag} . The decay rate ν depends on the quality factor $Q = \omega_0/\Gamma$ and chain properties, via α_Y (Eq. 8.25): using our previous result $\tau_{\text{lag}} \propto \Gamma/\omega_0^2$, we get $\nu = [0.26/(1 + \alpha_Y)]\omega_0^2/\Gamma$, which correctly reproduces the behaviour at large Wi (dotted line in Fig. 8.4a).

The present findings open new questions in several scenarios. For instance, although HI does not influence the 2/3 exponent of ω_0 (see e.g. [Schroeder 2005a]), it does increase ν (see Fig. 8.4a). Its quantitative relevance is however not clear: the only experimental values for ν [Gerashchenko 2006] are consistent with FENE-EV dumbbells but also with FENE-EV+HI $N = 30$ chains (not shown). Experimental confirmation of the role of EV in tumbling dynamics would require chains in good solvent, up to $\text{Wi} \sim 100$. Although these Wi might not be easily accessible with free chains, recent experiments with tethers [Lueth 2009] reported that the average time between consecutive chain-wall contacts scales like $\text{Wi}^{0.85}$. Interestingly, the similar exponent and the underlying “wagging” motion of the tether suggest a relation with τ_{lag} . New techniques allowing real-time determination of the chain breath in y -direction [Teixeira 2005, Lueth 2009] can provide experimental measures of τ_{lag} , whose role in semiflexible and stiff chains [Winkler 2010] and polyelectrolytes is yet to be explored.

Chapter 9

Conclusions / Conclusiones

Contents

9.1 English	163
9.2 Español	167

9.1 English

The subject of this thesis has been the development of novel computational tools for fluctuating hydrodynamics with immersed solute particles. We have derived the generalized particle-fluid equations of motion based on a coarse-grained approach, and we have implemented the corresponding discretized equations within the finite volume and immersed boundary method (IBM) approach. The codes have been written in CUDA to run on graphical processing units (GPUs) [Usabiaga], which are nowadays among the fastest architectures with an unprecedented efficiency-cost ratio. This fact, together with the use of efficient solvers place our codes among the fastest at present. Overall, we have derived solvers to work in a broad range of Boltzmann, Reynolds, Mach and Schmidt numbers and we have performed a large number of numerical experiments to validate our solvers.

We devoted the first part of the thesis (Chaps. 2-5) to derive the numerical solvers. Our approach has been to first derive thermodynamically consistent set of equations in the continuum limit and then proceed to discretize the equations. To derive thermodynamically consistent set of equations for isothermal systems we have employed the augmented Langevin formalism [Ramshaw 1986]; similarly, we could have been used the GENERIC formalism for systems in which the total coarse-grained energy is conserved [Grmela 1997, Öttinger 2005]. The discretization is a delicate process that can destroy the properties of the equations of motion in the continuum setting. We have paid special attention to the conservation of the fluctuation-dissipation balance and to the errors associated with the finite spatial resolutions of the discrete equations. In the Navier-Stokes solvers it is crucial to maintain the adjoint properties of the differential operators in the continuum setting [$(\nabla \cdot) = -\nabla^*$, $\nabla^2 = \nabla \cdot (\nabla)$ and $(v \cdot \nabla) = (v \cdot \nabla)^*$]. Adjointness has been also found essential for the spreading S and average $J = S^*$ operators that provides the fluid-particle coupling. In this thesis we have substantially contributed to the development of robust particle hydrodynamics solvers based on the no-slip constraint applied to a single-kernel particle, minimally resolved, blob model. We have shown that the benefits of such instantaneous coupling (compared with the relaxational or frictional one [Dünweg 2009]) spread over different essential aspects of the particle fluid dynamics, in quite different regimes. First, the no-

slip coupling (equipped with the immersed boundary kernels) allows for a well defined particle volume, mass and hydrodynamic radius. It offers a mutual mobility comparable with the Rotne-Prager description for finite particles and to some extent, the essence of lubrication forces (very large friction at close, overlapping, distances). This is a key issue for the resolution of the Brownian limit. But also, in the opposite regime (turbulence), we find that the finite size of the blob particle allows for a correct drag force, up to $\text{Re}_p \approx 300$ (which can correspond to very large values of the macroscopic Reynolds number $\text{Re} = (L/R)\text{Re}_p$). From a dynamic point of view, the instantaneous coupling behaves like an inertial coupling, which permits to describe arbitrarily fast momentum exchange between the fluid and the particle. As an example of such, involving nonlinear terms of the Navier-Stokes equations, are the acoustic forces, which we have correctly resolved for particles with arbitrary contrast factors.

In the second part of the thesis we have applied each of our solvers to some non-trivial application. We think they are nice examples of the powerful approach of our numerical methods to study fluctuating hydrodynamics systems. We want to stress that many of these applications, such as the problem of giant fluctuations (Chap. 6), can be very expensive from a computational point of view, for this reason our implementation of the solvers for GPUs [Usabiaga] has been an important part of the work developed in this thesis. We expect that these schemes will be useful to others researchers, for example, at this point they have started to be used by some of our collaborators [Donev 2013a]. Also, the ideas of the ICM could be implemented with other fluid solvers such as Lattice Boltzmann Methods.

To finish, we briefly discuss some of the possible lines of research, both algorithmic and applied, that could extend the work of this thesis. Between the methodological lines we have:

- **Thermodynamic properties:** The numerical solvers of Chaps. 2 and 3 can be extended to describe additional thermodynamic properties or more general equations of state. Two cases are particularly interesting. Our physical models can be extended to non-isothermal systems. This will require to include a dynamic equation for the internal energy of the fluid or equivalently for its temperature. The fluctuating hydrodynamics equations for non-isothermal system have been already implemented for compressible fluids in finite volume solvers [Bell 2007] and it could be extended to incompressible flows too. Similarly, the blob model can be generalized by including an additional degree of freedom to describe its internal energy. In this case, the fluid-particle coupling should be extended to include the heat transfer due to the difference of temperatures. The new coupling would be based on some form of the Fourier's law so the heat flux around the particle surface would take the form $\mathbf{q} = \kappa \nabla T$. Depending on the values of the thermal conductivity κ and the size of the particle such coupling can lead to very stiff equations; in that case it could be convenient to employ some generalization of the no-slip coupling so the particle and the fluid at the particle site would have the same temperature, that is $T_{\text{part.}} = JT_{\text{fluid}}$. Similar ideas have been used for reaction-diffusion problems with good results [Bhalla 2013].

Immiscible mixtures. Another interesting extension is to consider non-miscible binary mixtures. As we discussed in Chap. 2 this can be done by including the appropriate chemical potential in the Navier-Stokes equations. The Cahn-Hilliard model [Vorobev 2010] seems to be a good candidate to extend the internal energy of the fluid. In fact, fluctuating hydrodynamic has been already used to model non-miscible fluids [Shang 2011], however, Shang et al. did not derived their equations from GENERIC or another well established formalism and it is not clear if their model is thermodynamically consistent or not. As in the case of the non-isothermal systems the blob model can be extended to interact with the concentration field; this have been done to study reaction-diffusion problems by some close collaborators [Bhalla 2013] and similar ideas have been used to study wettability and critical Casimir forces in binary mixtures [Furukawa 2013].

- **Particle resolution:** An important extension of our work would be to improve the spatial reso-

lution of the blob model. We suspect that by including the rotational and stresslet terms in the equations of motion the spatial resolution could be dramatically improved. The stresslet term is specially important to recover the viscosity dependence on the particle concentration as well as other rheological properties of the fluid [Kim 2005, Yeo 2010]. At the continuum level, to include the rotational and stresslet terms does not present much problems as we saw in Chap. 3. Even in the stochastic setting the equations of motion are known [Keaveny 2013, Delong 2014], however, to discretize the equations is not trivial. The main problem is how to develop averaging and spreading operators for the stresslet and rotational terms that present good translational invariance; just as the Peskin’s kernels do for the monopole terms [Peskin 2002].

Multiblob model. Another extension to improve the spatial resolution of our particle methods (in which we are working now) is to link several blobs to create a “multiblob” which will represent an object with arbitrary shape. This route will lead to schemes similar to the IBM [Peskin 2002] but using only a small number of Lagrangian points per particle. This has been a common approach to represent polymer chains [Usta 2005] and it has been also used to study the hydrodynamic of rigid objects [Bringley 2008, Molina 2013]. In principle, it is straightforward to extend the method in this direction, however, many technical details have to be addressed. For example, it is necessary to determine the multiblob effective sizes such as its hydrodynamic and lubrication radius, its effective volume and how all of them depend with the number of blobs or its relative distance inside the multiblob. Also, a method to constraint the blob-blob distances would become quite useful to avoid spring stiffness.

- **Partial slippage:** Another open research line is the effect of partial slippage over the particle surface. Partial slip is related to a finite molecular relaxational time and therefore induces dissipation. We have derived an equation for the dynamics of a particle with partial (or full) slip, following the lines of our coarse-grained method (see Chap. 3). Apart from the implementation of Eq. (3.66) in the solver, current theoretical efforts are directed in the microscopic connection between friction and wettability [Bocquet 2007, Español 2014] so as to implement a fully consistent (yet coarse-grained) treatment of the particle boundary behaviour. A novelty of the derived equation is the presence of convective terms, which incorporate possible (non-trivial) effects of convective inertia. Slippage is, by the way, another hot topic in turbulence: deviations from the trajectories of ideal Lagrangian tracers (which just follow the fluid parcel) are observed in neutrally buoyant particles and are thought to be related to the particles slip properties [Cisse 2013].

The applied research topics that could benefit from the work of this thesis are:

- **Hydrodynamic effects:** Our numerical solvers can be used to study the role of hydrodynamic interactions on several regimes and physical phenomena. One line of research that we are currently pursuing, is the study of cluster formation and colloidal gelation. Literature results produce contradictory results with some works asserting the key role of hydrodynamic interactions [Furukawa 2010, Cao 2012] as well as other neglecting their effects as a secondary contribution [Lu 2008, Yamamoto 2008]. It is important to note that the so-called hydrodynamic interactions have several terms (Stokeslet, stresslet, lubrication...) and some simulation methods do not have much control about which ones are included and which ones are neglected, or at least, which one is responsible for the increase of percolation apparently induced by hydrodynamic interactions [Furukawa 2010, Whitmer 2011]. Therefore, hydrodynamic simulations performed by different methods are not always directly comparable and a systematic study of this problem could be useful to discern the role of hydrodynamics on the problem of gelation. Also, gelation studies can require astonishingly large simulation times [de Candia 2009], but those time scales are out of

reach for most hydrodynamic methods. Our minimal models together with our implementation for GPUs can be one of the few available solvers to track down these problems.

Particle turbulence. Another interesting problem well suited for our numerical solvers is the study of particulate flows at high Reynolds numbers. Turbulent flow is a very active line of research in fluid dynamics with many open questions; one of them is the role of solute particles in a turbulent flow. On one hand, computational methods based on fully resolved particle surface are the appropriate tool for very large particles compared with the smallest turbulent length (the Kolmogorov length). On the other hand, for very small particles compared with the Kolmogorov length it has been argued that one-way coupling methods for point particles [Maxey 1983] are appropriate. However, this approach neglects the effect of the particles in the turbulent flow; a problem that can be partially tackled with two-way coupling for point particles [Eaton 2009]. However, when the immersed particles are of a similar size than the Kolmogorov length, point particle approaches are unable to recover all the hydrodynamic effects. An efficient minimal model for finite size particles will be useful to disentangle the role of solute particles in turbulent flows. We saw in Chap. 3 that the ICM correctly reproduce the fluid and particle inertial effects (such as the added mass) and moreover, the blob drag is consistent with the drag for a rigid particle in a wide range of Reynolds number ($0 \leq \text{Re} \lesssim 300$). We expect that these features of the ICM together with our efficient implementation for GPUs will make our solvers a useful tool to study turbulent flows. Such research has been already started with the CIEMAT group.

- **Acoustic forces:** In Chap. 7 we demonstrated the ability of the ICM and the blob model to capture the effect of acoustic forces on small particles. In one of the tests we studied the Brownian diffusion of a small particle subject to an acoustic potential created by a standing plane wave propagating along the z axis. We observed that the particle spatial distribution agreed well with the Gibbs-Boltzmann distribution, however, preliminary results suggest that the picture is essentially different in the presence of several particles. We have observed that for massive particles ($m_e \neq 0$) with the same compressibility than the fluid ($\varepsilon_{pf} = 0$ or $c_p = c_f$) the sound amplitude is highly reduced even for very low particle concentrations (such as $\phi = 0.01$). Since the sound amplitude is lower, so is the Gor'kov potential and this provokes that the acoustic forces become less efficient to localize the particles. In the case of neutrally-buoyant particles but less compressible than the fluid ($c_p > c_f$) the effects are a little bit different. The sound wave amplitude is not reduced but the front of the wave is distorted, that is, the wave is not longer a plane wave propagating in the z direction. An important detail is that we observed these phenomena only in the presence of thermal fluctuations, switching off the stochastic forcing all the particles were collected exactly in the pressure node of the acoustic wave. To recover these results is crucial to resolve the particle-particle hydrodynamic interaction, therefore, one-way coupling methods [Muller 2012], typically used by the acoustic community, are not appropriate. These results are important to predict the capabilities of acoustic tweezers to focus small particles in the pressure nodes, however, further studies to determine the origin of these effects and their dependence with the particle concentration or the amplitude of the thermal fluctuations are necessary.
- **Colloid-polymer mixtures:** With our current schemes “gas-liquid” interfaces in colloid-polymer mixtures [Aarts 2004] can be studied at several levels of coarse-grain. A full representation of both, colloids and polymers, is probably too expensive to be performed. Therefore, at a first level of coarse-grain we could use blobs to represented colloids while the blob-blob conservative interactions would model the entropic forces due to the presence of polymer chains in the solution which, however, will not be explicitly solved. Another way to model these systems is

by using solvers for binary mixtures to represent the phase rich in colloids and poor in polymers and vice versa. The correct interface properties such as its surface tension and even the density difference between the two phases could be recovered by using the correct chemical potential [Vorobev 2010]. A very interesting point is that the less coarse-grained simulation can be used to determine the input parameters in the most coarse-grained simulation [Hijón 2010, Shang 2011]. This approach will allow us to study colloid-polymer mixtures at length and time scales much larger than with an explicit representation of the colloidal particles.

9.2 Español

El trabajo de esta tesis se ha centrado en el desarrollo de métodos computacionales para hidrodinámica fluctuante con partículas de soluto. Hemos derivado ecuaciones de movimiento para el sistema partícula fluido basados en métodos de granulado (*coarse-grain*) y hemos implementado la versión discreta de las ecuaciones empleando métodos de volúmenes finitos y fronteras inmersas (*immersed boundary method*, IBM). Nuestros códigos han sido escritos en CUDA para poder ser ejecutados en tarjetas gráficas (GPU) [Usabiaga] dado que es una de las arquitecturas más rápidas existentes hoy en día y con una ratio eficiencia coste increíblemente alto. En conjunto hemos desarrollado métodos numéricos capaces de trabajar en un amplio rango de números de Boltzmann, Reynolds, Mach y Schmidt y así mismo hemos realizado un amplio número de pruebas para validarlos.

La primera parte de la tesis (Caps. 2-5) está dedicada al desarrollo de los métodos numéricos. Nuestra estrategia ha sido, primero, derivar ecuaciones termodinámicamente consistentes en el límite continuo y proceder después a su discretización. Para derivar sistemas de ecuaciones termodinámicamente consistentes hemos empleado el formalismo de ecuaciones de Langevin aumentadas (*augmented Langevin formalism*); igualmente se podría haber usado el formalismo GENERIC para sistemas que conservasen la energía de las variables lentas [Grmela 1997, Öttinger 2005]. El proceso de discretización es delicado porque puede destruir las propiedades de las ecuaciones de movimiento en el límite continuo, hemos prestado especial atención a la conservación del balance de fluctuación disipación y a los errores debidos a la resolución espacial finita de las ecuaciones discretizadas. En el caso de las ecuaciones de Navier-Stokes es crucial mantener las relaciones de simetría de los operadores diferenciales en el espacio continuo [$(\nabla \cdot) = -\nabla^*$, $\nabla^2 = \nabla \cdot (\nabla)$ and $(v \cdot \nabla) = (v \cdot \nabla)^*$]. De forma similar las relaciones de simetría entre el operador reparto S y el operador promedio $J = S^*$ han sido fundamentales para derivar el acople entre el fluido y la partícula. En esta tesis hemos contribuido significativamente al desarrollo de métodos numéricos robustos basados en la ligadura de no deslizamiento (*no-slip constraint*) aplicado a modelos minimalistas de partículas descritas por una única función n úcleo. Hemos demostrado que los beneficios de nuestro acople instantáneo (comparados con métodos disipativos [Dünweg 2009]) se propagan a diferentes aspectos de la hidrodinámica de la partícula a lo largo de regímenes muy distintos. Primero, la condición de no deslizamiento usada en conjunto con los interpoladores de IBM permiten describir partículas con un volumen, masa y radio hidrodinámico bien definidos. Además, el tensor de movilidad relativa entre partículas es similar al tensor de Rotne-Prager y hasta cierto punto describe las fuerzas de lubricación (fricciones muy altas a distancias cortas). Este resultado es crucial para poder emplear estos métodos en el límite Browniano. También hemos visto que en el régimen de turbulencia el tamaño finito de las partículas reproduce correctamente las fuerzas de arrastre hasta límites de Reynolds de partículas altos, $Re_p \approx 300$, los cuales pueden corresponder a números de Reynolds en la escala macroscópica mucho mayores $Re = (L/R)Re_p$. Desde un punto de vista dinámico el acople instantáneo se comporta como un acople inercial que permite describir intercambio de momentos arbitrariamente rápidos entre el fluido y la partícula. Como ejemplo hemos demostrado que nuestros

algoritmos pueden describir las fuerzas acústicas para partículas con un factor de contraste arbitrario.

En la segunda parte de la tesis hemos empleado los métodos numéricos desarrollados en algunas aplicaciones no triviales, las cuales, creemos que representan ejemplos interesantes del alcance de nuestros algoritmos para estudiar sistemas con hidrodinámica fluctuante. Queremos enfatizar que muchas de estas aplicaciones, como el caso de las fluctuaciones gigantes (Cap. 6), pueden ser muy costosas desde un punto de vista computacional. Por este motivo, la implementación de nuestros algoritmos para GPUs [Usabiaga] ha sido una parte fundamental del trabajo desarrollado en esta tesis. Esperamos que nuestros algoritmos y códigos resulten útiles para otros investigadores, de hecho, están empezando a ser utilizados por alguno de nuestros más cercanos colaboradores [Donev 2013b].

Para terminar queremos discutir algunas de las líneas, metodológicas y aplicadas, que esta tesis ha dejado abiertas. Algunas extensiones de nuestro trabajo desde un punto metodológico podrían ser las siguientes:

- **Propiedades termodinámicas:** Los métodos numéricos de los Capítulos 2 y 3 se podrían extender para incluir ecuaciones de estado más generales o propiedades termodinámicas adicionales. Hay dos casos particularmente interesantes. El primero sería extender nuestros algoritmos a sistemas no isotermos, para ello sería necesario incluir una ecuación para describir la energía interna del fluido (o su temperatura). De hecho, algoritmos basados en el método de volúmenes finitos ya han sido empleado para estudiar fluidos compresibles en sistemas fluctuantes no isotermos [Bell 2007] y podrían ser extendidos al caso de flujos incompresibles. De forma similar, nuestros modelos de partícula se pueden generalizar para describir su energía interna. En este caso el acople fluido partícula tendría que ser generalizado para incorporar la transferencia de calor debido a las diferencias de temperatura. El nuevo acople tendría que estar basado en alguna forma de la ley de Fourier, de tal forma que el flujo de calor alrededor de la partícula tendría la forma $\mathbf{q} = \kappa \nabla T$. Dependiendo de los valores de la conductividad térmica κ y el tamaño de la partícula este tipo de acople puede dar lugar a ecuaciones muy rígidas; en ese caso sería conveniente generalizar la condición de no deslizamiento para que la partícula y el fluido en la posición de la partícula tuvieran la misma temperatura $T_{\text{part.}} = JT_{\text{fluido}}$. Ideas similares se han empleado en problemas de reacción difusión con buenos resultados [Bhalla 2013].

Mezclas inmiscibles. Otra extensión que resultaría interesante es extender nuestros modelos a mezclas no miscibles. Como discutimos en el Capítulo 2 esto se puede hacer incluyendo el potencial químico adecuado en las ecuaciones de Navier-Stokes. El modelo de Cahn-Hilliard [Vorobev 2010] parece ser una buena elección para extender el modelo. De hecho, las ecuaciones de hidrodinámica fluctuante ya se han empleado para simular fluidos no miscibles [Shang 2011]. Sin embargo, Shang et al. no derivaron sus ecuaciones por medio de GENERIC o algún otro formalismo bien establecido y no está claro si su modelo se termodinámicamente consistente o no. Como en el caso de sistemas no isotermos el modelo de partículas se puede extender para que estas interaccionen con el campo de concentración. Esta idea se ha empleado para estudiar problemas de reacción difusión por algunos de nuestros colaboradores [Bhalla 2013] y también se ha empleado para estudiar mojabilidad y fuerzas de Casimir en mezclas binarias [Furukawa 2013].

- **resolución de la partícula:** Una extensión de nuestro trabajo muy importante sería mejorar la resolución espacial con la que describimos nuestras partículas. Sospechamos que incluyendo los términos de torque y de no deformación la resolución mejoraría de forma dramática. El término de no deformación es especialmente importante para recuperar la dependencia de la viscosidad con la concentración de partículas así como otras propiedades rheológicas [Kim 2005, Yeo 2010]. En la descripción continua incluir estos términos extra no presenta demasiados problemas como ya

vimos en el Capítulo 3. Incluso en el caso estocástico las ecuaciones de movimiento son conocidas [Keaveny 2013, Delong 2014], sin embargo, la discretización no es trivial. El mayor problema es el desarrollo de operadores promedio y reparto con buena invarianza translacional de la misma forma que los interpoladores de Peskin lo hacen para los términos monopolares [Peskin 2002].

Multiblob. Otra extensión (en la que estamos trabajando ahora) para mejorar la resolución espacial de las partículas es ligar varias de ellas para crear un “multiblob”, el cual podría representar objetos de forma arbitraria. Esta ruta nos conduciría a métodos parecidos al IBM [Peskin 2002] pero usando sólo un pequeño número de marcadores Lagrangianos por partícula. Este tipo de estrategia se ha usado habitualmente para simular polímeros [Usta 2005] y también para el estudio del comportamiento hidrodinámico de objetos rígidos [Bringley 2008, Molina 2013]. En principio, extender nuestros métodos en esta dirección es trivial, sin embargo hay muchos detalles técnicos que deben ser resueltos. Por ejemplo, es necesario determinar los distintos tamaños del multiblob, radio hidrodinámico, de lubricación, volumen etc., su dependencia con el número de marcadores Lagrangianos y su distancia relativa dentro del multiblob. También sería interesante implementar ligaduras rígidas entre los marcadores Lagrangianos para evitar las límitaciones en el paso de tiempo asociadas al uso de muelles.

- **Deslizamiento parcial:** Otra línea de investigación abierta es el efecto de una condición de deslizamiento parcial sobre la superficie de la partícula. El deslizamiento parcial está relacionado con tiempos de relajación moleculares finitos y por tanto induce fuerzas disipativas. Siguiendo nuestros métodos de granulado en el Capítulo 3 derivamos las ecuaciones para las condiciones de deslizamiento parcial o total. A parte de implementar la ecuación (3.66) otra línea de investigación es conectar la condición de deslizamiento con una descripción microscópica del sistema [Bocquet 2007, Español 2014]. Una novedad de las ecuaciones derivadas es la presencia de términos convectivos que podrían dar lugar a efectos no triviales. Para terminar este punto, debemos mencionar que condiciones de deslizamiento parcial son un tema candente en la física de turbulencias porque se ha observado que partículas con la misma densidad que el fluido se desvían de las trayectorias Lagrangianas que en principio se esperaría que siguiesen [Cisse 2013].

Las líneas de investigación aplicada que se podrían beneficiar del trabajo desarrollado en esta tesis son:

- **Efectos hidrodinámicos:** Nuestros métodos numéricos pueden ser utilizados para estudiar el papel de las interacciones hidrodinámicas en varios fenómenos y regímenes físicos distintos. Una línea de investigación que estamos siguiendo actualmente es el estudio de la formación de clusters y la gelación coloidal. Los resultados publicados en la literatura son contradictorios, mientras algunos trabajos aseguran que las interacciones hidrodinámicas tienen un papel fundamental [Furukawa 2010, Cao 2012] otros las relegan a un papel secundario [Lu 2008, Yamamoto 2008]. Es importante resaltar que las llamadas interacciones hidrodinámicas contienen diversos términos (Stokeslet, tensor de no deformación, lubricación...) y muchos métodos numéricos no tienen demasiado control sobre que interacciones son incluidas y cuales no, o al menos, sobre cual es la responsable del incremento de percolación que aparentemente induce la hidrodinámica [Furukawa 2010, Whitmer 2011]. Debido a esto, simulaciones hidrodinámicas llevadas a cabo por distintos métodos no son siempre directamente comparables y un estudio sistemático de este problema resultaría útil para desvelar el papel de la hidrodinámica en el problema de gelación. Además, los estudios de gelación pueden requerir tiempos de simulación extremadamente largos [de Candia 2009] que la mayoría de códigos no son capaces de alcanzar. Nuestros modelos de

mínima resolución, junto con la implementación para GPUs puede ser uno de los pocos códigos capaces de tratar estos problemas.

Turbulencia. Otro problema interesante apropiado para ser estudiado con nuestros métodos numéricos es el estudio de flujos con partículas de soluto a alto número de Reynolds. Turbulencia es un campo de investigación muy activo en dinámica de fluidos y con muchas preguntas que permanecen abiertas. Una de ellas es el papel que juegan pequeñas partículas de soluto en los flujos turbulentos. Por un lado, métodos computacionales basados en partículas descritas con alta resolución son apropiados para estudiar partículas mucho más grandes que la escala turbulenta más pequeña, la escala de Kolmogorov. Por otro lado, para partículas muy pequeñas comparadas con la escala de Kolmogorov se ha argumentado que acoplamientos “one-way” para partículas puntuales [Maxey 1983] son apropiados. Sin embargo, estos métodos desprecian el efecto de las partículas en los flujos turbulentos; este problema se puede resolver parcialmente usando acoplamientos “two-way” para partículas puntuales [Eaton 2009]. Sin embargo, cuando las partículas inmersas en el fluido son de una tamaño similar a la escala de Kolmogorov, el uso de partículas puntuales no permite recuperar todos los efectos hidrodinámicos. Un modelo de mínima resolución para partículas de tamaño finito podría ser muy útil para desentrañar el papel de las partículas de soluto en los flujos turbulentos. Como vimos en el Capítulo 3 nuestro método de IC reproduce correctamente los efectos inerciales tanto del fluido como de la partícula (por ejemplo, el efecto del exceso de inercia debido a la incompresibilidad), e incluso más importante que eso, recupera las fuerzas de arrastre en un amplio número de Reynolds ($0 \leq Re \lesssim 300$). Creemos, que estas propiedades del ICM junto con la eficiencia computacional de nuestra implementación para GPUs puede hacer de nuestros códigos una herramienta muy útil para el estudio de flujos de turbulentos. Ya hemos comenzado a trabajar en esta línea de investigación en colaboración con grupos del CIEMAT.

- **Fuerzas acústicas:** En el Capítulo 7 demostramos que el ICM junto con el modelo de “blobs” es capaz de capturar el efecto de las fuerzas acústicas sobre pequeñas partículas. Uno de las pruebas que realizamos fue estudiar el movimiento Browniano de una pequeña partícula sometida a un potencial acústico creado por una onda estacionaria que variaba a lo largo del eje z . Observamos que la distribución espacial de la partícula coincidía con la predicción de Gibbs-Boltzmann, sin embargo, resultados preliminares sugieren que el efecto es esencialmente distinto en la presencia de varias partículas. Hemos observado que para partículas masivas ($m_e \neq 0$) con la misma compresibilidad que el fluido ($\varepsilon_{pf} = 0$ or $c_p = c_f$) la amplitud del sonido se reduce significativamente incluso para concentraciones de partículas muy bajas (por ejemplo $\phi = 0.01$). Al disminuir la amplitud del sonido también disminuye la el potencial de Gor’kov y esto provoca que las fuerzas acústicas sean menos efectivas para concentrar las partículas. En el caso de partículas sin exceso de inercia pero menos compresibles que el fluido ($c_p > c_f$) el efecto es ligeramente distinto. La amplitud del sonido no se reduce, sin embargo el frente de ondas se ve distorsionado con lo que dejamos de tener una onda plana a lo largo de la dirección z . Un detalle importante es que sólo observamos estos fenómenos en presencia de fluctuaciones térmicas; suprimiendo las fluctuaciones todas las partículas son colectadas exactamente en el nodo de presión de la onda. Para recuperar estos resultados es crucial resolver la interacciones hidrodinámicas partícula-partícula y por tanto, acoplamientos “one-way” [Muller 2012] que son típicamente usados por la comunidad acústica no son apropiados. Estos resultados son importantes para predecir la capacidad de las pinzas acústicas para colectar partículas en los nodos de presión, sin embargo más estudios son necesarios para determinar el origen de estos efectos y para determinar su dependencia con la concentración de partículas o con la amplitud de las fluctuaciones térmicas.

- **Mezclas coloide polímero:** Con nuestros métodos numéricos se podrían estudiar a distintos niveles de resolución las interfaces “líquido-vapor” en mezclas coloide polímero [Aarts 2004]. Una representación explícita de coloides y polímeros sería, probablemente, demasiado cara para ser llevada a cabo. A un primer nivel de resolución podríamos representar los coloides por medio de nuestros “blobs” usando las interacciones conservativas entre “blobs” para representar las fuerzas entrópicas debido a la presencia de polímeros en la disolución, que sin embargo, no serían descritos explícitamente. Otro posible camino para modelar estos sistemas sería usar los algoritmos para mezclas binarias, de tal forma que las dos especies representarían la fase rica en coloides y pobre en polímeros y vice versa. Las propiedades de la interfaz tal como su tensión superficial e incluso la diferencia de densidades entre las dos fases podría ser recuperada siempre que se use el potencial químico adecuado [Vorobev 2010]. Un aspecto muy interesante es que se podrían usar las simulaciones de más resolución para determinar los parámetros de entrada para la segunda simulación [Hijón 2010, Shang 2011]. Este método permitiría simular mezclas coloide polímero a escalas de longitud y tiempo mucho mayores de lo que se podría utilizando una representación explícita para las partículas coloidales.

Appendix A

Fluctuation dissipation theorem

In the Section 2.1.4 of Chapter 2 we introduced the formalism of augmented Langevin equation to show that the Navier-Stokes equation can be cast into this formalism. In this Appendix we use indicial notation to derive the dissipative matrix \mathcal{M}_{vv} from the stochastic forcing $\rho^{-1}\nabla \cdot \Sigma$.

From the Section 2.1.4, the stochastic forcing term in the momentum equation is

$$\rho^{-1}\nabla \cdot \Sigma = \rho^{-1}\nabla \cdot \left[\sqrt{2\eta k_B T} \widetilde{\mathcal{W}}_v + \left(\sqrt{\frac{\zeta k_B T}{3}} - \frac{\sqrt{2\eta k_B T}}{3} \right) \text{Tr}(\widetilde{\mathcal{W}}_v) \mathbf{I} \right], \quad (\text{A.1})$$

where Tr represent the trace, $\widetilde{\mathcal{W}}_v = (\mathcal{W}_v + \mathcal{W}_v^T)/\sqrt{2}$ and \mathcal{W}_v is an uncorrelated random Gaussian tensor with covariance

$$\langle \mathcal{W}_v^{ij}(\mathbf{r}, t) \mathcal{W}_v^{kl}(\mathbf{r}', t') \rangle = \delta_{ik} \delta_{jl} \delta(t - t') \delta(\mathbf{r} - \mathbf{r}'). \quad (\text{A.2})$$

We want to find the dissipative matrix \mathcal{M}_{vv} such that

$$\begin{aligned} 2k_B T \mathcal{M}_{vv} \delta(\mathbf{r} - \mathbf{r}') \delta(t - t') &= \langle \rho^{-1} \nabla \cdot \Sigma (\rho^{-1} \nabla \cdot \Sigma)^* \rangle \\ &= \langle \rho^{-1} \nabla \cdot \Sigma \Sigma^* \nabla \rho^{-1} \rangle. \end{aligned} \quad (\text{A.3})$$

Denoting the divergence operator by \mathbf{D} and the gradient by $\mathbf{G} = -\mathbf{D}^*$, the α -components of the divergence of the stochastic tensor are

$$(\mathbf{D}\widetilde{\mathcal{W}}_v)^\alpha = \sum_\beta \mathbf{D}^\beta \widetilde{\mathcal{W}}_v^{\beta\alpha}, \quad (\text{A.4})$$

$$(\mathbf{D}\text{Tr}(\widetilde{\mathcal{W}}_v)\mathbf{I})^\alpha = \sum_\beta \mathbf{D}^\beta \text{Tr}(\widetilde{\mathcal{W}}_v) \delta_{\beta\alpha} = \mathbf{G}^\alpha \text{Tr}(\widetilde{\mathcal{W}}_v), \quad (\text{A.5})$$

where α and β denote the spatial directions. The product of the first terms is

$$\begin{aligned} \langle (\mathbf{D}\widetilde{\mathcal{W}}_v)_i (\mathbf{D}\widetilde{\mathcal{W}}_v)_k^* \rangle &= -\langle \sum_{j,l} \partial_j \widetilde{\mathcal{W}}_v^{ji} \widetilde{\mathcal{W}}_v^{kl} \partial_l \rangle \\ &= -\sum_{j,l} \partial_j (\delta_{jk} \delta_{il} + \delta_{jl} \delta_{ik}) \partial_l \delta(\mathbf{r} - \mathbf{r}') \delta(t - t') \\ &= -\left(\partial_k \partial_i + \delta_{ik} \sum_j \partial_j^2 \right) \delta(\mathbf{r} - \mathbf{r}') \delta(t - t'). \end{aligned} \quad (\text{A.6})$$

Note that the minus sign appears because the divergence and the gradient are negative adjoint. The product of the second terms is

$$\begin{aligned}\langle \left(DTr(\widetilde{\mathcal{W}}_v) I \right)_i \left(DTr(\widetilde{\mathcal{W}}_v) I \right)_k^* \rangle &= -\langle \sum_{jl} \partial_i \widetilde{\mathcal{W}}_v^{jj} \widetilde{\mathcal{W}}_v^{ll} \partial_k \rangle \\ &= -\sum_{jl} \partial_i 2\delta_{jl} \partial_k \delta(\mathbf{r} - \mathbf{r}') \delta(t - t') \\ &= -6\partial_i \partial_k \delta(\mathbf{r} - \mathbf{r}') \delta(t - t').\end{aligned}\quad (\text{A.7})$$

The product of the first term with the second is

$$\begin{aligned}\langle \left(D\widetilde{\mathcal{W}}_v \right)_i \left(DTr(\widetilde{\mathcal{W}}_v) I \right)_k^* \rangle &= -\langle \sum_{jl} \partial_j \widetilde{\mathcal{W}}_v^{ji} \widetilde{\mathcal{W}}_v^{ll} \partial_k \rangle \\ &= -2\partial_i \partial_k \delta(\mathbf{r} - \mathbf{r}') \delta(t - t'),\end{aligned}\quad (\text{A.8})$$

and finally, the product of the second term with the first is

$$\langle \left(DTr(\widetilde{\mathcal{W}}_v) I \right)_i \left(D\widetilde{\mathcal{W}}_v \right)_k^* \rangle = -2\partial_i \partial_k \delta(\mathbf{r} - \mathbf{r}') \delta(t - t').\quad (\text{A.9})$$

Using the above results and the fact that the viscosities are constant, one can find

$$\langle (\nabla \cdot \Sigma)_i (\nabla \cdot \Sigma)_k^* \rangle = -(2k_B T) \left(\eta \delta_{ik} \sum_j \partial_j^2 + \left(\zeta + \frac{1}{3} \eta \right) \partial_i \partial_k \right) \delta(\mathbf{r} - \mathbf{r}') \delta(t - t')\quad (\text{A.10})$$

Therefore, the final result is

$$[\mathcal{M}_{vv}]_{ik} = -\rho^{-1} \left[\eta \delta_{ik} \sum_j \partial_j^2 + \left(\zeta + \frac{1}{3} \eta \right) \partial_i \partial_k \right] \rho^{-1},\quad (\text{A.11})$$

or using vector notation

$$\mathcal{M}_{vv} = -\rho^{-1} \left[\eta \nabla^2 + \left(\zeta + \frac{1}{3} \eta \right) \nabla(\nabla \cdot) \right] \rho^{-1}.\quad (\text{A.12})$$

Appendix B

Finite differential operators in Fourier space

Following the Chapter 14 in Ref. [Othmer 1997] we explain how to derive the Fourier expressions for the gradient, divergence and Laplacian operators introduced in the Chapter 2. First, consider a 3-dimensional periodic domain with N cells per side and length $L = Nh$ where a scalar function ϕ_r is defined at the center of the cells, that is $r = (j_1, j_2, j_3)h$ for integers j_1, j_2 and j_3 . The discrete Fourier transform of ϕ is defined by

$$\hat{\phi}_k = \frac{1}{N^3} \sum_{j_1, j_2, j_3=0}^{N-1} e^{-\frac{2\pi i}{N}(m_1 j_1 + m_2 j_2 + m_3 j_3)} \phi_r \quad (\text{B.1})$$

where $k = (m_1, m_2, m_3)2\pi/L$ and m_1, m_2 and m_3 are also integer numbers taking values from 0 to $N - 1$. From the above equation follows

$$\phi_r = \sum_{m_1, m_2, m_3=0}^{N-1} e^{\frac{2\pi i}{N}(m_1 j_1 + m_2 j_2 + m_3 j_3)} \hat{\phi}_k \quad (\text{B.2})$$

Now, we apply the discrete gradient defined in the Chapter 2 to ϕ . The first component of $G\phi$ is defined at $r + he_1/2$ where e_1 is the normal vector along the first direction, and it is given by

$$\begin{aligned} (\mathbf{G}\phi)_{r+\frac{h}{2}e_1}^1 &= \frac{1}{h} (\phi_{r+he_1} - \phi_r) \\ &= \frac{1}{h} \sum_{m_1, m_2, m_3=0}^{N-1} \left(e^{\frac{2\pi i}{N}((j_1+1)m_1 + j_2 m_2 + j_3 m_3)} - e^{\frac{2\pi i}{N}(j_1 m_1 + j_2 m_2 + j_3 m_3)} \right) \hat{\phi}_k \\ &= \frac{1}{h} \sum_{m_1, m_2, m_3=0}^{N-1} \left(e^{\frac{\pi i}{N}m_1} - e^{-\frac{\pi i}{N}m_1} \right) e^{\frac{2\pi i}{N}((j_1+\frac{1}{2})m_1 + j_2 m_2 + j_3 m_3)} \hat{\phi}_k \end{aligned} \quad (\text{B.3})$$

Therefore the gradient is given in the Fourier space by

$$\begin{aligned} \hat{\mathbf{G}}_k^1 &= \frac{1}{h} \left(e^{\frac{\pi i}{N}m_1} - e^{-\frac{\pi i}{N}m_1} \right) \\ &= \frac{2i}{h} \sin\left(\frac{\pi m_1}{N}\right) \\ &= \frac{2i}{h} \sin\left(\frac{k_1 h}{2}\right) \end{aligned} \quad (\text{B.4})$$

Following similar steps it is easy to derive the expressions for the divergence and Laplacian that we gave in the Eqs. (2.107)-(2.109).

Appendix C

List of Publications

Regular journals

1. F. Balboa Usabiaga, R. Delgado-Buscalioni, B. E. Griffith and A. Donev. *Inertial coupling method for particles in an incompressible fluctuating fluid.* Computer Methods in Applied Mechanics and Engineering, **269**, 139 (2014).
2. F. Balboa Usabiaga and R. Delgado-Buscalioni. *Minimal model for acoustic forces on Brownian particles.* Physical Review E, **88**, 063304 (2013).
3. F. Balboa Usabiaga, X. Xie, R. Delgado-Buscalioni and A. Donev. *The Stokes-Einstein relation at moderate Schmidt number.* The Journal of Chemical Physics, **139**, 214113 (2013).
4. F. Balboa Usabiaga, I. Pagonabarraga and R. Delgado-Buscalioni. *Inertial coupling for point particle fluctuating hydrodynamics.* Journal of Computational Physics, **235**, 701 (2013).
5. F. Balboa Usabiaga, J. B. Bell, R. Delgado-Buscalioni, A. Donev, T. G. Fai, B. E. Griffith and C. S. Peskin. *Staggered schemes for fluctuating hydrodynamics.* Multiscale Modeling & Simulations, **10**, 1369 (2012).
6. F. Balboa Usabiaga and R. Delgado-Buscalioni. *Characteristic times of polymer tumbling under shear flow.* Macromolecular Theory and Simulations, **20**, 466 (2011).
7. F. Balboa Usabiaga and D. Duque. *Applications of computational geometry to the molecular simulations of interfaces.* Physical Review E, **79**, 046709 (2009).

Conference Proceedings

8. F. Balboa Usabiaga, A. Donev and R. Delgado-Buscalioni. *Inertial coupling method for blob-model particle hydrodynamics: from Brownian motion to inertial effects.* Hybrid Particle-Continuum Methods in Computational Materials Physics, Jülich, Germany (2013).
9. R. Delgado-Buscalioni and F. Balboa Usabiaga. *Particle hydrodynamics: from molecular to colloidal fluids.* II International Conference on Particle-based Methods - Fundamentals and Applications, PARTICLES 2011, Barcelona (2011).

Preprints

10. S. Delong, F. Balboa Usabiaga, R. Delgado-Buscalioni, B. E. Griffith and A. Donev. *Brownian dynamics without Green's functions.* arXiv:1401.4198 (2014).

Bibliography

- [Aarts 2004] Dirk G. A. L. Aarts, Matthias Schmidt and Henk N. W. Lekkerkerker. *Direct Visual Observation of Thermal Capillary Waves*. Science, vol. 304, page 847, 2004. (Cited on pages [166](#) and [171](#).)
- [Ailawadi 1971] Narinder K. Ailawadi, Bruce J. Berne and Dieter Forster. *Hydrodynamics and Collective Angular-Momentum Fluctuations in Molecular Fluids*. Physical Review A, vol. 3, page 1462, 1971. (Cited on page [30](#).)
- [Allen 1991] M. P. Allen and D. J. Tildesley. Computer simulation of liquids. Clarendon Press - Oxford, 1991. (Cited on page [75](#).)
- [Arfken 1985] George Arfken. Mathematical methods for physicists. Academic Press, 1985. (Cited on pages [31](#) and [118](#).)
- [Aris 1962] Rutherford Aris. Vectors, tensors and the basic equations of fluid mechanics. Dover Publications Inc., 1962. (Cited on pages [29](#) and [33](#).)
- [Atzberger 2006] Paul J. Atzberger. *Velocity correlations of a thermally fluctuating Brownian particle: A novel model of the hydrodynamic coupling*. Physics Letters A, vol. 351, page 225, 2006. (Cited on page [99](#).)
- [Atzberger 2007] Paul J. Atzberger, Peter R. Kramer and Charles S. Peskin. *A stochastic immersed boundary method for fluid-structure dynamics at microscopic length scales*. Journal of Computational Physics, vol. 224, page 1255, 2007. (Cited on pages [60](#) and [69](#).)
- [Atzberger 2010] Paul J. Atzberger. *Spatially adaptive stochastic numerical methods for intrinsic fluctuations in reaction-diffusion systems*. Journal of Computational Physics, vol. 229, no. 9, page 3474, 2010. (Cited on pages [28](#) and [116](#).)
- [Atzberger 2011] Paul J. Atzberger. *Stochastic Eulerian Lagrangian methods for fluid-structure interactions with thermal fluctuations*. Journal of Computational Physics, vol. 230, page 2821, 2011. (Cited on pages [18](#), [27](#), [60](#), [61](#), [64](#), [71](#), [89](#), [113](#) and [115](#).)
- [Balachandar 2010] S. Balachandar and John E. Eaton. *Turbulent dispersed multiphase flow*. Annual Review of Fluid Mechanics, vol. 42, page 111, 2010. (Cited on pages [16](#), [17](#), [18](#) and [94](#).)
- [Banchio 2003] Adolfo J. Banchio and John F. Brady. *Accelerated Stokesian dynamics: Brownian motion*. Journal of Chemical Physics, vol. 118, no. 22, page 10323, 2003. (Cited on pages [113](#) and [115](#).)
- [Bannon 2003] Peter R. Bannon. *Hamiltonian description of idealized binary geophysical fluids*. Journal of the atmospheric sciences, vol. 60, page 2809, 2003. (Cited on page [28](#).)

- [Bruus 2010] Henrik Bruus. Microfluidics and ultrasound acoustophoresis. 2010. Lecture notes for the advanced CISM school. (Cited on pages 135 and 136.)
- [Bruus 2011] Henrik Bruus, Jurg Dual, Jeremy Hawkes, Martyn Hill, Thomas Laurell, Johan Nilsson, Stefan Radel, Satwindar Sadhal and Martin Wiklund. *Acoustofluidics exploiting ultrasonic standing wave forces and acoustic streaming in microfluidic systems for cell and particle manipulation*. Lab on a chip, 2011. (Cited on pages 61, 143 and 144.)
- [Bschorr 1999] O. Bschorr. *The force between two parallel rigid plates due to the radiation pressure of phonons*. Journal of Acoustical Society of America, vol. 106, no. 6, page 3730, 1999. (Cited on page 107.)
- [Callen 1985] Herbert B. Callen. Thermodynamics and an introduction to thermostatics. John Wiley and Sons, 1985. (Cited on page 28.)
- [Cao 2002] Renfeng Cao and Stephen B. Pope. *Numerical integration of stochastic differential equations: weak second-order mid-point scheme for application in the composition PDF method*. Journal of Chemical Physics, vol. 185, page 194, 2002. (Cited on page 43.)
- [Cao 2012] X.J. Cao, H.Z. Cummins and J.F. Morris. *Hydrodynamic and interparticle potential effects on aggregation of colloidal particles*. Journal of colloid and interface science, vol. 368, no. 1, page 86, 2012. (Cited on pages 121, 165 and 169.)
- [Celani 2005] A. Celani, A. Puliafito and K. Turitsyn. *Polymers in linear shear flow: A numerical study*. Europhysics Letters, vol. 70, no. 4, page 464, 2005. (Cited on pages 153, 154, 156 and 159.)
- [Chertkov 2005] M. Chertkov, I. Kolokolov, V. Lebedev and K. Turitsyn. *Polymer statistics in a random flow with mean shear*. Journal of Fluid Mechanics, vol. 531, page 251, 2005. (Cited on pages 154, 156, 159 and 160.)
- [Cisse 2013] Mamdou Cisse, Holger Homann and Jérémie Bec. *Slipping motion of large neutrally buoyant particles in turbulence*. Journal of Fluid Mechanics, vol. 735, page R1, 2013. (Cited on pages 165 and 169.)
- [Clift 1978] R. Clift, J. R. Grace and M. E. Weber. Bubbles, drops and particles. Academic Press, 1978. (Cited on page 93.)
- [Courant 1967] R. Courant, K. Friedrichs and H Lewy. *On the Partial Difference Equations of Mathematical Physics*. IBM Journal of Research and Development, vol. 11, no. 2, page 215, 1967. Originally appeared in Mathematische Annalen 100, 32-74 (1928). (Cited on page 42.)
- [Crum 1975] Lawrence A. Crum. *Bjerknes forces on bubbles in a stationary sound field*. Journal of Acoustical Society of America, vol. 57, no. 6, page 1363, 1975. (Cited on pages 137, 140 and 141.)
- [Das 2008] Dibyendu Das and Sanjib Sabhapandit. *Accurate Statistics of a Flexible Polymer Chain in Shear Flow*. Physical Review Letters, vol. 101, page 188301, 2008. (Cited on pages 154, 156 and 159.)
- [de Candia 2009] A. de Candia, E. Del Gado, A. Fierro and A. Coniglio. *Length scale dependence of the dynamical heterogeneities in colloidal gelation at low volume fraction*. Journal of Statistical Mechanics: Theory and Experiment, page P02052, 2009. (Cited on pages 165 and 169.)

- [de Groot 1984] S. R. de Groot and P. Mazur. Non-equilibrium thermodynamics. Dover Publications Inc., 1984. (Cited on pages 13, 22, 30 and 107.)
- [de Zárate 2004] J. M. Ortiz de Zárate, F. Peluso and J. V. Sengers. *Nonequilibrium fluctuations in the Rayleigh-Bénard problem for binary fluid mixtures*. The European Physical Journal E, vol. 15, no. 3, page 319, 2004. (Cited on pages 40, 123, 124, 125 and 131.)
- [de Zárate 2006] José M. Ortiz de Zárate and Jan V. Sengers. Hydrodynamic fluctuations in fluids and fluid mixtures. Elsevier, 2006. (Cited on pages 13, 21, 25, 26, 48, 55 and 124.)
- [Delgado-Buscalioni 2006] Rafael Delgado-Buscalioni. *Cyclic Motion of a Grafted Polymer under Shear Flow*. Physical Review Letters, vol. 96, page 088303, 2006. (Cited on pages 52, 153 and 155.)
- [Delgado-Buscalioni 2008a] R. Delgado-Buscalioni, E. Chacón and P. Tarazona. *Hydrodynamics of nanoscopic capillary waves*. Phys. Rev. Lett., vol. 101, page 106102, 2008. (Cited on page 25.)
- [Delgado-Buscalioni 2008b] Rafael Delgado-Buscalioni and Anne Dejoan. *Nonreflecting boundaries for ultrasound in fluctuating hydrodynamics of open systems*. Physical Review E, vol. 78, page 046708, 2008. (Cited on pages 41 and 93.)
- [Delong 2013] Steven Delong, Boyce E. Griffith, Eric Vanden-Eijnden and Aleksandar Donev. *Temporal integrators for fluctuating hydrodynamics*. Physical Review E, vol. 87, page 033302, 2013. (Cited on pages 40, 44, 45, 46, 47, 48, 55 and 120.)
- [Delong 2014] S. Delong, F. Balboa Usabiaga, R. Delgado-Buscalioni, B. E. Griffith and A. Donev. *Brownian dynamics without Green's functions*, 1 2014. arXiv:1401.4198. (Cited on pages 115, 120, 165 and 169.)
- [Ding 2012] Xiaoyun Ding, Jinjie Shi, Sz-Chin Steven Lin, Shahrzad Yazdi, Brian Kiralya and Tony Jun Huang. *Tunable patterning of microparticles and cells using standing surface acoustic waves*. Lab on a Chip, vol. 12, page 2491, 2012. (Cited on page 134.)
- [Dion 1982] J. L. Dion, A. Malutta and P. Cielo. *Ultrasonic inspection of fiber suspensions*. Journal of the Acoustical Society of America, vol. 72, no. 5, page 1524, 1982. (Cited on page 134.)
- [Doi 1994] M. Doi and S. F. Edwards. The theory of polymer dynamics. Clarendon Press - Oxford, 1994. (Cited on pages 14, 148, 149, 150, 151, 152, 154 and 157.)
- [Doinikov 1994] A. A. Doinikov. *Acoustic radiation pressure on a rigid sphere in a viscous fluid*. Proceedings: Mathematical and Physical Sciences, vol. 447, pages 447–466, 1994. (Cited on page 134.)
- [Doinikov 1997] Alexander A. Doinikov. *Acoustic radiation force on a spherical particle in a viscous heat-conducting fluid. I. General formula*. Journal of the Acoustical Society of America, vol. 101, no. 2, page 713, 1997. (Cited on pages 134 and 135.)
- [Donev 2010a] Aleksandar Donev, John B. Bell, Alejandro L. García and Berni J. Alder. *A hybrid particle-continuum method for hydrodynamics of complex fluids*. Multiscale Modeling and Simulation, vol. 8, no. 3, page 871, 2010. (Cited on page 41.)

- [Donev 2010b] Aleksandar Donev, Eric Vanden-Eijnden, Alejandro L. García and John B. Bell. *On the accuracy of finite-volume schemes for fluctuating hydrodynamics*. Communications in Applied Mathematics and Computational Science, vol. 5, no. 2, page 149, 2010. (Cited on pages 28, 44, 45, 49 and 51.)
- [Donev 2011a] Aleksandar Donev, John B. Bell, Anton de la Fuente and Alejandro L. Garcia. *Diffusive Transport by Thermal Velocity Fluctuations*. Physical Review Letters, vol. 106, page 204501, 2011. (Cited on page 144.)
- [Donev 2011b] Aleksandar Donev, John B Bell, Anton de la Fuente and Alejandro L Garcia. *Enhancement of diffusive transport by non-equilibrium thermal fluctuations*. Journal of Statistical Mechanics: Theory and Experiment, page 06014, 2011. (Cited on pages 101 and 102.)
- [Donev 2012] Aleksandar Donev, Andy Nonaka, Yifei Sun, Thomas G. Fai, Alejandro L. Garcia and John B. Bell. *Low Mach Number Fluctuating Hydrodynamics of Diffusively Mixing Fluids*, 2012. (Cited on page 125.)
- [Donev 2013a] Aleksandar Donev, Thomas G. Fai and Eric Vanden-Eijnden. *The importance of hydrodynamic fluctuations for diffusion in liquids*, 12 2013. (Cited on page 164.)
- [Donev 2013b] Aleksandar Donev, Thomas G. Fai and Eric Vanden-Eijnden. Reversible diffusive mixing by thermal velocity fluctuations. <http://arxiv.org/abs/1306.3158>, 2013. (Cited on pages 25 and 168.)
- [Dual 2012] Jürg Dual, Philipp Hahn, Ivo Leibacher, Dirk Möller, Thomas Schwarz and Jingtao Wang. *Acoustofluidics 19: Ultrasonic microrobotics in cavities: devices and numerical simulation*. Lab on a Chip, vol. 12, no. 20, page 4010, 2012. (Cited on page 134.)
- [Dukhin 2002] A. S. Dukhin and P. J. Goetz. Characterization of liquids, nano- and microparticulates, and porous bodies using ultrasound. Elsevier, 2002. (Cited on page 61.)
- [Dünweg 2009] Burkhard Dünweg and Anthony J. C. Ladd. *Lattice Boltzmann Simulations of Soft Matter Systems*. Advances in Polymer Science, vol. 221, page 89, 2009. (Cited on pages 14, 16, 17, 18, 60, 61, 70, 72, 75, 86, 89, 92, 102, 113, 115, 149, 163 and 167.)
- [Eaton 2009] John K. Eaton. *Two-way coupled turbulence simulations of gas-particle flows using point-particle tracking*. International Journal of Multiphase Flow, vol. 35, page 792, 2009. (Cited on pages 60, 61, 166 and 170.)
- [Ermak 1978] Donald L. Ermak and J. A. McCammon. *Brownian dynamics with hydrodynamic interactions*. The Journal of Chemical Physics, vol. 69, page 1352, 1978. (Cited on page 113.)
- [Español 1995] P. Español and P. Warren. *Statistical Mechanics of Dissipative Particle Dynamics*. Europhysics Letters, vol. 30, no. 4, page 191, 1995. (Cited on pages 17 and 60.)
- [Español 1998] Pep Español. *Stochastic differential equations for non-linear hydrodynamics*. Physica A, vol. 248, page 77, 1998. (Cited on page 21.)
- [Español 2003] Pep Español and Mariano Revenga. *Smoothed dissipative particle dynamics*. Physical Review E, vol. 67, page 026705, 2003. (Cited on pages 18 and 60.)
- [Español 2004] Pep Español. Statistical mechanics of coarse-graining. Novel methods in soft matter simulations. Lectures in Physics, 2004. (Cited on pages 13 and 15.)

- [Español 2009] Pep Español, Jesús G. Anero and Ignacio Zúñiga. *Microscopic derivation of discrete hydrodynamics*. The Journal of Chemical Physics, vol. 131, page 244117, 2009. (Cited on page 34.)
- [Español 2014] Pep Español and R. Delgado-Buscalioni. To be submitted, 2014. (Cited on pages 165 and 169.)
- [Fabritiis 2007] G. De Fabritiis, M. Serrano, R. Delgado-Buscalioni and P. V. Coveney. *Fluctuating hydrodynamic modeling of fluids at the nanoscale*. Physical Review E, vol. 75, page 026307, 2007. (Cited on pages 23, 38, 39, 57 and 61.)
- [Fai 2013] Thomas G. Fai, Boyce E. Griffith, Yoichiro Mori and Charles S. Peskin. *Immersed Boundary Method for Variable Viscosity and Variable Density Problems Using Fast Constant-Coefficient Linear Solvers I: Numerical Method and Results*. SIAM Journal on Scientific Computing, vol. 35, no. 5, page B1132, 2013. (Cited on pages 61, 103 and 145.)
- [Felderhof 2012] B. U. Felderhof. *Hydrodynamic force on a particle oscillating in a viscous fluid near a wall with dynamic partial-slip boundary condition*. Physical Review E, vol. 85, page 046303, 2012. (Cited on pages 61 and 62.)
- [Feuillade 1995] C. Feuillade. *Scattering from collective modes of air bubbles in water and the physical mechanism of superresonances*. Journal of the Acoustical Society of America, vol. 98, no. 2, page 1178, 1995. (Cited on pages 141 and 145.)
- [Feuillade 1996] C. Feuillade. *The attenuation and dispersion of sound in water containing multiply interacting air bubbles*. Journal of the Acoustical Society of America, vol. 99, no. 6, page 3412, 1996. (Cited on page 134.)
- [Fixman 1986] Marshall Fixman. *Construction of Langevin Forces in the Simulation of Hydrodynamic Interaction*. Macromolecules, vol. 19, page 1204, 1986. (Cited on pages 117, 118 and 120.)
- [Flory 1949] Paul J. Flory. *The Configuration of Real Polymer Chains*. The Journal of Chemical Physics, vol. 17, page 303, 1949. (Cited on page 149.)
- [Franosch 2011] Thomas Franosch, Matthias Grimm, Maxim Belushkin, Flavio M. Mor, Giuseppe Foffi, Laszlo Forro and Sylvia Jeney. *Resonances arising from hydrodynamic memory in Brownian motion*. Nature, vol. 478, page 85, 2011. (Cited on page 61.)
- [Friend 2011] James Friend and Leslie Y. Yeo. *Microscale acoustofluidics: Microfluidics driven via acoustics and ultrasonics*. Review of Modern Physics, vol. 83, page 647, 2011. (Cited on page 134.)
- [Furukawa 2010] Akira Furukawa and Hajime Tanaka. *Key Role of Hidrodynamics Interaction in Colloidal Gelation*. Physical Review Letters, vol. 104, page 245702, 2010. (Cited on pages 121, 165 and 169.)
- [Furukawa 2013] Akira Furukawa, Andrea Gambassi, Siegfried Dietrich and Hajime Tanaka. *Nonequilibrium Critical Casimir Effect in Binary Fluids*. Physical Review Letters, vol. 111, page 055701, 2013. (Cited on pages 104, 111, 164 and 168.)

- [Garbin 2009] Valeria Garbin, Benjamin Dollet, Marlies Overvelde, Dan Cojoc, Enzo Di Fabrizio, Leen van Wijngaarden, Andrea Prosperetti, Nico de Jong, Detlef Lohse and Michel Versluis. *History force on coated microbubbles propelled by ultrasound*. Physics of Fluids, vol. 21, no. 9, page 092003, 2009. (Cited on pages 138, 140, 141 and 145.)
- [Gerashchenko 2006] Sergiy Gerashchenko and Victor Steinberg. *Statistics of Tumbling of a Single Polymer Molecule in Shear Flow*. Physical Review Letters, vol. 96, page 038304, 2006. (Cited on pages 153, 154, 156, 159 and 161.)
- [Giupponi 2007] G. Giupponi, G. De Fabritiis and Peter V. Coveney. *Hybrid method coupling fluctuating hydrodynamics and molecular dynamics for the simulation of macromolecules*. Journal of Chemical Physics, vol. 126, page 154903, 2007. (Cited on pages 60, 70, 89 and 102.)
- [Goldstein 2000] Herbert Goldstein, Charles Poole and John Safko. Classical mechanics. Addison Wesley, 2000. (Cited on page 62.)
- [Gor'kov 1962] L. P. Gor'kov. *On the forces acting on a small particle in an acoustic field in an ideal fluid*. Sov. Phys. Dokl., vol. 6, page 773, 1962. (Cited on pages 20, 133, 135 and 138.)
- [Gottlieb 2001] Sigal Gottlieb, Chi-Wang Shu and Eitan Tadmor. *Strong Stability-Preserving High-Order Time Discretization Methods*. SIAM R, vol. 43, no. 1, page 89, 2001. (Cited on pages 34, 42 and 43.)
- [Griffith] Boyce E. Griffith. *IBAMR*. Software available at <http://ibamr.googlecode.com>. (Cited on pages 51, 52 and 127.)
- [Griffith 2005] Boyce Eugene Griffith. *Simulating the blood-muscle-valve mechanics of the heart by an adaptive and parallel version of the immersed boundary method*. PhD thesis, New York University, 2005. (Cited on page 75.)
- [Griffith 2007] Boyce E. Griffith, Richard D. Hornung, David M. McQueen and Charles S. Peskin. *An adaptive, formally second order accurate version of the immersed boundary method*. Journal of Computational Physics, vol. 223, no. 1, page 10, 2007. (Cited on pages 18 and 75.)
- [Griffith 2009] Boyce E. Griffith. *An accurate and efficient method for the incompressible Navier-Stokes equations using the projection method as a preconditioner*. Journal of Computational Physics, vol. 228, no. 20, page 7565, 2009. (Cited on pages 44 and 46.)
- [Griffith 2012a] Boyce E. Griffith. *Immersed boundary model of aortic heart valve dynamics with physiological driving and loading conditions*. International Journal for Numerical Methods in Biomedical Engineering, vol. 28, page 317, 2012. (Cited on pages 46 and 60.)
- [Griffith 2012b] Boyce E. Griffith and Xiaoyu Luo. *Hybrid finite difference/finite element version of the immersed boundary method*, 2012. (Cited on page 81.)
- [Grmela 1997] Miroslav Grmela and Hans Christian Öttinger. *Dynamics and thermodynamics of complex fluids. I. Development of a general formalism*. Physical Review E, vol. 56, no. 6, page 6620, 1997. (Cited on pages 14, 26, 163 and 167.)
- [Gröschl 1998] Martin Gröschl. *Ultrasonic Separation of Suspended Particles - Part I: Fundamentals*. Acustica, vol. 84, page 432, 1998. (Cited on page 141.)

- [Haake 2004] Albrecht Haake. *Micromanipulation of Small Particles with Ultrasound*. PhD thesis, Swiss federal institute of technology Zurich, 2004. (Cited on page 138.)
- [Haake 2005a] Albrecht Haake and Jurg Dual. *Contactless micromanipulation of small particles by an ultrasound field excited by a vibrating body*. Journal of the Acoustical Society of America, vol. 117, no. 5, page 2752, 2005. (Cited on pages 16, 61, 138 and 139.)
- [Haake 2005b] Albrecht Haake, Adrian Neild, Gerald Radziwill and Jurg Dual. *Positioning, displacement, and localization of cells using ultrasonic forces*. Biotechnology and Bioengineering, vol. 92, no. 1, page 8, 2005. (Cited on page 134.)
- [Hagen 1997] M. H. J. Hagen, I. Pagonabarraga, C. P. Lowe and D. Frenkel. *Algebraic Decay of Velocity Fluctuations in a Confined Fluid*. Physical Review Letters, vol. 78, no. 19, page 3785, 1997. (Cited on page 40.)
- [Hansen 2011] J. S. Hansen, Jeppe C. Dyre, Peter J. Daivis, B. D. Todd and Henrik Bruus. *Nanoflow hydrodynamic*. Physical Review E, vol. 84, page 036311, 2011. (Cited on page 30.)
- [Harlow 1965] Francis H. Harlow and J. Eddie Welch. *Numerical Calculation of Time-Dependent Viscous Incompressible Flow of Fluid with Free Surface*. Physics of Fluids, vol. 8, page 2182, 1965. (Cited on page 34.)
- [Hasegawa 1979] Takashi Hasegawa. *Acoustic radiation force on a sphere in a quasistationary wave field-theory*. Journal of the Acoustical Society of America, vol. 65, no. 1, page 32, 1979. (Cited on page 135.)
- [Hatfield 1999] John William Hatfield and Stephen R. Quake. *Dynamic Properties of an Extended Polymer in Solution*. Physical Review Letters, vol. 82, no. 17, page 3548, 1999. (Cited on page 150.)
- [Heemels 1998] M. W. Heemels, C. P. Lowe and A. F. Bakker. *The wavelength dependence of the high-frequency shear viscosity in a colloidal suspension of hard spheres*. Progress in Colloid & Polymer Science, vol. 110, page 150, 1998. (Cited on page 38.)
- [Higashitani 1981] Ko Higashitani, Masahiro Fukushima and Yoshizo Matsuno. *Migration of suspended particles in plane stationary ultrasonic field*. Chemical Engineering Science, vol. 36, no. 12, page 1877, 1981. (Cited on pages 134, 143 and 144.)
- [Hijón 2010] Carmen Hijón, Pep Español, Eric Vanden-Eijnden and Rafael Delgado-Buscalioni. *Mori-Zwanzig formalism as a practical computational tool*. Faraday discussions, vol. 144, page 301, 2010. (Cited on pages 167 and 171.)
- [Hinch 1975] E. J. Hinch. *Application of the Langevin equation to fluid suspensions*. Journal of Fluid Mechanics, vol. 72, no. 3, page 499, 1975. (Cited on pages 73, 96, 97 and 98.)
- [Hoogerbrugge 1992] P. J. Hoogerbrugge and J. M. V. A. Koelman. *Simulating Microscopic Hydrodynamic Phenomena with Dissipative Particle Dynamics*. Europhysics Letters, vol. 19, no. 3, page 155, 1992. (Cited on page 17.)
- [Hsieh 2003] Chih-Chen Hsieh, Lei Li and Ronald G. Larson. *Modeling hydrodynamic interaction in Brownian dynamics: simulations of extensional flows of dilute solutions of DNA and polystyrene*. Journal of Non-Newtonian Fluid Mechanics, vol. 113, page 147, 2003. (Cited on page 147.)

- [Hu 2001] Howard H. Hu, N. A. Patankar and M. Y. Zhu. *Direct Numerical Simulations of Fluid–Solid Systems Using the Arbitrary Lagrangian–Eulerian Technique*. Journal of Computational Physics, vol. 169, page 427, 2001. (Cited on page 18.)
- [Hur 2000] Joe S. Hur, Eric S. G. Shaqfeh and Ronald G. Larson. *Brownian dynamics simulations of single DNA molecules in shear flow*. Journal of Rheology, vol. 44, no. 4, page 713, 2000. (Cited on pages 153 and 158.)
- [Hütter 1998] Markus Hütter and Hans Christian Öttinger. *Fluctuation-dissipation theorem, kinetic stochastic integral and efficient simulations*. Journal of the Chemical Society, Faraday Transactions, vol. 94, no. 10, page 1403, 1998. (Cited on page 120.)
- [Jendrejack 2000] Richard M. Jendrejack, Michael D. Graham and Juan J. de Pablo. *Hydrodynamic interactions in long chain polymers: Application of the Chebyshev polynomial approximation in stochastic simulations*. Journal of Chemical Physics, vol. 113, no. 7, page 2894, 2000. (Cited on pages 115, 117 and 118.)
- [Jendrejack 2002] Richard M. Jendrejack, Juan J. de Pablo and Michael D. Graham. *Stochastic simulations of DNA in flow: Dynamics and the effects of hydrodynamic interactions*. Journal of Chemical Physics, vol. 116, no. 17, page 7752, 2002. (Cited on pages 114, 115 and 117.)
- [Johansson 2012] Linda Johansson, Johannes Enlund, Stefan Johansson, Ilia Katardjiev and Ventsislav Yantchev. *Surface acoustic wave induced particle manipulation in a PDMS channel-principle concepts for continuous flow applications*. Biomed Microdevices, vol. 14, page 279, 2012. (Cited on pages 143 and 144.)
- [Jones 2004] R. B. Jones. *Spherical particle in Poiseuille flow between planar walls*. The Journal of Chemical Physics, vol. 121, page 483, 2004. (Cited on page 116.)
- [Kaehler 2011] Goetz Kaehler and Alexander Wagner. *Cross Correlators and Galilean Invariance in Fluctuating Ideal Gas Lattice Boltzmann Simulations*. Communication in Computational Physics, vol. 9, page 1315, 2011. (Cited on page 61.)
- [Keaveny 2013] Eric E. Keaveny. *Fluctuating force-coupling method for simulations of colloidal suspensions*, 2013. (Cited on pages 67, 165 and 169.)
- [Kekre 2010] Rahul Kekre, Jason E. Butler and Anthony J. C. Ladd. *Comparison of lattice-Boltzmann and Brownian-dynamics simulations of polymer migration in confined flows*. Physical Review E, vol. 82, page 011802, 2010. (Cited on pages 60, 61, 115 and 116.)
- [Kim 2005] Sangtae Kim and Seppo J. Karrila. *Microhydrodynamics: Principles and selected applications*. Dover Publications Inc., 2005. (Cited on pages 116, 165 and 168.)
- [King 1934] Louis V. King. *On the Acoustic Radiation Pressure on Spheres*. Proceedings of the Royal Society of London A, vol. 147, page 212, 1934. (Cited on page 133.)
- [Kinsler 2000] Lawrence E. Kinsler, Austin R. Frey, Alan B. Coppens and James V. Sanders. *Fundamentals of acoustics*. John Wiley and Sons, New York, 2000. (Cited on page 145.)
- [Kirkpatrick 2013] T. R. Kirkpatrick, J. M. Ortiz de Zárate and J. V. Sengers. *Giant Casimir Effect in Fluids in Nonequilibrium Steady States*. Physical Review Letters, vol. 110, page 235902, 2013. (Cited on page 107.)

- [Kobayashi 2010] Hideki Kobayashi and Ryoichi Yamamoto. *Tumbling motion of a single chain in shear flow: A crossover from Brownian to non-Brownian behavior.* Physical Review E, vol. 81, page 041807, 2010. (Cited on page 157.)
- [Kubo 1966] R. Kubo. *The fluctuation-dissipation theorem.* Reports on progress in physics, vol. 29, no. 1, page 255, 1966. (Cited on page 100.)
- [Kwatra 2009] Nipun Kwatra, Jonathan Su, Jón T. Grétarsson and Ronald Fedkiw. *A method for avoiding the acoustic time step restriction in compressible flow.* Journal of Computational Physics, vol. 228, page 4146, 2009. (Cited on pages 48 and 52.)
- [Ladd 1990] Anthony J. C. Ladd. *Hydrodynamic transport coefficients of random dispersions of hard spheres.* Journal of Chemical Physics, vol. 93, no. 5, page 3484, 1990. (Cited on page 115.)
- [Ladd 1994] Anthony J. C. Ladd. *Numerical simulations of particulate suspensions via discretized Boltzmann equation. Part 1. Theoretical fundation.* Journal of Fluid Mechanics, vol. 271, page 285, 1994. (Cited on page 17.)
- [Landau 1987] L. D. Landau and E. M. Lifshitz. Fluid mechanics. Pergamon Press, Oxford, England, 1987. (Cited on pages 13, 15, 21, 22, 26, 28, 30, 38, 61, 65, 73, 86, 107 and 135.)
- [Larraza 1998] Andrés Larraza and Bruce Denardo. *An acoustic Casimir effect.* Physics Letters A, vol. 248, page 151, 1998. (Cited on page 107.)
- [Larson 1998] Ronald G. Larson. The structure and rheology of complex fluids. Oxford University Press, 1998. (Cited on pages 38 and 89.)
- [Larson 2005] Ronald G. Larson. *The rheology of dilute solutions of flexible polymers: Progress and problems.* Journal of Rheology, vol. 49, page 1, 2005. (Cited on page 147.)
- [Laso 1993] M. Laso and H. C. Öttinger. *Calculation of viscoelastic flow using molecular models: the CONNFFESSIT approach.* Journal of Non-Newtonian Fluid Mechanics, vol. 47, page 1, 1993. (Cited on page 103.)
- [LeDuc 1999] Philip LeDuc, Charbel Haber, Gang Bao and Denis Wirtz. *Dynamics of individual flexible polymers in a shear flow.* Nature, vol. 399, page 564, 1999. (Cited on page 147.)
- [Lee 2004] Song Hi Lee and Raymond Kapral. *Friction and diffusion of a Brownian particle in a mesoscopic solvent.* The Journal of Chemical Physics, vol. 121, page 11163, 2004. (Cited on page 98.)
- [Lehoucq 1997] R. B. Lehoucq, D. C. Sorensen and C. Yang. *ARPACK Users' Guide: Solution of Large Scale Eigenvalue Problems with Implicitly Restarted Arnoldi Methods.*, 1997. <http://www.caam.rice.edu/software/ARPACK/>. (Cited on pages 118 and 119.)
- [Lenshof 2010] Andreas Lenshof and Thomas Laurell. *Continuous separation of cells and particles in microfluidic systems.* Chemical Society Reviews, vol. 39, page 1203, 2010. (Cited on page 14.)
- [Lomholt 2001] Sune Lomholt. *Numerical Investigations of Macroscopic Particle Dynamics in Microflows.* PhD thesis, Risø National Laboratory, Roskilde, Denmark, 2001. (Cited on pages 60 and 93.)

- [Lomholt 2003] Sune Lomholt and Martin R. Maxey. *Force-coupling method for particulate two-phase flow: Stokes flow.* Journal of Computational Physics, vol. 184, page 381, 2003. (Cited on pages 65 and 115.)
- [Lowengrub 1998] J. Lowengrub and L. Truskinovsky. *Quasi-incompressible Cahn-Hilliard fluids and topological transitions.* Proceedings of the Royal Society of London A, vol. 454, page 2617, 1998. (Cited on pages 29 and 43.)
- [Lu 2008] Peter J. Lu, Emanuela Zaccarelli, Fabio Ciulla, Andrew B. Schofield, Francesco Sciortino and David A. Weitz. *Gelation of particles with short-range attraction.* Nature, vol. 453, page 499, 2008. (Cited on pages 121, 165 and 169.)
- [Lueth 2009] Christopher A. Lueth and Eric S. G. Shaqfeh. *Experimental and Numerical Studies of Tethered DNA Shear Dynamics in the Flow-Gradient Plane.* Macromolecules, vol. 42, page 9170, 2009. (Cited on pages 153 and 161.)
- [Malevanets 1999] Anatoly Malevanets and Raymond Kapral. *Mesoscopic model for solvent dynamics.* Journal of Chemical Physics, vol. 110, no. 17, page 8605, 1999. (Cited on pages 17 and 60.)
- [Marchetti 2013] M. C. Marchetti, J. F. Joanny, S. Ramaswamy, T. B. Liverpool, J. Prost, Madan Rao and R. Aditi Simha. *Hydrodynamics of soft active matter.* Review of Modern Physics, vol. 85, page 1143, 2013. (Cited on page 14.)
- [Maxey 1983] Martin R. Maxey and James J. Riley. *Equation of motion for a small rigid sphere in a nonuniform flow.* Physics of Fluids, vol. 26, no. 4, page 883, 1983. (Cited on pages 60, 68, 134, 166 and 170.)
- [Mazur 1974a] P. Mazur and D. Bedeaux. *A generalization of Faxén's theorem to nonsteady motion of a sphere through an incompressible fluid in arbitrary flow.* Physica, vol. 76, no. 2, page 235, 1974. (Cited on page 63.)
- [Mazur 1974b] P. Mazur and D. Bedeaux. *Renormalization of the diffusion coefficient in a fluctuating fluid II.* Physica, vol. 75, no. 1, page 79, 1974. (Cited on page 101.)
- [Melchionna 2011] Simone Melchionna. *Incorporation of smooth spherical bodies in the Lattice Boltzmann method.* Journal of Computational Physics, vol. 230, page 3966, 2011. (Cited on page 63.)
- [Mettin 1997] R. Mettin, I. Akhatov, U. Parlitz, C. D. Ohl and W. Lauterborn. *Bjerknes forces between small cavitation bubbles in a strong acoustic field.* Physical Review E, vol. 56, no. 3, page 2924, 1997. (Cited on page 141.)
- [Milstein 2004] G. N. Milstein and M. V. Tretyakov. Stochastic numerics for mathematical physics. Springer, 2004. (Cited on page 120.)
- [Molina 2013] John J. Molina and Ryoichi Yamamoto. *Direct numerical simulations of rigid body dispersions. I. Mobility/Friction tensors of assemblies of spheres,* 2013. (Cited on pages 165 and 169.)
- [Monaghan 1992] J. J. Monaghan. *Smoothed particle hydrodynamics.* Annual review of astronomy and astrophysics, vol. 30, page 543, 1992. (Cited on pages 18 and 60.)

- [Mori 2008] Yoichiro Mori and Charles S. Peskin. *Implicit second-order immersed boundary methods with boundary mass*. Computer methods in applied mechanics and engineering, vol. 197, page 2049, 2008. (Cited on pages 61, 69 and 82.)
- [Morrison 1998] P. J. Morrison. *Hamiltonian description of the ideal fluid*. Review of Modern Physics, vol. 70, no. 2, page 467, 1998. (Cited on pages 28 and 69.)
- [Muller 2012] Peter Barkholt Muller, Rune Barnkob, Mads Jakob Herring Jensenc and Henrik Bruus. *A numerical study of microparticle acoustophoresis driven by acoustic radiation forces and streaming-induced drag forces*. Lab on a Chip, vol. 12, no. 22, page 4617, 2012. (Cited on pages 23, 134, 166 and 170.)
- [Nakayama 2005] Yasuya Nakayama and Ryoichi Yamamoto. *Simulation method to resolve hydrodynamic interactions in colloidal dispersions*. Physical Review E, vol. 71, page 036707, 2005. (Cited on pages 60 and 63.)
- [Nguyen 2002] N.-Q. Nguyen and A. J. C. Ladd. *Lubrication corrections for lattice-Boltzmann simulations of particle suspensions*. Physical Review E, vol. 66, page 046708, 2002. (Cited on page 92.)
- [Nigam 1983] N. C. Nigam. Introduction to random vibrations (structural mechanics). MIT Press, 1983. (Cited on pages 154, 159 and 160.)
- [Nyborg 1965] W. L. M. Nyborg. *Acoustic streaming*. Physical Acoustics, vol. 2, page 265, 1965. (Cited on pages 143 and 144.)
- [Oberti 2007] Stefano Oberti, Adrian Neild and Jürg Dual. *Manipulation of micrometer sized particles within a micromachined fluidic device to form two-dimensional patterns using ultrasound*. Journal of Acoustical Society of America, vol. 121, no. 2, page 778, 2007. (Cited on pages 61 and 134.)
- [Othmer 1997] H. G. Othmer, F. R. Adler, M. A. Lewis and J. C. Dallon. Case studies in mathematical modeling-ecology, physiology, and cell biology. Prentice-Hall, 1997. (Cited on pages 45 and 175.)
- [Öttinger 2005] Hans Christian Öttinger. Beyond equilibrium thermodynamics. Wiley-Interscience, 2005. (Cited on pages 14, 26, 163 and 167.)
- [Padding 2006] J. T. Padding and A. A. Louis. *Hydrodynamic interactions and Brownian forces in colloidal suspensions: Coarse-graining over time and length scales*. Physical Review E, vol. 74, page 031402, 2006. (Cited on pages 14, 15, 17, 43, 60, 98, 99 and 126.)
- [Patankar 1980] Suhas V. Patankar. Numerical heat transfer and fluid flow. McGraw-Hill, 1980. (Cited on pages 14 and 34.)
- [Pelekasis 2004] Nikolaos A. Pelekasis, Alexandra Gaki, Alexander Doinikov and John A. Tsamopoulos. *Secondary Bjerknes forces between two bubbles and the phenomenon of acoustic streamers*. Journal of Fluid Mechanics, vol. 500, page 313, 2004. (Cited on pages 138 and 141.)
- [Peskin 2002] Charles S. Peskin. *The immersed boundary method*. Acta Numerica, vol. 11, page 479, 2002. (Cited on pages 14, 18, 60, 69, 70, 74, 75, 78, 90, 145, 165 and 169.)

- [Pinelli 2010] A. Pinelli, I. Z. Naqavi, U. Piomelli and J. Favier. *Immersed-boundary methods for general finite-difference and finite-volume Navier–Stokes solvers*. Journal of Computational Physics, vol. 229, page 9073, 2010. (Cited on page 75.)
- [Poinsot 1992] T.J Poinsot and S.K Lele. *Boundary conditions for direct simulations of compressible viscous flows*. Journal of Computational Physics, vol. 101, no. 1, page 104, 1992. (Cited on page 93.)
- [Pomeau 1975] Y. Pomeau and P. Résibois. *Time dependent correlation functions and mode-mode coupling theories*. Physics Reports, vol. 19, no. 2, page 63, 1975. (Cited on pages 98 and 99.)
- [Puliafito 2005] A. Puliafito and K. Turitsyn. *Numerical study of polymer tumbling in linear shear flows*. Physica D, vol. 211, pages 9–22, 2005. (Cited on pages 153 and 159.)
- [Quarteroni 2000] Alfio Quarteroni, Riccardo Sacco and Fausto Saleri. Numerical mathematics. Springer, 2000. (Cited on pages 42, 43 and 81.)
- [Ramshaw 1986] John D. Ramshaw and Katja Lindenberg. *Augmented Langevin Description of Multiplicative Noise and Nonlinear Dissipation in Hamiltonian Systems*. Journal of Statistical Physics, vol. 45, no. 1/2, page 295, 1986. (Cited on pages 14, 26, 27 and 163.)
- [Riese 1999] Dirk O. Riese and Gerard H. Wegdam. *Sound propagation in suspensions of colloidal spheres with viscous coupling*. Physical Review Letters, vol. 82, no. 8, page 1676, 1999. (Cited on pages 38 and 145.)
- [Ripoll 2002] Marisol Ripoll. *Kinetic Theory of Dissipative Particle Dynamics Models*. PhD thesis, UNED, 2002. (Cited on page 103.)
- [Ripoll 2005] M. Ripoll and M. H. Ernst. *Power law tails of time correlations in a mesoscopic fluid model*. Physical Review E, vol. 72, page 011101, 2005. (Cited on page 103.)
- [Risken 1989] Hannes Risken. The fokker-planck equation: Methods of solutions and applications. Springer-Verlag, 1989. (Cited on pages 27, 28 and 40.)
- [Roma 1999] Alexandre M. Roma, Charles S. Peskin and Marsha J. Berger. *An Adaptive Version of the Immersed Boundary Method*. J. Comput. Phys., vol. 153, pages 509–534, 1999. (Cited on pages 62 and 74.)
- [Römer 2013] Frank Römer, Zilin Wang, Simone Wiegand and Fernando Bresme. *Alkali Halide Solutions under Thermal Gradients: Soret Coefficients and Heat Transfer Mechanisms*. The Journal of Physical Chemistry B, vol. 117, no. 27, page 8209, 2013. (Cited on page 123.)
- [Rotne 1969] Jens Rotne and Stephen Prager. *Variational Treatment of Hydrodynamic Interaction in Polymers*. Journal of Chemical Physics, vol. 50, page 4831, 1969. (Cited on page 116.)
- [Rubinstein 2003] Michael Rubinstein and Ralph H. Colby. Polymer physics. Oxford University Press, 2003. (Cited on pages 148 and 154.)
- [Schmidt 2003] J. R. Schmidt and J. L. Skinner. *Hydrodynamic boundary conditions, the Stokes–Einstein law, and long-time tails in the Brownian limit*. Journal of Chemical Physics, vol. 119, page 8062, 2003. (Cited on page 98.)

- [Schmidt 2011] Ricardo Rodríguez Schmidt, José G. Hernández Cifre and José García de la Torre. *Comparison of Brownian dynamics algorithms with hydrodynamic interaction*. The Journal of Chemical Physics, vol. 135, page 084116, 2011. (Cited on page 117.)
- [Schroeder 2005a] Charles M. Schroeder, Rodrigo Teixeira, Eric S. G. Shaqfeh and Steven Chu. *Characteristic Periodic Motion of Polymers in Shear Flow*. Physical Review Letters, vol. 95, page 018301, 2005. (Cited on pages 153, 154 and 161.)
- [Schroeder 2005b] Charles M. Schroeder, Rodrigo E. Teixeira, Eric S. G. Shaqfeh and Steven Chu. *Dynamics of DNA in the Flow-Gradient Plane of Steady Shear Flow: Observations and Simulations*. Macromolecules, vol. 38, page 1967, 2005. (Cited on pages 116 and 147.)
- [Segrè 1993] P. N. Segrè and J. V. Sengers. *Nonequilibrium fluctuations in liquid mixtures under the influence of gravity*. Physical A, vol. 198, no. 1-2, page 46, 1993. (Cited on pages 25 and 124.)
- [Settnes 2012] Mikkel Settnes and Henrik Bruus. *Forces acting on a small particle in an acoustical field in a viscous fluid*. Physical Review E, vol. 85, page 016327, 2012. (Cited on pages 14, 133, 134, 135, 136, 137, 138, 141 and 145.)
- [Shang 2011] Barry Z. Shang, Nikolaos K. Voulgarakis and Jhih-Wei Chu. *Fluctuating hydrodynamics for multiscale simulation of inhomogeneous fluids: Mapping all-atom molecular dynamics to capillary waves*. Journal of Chemical Physics, vol. 135, page 044111, 2011. (Cited on pages 29, 129, 164, 167, 168 and 171.)
- [Skafte-Pedersen 2008] Peder Skafte-Pedersen. Acoustic forces on particles and liquids in microfluidic systems. Master's thesis, Technical University of Denmark, 2008. (Cited on page 134.)
- [Smith 1999] Douglas E. Smith, Hazen P. Babcock and Steven Chu. *Single-Polymer Dynamics in Steady Shear Flow*. Science, vol. 283, page 1724, 1999. (Cited on pages 14 and 147.)
- [Strobl 1997] G. Strobl. The physics of polymers. Springer-Verlag, 1997. (Cited on page 148.)
- [Tanaka 2010] Tomohiko Tanaka and John K. Eaton. *Sub-Kolmogorov resolution partical image velocimetry measurements of particle-laden forced turbulence*. Journal of Fluid Mechanics, vol. 643, page 177, 2010. (Cited on page 61.)
- [Teixeira 2005] Rodrigo E. Teixeira, Hazen P. Babcock, Eric S. G. Shaqfeh and Steven Chu. *Shear Thinning and Tumbling Dynamics of Single Polymers in the Flow-Gradient Plane*. Macromolecules, vol. 38, page 581, 2005. (Cited on pages 153, 156, 158 and 161.)
- [Thompson 1987] Kevin W. Thompson. *Time dependent boundary conditions for hyperbolic systems*. Journal of Computational Physics, vol. 68, page 1, 1987. (Cited on page 41.)
- [Trottenberg 2001] Ulrich Trottenberg, Cornelis Oosterlee and Anton Schüller. Multigrid. Academic Press, 2001. (Cited on page 18.)
- [Uhlmann 2005] Markus Uhlmann. *An immersed boundary method with direct forcing for the simulation of particulate flows*. Journal of Computational Physics, vol. 209, pages 448–476, 2005. (Cited on pages 60, 62 and 76.)
- [Usabiaga] Florencio Balboa Usabiaga. *fluam*, available at <https://code.google.com/p/fluam/>. (Cited on pages 14, 163, 164, 167 and 168.)

- [Usabiaga 2012] Florencio Balboa Usabiaga, John B. Bell, Rafael Delgado-Buscalioni, Aleksandar Donev, Thomas G. Fai, Boyce E. Griffith and Charles S. Peskin. *Staggered Schemes for Fluctuating Hydrodynamics*. Multiscale Modeling & Simulation, vol. 10, no. 3, page 1369, 2012. (Cited on pages 27, 44, 45, 51, 52 and 127.)
- [Usabiaga 2013a] F. Balboa Usabiaga and R. Delgado-Buscalioni. *Minimal model for acoustic forces on Brownian particles*. Physical Review E, vol. 88, no. 6, page 063304, 2013. (Cited on page 72.)
- [Usabiaga 2013b] F. Balboa Usabiaga, I. Pagonabarraga and R. Delgado-Buscalioni. *Inertial coupling for point particle fluctuating hydrodynamics*. Journal of Computational Physics, vol. 235, page 701, 2013. (Cited on page 86.)
- [Usabiaga 2013c] Florencio Balboa Usabiaga, Xiaoyi Xie, Rafael Delgado-Buscalioni and Aleksandar Donev. *The Stokes-Einstein relation at moderate Schmidt number*. The Journal of Chemical Physics, vol. 139, page 214113, 2013. (Cited on pages 15 and 130.)
- [Usabiaga 2014] Florencio Balboa Usabiaga, Rafael Delgado-Buscalioni, Boyce E. Griffith and Aleksandar Donev. *Inertial coupling method for particles in an incompressible fluctuating fluid*. Computer Methods in Applied Mechanics and Engineering, vol. 269, page 139, 2014. (Cited on pages 74 and 115.)
- [Usta 2005] O. Berk Usta, Anthony J. C. Ladd and Janson E. Butler. *Lattice-Boltzmann simulations of the dynamics of polymer solutions in periodic and confined geometries*. Journal of Chemical Physics, vol. 122, page 094902, 2005. (Cited on pages 165 and 169.)
- [Vailati 1998] Alberto Vailati and Marzio Giglio. *Nonequilibrium fluctuations in time-dependent diffusion processes*. Physical Review E, vol. 58, no. 4, page 4361, 1998. (Cited on pages 123 and 124.)
- [Vailati 2011] Alberto Vailati, Roberto Cerbino, Stefano Mazzoni, Christopher J. Takacs, David S. Cannell and Marzio Giglio. *Fractal fronts of diffusion in microgravity*. Nature communications, vol. 2, page 290, 2011. (Cited on pages 14, 19, 123, 124, 125, 126, 127, 128 and 130.)
- [Vorobev 2010] Anatoliy Vorobev. *Boussinesq approximation of the Cahn-Hilliard-Navier-Stokes equations*. Physical Review E, vol. 82, page 056312, 2010. (Cited on pages 43, 164, 167, 168 and 171.)
- [Voulgarakis 2009] Nikolaos K. Voulgarakis and Jhih-Wei Chu. *Bridging fluctuating hydrodynamics and molecular dynamics simulations of fluids*. Journal of Chemical Physics, vol. 130, page 134111, 2009. (Cited on page 39.)
- [Vázquez-Quesada 2009] Adolfo Vázquez-Quesada, Marco Ellero and Pep Español. *Smoothed particle hydrodynamic model for viscoelastic fluids with thermal fluctuations*. Physical Review E, vol. 79, page 056707, 2009. (Cited on page 103.)
- [Wang 2009] Jingtao Wang and Jurg Dual. *Numerical simulations for the time-averaged acoustic forces acting on rigid cylinders in ideal and viscous fluids*. Journal of Physics A: Mathematical and Theoretical, vol. 42, page 285502, 2009. (Cited on page 134.)
- [Wang 2011] Jingtao Wang and Jurg Dual. *Theoretical and numerical calculations for the time-averaged acoustic force and torque acting on a rigid cylinder of arbitrary size in a low viscosity*

- fluid.* Journal of Acoustical Society of America, vol. 129, no. 6, page 3490, 2011. (Cited on pages 133 and 134.)
- [Whitmer 2011] Jonathan K. Whitmer and Erik Luijten. *Influence of Hydrodynamics on Cluster Formation in Colloid Polymer Mixtures.* The Journal of Physical Chemistry B, vol. 115, page 7294, 2011. (Cited on pages 121, 165 and 169.)
- [Winkler 2006] Roland G. Winkler. *Semiflexible Polymers in Shear Flow.* Physical Review Letters, vol. 97, page 128301, 2006. (Cited on page 116.)
- [Winkler 2010] Roland G. Winkler. *Conformational and rheological properties of semiflexible polymers in shear flow.* Journal of Chemical Physics, vol. 133, page 164905, 2010. (Cited on pages 159 and 161.)
- [Yamamoto 2008] Ryoichi Yamamoto, Kang Kim, Yasuya Nakayama, Kunimasa Miyazaki and David R. Reichman. *On the Role of Hydrodynamic Interactions in Colloidal Gelation.* Journal of the Physical Society of Japan, vol. 77, page 084804, 2008. (Cited on pages 121, 165 and 169.)
- [Yeo 2010] Kyongmin Yeo and Martin R. Maxey. *Simulation of concentrated suspensions using the force-coupling method.* Journal of Computational Physics, vol. 229, page 2401, 2010. (Cited on pages 67, 165 and 168.)
- [Yosioka 1955] K. Yosioka and Y. Kawasima. *Acoustic radiation pressure on a compressible sphere.* Acustica, vol. 5, page 167, 1955. (Cited on page 133.)
- [Zhang 2009] Yu Zhang, Aleksandar Donev, Todd Weisgraber, Berni J. Alder, Michael D. Graham and Juan J. de Pablo. *Tethered DNA dynamics in shear flow.* The Journal of Chemical Physics, vol. 130, page 234902, 2009. (Cited on page 153.)
- [Zhang 2012] Yu Zhang, Juan J. de Pablo and Michael D. Graham. *An immersed boundary method for Brownian dynamics simulation of polymers in complex geometries: Application to DNA flowing through a nanoslit with embedded nanopits.* Journal of Chemical Physics, vol. 136, no. 1, page 014901, 2012. (Cited on page 116.)
- [Zhu 2002] Louding Zhu and Charles S. Peskin. *Simulation of a Flapping Flexible Filament in a Flowing Soap Film by the Immersed Boundary Method.* J. Comput. Phys., vol. 179, page 452, 2002. (Cited on page 82.)
- [Zwanzig 1975] Robert Zwanzig and Mordechai Bixon. *Compressibility effects in the hydrodynamic theory of Brownian motion.* Journal of Fluid Mechanics, vol. 69, no. 1, page 21, 1975. (Cited on pages 73, 96 and 97.)

